SAPIENZA
UNIVERSITÀ DI ROMA

Multidisciplinary modelling and parameter optimization of piezoelectric beams for energy harvesting from vibrations

University of Rome La Sapienza
Department of Mechanical and Aerospace Engineering

PhD in Theoretical and Applied Mechanics XXXIII course

Candidate
Giorgia Leonardi
Matricola 1534122

Advisor
Prof. Antonio Culla

Tutor
Prof. Daniele Dessi

Academic Year 2020/2021

Contents

Abstract

The present thesis deals with numerical and experimental modelling of energy harvesting from ambient vibrations with piezoelectric materials. The aim of the work is indeed to study the system with a multi-physics approach, describing not only the electromechanical behaviour of the device, but also its interaction with the electric conversion system closing the circuit on the external load. This holistic procedure fills a gap in past literature, in which usually mechanical and electrical description are addressed separately for this kind of devices, thus preventing from a global optimization. Indeed, finding the optimum set of material, geometrical, and electric parameters is fundamental to maximise the overall efficiency and make the power produced by the energy harvester suitable for real-life applications. Moreover, exploring optimal combinations of mechanical and electrical parameters through optimization techniques, or even new configurations, requires efficient numerical tools to evaluate a large number of times the concurrent solutions. Thus, as a second main point of thesis, reduced-order models of the electro-mechanical system are developed here to overcome problems usually occurring when interfacing computational expensive models, and are experimentally validated to demonstrate their effectiveness.

The investigated system, aimed at harvesting energy from basement vibrations, is a cantilever multi-layer structure with a unique piezoelectric lamina glued on the supporting material (unimorph configuration, like in many commercial devices), the latter being in charge of several functions: facilitating the device installation, ensuring structural integrity and mechanical stability, and avoiding charge cancellation. The connection between support layer and piezoelectric lamina is supposed to be perfect, without any loss in mechanical energy transmission. Since piezoceramics perform only if working in their narrow resonance bandwidth, the cantilevered plate configuration allows for accurate prediction of its bending frequencies with a simple and efficient layout. Indeed, the investigated device exhibits significant oscillation amplitudes at resonance frequencies under vertical basement vibrations applied at the clamped end. Nonetheless, this layout can be easily adapted for different energy sources, like wind (for fluttering flags) or waves (for wave energy converters).

Furthermore, the conversion circuit connected to the device is modelled as well, being indispensable to convert AC voltage produced by the piezoelectric harvester into a DC voltage suitable for electronic devices, and so of primary concern in building realistic energy harvesters. The circuit can also play a role in enhancing the power production, increasing the efficiency of the whole energy chain. Moreover, storage capacitance, fundamental to decouple power demand and production, is introduced. Finally, segmentation of the device electrodes in width or length is explored, showing the benefit in supporting with the conversion circuit functionalities and in avoiding charge cancellation, respectively. Being the latter not a frequent topic in a thesis of the PhD course of Theoretical and Applied Mechanics, the electric system is explained in detail to clarify every aspect of the investigated circuits behaviour.

As said previously, the system has been described with a reduced-order model (ROM), allowing an easier data exchange between piezoelectric plate and electric conversion system, and a simple interaction with the optimization algorithm. The piezoelectric plate is described as a multi-layer composite cantilevered Euler – Bernoulli beam model with non-uniform material distribution through its length. Though geometrically approximated, the beam model captures the system response in design excitation conditions. The electromechanical coupling has been introduced in the structural model by using the linear piezoelectric constitutive equations. A tip mass is positioned on the free edge to tune harvester's natural frequencies

with lower excitation frequencies and to enhance oscillations. Although a concentrated mass model is initially considered, the not-negligible mass extension and associated rotational inertia effect are later taken into account to obtain a more accurate natural frequency estimation. Finally, to simulate a non-perfect clamping, yielding in rotation, a torsional spring is added at $x = 0$. The elastic constant k_{rot} will be defined by tuning the eigenfrequencies of the structure, analytically found, with those measured in dedicating vibration testing of the simulated device. Both tip mass and yielding clamp have been introduced to better describe possible commercial and custom solutions.

By analytically developing Lagrange equations from extended Hamilton's principle including also electrical potential energy and electric load interactions, a partial differential equation system is found and then projected on the exact bending modes of the structure. Thanks to the analytical determination of the not-uniform beam modes, the developed ROM allows mechanically decoupling modal oscillators and then easily neglecting those modes not contributing to energy production. The set of ordinary differential equations is numerically solved both in MATLAB and Simulink. The electric conversion system is developed in Simulink by Simscape's blocks, allowing for a simple simulation of voltage rectifier, storage capacitance, Maximum Power Point Tracking system, and resistive load, with an easy data exchange with the ROM model.

Results on non-uniform bending modes, and thus resonance frequencies, are then compared with a 3D high-fidelity model of the harvester in Comsol Multiphysics, to show that geometrical and mechanical hypothesis do not undermine the overall consistency of the ROM.

To enhance the accuracy of the model, an identification of the torsional spring and modal damping coefficients is carried out. Then, the developed theory is compared with experiments on a prototype of the investigated energy harvester. The device is tested under sinusoidal excitation, imposed by a shaker, finding the acceleration - voltage frequency transfer function of the energy harvester for different resistive load and tip mass conditions. Experimental data and numerical results of the ROM model are found in good agreement and thus validating the developed theory.

Finally, some mechanical and electrical parameters describing the main features of the system are chosen as design variables to be optimized so as to maximise the power output. Different optimization procedures are carried out with the *patternsearch* algorithm in MATLAB, investigating the device sensitivity to parameters change and underlying the crucial co-dependency of mechanical and electrical behaviour, linked together by means of the piezoelectric effect. Moreover, it is demonstrated how an optimization procedure comprehensive of both mechanical and electrical design variables leads to better results than separate and single discipline optimizations. Finally, the optimization problem with duty cycle as design variable is explored, finding a more efficient solution than Open Circuit Voltage MPPT method, and thus, leading the way for further studies on Machine Learning MPPT implementation.

As a concluding remark, the combination of a multi-physics efficient and robust ROM model with an optimization approach constitutes the novelty proposed in this thesis to provide a useful tool for improving the design of piezoelectric energy harvesters for real life applications, paving the way for a significant increase in the device performances.

Chapter 1

Introduction

1.1 Energy harvesting: applications, energy sources, and harvesting techniques

Electronic devices have become, in the last few years, more and more important in everyday life. Although facing a quick increase of functions, their size is getting so small that we can expect them to pass from mobile to wearable soon, making self-powering a fundamental feature to be developed. However, the miniaturization and long autonomy trends are threatened by a not equivalently fast evolution of batteries, still representing a great percentage of electronics weight and an issue for maintenance because of recharge and replacement. Indeed, despite the fast growth of many electronic devices such as disk capacity, processor speed and available memory (more than 250 times in ten years) [Anton et al. 2007], battery energy density has seen an average increase rate of only 5 % since 1970 , as shown in Fig. 1.1. Indeed, in 2018 the highest energy density achieved was still below 400 Wh/kg, with a likely maximum increase in performance of only 10 % per year (Fig. 1.2), due to challenges connected with optimal balance among battery components and to development of new materials combinations [Winter et al. 2018].

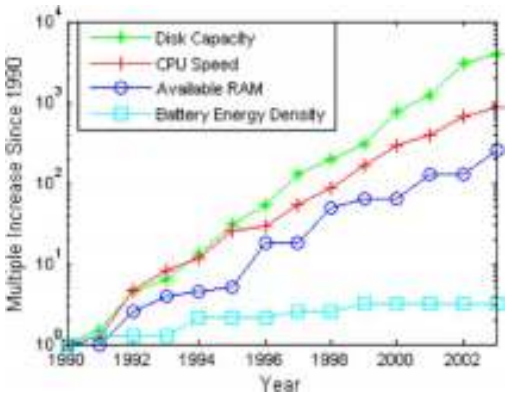

Figure 1.1: Development of some electronic devices since 1990 [Anton et al. 2007].

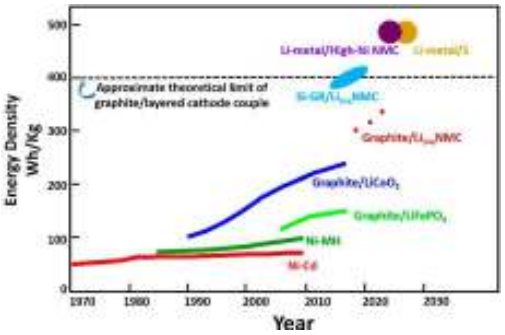

Figure 1.2: Energy density evolution for different battery technologies [Winter et al. 2018].

Therefore, a new powering solution is spreading: energy harvesting, the direct conversion of ambient energy into electricity, making battery recharge or even direct device powering possible with no need for grid connection. Indeed, despite growth in functions, nowadays electronics need very low amounts of energy, as shown with some examples in Table 1.1 and Fig. 1.3, especially in fields like Internet of Things (IoT), Wireless Sensor Networks (WSNs), Home Automation, and Human Health.

Table 1.1: Examples of average power consumption for electronic devices [Priya 2007] [Sojan et al. 2016] [Sachan et al. 2012] [Jackson; Olszewski, et al. 2017] [Anton et al. 2007] [Khan 2016].

Electronic device	Average power consumption [mW]
TV controller	100
Small FM radio	30
Leadless pacemaker	$5\text{-}10 \cdot 10^{-3}$
Blood coagulation monitor	500
Temperature sensor	0.5-5
Pressure sensor	10-15
Accelerometer	2
Microprocessor	0.05

Figure 1.3: Power consumption for electronic devices and potential power supply gaps covered by different energy sources [Todaro et al. 2018].

WSNs are constituted by a high number of spatially spread, autonomous electronic devices, able to collect data from the environment and send them to a central location. WSNs can be employed for example in structural health monitoring for bridges [H.-J. Jung et al. 2011] [Gaglione et al. 2018], railways [Tianchen et al. 2014], and roads [Moure et al. 2016], with accelerometers, displacements and force sensors, strain gauges, and optical fibres powered by energy recovering from vibrations with energy harvesters (EHs), in order to avoid frequent maintenance. Another interesting application is energy recovery from pressure fluctuations due to circuit instabilities or heat change for health monitoring of hydraulic systems. Different configurations have been studied, from piezoelectric stack interface membranes [Aranda et al. 2017] [Monroe et al. 2017] (Fig. 1.4b), to piezoelectric cylindrical tubes proposed by Zhou *et al.* [M. Zhou et al. 2018].

Energy harvesting can also be useful in applications where external power sources cannot be employed, as in Human Health Engineering. For example, a leadless pacemaker can be powered by MEMS piezoelec-

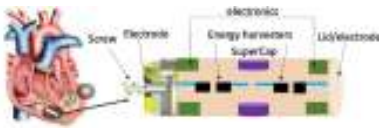

(a) *Pacemaker located in the right ventricle (left) and schematic representation of piezoelectric energy harvesters and storage supercapacitors (right) [Jackson; Olszewski, et al. 2017].*

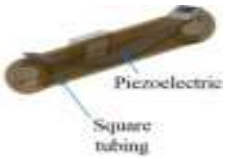

(b) *Piezoelectric energy harvester inside oscillating heat pipe harvesting energy from pressure fluctuations due to non-uniform steam [Monroe et al. 2017].*

Figure 1.4: Examples of health monitoring in Humans (a) and hydraulic systems (b).

tric energy harvesters, exploiting shock induced by low-frequency, high acceleration vibrations of the heart (Fig. 1.4a) [Jackson; Olszewski, et al. 2017], or a knee can be monitored by wireless-transmitting sensors with energy recovery from knee motion itself [Kuang et al. 2016].

Finally, local power production can be useful for many different IoT applications even when grid connection is available. Indeed, a large number of autonomous electronic devices would also mean relevant savings in cabling and easier plants structures, whether this is about industrial production of smart appliances or sensing for pollution control in cities and so on. For instance, on roads, vibration energy recovery could power surface temperature monitoring and anti-icing systems [Morita et al. 2000] [Pan et al. 2015] or traffic devices [Moure et al. 2016]. An example is Lybra, run by Underground Power SRL, a smart speed absorber recovering energy (1 kWh/100 cars) from braking in areas where a vehicle is expected to reduce the speed for safety reasons, like the entrance of a petrol station, as shown in Fig. 1.5a [Power n.d.]. Another application is the one proposed by Maurya *et al.* [Maurya et al. 2018], in which with energy harvesting smart tires pressure is controlled by strain sensing and wireless data transfer.

(a) *Lybra project run by Underground Power [Power n.d.].*

(b) *Piezoelectric tiles installation at the Tokyo Station's Yaesu North Exit [Company 2008].*

(c) *Dance Floor tiles powering the Off Corso disco in Rotterdam [Roosegaarde n.d.].*

(d) *Example of self-powered wireless switch produced by Illumra [Illumra n.d.].*

Figure 1.5: Applications of distributed energy production and consumption.

More in general, energy harvesting could work in synergy with other renewables (photovoltaic, microwind, geothermal,...) for applications both off-grid, like in small islands, mountain huts, or developing Countries with not spread national electric grid, and grid-connected, in a distributed generation scenario. For example, in both frameworks piezoelectric tiles could work, like proposed by Sharpes *et al.* [Sharpes; Vučković, et al. 2016], to power presence sensors and home automation devices. A similar idea has been tested inside Tokyo Station's Yaesu North Exit by the JR East [Company 2008] with a power-generating floor at ticket gates (Fig. 1.5b) aimed to satisfy energy demand of the led lighting system and, in the future, part of the station's facilities (displays, ticket gates,...). Same application can be found in Nederland at the Off Corso, an eco-disco project carried out by Studio Roosegaarde [Roosegaarde n.d.] in Rotterdam, producing

up to 25 W per piezoelectric tile of Sustainable Dance Floor by exploiting dance steps (Fig. 1.5c) and then powering lights and DJ booth. Despite these examples, energy harvesting in general could be very useful in building automation, saving in cabling by powering wireless devices, such as switches (Fig. 1.5d) and IoT sensors.

Before designing an EH, the energy source to exploit must be taken into account. In Fig. 1.6 [Boisseau; Despesse, and Seddik 2012] energy densities for the main sources are reported. The radiant source provided by the sun in outdoor environments seems the most attractive, but it depends on weather and night hours, and thus, not being available continuously, needs high capacity storages to supply energy constantly. Thermal sources can be easily exploited by thermocouples thanks to the Seebeck effect, with productivity limited by the Carnot efficiency, but rarely adequate temperature gradients are available [Mateu et al. 2005]. Thus, mechanical energy sources are the most interesting, being represented mainly by different forms of kinetic energy: vibrations, air flow, and human motion. To exploit them, three different electromechanic energy harvesters are mainly used: electrostatic (EEH), magnetic induction (MEH), and piezoelectric (PEH). However, although dealing with the same energy sources, these three kind of EH are very different from each other and, since not being industrially spread yet, there is no standardized efficiency definition to compare them to each other. Despite this, a brief overview of the three EHs will be now given.

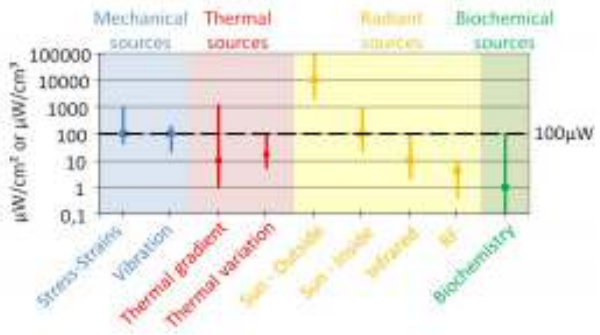

Figure 1.6: Power densities for different energy sources [Boisseau; Despesse, and Seddik 2012].

Electrostatic devices are based on the variation of distance between the electrodes, inducing a change in quantity of dielectric material interposed and, consequently, in capacitance. Through this phenomenon, the capacitor gets charged and discharged, producing energy. EEHs are suitable for miniaturization, but smaller sizes also induce voltage decrease, not suitable for common electronic applications. Moreover, the device needs an external voltage source to work. An example of EEH is the one proposed by Boisseau *et al.* [Boisseau; Despesse; Ricart, et al. 2011], in which a cantilevered electrode exploits vibration induced oscillations with respect to an external fixed electret to produce a change in capacitance, as shown in Fig. 1.7b. Being the power proportional to the mobile mass, a tip mass is added to increase energy production. Another interesting configuration is the honeycomb structure presented by Tashiro *et al.* [Tashiro et al. 2002], with capacitance increasing with compression and decreasing with expansion of an internal gas (Fig. 1.7a). The EEHs are also suitable for wind applications, like the one, shown in Fig. 1.7c, proposed by Perez *et al.* [Perez et al. 2015]. A PTFE membrane undergoes to periodic oscillations due to flutter, thus changing its distance from the upper and lower electrodes.

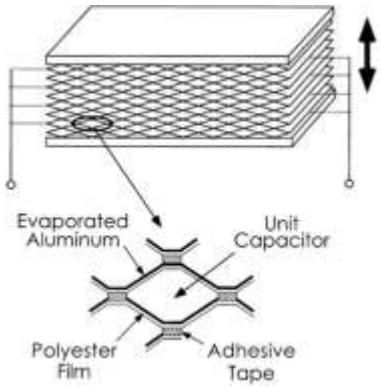

(a) *Honeycomb structure of the EEH proposed by Tashiro et al. [Tashiro et al. 2002].*

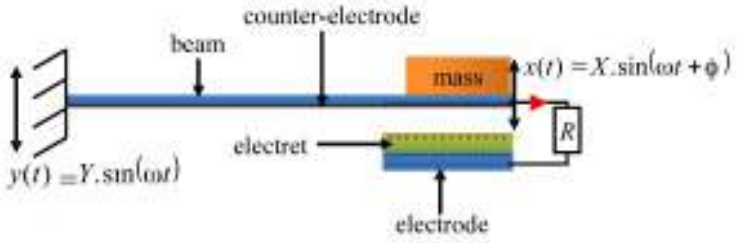

(b) *Cantilevered EEH proposed by Boisseau et al. [Boisseau; Despesse; Ricart, et al. 2011].*

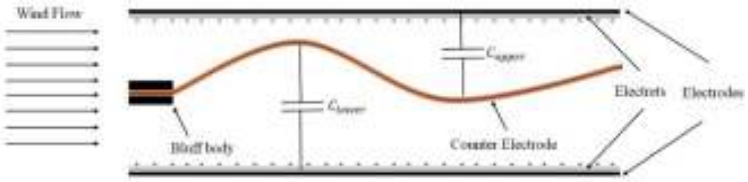

(c) *Fluttering EEH proposed by Perez et al. [Nabavi et al. 2016].*

Figure 1.7: Examples of electrostatic energy harvesters.

Magnetic induction Energy Harvesters are based on Faraday's law: an electric field is generated by varying the magnetic flux through an electric circuit. Usually the effect is induced with a magnet moving with respect to a coil. The energy produced is proportional to the coil area, making MEHs not particularly suitable for miniaturization. Moreover, these devices produce a relatively low voltage. A typical MEH configuration consists of an inertial mass moving in response to external forces and storing mechanical energy in springs, resonating at frequency higher than the excitation one and thus activating the magnetic transducer. This frequency increased generator is suitable for recovery of any external kinetic energy, such as human-induced vibrations [Halim et al. 2014] like hand-shaking (Fig. 1.8c), or vibrations of civil structures like bridges [Galchev; McCullagh, et al. 2011] (Fig. 1.8a). As for EEHs, also MEHs can be used to harvest energy from air flows, as proposed, for example, by Weimer *et al.* [Weimer et al. 2006], presenting an horizontal axis turbine with magnets on rotor and coils on stator (Fig. 1.8b).

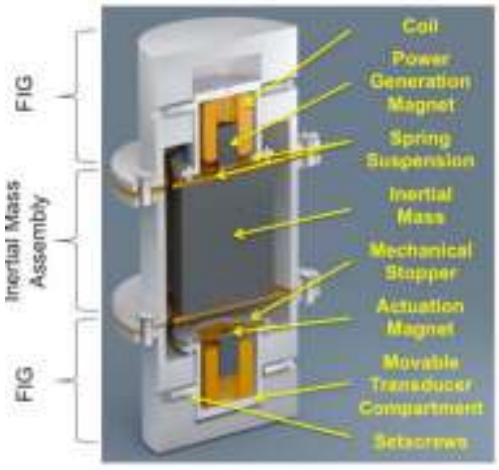

(a) *Representation of MEH proposed by Galchev et al. for bridge vibrations recovery [Galchev; McCullagh, et al. 2011].*

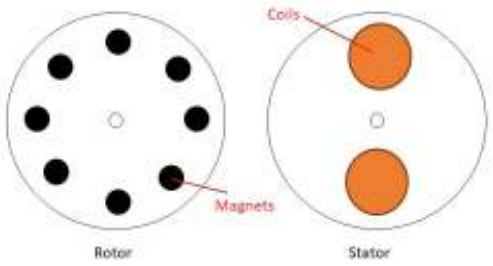

(b) *Schematic representation of rotor and stator for the axial-flux alternator in the magnetic energy harvester by Weimer [Nabavi et al. 2016].*

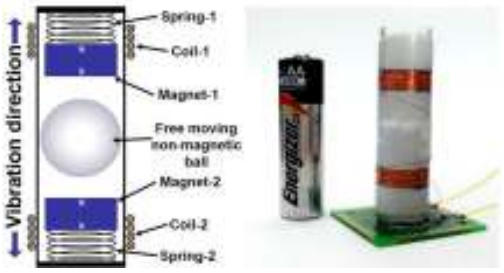

(c) *MEH for hand-shaking energy recovery proposed by Halim et al. [Halim et al. 2014].*

Figure 1.8: Examples of magnetic induction energy harvesters.

Finally, PEHs are based on piezoelectric materials, producing superficial electric charge when undergoing to external stress, and show voltage levels suitable for electronics applications. The most performing piezoelectric materials are ceramic (typically PZT), but they have an high energy efficiency only in narrow bands close to their resonance frequencies. Thus, many piezoceramic devices are design to tune their resonance frequencies with the main frequency of vibration sources, like the bimorph resonator studied by Lu *et al.* [Lu et al. 2003] (Fig. 1.9a), or to work with shock-induced free vibrations, like the clam shell-structure PEH in the shoe's heel proposed by Shenck *et al.* [Shenck et al. 2001] (Fig. 1.9e). Other PEHs exploit polymeric piezoelectric materials, less performing than piezoceramics but working with good efficiencies for wider frequency bands. An example is the the raindrop harvester [Ilyas et al. 2015] [Acciari et al. 2018], shown in Figures 1.9b and 1.9c, working with PVDF (polyvinylidene fluoride), a flexible piezoelectric material suitable for outdoor and shock excitation applications, being fatigue and corrosion resistant. The same material has been used by Li *et al.* [Li et al. 2009] in the stalk of a polymer flapping leaf (Fig. 1.9d) and by Shenck *et al.* [Shenck et al. 2001] in the front of the shoe.

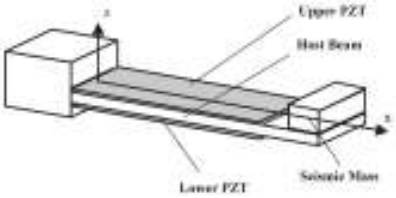

(a) *Bimorph piezoelectric resonant energy harvester proposed by Lu et al. [Lu et al. 2003].*

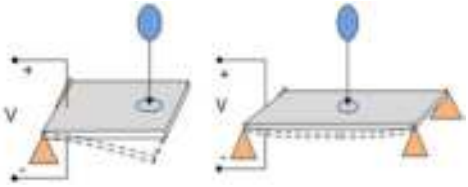

(b) *Energy harvesting from raindrop impact: single PEH in clamped-free (left) and clamped-clamped (right) configuration [Acciari et al. 2018].*

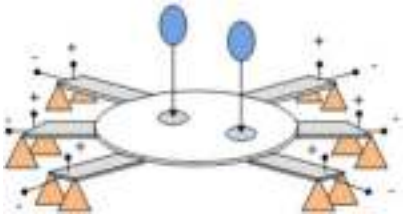

(c) *Energy harvesting from raindrop impact: multi-PEH configurations [Acciari et al. 2018].*

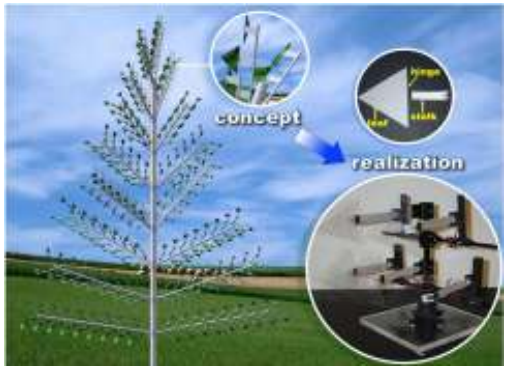

(d) *Piezoelectric wind energy harvester proposed by Li et al. [Li et al. 2009].*

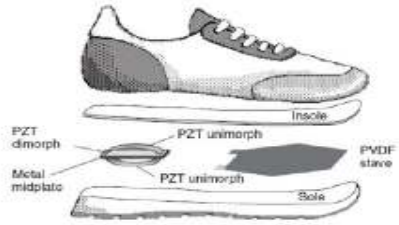

(e) *Schematic representation of the piezoelectric shoe proposed by Shenck et al. [Shenck et al. 2001].]*

Figure 1.9: Examples of piezoelectric energy harvesters.

Although perceived as the less mature among these technologies [AL-Oqla et al. 2018] and difficult to be integrated in microsystems, PEHs are the most promising among the three main mechanical energy harvesters, showing a magnitude of energy density three times higher than EEHs and MEHs, as shown in Fig. 1.10. Thus the following sections will give a further insight on PEHs technologies and modelling.

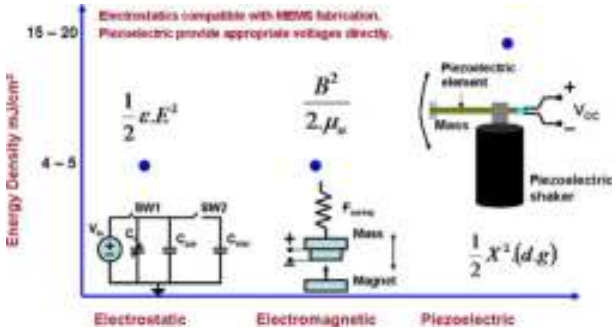

Figure 1.10: Comparison of the three main energy harvesting technologies with respect to their energy density [Priya 2007]. In the figure ϵ is the dielectric constant, E is the electric field, B is the magnetization, X is the stress, d is the piezoelectric strain constant, and g the piezoelectric voltage constant.

1.2 Piezoelectric energy harvesters technology

Piezoelectric harvesters are widely studied for kinetic energy recovery from low-frequency (<100 Hz) phenomena, like vibrations or fluid flows. For this reason, the device in cantilevered configuration, allowing for large mechanical strain and characterized by a relatively low resonance frequency of the fundamental flexural mode, is the most commonly used in literature. In particular, the main configurations are the unimorph (Fig. 1.11(a)) and the bimorph (Fig. 1.11(b)), both having a support layer carrying out a structural function, the first with only one piezoelectric lamina and the latter with two. Piezoelectric layers have top and bottom electrodes to collect the charge produced. Moreover, to further lower the natural frequency and enhance oscillations amplitude, a proof mass is typically positioned at the tip of the beam. Although bimorphs have more active material, unimorphs are useful for micro-electromechanical systems (MEMS), being of easier manufacturing with existing micro-fabrication techniques [H. Liu et al. 2018].

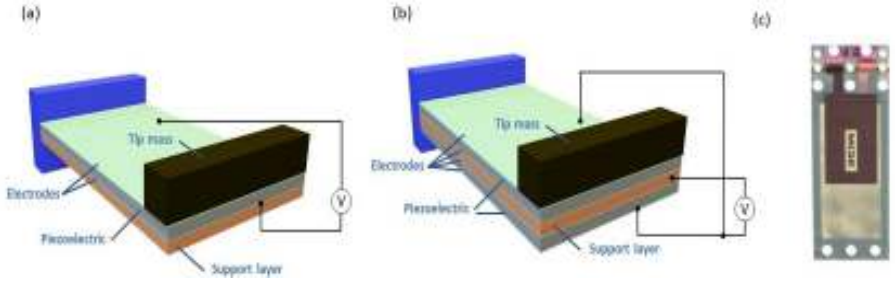

Figure 1.11: Typical piezoelectric energy harvester in cantilevered configurations: unimorph (a) and bimorph (b). The proof mass on the free edge enhances oscillation amplitude and tunes the first bending mode frequency with the excitation frequency. (c) shows a commercial PEH device produced by MIDE in unimorph configuration.

Most research is focused on rectangular piezoelectric layers because of their easy implementation and high stress distribution, although other shapes could be more suitable in some applications. For example Jia and Seshia explored five different piezoelectric material distribution, shown in Fig. 1.12, finding that only a cantilever with coupled subsidiary beams (b) could outperform the classical shape (a) [Jia and Seshia 2016].

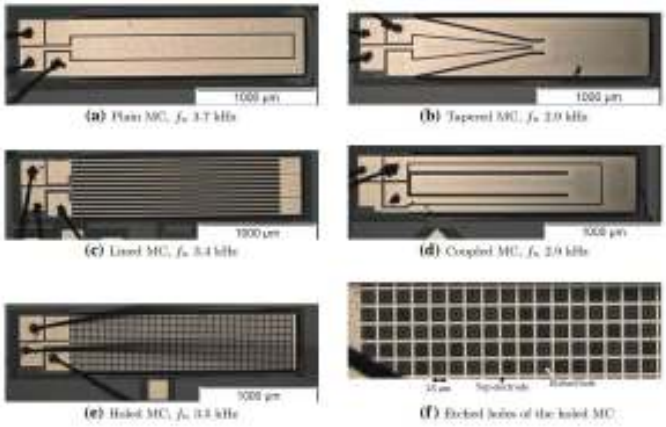

Figure 1.12: Five cantilevered beams with different piezoelectric material distribution [Jia and Seshia 2016].

Besides high resonance frequencies, PEHs suffer also for good transduction efficiency only in a narrow frequency bandwidths, close to the resonance condition (Fig. 1.13). Although this issue can be fixed with proof mass tuning for sinusoidal excitations, usually in nature energy sources exhibit random spectra, and then more complicated solutions are needed.

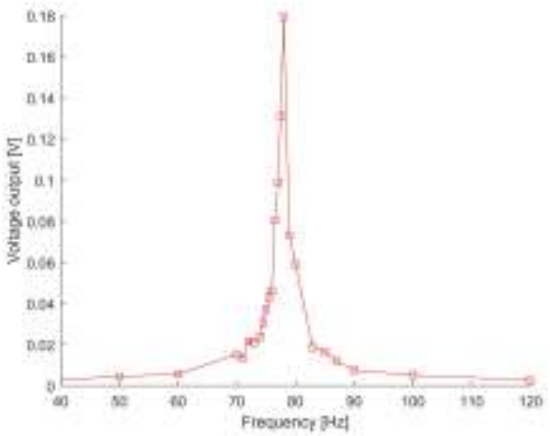

Figure 1.13: Voltage output of a typical PEH in function of the frequency. The performing area is achieved in a narrow interval in the neighbourhood of the resonance frequency of the device.

In this section then the most relevant frequency tuning and bandwidth widening techniques will be investigated and compared in performance, underlying though how they have not brought yet to definitive solutions and trying to explain why.

1.2.1 Frequency lowering techniques

As previously mentioned, one of the main issues of piezoelectric energy harvesters is frequency tuning of the device resonance condition with the external excitation. This can be achieved by reducing the natural frequency of the PEH with a tip mass or an increase of the device footprint and complexity. Jia and Seshia [Jia and Seshia 2015] have investigated the effect of tip mass distribution on the beam structure, finding the optimum configuration for linear PEHs with a mass occupying 60-70 % of the beam length. Jackson *et al.* [Jackson; Stam, et al. 2015] have studied a liquid filled tip mass (Fig. 1.14b). The sliding fluid behaves like a non-linear mass distribution for high amplitude and low frequency excitations, since the centre of mass changes depending on the oscillations. This phenomenon alters the resonance frequency, thus broadening the bandwidth without excessively affecting the voltage peak value. Moreover, 50 % of filled mass was found to give the maximum frequency bandwidth, with fluid viscosity to be decreased for low-energy excitations. From the other hand, Jia *et al.* [Jia; Arroyo, et al. 2018] proposed a MEMS PEH interdigitated fork array, as shown in Fig. 1.14a, obtaining a reduction in resonant frequency by only changing the beam length, with no need for tip mass.

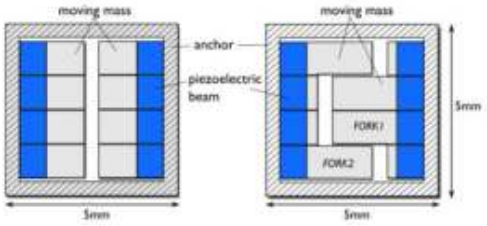

(a) *Comparison between a classical cantilever (left) and the low-frequency PEH proposed by Jia et al. [Jia; Arroyo, et al. 2018].*

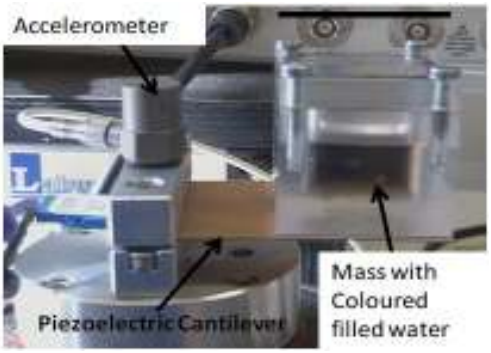

(b) *Piezoelectric energy harvester with liquid filled tip mass proposed by Jackson et al. [Jackson; Stam, et al. 2015].*

Figure 1.14: Examples of frequency lowering in piezoelectric energy harvesting with tip mass or surface change.

However, since, in particular for MEMS applications, a tip mass could threaten the device structural integrity and higher surfaces suffer for charge cancellation due to torsional modes, shapes different form the traditional cantilevered plate have been investigated [Priya; Song, et al. 2019].

One widely studied solution is the Zigzag-shape cantilever. Abdelmoula *et al.* [Abdelmoula; Sharpes; H. Lee, et al. 2016] have derived the optimal power output from higher order modes of the device in Fig. 1.15a, proving that torsional modes contribution is fundamental in this configuration [Abdelmoula; Sharpes; Abdelkefi, et al. 2017] and that power production depends on proof masses [H. Lee et al. 2018]. The Inman group investigated frequency dependence on beam length and number of segments [S. Zhou; W. Chen, et al. 2017] and proof masses (Fig. 1.15b). Moreover, they also demonstrated that the harvester can recover energy from vibrations in different directions [S. Zhou; J. D. Hobeck, et al. 2017]. Finally, The group provided a case study for wireless sensing application by successfully testing the device on vibration data collection from a pumping station [Essink et al. 2017].

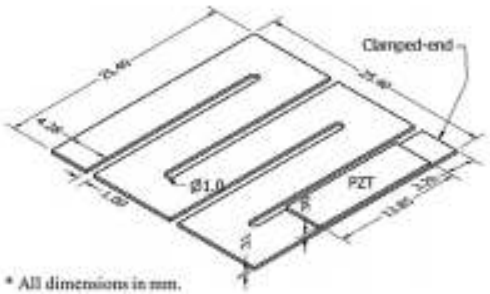

(a) *Two-dimensional PEH with large joint blocks as proof mass proposed by Abdelmoula et al. [H. Lee et al. 2018].*

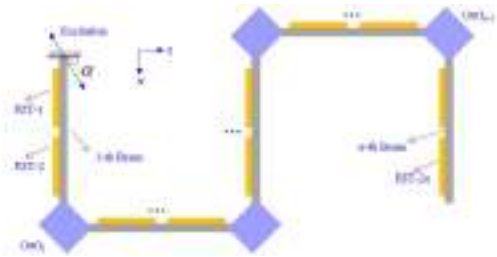

(b) *Two-dimensional PEH proposed by Zhou et al. [H. Lee et al. 2018].*

Figure 1.15: Examples of Zigzag-shaped piezoelectric energy harvesters.

Another popular shape adopted for piezoelectric energy harvesters is the spiral, bringing even MEMS

devices to very low resonance frequency [Song; P. Kumar; Maurya, et al. 2017] and having a foot print smaller than the Zigzag structures one [R. P. Varghese 2013]. Spirals natural frequency is proportional to number of turns, but Deterre *et al.* [Deterre et al. 2013] demonstrated that voltage decreases after 5 turns due to charge cancellation of higher order modes. The device presented, shown in Fig. 1.16a, is thought to power a pacemaker by harvesting energy from blood pressure variations. Dos Santos *et al.* [Santos et al. 2018] presented an orthogonal spiral structure, combining the simplicity of zigzag cantilevers with spiral compactness, as shown in Fig. 1.16b.

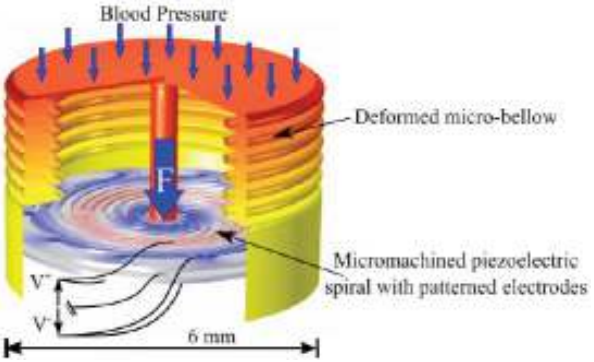

(a) *Device for energy harvesting from blood pressure variations proposed by Deterre et al. [Deterre et al. 2013].*

(b) *Orthogonal spiral device proposed by Dos Santos et al. [Santos et al. 2018].*

Figure 1.16: Examples of spiral-shaped piezoelectric energy harvesters.

A modification of the Zigzag shape is the arc-based structure proposed by Apo [Apo 2014], a cantilevered made of purely circular arc segments, with the first bending mode being dominant in structure strains. Among the configurations proposed, the S-shaped and C-shaped exhibited lower frequencies and higher tip displacements for lower stiffness and mass conditions if compared to ArcSimple and ArcZigzag, all shown in Fig. 1.17a.

Another interesting configuration is the two-dimensional elephant-shape beam by Sharpes *et al.* , shown in Fig. 1.17b. The device was first compared with the Zigzag shape through experiments and simulations, identifying the area with the highest concentrated stress where the piezoelectric must be placed [Sharpes; Abdelkefi, and Priya 2015]. Then first and second mode of the structure were investigated via finite element simulations, demonstrating that both are exploitable for power production, with frequency tuning possible by properly proof mass placing [Sharpes; Abdelkefi; Abdelmoula, et al. 2016].

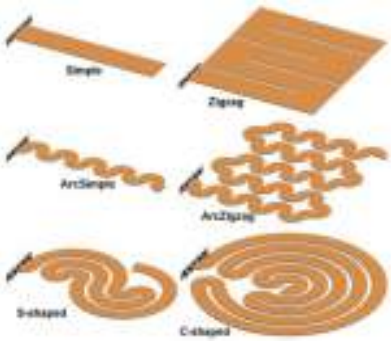

(a) *Different arc-based shapes for MEMS PEHs for low-frequency structures [Apo 2014].*

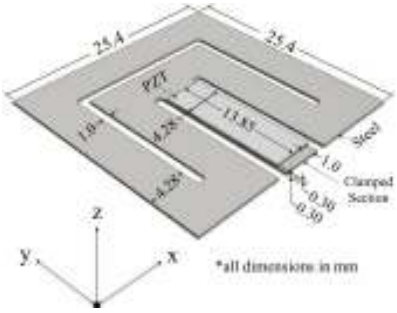

(b) *Elephant-shape two-dimensional PEH proposed by Sharpes et al. [Sharpes; Abdelkefi; Abdelmoula, et al. 2016].*

Figure 1.17: Examples of complex shapes for piezoelectric energy harvesters

1.2.2 Active self-tuning techniques

Another frequency lowering and tuning solution proposed in literature is the active self-tuning technique, adjusting the resonance frequency of the device by altering the centre of mass or the spring stiffness of the system.

A piezoelectric clamped-clamped beam with a proof mass in the centre was proposed by Leland and Wright first [Leland et al. 2006] and by Hu *et al.* then [Hu et al. 2007]. The resonance frequency is tuned by changing an axial compressing preload and thus the stiffness of the system, as shown schematically in Fig. 1.18a. Challa *et al.* [Challa et al. 2008] worked on a cantilevered PEH with magnetic tip mass, having a repulsive interaction with external magnets, as shown in Fig. 1.18b. By varying magnets distance from the beam, a natural frequency tuning of $\pm 20\,\%$ is obtained. The magnetic interaction could be used also as variable axial compressive load, as shown by Ayala-Garcia *et al.* [Ayala-Garcia et al. 2010].

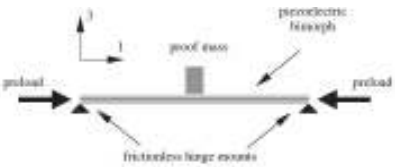

(a) *Piezoelectric harvester in clamped-clamped configuration with stiffness adjustment via variable axial compressive preload [Leland et al. 2006].*

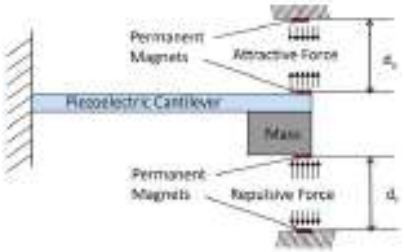

(b) *Piezoelectric harvester with centre of mass adjustment via magnetic interaction [Challa et al. 2008].*

Figure 1.18: Examples of active self-tuning piezoelectric energy harvesters.

However, active self-tuning systems require actuators, consuming almost all the produced energy, as analytically demonstrated by both Roundy and Zhang [Roundy et al. 2005], and Zhu *et al.* [D. Zhu et al. 2010]. Thus, this technique is not widely studied if compared with all the other solutions presented in this section.

1.2.3 Multi-frequency techniques

The multi-frequency technique aims to widen the bandwidth by exploiting multiple resonant modes at discrete frequencies. Indeed, by acting on mass and stiffness (particular shapes, proof mass, etc.) of the PEH, it is possible to obtain resonance frequencies of different modes close to each other, overlapping their bands and thus widening the device total bandwidth (Fig. 1.19).

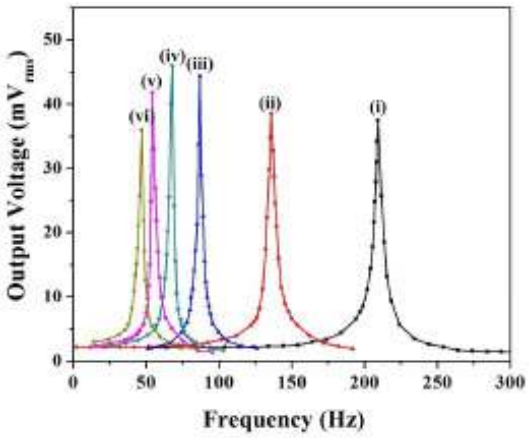

Figure 1.19: Example of frequency bands overlapping for different modes of the structure [Song; P. Kumar; Sriramdas, et al. 2018].

Very different from each others, the examples of this technique in literature are many. Vullers *et al.* [Vullers et al. 2012] presented a stack of cantilevered piezoelectric beams attached at the tip of an external metallic plate, as shown in Fig. 1.20a, creating a coupled resonator. Thanks to high mass and stiffness of the system, a power amplification of more than 51 times was obtained. Rezaeisarav *et al.* [Rezaeisaray et al. 2015] proposed a device, shown in Fig. 1.20b, exhibiting first, second and third mode frequencies close to each other and within a range suitable for ambient vibration recovery. Berdy *et al.* [Berdy et al. 2012] utilized the sensor node electronics for structural condition monitoring as a distributed proof mass, as shown in Fig. 1.20d, allowing for two modes exploitation. Iannacci *et al.* [Iannacci; Serra, et al. 2014] [Iannacci; Sordo, et al. 2016] proposed a four-leaf clover shape, a four petal-like mass-spring system which can be exploited for many resonant frequencies. The piezoelectric patches are on the top of the petals and the proof masses are placed on the bottom to adjust the frequency modes, as shown in Fig. 1.20c.

Song *et al.* [Song; P. Kumar; Sriramdas, et al. 2018] presented an array of piezoelectric beams with different natural frequencies and magnet as tip masses, as shown in Fig. 1.20e. Different from all the previous applications, the vibration of all the beams on a wide frequency is due to magnetic induction and not to mass-spring optimization, although frequency bands overlapping is still present. Indeed, if one PEH resonates, the magnetic mass interacts with the others, inducing oscillations in the remaining beams. Moreover, this device can harvest energy from both vibrations and electromagnetic fields.

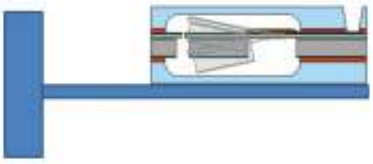

(a) *Coupled resonator proposed by Vullers et al. [Vullers et al. 2012].*

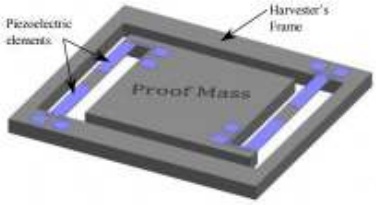

(b) *Device proposed by Rezaeisaray et al. [Rezaeisaray et al. 2015].*

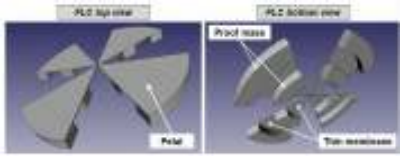

(c) *Four-leaf clover device proposed by Iannacci et al. [Iannacci; Sordo, et al. 2016].*

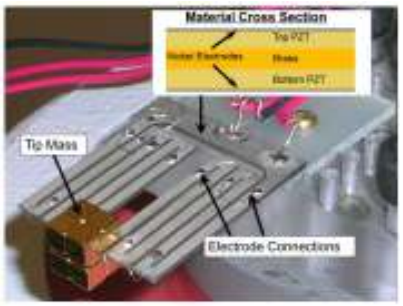

(d) *Device proposed by Berdy et al. [Berdy et al. 2012].*

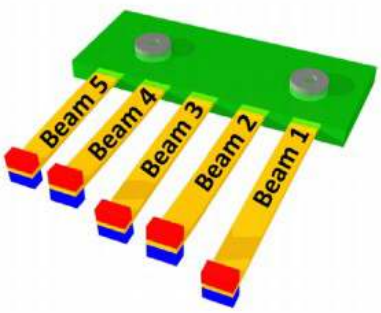

(e) *Piezoelectric beams array proposed by Song et al. [Song; P. Kumar; Sriramdas, et al. 2018].*

Figure 1.20: Examples of multi-frequency piezoelectric energy harvesters.

Although promising in performance, this method suffers for high footprint and thus low power density.

1.2.4 Frequency-up conversion techniques

Since low frequency harvesters typically produce less power and have narrow frequency bandwidth, another good solution can be the Frequency Up-conversion mechanism (FU).

One FU approach consist in inducing free vibrations in the piezoelectric beam via impact. This FU can be coupled with the Multi-modal technique (see Sec. 1.2.3). Yu *et al.* [Yu et al. 2015] proposed a PEH in which vibrations are transmitted through a cylindrical spring system hitting the piezoelectric beams, as shown in Fig. 1.21a. The vertical spring allows a three dimensional response to external vibrations and a bandwidth widening. Zhang *et al.* [H. Zhang et al. 2017] proposed a similar device. A bracket supported by a spring has bimorph piezoelectric on the walls and a free bead on the inside, as shown in Fig. 1.21b. Low-frequency excitations are sufficient to induce collisions of the steel ball on the piezoelectrics, that freely vibrate. Viñolo's group [Toma et al. 2013] [Viñolo et al. 2013] [Carlos Viñolo et al. 2013] used these impact approach with a pendulum mechanism inside buoys for wave energy converting, shown in Fig. 1.21c. The pendulum oscillates with the periodical wave motion and hits the cantilevered piezoelectric beams.

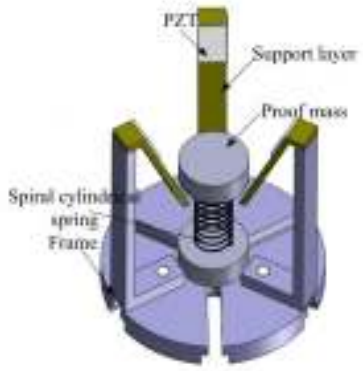

(a) *Device proposed by Yu et al. [Yu et al. 2015].*

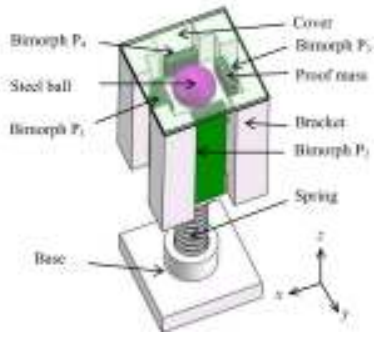

(b) *Device proposed by Zhang et al. [H. Zhang et al. 2017].*

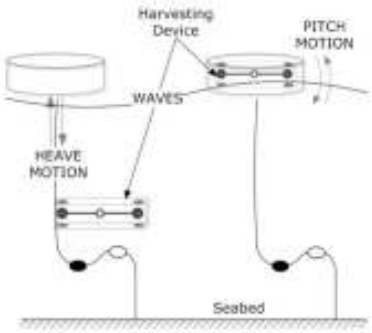

(c) *Device proposed by Viñolo et al. [Viñolo et al. 2013].*

Figure 1.21: Examples of impact-based FU piezoelectric energy harvesters.

Zhang *et al.* [J. Zhang et al. 2016] proposed a slightly different FU technique with a high resonance frequency piezoelectric cantilever (HFGB) driven by ropes attached to a low-frequency beams (LFDB) array, as shown in Fig. 1.22. Although the action is transmitted by ropes instead of impact, the piezoelectric beam experiences free vibration as in the previous applications.

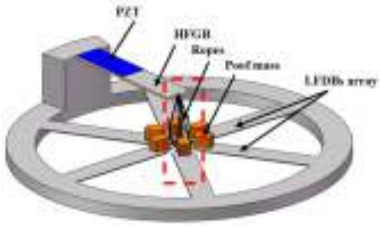

Figure 1.22: Multi-frequency piezoelectric energy harvester proposed by Zhang *et al.* [J. Zhang et al. 2016].

Another FU approach exploits plucking, with a plectrum inducing tip displacement in piezoelectric cantilevers. However, this technique suffers for difficult adjusting of the overlapping distance for optimal working condition. Pozzi *et al.* [Pozzi and M. Zhu 2011] [Pozzi; Aung, et al. 2012] proposed a plucking device for knee wearable applications with rotating piezoelectric bimorphs deflected by plectrums on a stator, as shown in Fig. 1.23a. A similar configuration has been used by Priya [Priya; C.-T. Chen, et al. 2004] Priya 2005 for a windmill (Fig. 1.23b), with plectrums placed on the rotor to allow fixed electrical connection of the harvesters on the stator.

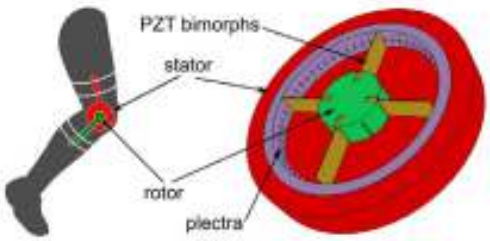

(a) *Device proposed by Pozzi et al. [Pozzi and M. Zhu 2011].*

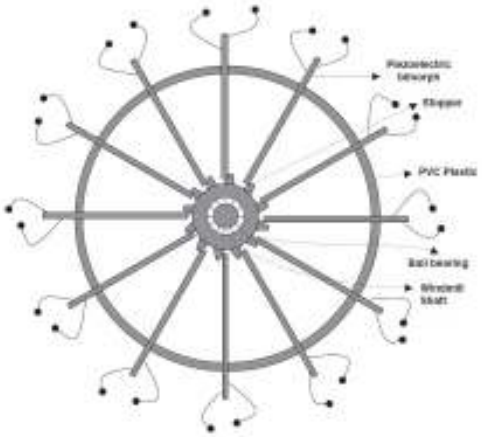

(b) *Device proposed by Priya et al. [Priya 2005].*

Figure 1.23: Examples of plucking-based FU piezoelectric energy harvesters.

Impact and plucking FU may cause PEH breakage and fatigue damages, thus shorter life [Kuang et al. 2017]. For this reason other solutions have been developed.

The buckling FU technique allows for high amplitude oscillations in off-resonance conditions, although the snap-through needs relatively high accelerations to occur. Despite classified here as FU, the snap-through is a bistable behaviour (further investigated in 1.2.5) with high displacement and velocity of energy orbits, but not depending on the excitation frequency (thus with wide bandwidth). Jung *et al.* [S.-M. Jung et al. 2010] presented a device made of blucked slender bridges with a central proof mass (Fig. 1.24a), that, when snapping through, induces free vibrations at high acceleration in the attached piezoelectric cantilevered beams. The similarly buckled bridge proposed by Han and Yun [Han et al. 2014], with piezoelectric cantilevers placed on the central proof mass (Fig. 1.24b), exhibits a lower snap-through threshold thanks to the flexible sidewalls. Inman's group widely studied the buckling phenomenon for energy harvesting [Betts et al. 2013] [Tavakkoli et al. 2015] [Emam and Daniel J. Inman 2015] [Emam; J. Hobeck, et al. 2017] [A. J. Lee et al. 2018], using the piezoelectric for both power production and initial condition setting (Fig. 1.24c). Another interesting application is the one proposed by Zhu and Zu [Y. Zhu et al. 2013], in which the buckling phenomenon is enhanced by a magnetic proof mass interacting with external magnets (Fig. 1.24d). Buckling has been obtained also with axial pre-loads [Ravindra Masana et al. 2013] [Masana et al. 2012], sometimes coupled with proof mass in the centre of the beam [Xu et al. 2013].

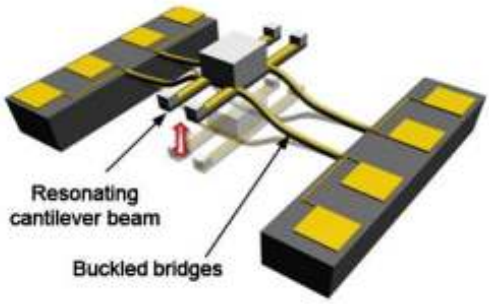

(a) *Device proposed by Jung et al. [S.-M. Jung et al. 2010].*

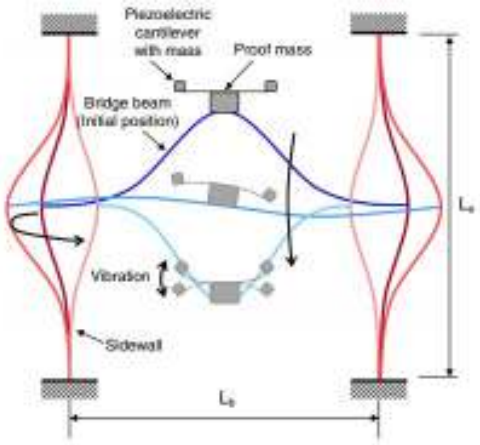

(b) *Device proposed by Han and Yun [Han et al. 2014].*

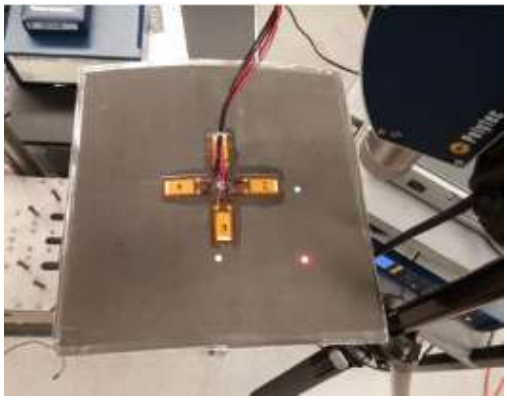

(c) *Device proposed by Inman group [Emam; J. Hobeck, et al. 2017].*

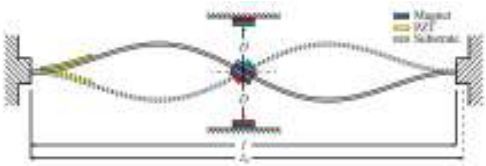

(d) *Device proposed by Zhu and Zu [Y. Zhu et al. 2013].*

Figure 1.24: Examples of buckling FU piezoelectric energy harvesters.

Finally, to overcome the acceleration threshold issue of the buckling FU technique, a magnetic force-induced FU method is used. Fan *et al.* [Fan; Chang, et al. 2015] proposed four piezoelectric beams with magnetic tip masses coupled with a ferromagnetic ball, shown in Fig. 1.25a. The device can harvest vibrations energy in perpendicular direction with the classical basement excitation or in horizontal direction thanks to the ball moving and inducing tip displacements in beams. Pillatsch *et al.* [Pillatsch; Yeatman, and Holmes 2014] [Pillatsch; Yeatman; Holmes, and Wright 2016] and similarly Ramezanpour *et al.* [Ramezanpour et al. 2016] proposed devices for human motion energy recovery. A pendulum with a magnetic tip interacts with an external fix magnet and performs the frequency-up conversion, as shown in Fig. 1.25b, making the PEH suitable for human motion applications. Karami *et al.* [Karami et al. 2013], claiming that piezoelectric harvesters are more efficient than a small electromagnetic transducer, developed a vertical axis wind turbine with magnets attached to blades, inducing oscillation in piezoelectric beams positioned underneath in tangential (left) or radial (right) configuration, as shown in Fig. 1.25c.

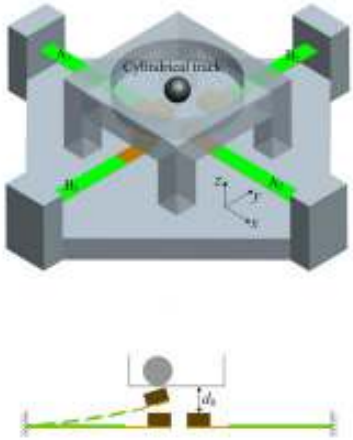

(a) *Device proposed by Fan et al. [Fan; Chang, et al. 2015].*

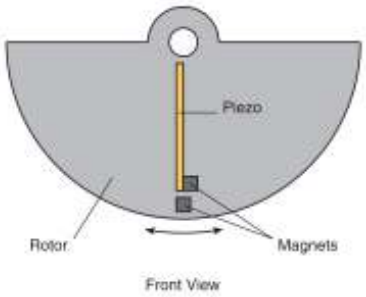

(b) *Device proposed by Pillatsch et al. [Pillatsch; Yeatman, and Holmes 2014].*

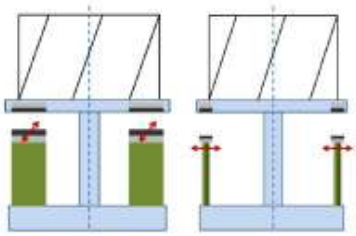

(c) *Device proposed by Karami et al. [Karami et al. 2013].*

Figure 1.25: Examples of magnetic-induced FU piezoelectric energy harvesters.

1.2.5 Non-linear frequency broadband techniques

Another technique to widen the frequency bandwidth is the introduction of non-linearities, expressed in term of Duffing potential $U(x)$. Spontaneous non-linearities can occur due to large strain deflections or non-linear piezoelectricity, although they have limited effect, being usually negligible, and are difficult to be controlled. Anyway, they also can be induced by introducing magnetic or mechanical restoring forces $F(x)$.

The following equations give the Duffing potential and restoring force expressions respectively.

$$U(x) = \frac{1}{2}k_1(1-\gamma)x^2 + \frac{1}{4}k_3x^4 \tag{1.1}$$

$$F(x) = \frac{dU(x)}{dx} = k_1(1-\gamma)x + k_3x^3 \tag{1.2}$$

where k_1 is the linear stiffness coefficient, varying in function of γ in the neighbourhood of its nominal value, x is the displacement, and k_3 is the non linear stiffness coefficient [Daqaq; Ravindra Masana, et al. 2014]. The restoring force and the Duffing potential depend on γ and $\delta = k_3/k_1$, coefficient of cubic non-linearity or non-linearity strength. If $\delta = 0$ and $\gamma < 1$, non-linearities are negligible and the PEH has a linear behaviour, with a restoring force linear function of the displacement. In Fig. 1.26 the restoring force (a) and potential energy (b) are shown for different non-linear conditions, depending on γ and δ.

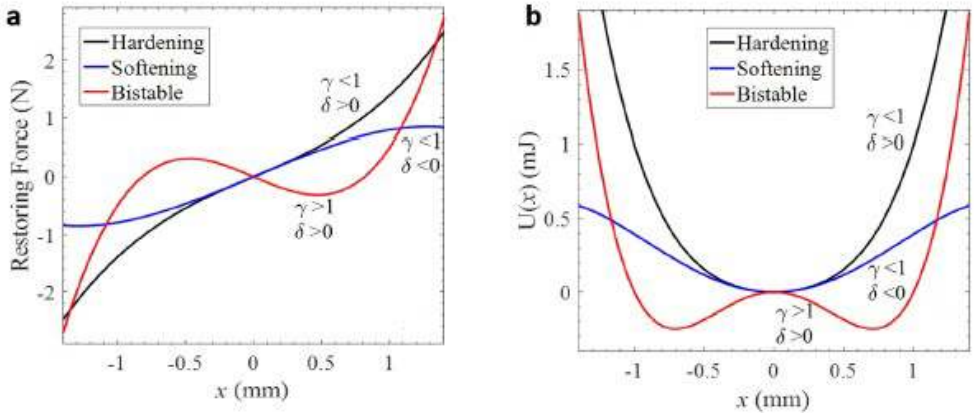

Figure 1.26: Monostable (hardening and softening) and bistable behaviours of PEHs in restoring force (a) and Duffing potential energy (b) [H. Liu et al. 2018].

The non-linear monostable condition occurs when $\gamma \leq 1$ and the coefficient of cubic non linearity is whether $\delta > 0$, with hardening restoring force increasing with displacement, or $\delta < 0$, with softening restoring force decreasing with displacement.

In case of $\gamma > 1$ and $\delta > 0$ the structure faces bistability, with two equilibrium points, or potential wells, divided by a potential barrier, inversely proportional to δ in both high and length. A shallow potential well allows for easier inter-well oscillations, resulting in high strains and thus increased power production.

Monostable devices

As seen before, non-linear monostable condition can be of hardening or softening type. As shown in Fig. 1.27, the frequency response curve bends right or left if respectively a hardening or softening non-linearity occurs. The B_r and B_n branches correspond respectively to the resonant and non-resonant behaviours, while the part in dashed line is the unstable condition. For instance, a PEH with hardening non-linearity undergoing to a frequency sweep up follows the resonant branch until the upper saddle-node bifurcation point is reached, and then jumps and continues moving on the non-resonant branch, if frequency keeps increasing. An analogous behaviour can be seen for the softening non-linearity condition.

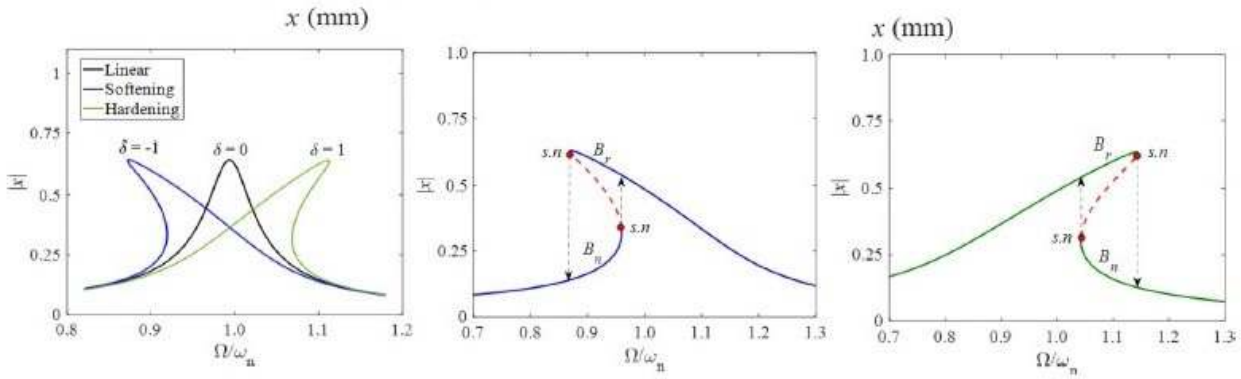

Figure 1.27: Linear and non-linear monostable response in function of frequency [H. Liu et al. 2018].

Thus, non-linear monostable resonance depends on the non-linearity kind, on the initial condition, and on whether the frequency is increasing or decreasing, making a unique solution difficult to be identified. Indeed, a non-linear monostable PEH exhibits resonance only if an initial condition is imposed, although actuators consume additional power. Moreover, the monostable non-linearity is relevant only with high excitation levels [Sebald et al. 2011b] and, in case of electrical load optimization for impedance matching, an output power increases corresponds to a frequency band shrinkage. Although there is still no design tool to predict the non-linear monostable behaviour under random excitation, it has been experimentally shown that hardening non-linear devices do not outperform linear ones, while softening non-linear harvesters can [Nguyen et al. 2010].

To induce non-linearities, magnetic interaction is typically used. One of the first applications has been presented by Stanton *et al.* [Stanton; McGehee, et al. 2009]. A magnetic proof mass has been placed on the free end of a cantilevered piezoelectric beam, interacting with external magnets, as shown in Fig. 1.28a. By changing the external magnets distance from the clamping, softening or hardening non-linearities have been obtained. With a similar configuration, Sebald *et al.* [Sebald et al. 2011a] have introduced a fast voltage burst to change the initial condition and thus always induce the higher branch solution, although with an energetic cost. Fan *et al.* [Fan; Tan, et al. 2018] have proposed a device with attractive external magnet and mechanical stoppers to contain the oscillation amplitude (Fig. 1.28b). A softening non-linearity has been obtained, producing a great improvement in bandwidth (54 %) and power output (253 %) with respect to the analogous linear device.

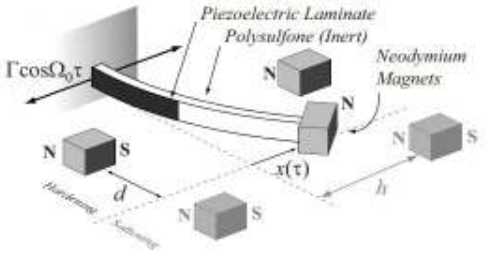

(a) *Schematic representation of the device proposed by Stanton et al. [Stanton; McGehee, et al. 2009].*

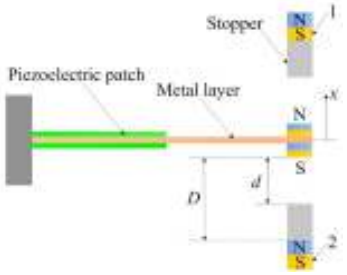

(b) *Schematic representation of the device proposed by Fan et al. [Fan; Tan, et al. 2018].*

Figure 1.28: Examples of magnetic induced non-linear monostable piezoelectric energy harvesters.

Axial pre-loads represent another method to induce monostable non-linearities. For example, Masana and Daqaq [Ravindra Masana et al. 2011] [Ravindra Masana et al. 2013] proposed a bimprph PEH in clamped-clamped configuration (Fig. 1.29a) with a static compressive axial load, adjusting the device natural frequency for both sinusoidal and band-limited noisy excitations. This configuration can be whether monostable or bistable depending on the axial load being respectively lower or higher than a critical buckling condition. Another clamped-clamped harvesters has been studied [Marzencki et al. 2009] [Hajati et al. 2011], although differently pre-stressed with a central proof mass (Fig. 1.29b).

Despite enhanced power production and frequency broadband with respect to the linear configuration, non-linear monostable energy harvesters typically need high acceleration amplitudes ($\geq$1 g) for non-linearities to be relevant, making difficult for them to suit real-life vibration sources.

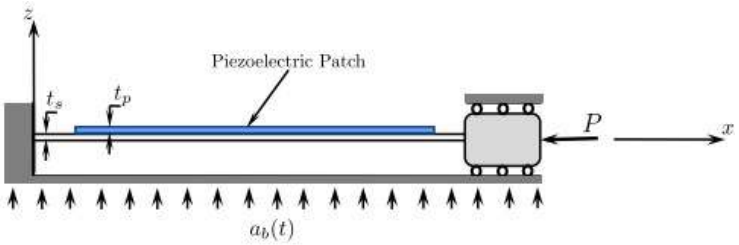

(a) *Schematic representation of the device proposed by Masana and Daqaq [Ravindra Masana et al. 2011].*

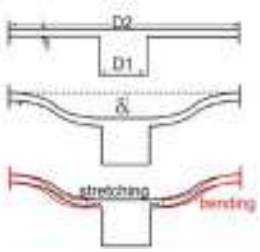

(b) *Schematic representation of the device proposed by Hajati and Kim [Hajati et al. 2011].*

Figure 1.29: Examples of pre-load induced non-linear monostable piezoelectric energy harvesters.

Bistable devices

As mentioned before, bistable energy harvesters are characterized by two equilibrium points (potential wells). Depending on vibration amplitude levels, a device can experience intra-well, chaotic, or inter-well oscillations. The first occur for low-energy vibrations, when the beam oscillates around one single potential well, acting like a monostable device under softening non-linearity. As the acceleration amplitude reaches a threshold, chaotic (random amplitude) or inter-well (high amplitude) oscillations between the two potential wells occur. Erturk *et al.* [Erturk; Hoffmann, et al. 2009] [Erturk and Daniel J. Inman 2011a] [Erturk and Daniel J. Inman 2011b] have found that inter-well oscillations induce large-orbit response, producing more power and wider frequency bandwidth than linear PEHs. Moreover, De Paula *et al.* [De Paula et al. 2015] compared bistable, linear monostable and non-linear monostable devices, confirming that bistable devices are more performing if working in the inter-well oscillation region. However, identifying the threshold acceleration is not sufficient to activate the inter-well oscillation, since a unique solution does not exist to avoid the chaotic response (like in non-linear monostability). To overcome this issue, a correlation between the main parameters (potential shape, electromechanical coupling, damping, excitation levels) and the bistability phenomenon should be known. However, non-linear bistable energy harvesters still suffer for lack of analytical tools to characterize their actual performance under sinusoidal and random excitations. Indeed, numerical and experimental investigations still do not provide evident correlations between parameters and oscillation conditions, thus making control difficult to be performed [Daqaq; Ravindra Masana, et al. 2014].

The three most common bistable PEH configurations are shown in Fig. 1.30, with bistability induced by (a) magnetic attraction (MAI), (b) magnetic repulsion (MRI), and (c) mechanical pre-loading (MPI) [H. Liu et al. 2018].

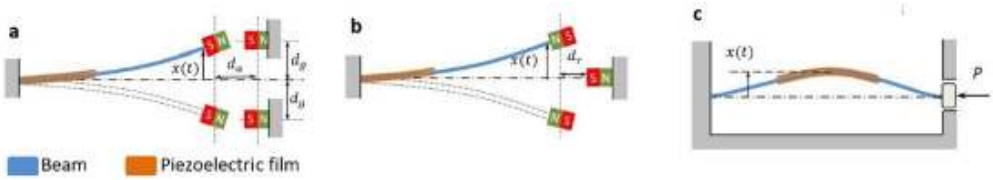

Figure 1.30: Three most common bistable PEH configurations: (a) magnetic attraction induced (MAI), (b) magnetic repulsion induced (MRI), and (c) mechanical preload induced (MPI) [H. Liu et al. 2018].

The MPI device is the same seen for monostability, but with axial load overcoming the buckling threshold, as seen for Masana and Daqaq [Ravindra Masana et al. 2011] [Ravindra Masana et al. 2013] in the previous section.

Zhao and Erturk [Zhao et al. 2013] have demonstrated that the MAI bistable configuration outperforms its monostable linear counterpart only for a specific excitation interval, corresponding to the inter-well oscillation. Indeed, for very low excitation levels, the monostable behaviour is more efficient than the bistable one. Moreover, under broadband stochastic excitations, bistable devices can be advantageous only if the excitation intensity is high, otherwise a monostable PEH is more robust and practical. Zhou *et al.* [S. Zhou; Cao; Erturk, et al. 2013] [Cao; S. Zhou; Daniel J. Inman, et al. 2015b] have investigated the influence of external magnets angle on a MAI device, shown in Fig. 1.31a, demonstrating that the frequency bandwidth can be enhanced by optimizing magnets orientation. The same configuration has been further investigated by the same group [Cao; S. Zhou; Daniel J Inman, et al. 2015a] [Cao; Syta, et al. 2015], analysing both chaotic and inter-well oscillations behaviour, and verifying the device's effectiveness in human motion applications [Cao; Wang, et al. 2015]. A slightly different configuration has been proposed (Fig. 1.31b) [S. Zhou; Cao; Daniel J Inman; S. Liu, et al. 2015], introducing impact induced excitation to provide an adequate initial condition that enables inter-well oscillations also for low-energy vibrations.

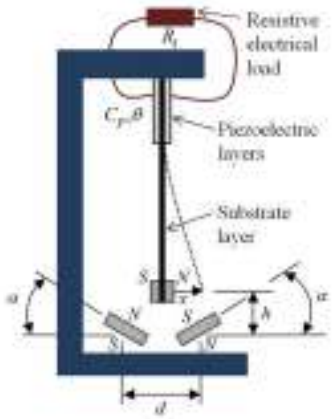

(a) *MAI bistable device with external magnets variable angle proposed by Zhou et al. [S. Zhou; Cao; Erturk, et al. 2013].*

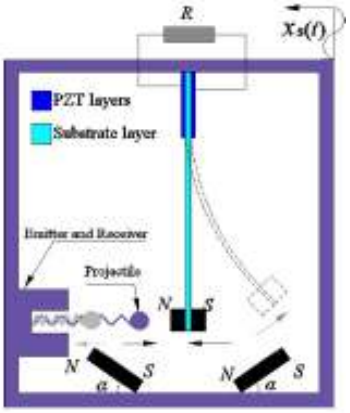

(b) *MAI bistable device with impact excitation proposed by Zhou et al. [S. Zhou; Cao; Daniel J Inman; S. Liu, et al. 2015].*

Figure 1.31: Examples of magnetic attraction induced bistable piezoelectric energy harvesters.

An example of the magnetic repulsive induced bistable PEH has been proposed by Ferrari *et al.* [Marco Ferrari et al. 2010] [Ferrari et al. 2011], who have studied the device response to white noise vibrations, finding, under proper coupling of the external magnet, a 400 % improvement of rms voltage output with respect to an analogous linear harvester. However, bistable PEHs respond well to white noise only if the electrical time constant is very high, and then the voltage is proportional to displacement instead of velocity [Cottone et al. 2009].

Multi-stable devices

Zhou *et al.* [S. Zhou; Cao; Daniel J Inman; Jing Lin, et al. 2014] have designed a magnetic field induced multi-stable harvester with three potential wells, shown in Fig. 1.32, by setting the external magnet angle of the bistable device in Fig. 1.31a at 90°. Compared to the bistable one, the tristable PEH has lower potential barriers, obtaining inter-well oscillations for a lower activation threshold, and thus generating high power output on a wider frequency bandwidth. The same group have investigated the influence of the potential well depth on the harvesting performance, changing magnet distance to each other d, and vertical distance from the bender h [Cao; S. Zhou; Wang, et al. 2015], as shown in Fig. 1.33. They have found d to be directly proportional to the two external potential wells depth, and h to the central potential well depth. Wang *et al.* [Wang; Cao; Bowen; S. Zhou, et al. 2017] [Wang; Cao; Bowen; Daniel J Inman, et al. 2018] have applied the tristable PEH to human motion, verifying its effectiveness and finding the optimal resistive load.

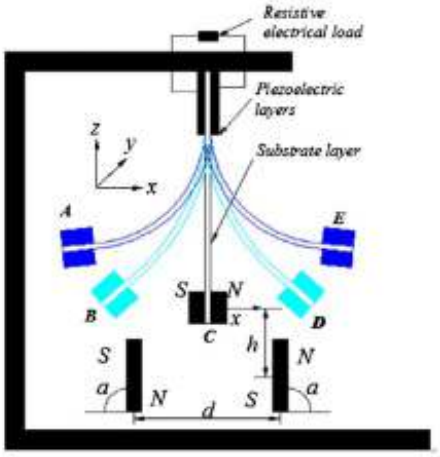

Figure 1.32: Tristable piezoelectric energy harvester proposed by Zhou *et al.* [S. Zhou; Cao; Daniel J Inman; Jing Lin, et al. 2014].

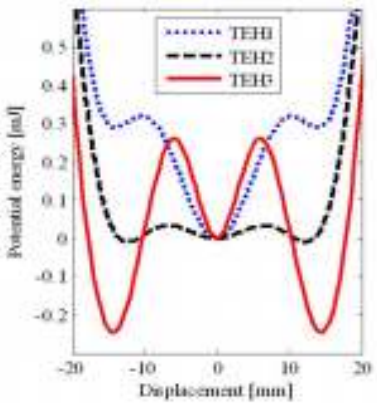

Figure 1.33: Tristable potential energy function proposed by Cao *et al.* [Cao; S. Zhou; Wang, et al. 2015].

Zhou *et al.* [Z. Zhou et al. 2017] proposed a magnet repulsion induced quadstable harvester , as shown in Fig. 1.34, with four potential wells characterized by low potential barriers. Indeed, the threshold in excitation amplitude is much lower than the bistable one, allowing also in this application for greater energy production and wider frequency band. Moreover, the same group [Z. Zhou et al. 2018] has investigated the dependence of energy potential on distance among the magnets and distance between external magnets and beam free end, optimizing the output for a given excitation intensity.

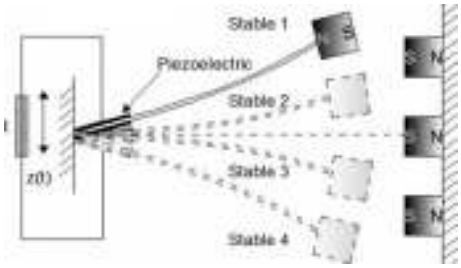

Figure 1.34: Quadstable piezoelectric energy harvester proposed by Zhou *et al.* [Z. Zhou et al. 2017].

1.2.6 Parametric resonance based techniques

Parametric resonance deals with device parameters periodic change due to external forcing (heteroparametric resonance or parametric resonance) or to internal excitation performed by connections among different modes of a multiple degree-of-freedom system (autoparametric resonance). This phenomenon potentially can both widen the frequency band gap and increase power density of the PEH. However, to induce the parametric resonance, an amplitude and frequency critical condition have to be reached [Daqaq; Stabler, et al. 2009], being sometimes too onerous to be exploited [Jia 2020], also considering that higher parametric resonance orders show only for low damping coefficients [Turner et al. 1998].

Jia *et al.* [Jia; Du, et al. 2018b] proposed a micromachined membrane, with proof masses enhancing nonlinearities, that exhibits over a hundred order parametric resonance (Fig. 1.35a). The same group presented also a coupled pendulum-lever system with a spring giving an initial condition on the cantilever [Jia; Yan; Soga, et al. 2014] and thus lowering the parametric resonance threshold more than one order of magnitude. The device had increased power output and frequency bandwidth with respect to a direct resonance, thanks to vibration amplitude enhancement. Both devices exhibited high orders parametric resonance thanks to a low damping, enabling the instability region [Jia 2020]. Indeed, although more suitable for MEMS scales [Jia; Du, et al. 2018a], parametric resonance higher orders can be useful to widen the frequency bandwidth [Jia 2020], even if providing frequency band windows smaller than the one of the first order. Jia *et al.* [Jia; Yan; Du, et al. 2018] also demonstrate that parametric resonance based devices are suitable for real-life applications, such as vibration energy recovery from bridges and vehicle's engines.

Galchev *et al.* [Galchev; Aktakka, et al. 2012] presented a device to harvest low-frequency non-periodic vibrations with parametric resonance. As shown in Fig. 1.35b, an internal mass is suspended inside the box and, responding to vibration, stores energy in springs. When the spring force overcomes the magnetic action, the mass is pulled away and the spring resonates together with the piezoelectric beam.

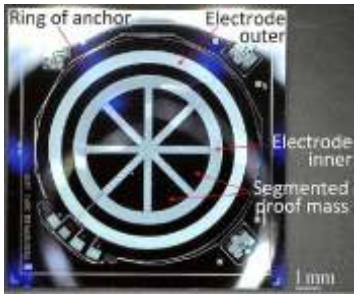

(a) *Device proposed by Jia et al. [Jia; Du, et al. 2018b].*

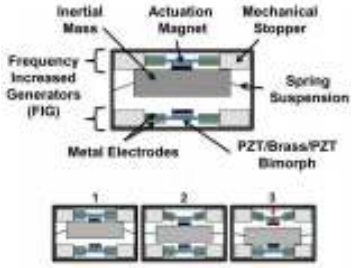

(b) *Device proposed by Galchev et al. [Galchev; Aktakka, et al. 2012].*

Figure 1.35: Examples of parametric resonance based devices

1.3 Piezoelectric energy harvesting techniques: comparison and challenges

1.3.1 Remarks on current status of harvester design

In the previous sections many techniques for frequency tuning and bandwidth widening have been presented. To better compare their performance to the Linear Monostable configuration and to each other, the power output per volume of active piezoelectric material (*Power/Piezoelectric volume* in $[\mu W/mm^3]$) in function of the excitation level (acceleration amplitude in [g]) has been calculated and reported in Fig. 1.36 for different PEH. Only tests under sinusoidal excitations are taken into account. The desired working area has high power density, ensuring good performance, for low vibration levels, since typically ambient vibrations are characterized by low accelerations. Low frequency energy harvesters have power density close to the Linear Monostable configuration, since they aim more to frequency tuning than to efficiency improvement. Conversely, Frequency Up-converters seems to be one of the most performing kind of PEH, since the structure vibrates at its resonance frequency for any the external excitation. However, the best FUs are non-linear (with buckling bistability and magnetic induced non-linear monostability), needing indeed high acceleration amplitudes to be performing and thus being not suitable for real-life applications. Also the Non-linear Monostable configuration has high power density, but, as mentioned before, to perform at low acceleration levels, it strictly depends on the initial condition, setting which requires additional energy consumption. Similarly, the Bistable device outperforms the Linear Monostable configuration only under inter-well oscillations, induced by high acceleration amplitude or a properly set initial condition. Additional energy consumption is required as well for the Active Self-tuning devices, vanishing in the end the advantage in power production gained with fine frequency tuning. Parametric devices have no clear behaviour since they still need further investigations. Finally, Multi-frequency PEHs seem promising, but they need a precise device characterization and comprehension of mechanical behaviour.

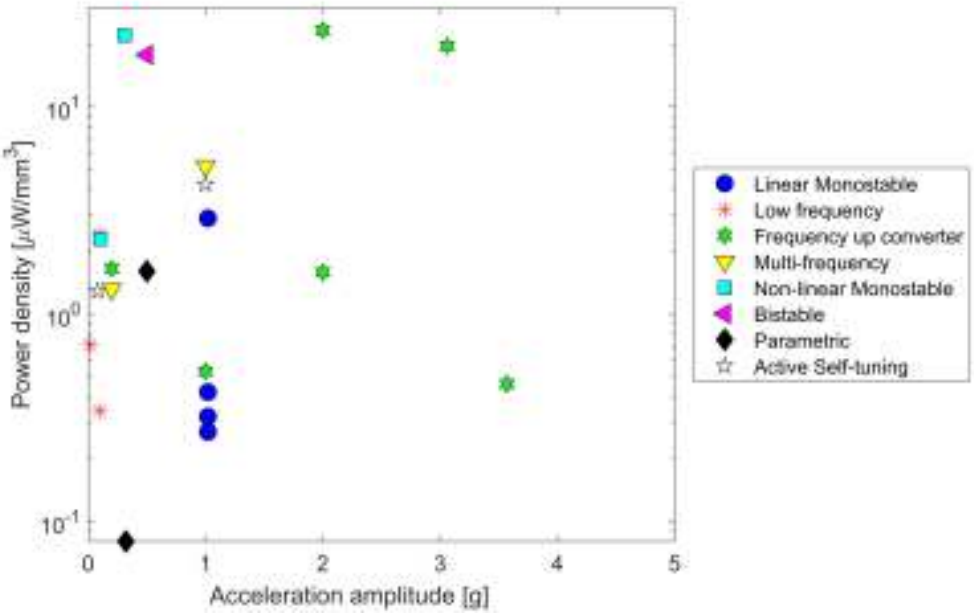

Figure 1.36: Comparison of power density in function on the excitation acceleration amplitude for different device typology.

Analogously, the frequency band, expressed in percentage of the device resonance frequency ($(f_{max} - f_{min}) \cdot 100/f_r$ in %), has been calculated for different kind of PEHs and it is shown in Fig 1.37. As expected, Multi-frequency and Frequency up converters show an improvement in bandwidth, reaching an acceptable value of 20 % on average and thus outperforming Linear Monostable configuration, with a typical 1-7 % bandwidth. The Non-linear Monostable devices show a great enhancement, since its frequency response can cover wide ranges. It must be underlined though that the 80 % is referred to a low resonance frequency (9.4 Hz), resulting in a band gap of only 7.4 Hz, less than what typically is found in literature for broad-band applications (till 30 Hz). Obviously Self-tuning devices are also performing, thanks to their active mechanisms adjusting the structure resonance frequency depending on the external excitation.

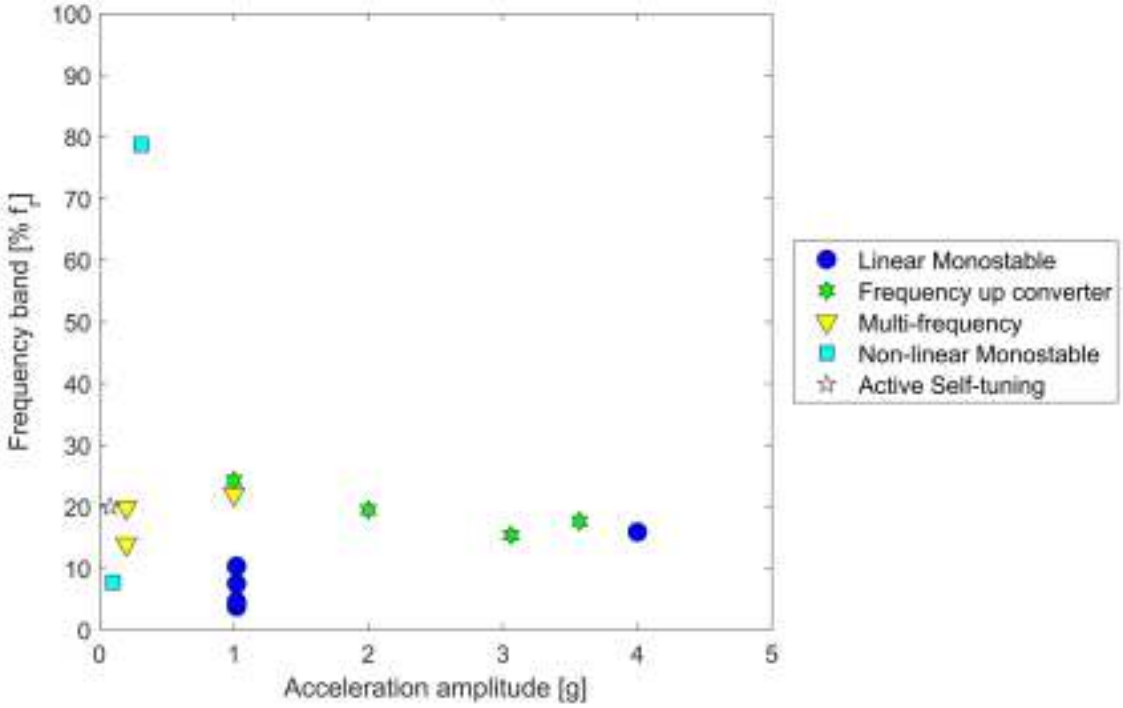

Figure 1.37: Comparison of frequency bandwidth (% of the PEH resonance frequency) in function on the excitation acceleration amplitude for different device typology.

From previous overviews and comments it is evident that no technique outperforms the others neither is ready for real-life applications. Indeed, each configuration provides some advantages on one hand but causes issues on the other (Table 1.2). Bistable and Non-linear monostable energy harvesters still face challenges with lowering acceleration thresholds to activate non-linear behaviours and setting initial conditions with passive techniques. Moreover, they do not show better performances than the Linear Monostable configuration under random excitations, underlining how far from real-world applications they are. Parametric resonance devices need further investigations too, solving issues connected with impedance matching and structural damping. Multi-frequency and Frequency up conversion are based on the ability to change the Linear Monostable parameters to enhance its performance and match natural frequencies with the excitation ones. Therefore, all PEH techniques still need a deeper comprehension to really become performing, starting from the Linear Monostable mechanical behaviour. The technological approach indeed is not sufficient to optimize the harvester parameters with respect to external non-ideal conditions. Moreover, the electrical conversion system, fundamental to make PEH power output suitable for electronics, is rarely taken into account during tests, since would make the system even more complex to understand. However, the electrical interaction is a fundamental part of the device optimization, influencing both oscillations damping and power production. Thus, to reach an efficient piezoelectric energy harvester, a deep comprehension of the Linear Monostable configuration must be firstly reached.

Table 1.2: Advantages and disadvantages of different piezoelectric energy harvester kinds.

PEH kind	Advantages	Disadvantages
Active self - tuning	Wide frequency bandwidth	Additional power consumption
Low frequency	Low resonance frequency	No improvement in power production
Frequency - up converter	Wide frequency bandwidth High power density	High footprint Easier breakage and fatigue damages High accelerations or preload needed
Multi-frequency	Wide frequency bandwidth	High footprint
Non - linear Monostable	Wide frequency bandwidth High power density	High accelerations or preload needed Not performing under random excitations Complex to be modelled
Bistable	Wide frequency bandwidth High power density	High accelerations or preload needed Not performing under random excitations Complex to be modelled
Parametric	Wide frequency bandwidth High power density	Difficult impedance matching Acceleration amplitude threshold Complex to be modelled

1.3.2 Future challenges and scope of the present thesis

The aim of the present work is the development of a a reduced-order model (ROM), based on a multi-physical approach, able to describe a Linear Monostable energy harvester taking into account all the parameters characterizing the entire system (material, structure, electric circuit). Thus, the coupled ROM of a cantilevered piezoelectric device, with a single and spatially bounded piezoelectric layer and an extended tip mass at the free edge, is analytically developed, including also the possibility of an imperfect clamping. The ROM is intended to provide an effective data exchange with the simulation framework of the electric conversion system. Moreover, all the developed model will be inserted within an optimization algorithm, that will benefit from the comprehensive multidisciplinary description of the device. Indeed, the followed approach enables a robust and computationally efficient analysis of PEH performance, exploring optimal combinations of mechanical and electrical parameters through optimization techniques. Based on this multi-physics model, some improvements in the PEH layout can be then further investigated, developing the required analytical models and implementing control techniques to maximize performances when possible.

Chapter 2

Theory of linear piezoelectricity

In order to gain a more complete comprehension of the piezoelectric energy harvester studied in this thesis, a physical insight on piezoelectricity is presented. The structure and ions influence on the material, and the polarization process to induce the piezoelectric effect are explained, underlying their relationship with material characteristics. Moreover, limit working conditions to keep constant piezoelectric properties are defined through thermal, mechanical and electrical thresholds. Finally the piezoelectric constitutive equations, relating material stress, strain, and charge production, are presented, also defining the main piezoelectric coefficient, fundamental to identify the most suitable material for any desired energy harvesting application.

2.1 Piezoelectric effect

The piezoelectric effect is a phenomenon connecting mechanical strain and electric charge production inside a material and can manifest in direct or converse form. The direct effect (or generator behaviour) happens when an imposed mechanical stress induces a surface charge production in the material. On the contrary, the converse effect (or motor behaviour) occurs when an external electric field (or voltage) induces a material strain. The previous definitions are exemplified in Fig. 2.1.

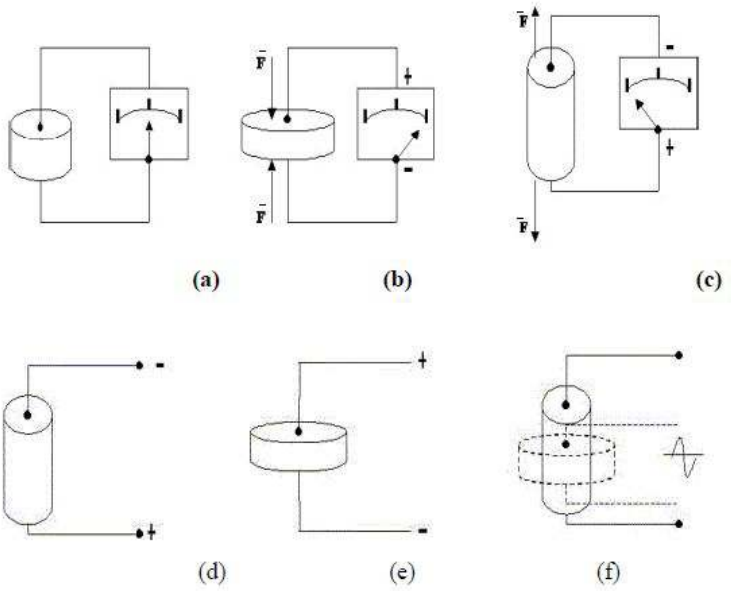

Figure 2.1: Piezoelectric material a) at rest; b) under compression; c) under stretching; d) under constant voltage; e) under constant voltage opposite to d); f) under alternate voltage.

Figs. 2.1(b) and 2.1(c) show how opposite applied forces induce charge production opposite in sign. The charge output remains constant until the constant mechanical stress produces a strain rate. Conversely, a constant strain does not cause any superficial charge generation. Figs. 2.1(d), 2.1(f), and 2.1(e) represent the converse effect. In particular, the first and second differs only in voltage sign, obviously causing opposite strain (elongation and shortening of the cylinder in high). An alternate voltage induces a sinusoidal strain, varying similarly to the voltage signal itself. Then, from Fig. 2.1 comments, it is trivial that piezoelectric materials have some properties connecting strain, stress, and electric field (*i.e.*, voltage), that will be investigated in the following sections after an overview of applications and exploring the physics of piezoelectricity.

2.1.1 Historical review of piezoelectric applications

In 1880, Jacques and Pierre Curie discovered the piezoelectric effect while working on quartz crystals. The word "piezoelectricity" etymologically comes from Greek $\pi\iota\varepsilon\zeta\varepsilon\iota\nu$, meaning "push" and thus referring to charge generation due to a mechanical pressure applied [Haertling 1999].

Despite piezoelectricity being an interesting subject, its spread worldwide was delayed due to previous use of well known electromagnetic devices, like switches and engines. The first relevant application was in 1920s, forty years after Curies brothers' discover, with quartz crystal based radio transmitters, application dominated by piezoelectricity from 1930 till now. Despite this lucky application, piezoelectric materials did not spread until the barium titanate was first produced in 1946 and, in general, until ferroelectric materials became easy to be made. The first $BaTiO_3$ based devices were pickup phonographs, on the market since 1947 [Heywang et al. 2008]. Then, in 1959 the first gas ignition for lighters came out, generating, thanks to the piezoelectric effect, an open circuit voltage higher than 10 kV, sufficient to break the dielectric gas and

then generate a sparkle for gas ignition (Fig. 2.2).

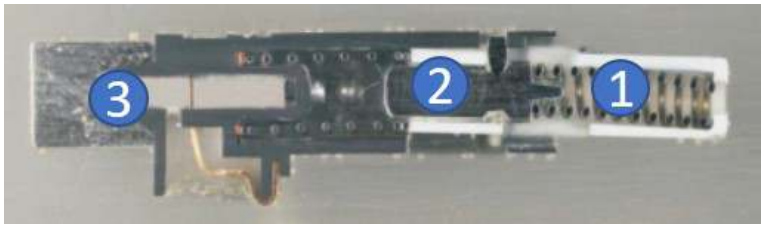

Figure 2.2: Section of a piezoelectric sparkle generator of a lighter. The spring (1) is activated by the finger, applying a pre-set stress to the mechanism (2) that hit the piezoelectric (3) [Doremus 1959].

In 1980 the first application of piezo-generators and power electronics came out: a piezoelectric transducer was used to monitor the pressure levels in car and truck tires, being a low pressure level identified by higher stress acting on the piezoelectric. In 2003 Enocean GmbH put on the market, in building automation field, wireless switches for lights with working distance up to 300 m, whose mechanical energy input gained by pushing the button was used to stress a piezoelectric bender [Rödig et al. 2010]. After that, piezoelectrics spread on the market very fast, experiencing an increment of 5 billions dollars by 1990 only in the sensor field [Akdogan et al. 2005].

Nowadays, piezoelectric materials are used in many different applications. A particularly interesting field is that of the self-powered sensors, for devices life monitoring, building and environment management, and process control [Rödig et al. 2010]. For example sensor working in frequency ranges from Hz to MHz can identify precisely displacements of few μm and forces from mN till kN, while facing difficult environments, dirty conditions, chemical and aggressive atmospheres, mechanical hits, and high temperatures [Tressler et al. 1998]. Indeed, wireless grids require a flexible and low-maintenance energy production system, able to work continuously for years. Piezoelectric sensors and actuators happen to be particularly feasible for this kind of applications, having an high energy density, a low strain-stress level necessary to work, and also being able to recover energy from vibration (available almost everywhere) [Rödig et al. 2010]. Apart from energy production, piezoelectric can also perform vibration suppression, useful in many different fields: a sensor measures vibration of a point on the structure and then an actuator responds to suppress it. Both sensor and actuator are piezoelectric and connected to shunt piezoelectric, dissipating energy surplus on a RL passive circuit [Moheimani 2003]. Such devices are useful especially in the aeronautic field for aerofoil, but can work also in sport, for instance, on tennis rackets to reduce the frame vibrations [C. Ferrari n.d.]. Another application is about printers, in which very fast and compact piezoelectric actuators makes printing possible at higher speed and resolution. Also, piezoelectric fuel injectors are ten times faster than the traditional coil ones, performing a better engine control and reduction in emissions. Moreover, thanks to their unlimited resolution, it is possible to operate micro-manipulations useful for laser, optical fibres, and equipment positioning, like precision positioning at commutation velocity for weaving machines needles. Another meaningful example for low-space consumption, communication speed, and low energy is piezoelectric valve (Fig. 2.3) [Lecce 2002].

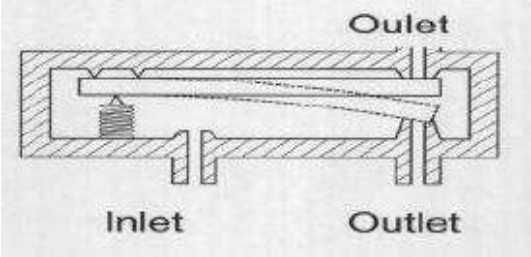

Figure 2.3: Piezoelectric valve.

Interesting application is the piezoelectric transformers for grid adapters, being small, high efficient, and low weight [Lecce 2002]. In health field ultrasonic transducers are then highly relevant, allowing high resolution ultrasounds tests, capable to explore particular parts of the body, like the anterior part of the eye, the skin or the vascular system [Shung et al. 2007]. Also, the Surgybone surgical scalpel can cut only hard and mineralized tissues, while not acting on the soft ones like gums [C. Ferrari n.d.]. Other promising projects under development are ultrasonic engines, compact and highly efficient, that in the future could replace all hydraulic systems in planes. Finally, a funny and weird application is E-Nose, a synthetic nose able to classify smells in which piezoelectrics act as mass sensors [Arshak et al. 2004].

In Table 2.1 other remarkable applications for piezoelectric materials are reported [Heywang et al. 2008][Lecce 2002].

Table 2.1: Piezoelectric materials applications.

Category	Device innovation	Application
Frequency control and signal elaboration	Standard time/frequency	High precision frequency control
	mechanical frequency filter	Frequency control and filter
	SAW devices	Passive signal elaboration for wireless communication
Sounds and ultrasounds	Buzzer	Sound alarms
	Microphones and speaker	telephones, blood pressure
	Ultrasound	Medical diagnosis
	Hydrophones	Sound identification and research
	High power transducers and shock wave generators	Lithotripsy, ultrasound cleaning
	Atomizer	Oil atomization, humidifier, aerosol
	In air ultrasound	Intrusion alarms, distance measuring, sonar
Actuators and engines	Printers	Ink jet, needles
	Engines and transformers	Miniaturized engines and transformers
	Bimorph actuators	Tires, micro-pumps, Braille alphabet
	Multilayer actuators	High precision positioning, optics
	Injection systems	Fuel valves for automotive
Sensors	Accelerometers	Automotive, automation, medicine
	High precision sensors, shock waves, flow, mass, level, motion, position	Automation, medicine
Start up		Gas and fuel injection
Adaptronics	Adaptive devices	Noise and vibration suppression

2.1.2 Material classification and structure

Being clear what direct and converse piezoelectric effects are, it is still not obvious which is the physical phenomenon that induces them. Cady [Cady 1946] defines piezoelectricity as "electric polarization produced by mechanical strain in crystals belonging to certain classes, the polarization being proportional to

the strain changing sign with it", from which is trivial that the phenomenon depends on the material microscopic structure. For this reason a physical insight into piezoelectricity and its dependency from material structure is given in the following.

A crystal is made of ions, connected to each other and occupying ordered and repeated positions in space: such a structure is called crystal lattice. Its smallest unit, repeating itself identical to the previous one is called unit cell, whose symmetry defines whether or not the crystal is piezoelectric. The asymmetric structure has a fundamental role in piezoelectricity, since a uniform mechanical stress could not produce asymmetric effects unless these are inside the material yet. Indeed, an electric charge distribution would not be possible without a flow of ions, due to the presence of electric dipoles (polarization) in the asymmetric structure. Thus, depending on the cell centre of symmetry, rotation axis, and mirror plane, crystals are classified in 32 structures, in turn again distinguished on 7 crystal geometries: triclinic, monoclinic, orthorhombic, tetragonal, rhombohedral (trigonal), hexagonal, and cubic (in symmetry ascending order), showed in Fig. 2.4

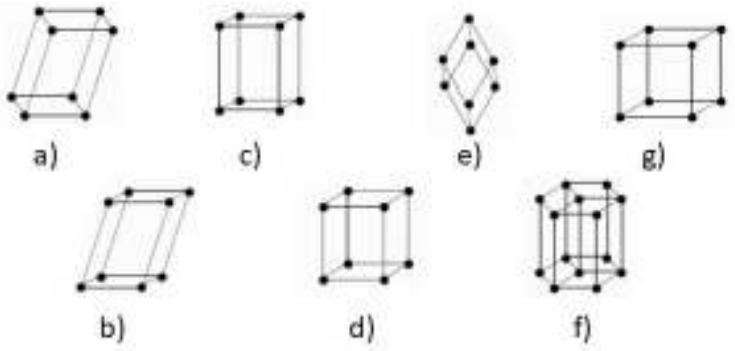

Figure 2.4: Unit cell structure a) triclinic, b) monoclinic, c) orthorhombic, d) tetragonal, e) rhombohedral, f) hexagonal, g) cubic.

Among these 32 classes, only 20 are piezoelectric, with noncentrosymmetric crystals and unique polar axis. However, the subgroup of ferroelectrics is the only one of useful application, since can exhibit a permanent spontaneous electric dipole. Ferroelectricity is the ability of a polarized crystal to adjust its global electric dipole with respect to the direction of an external electric field applied. As for ferromagnetic materials, the ferroelectric ceramics have a structure divided in Weiss domains, areas having a common electric dipoles orientation, but still having different orientations from each other and thus determining a global electric dipole equal to zero for the material. Nonetheless, those areas allow an easier polarization process and a residual orientation of the microscopic dipoles.

Ferroelectric materials are divided into groups, different in crystal lattice, among which the one with perovskite structure (Fig. 2.5) is the most performing and industrially used. Common materials with perovskite structure are $BaTiO_3$, PZT, and PLZT [Haertling 1999].

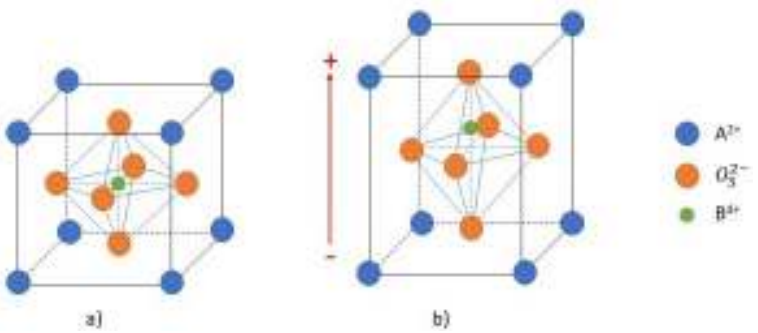

Figure 2.5: Perovskite cell structure ($BaTiO_3$) before (a) and after (b) polarization.

The rhombohedral or tetragonal unit cell has a generic formula $A^{2+}B^{4+}O_3^{2-}$, with A a covalent metallic ion (like Ba and Pb) and B a tetravalent metallic ion (like Ti and Zr).

The barium titanate (example in Fig. 2.5) has been the most common piezoelectric material on the market for many years, used in phonographs, ultrasonic transducers, and sonar. However, nowadays PZT ($Pb(Zr, Ti)O_3$) is the most widespread piezoceramic, thanks to its stability, energy conversion efficiency, low price, and easy property definition. Indeed, changing PZT characteristics is easy thanks to simple Zr-Ti ratio alterations. When Zr and Ti content are almost the same with a slightly higher Zr content ($Pb(Ti_{0.465}, Zr0.535)O_3$), the ferroelectric behaviour is enhanced, allowing for a greater number of domains orientations and thus higher polarization [Fabbri 1998]. However, a small predominance of Ti increases the piezoelectric constant d, responsible for the electromechanical transduction (as will be seen in the following sections).

Finally, to make PZT materials even more versatile in characteristic definition, dopants are used:

- for higher permittivity, but lower Curie point, Ca^{2+}, Sr^{2+}, and Ba^{2+} ions can replace Pb^{2+};
- for higher piezoelectric coefficients, permittivity, compliance, and service life a Nb^{5+} ion can replace $(Ti, Zr)^{4+}$ or a La^{3+} ion a Pb^{2+};
- for lower piezoelectric coefficients, permittivity, compliance, but also service life Sc^{3+} or Fe^{3+} ions can replace $(Ti, Zr)^{4+}$.

2.1.3 Curie temperature

Piezoelectric internal structure depends not only on the ions contents, as seen in the previous section, but also on the temperature at which the material is exposed. Indeed, there is a temperature threshold, called Curie temperature T_c, at which most of materials perform a transition from ferroelectric to non-ferroelectric phase (Fig. 2.6) [Damjanovic 1998].The new phase can be or not piezoelectric, but usually it has a more symmetric structure than the ferroelectric one, losing the total non-zero electric dipole.

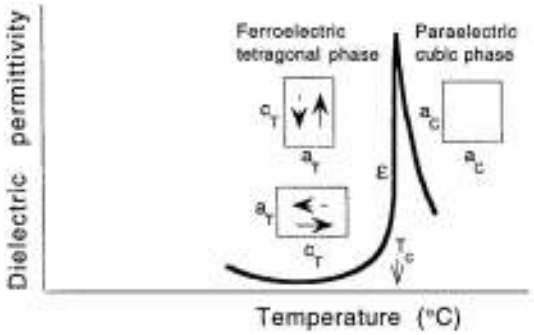

Figure 2.6: Phase transition from ferroelectric with Weiss domains to non ferroelectric and dielectric permittivity ϵ behaviour for a piezoelectric material undergoing temperature change [Damjanovic 1998].

Moreover, beyond Curie point the dielectric permittivity ϵ shows a significant reduction (Fig. 2.6), following the Curie-Weiss law:

$$\epsilon = \epsilon_0 + \frac{C}{T - T_c} \tag{2.1}$$

where ϵ_0 is the vacuum permittivity ($8.854 \cdot 10^{-12} F/m$) and C is the Curie constant of the material. The Curie temperature is thus a threshold for piezoelectrics working conditions, since, if the material undergoes to higher temperatures, it loses its global electric dipole because of thermal excitation phenomenon. For this reason, typically piezoelectric materials are used in applications at maximum temperatures approximately equal to $T_c/2$, in order to avoid a return to the virgin condition. Piezoelectric ceramics Curie temperatures vary from a minimum of 130 °C (barium titanate), to 360 °C (PZT), to a maximum of 700 °C (bismuth doped PZT) [Cook et al. 1971]. However, the most performing piezoelectric material for high temperature applications is the aluminium nitride (AlN), investigated by Arroyo *et al.* [Arroyo et al. 2016] [Arroyo et al. 2017] with an temperature-dependent model. Indeed, it's Curie temperature is equal to 2000 °C, and thus it is successfully used up to 1000 °C in high temperature applications (automotive, industrial, aerospace).

2.1.4 Polarization process

As mentioned before, ferroelectrics are the most performing among piezoelectric materials, since they exhibit a total residual polarization, fundamental for a strong piezoelectric behaviour. However, at their initial state (virgin condition), ferroelectrics show a global electric dipole equal to zero, with random orientation of Weiss domains, that however can be adjusted in one unique direction through a polarization process, described in this section [Cook et al. 1971].

To be effective, the polarization must be performed at a temperature lower than the material Curie temperature T_c, to be found before. An external electric field $\boldsymbol{E}$ is applied, adjusting the microscopic electric dipoles with its direction. Then, after the field is removed, a remanent polarization close to the electric field direction (new microscopic electric dipoles stable low-energy position) is obtained along with a geometric strain in the crystal lattice, making the material anisotropic. In Fig. 2.7 a sketch of the process is shown.

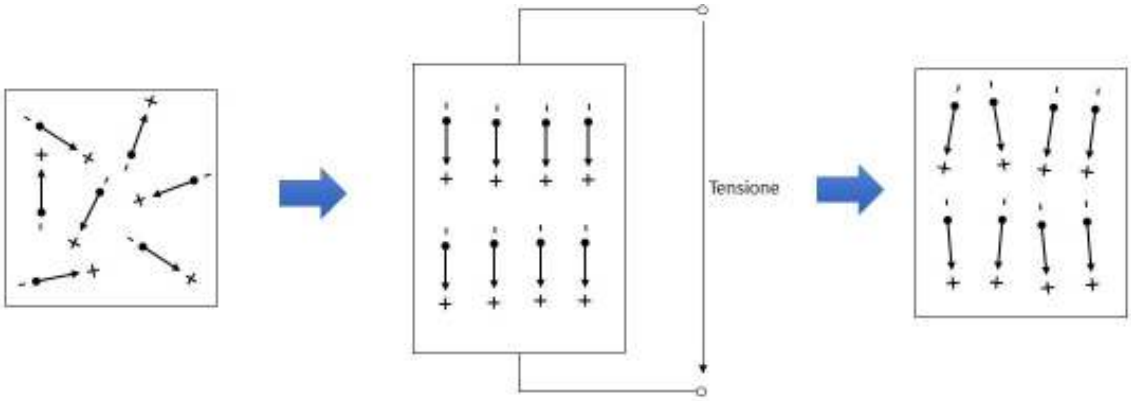

Figure 2.7: Polarization process for a ferroelectric material: sketch of microscopic electric dipoles orientation adjustment.

The polarization process is limited by the electric breakdown phenomenon, that causes material break. So, even if in theory any material could be polarized, for some of them the breakdown would occur before polarization is over. Obviously, the limit is even lower if vacancies, cracks, and other physical imperfections exist and it is influenced by electrode shape and position. Moreover, mechanical strain also limits polarization, since it could induce relevant internal stress leading to material break even before electric breakdown occurs. For example the PZT ceramics can reach strains of 0.5% in the electric field direction and -0.2% in the normal direction [Fabbri 1998]. Typically, being conscious of the previous limits allows for a good and long-lasting remanent polarization to be induced. Time and intensity of the electric field to obtained the final result depend then on material characteristics. At the end of the process, the material behaves as a piezoelectric crystal responding linearly to stress and external electric fields.

From an electric point of view, the polarization process in a dielectric medium (as piezoelectric materials), can be expressed as follow:

$$\boldsymbol{D} = \epsilon_0 \, \boldsymbol{E} + \boldsymbol{P} = \epsilon_0 \, \boldsymbol{E} + (\epsilon_r - 1)\epsilon_0 \, \boldsymbol{E} = \epsilon_r \, \epsilon_0 \, \boldsymbol{E} \tag{2.2}$$

where $\boldsymbol{D}\,[C/m^2]$ is the electric displacement representing the charge quantity stored per unit of area, $\boldsymbol{E}\,[V/m]$, as mentioned before, is the electric field, $\boldsymbol{P}\,[C/m^2]$ is the polarization, and ϵ_r is the relative permittivity of the material. All boldface quantities denote vectors in physical (3D) space. If a virgin sample undergoes to an electric field $\boldsymbol{E}$ at a temperature close to but lower than T_c, it will act as in the hysteresis diagram in Fig. 2.8.

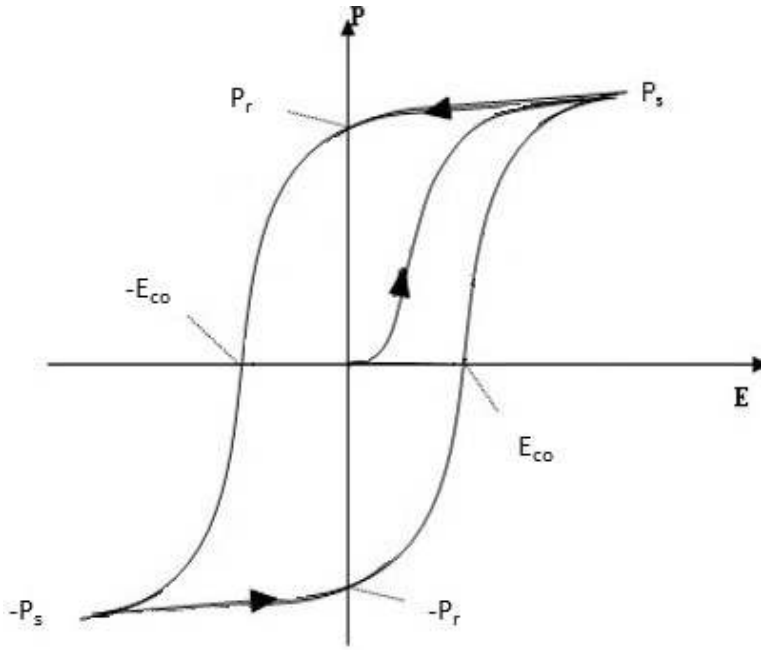

Figure 2.8: Typical ferroelectric material hysteresis cycle.

The electric field induces a polarization field $\boldsymbol{P}$, rising with the trend shown in figure (internal dipoles aligning in the same direction). With $\boldsymbol{E}$ raising, $\boldsymbol{P}$ increases too until it reaches the saturation level $\boldsymbol{P}_s$ when all dipoles are aligned with the external electric field. When $\boldsymbol{E}$ decreases, $\boldsymbol{P}$ decreases too, but less fast than before, reaching a remanent polarization $\boldsymbol{P}_r$ when the external electric field goes to zero, with internal dipoles in a stable position close to the saturation one. If an electric field opposite in sign is applied, then $\boldsymbol{P}$ will decrease again till it reaches zero for the coercive electric field value $\boldsymbol{E}_{co}$, and then changes in sign till the new saturation point $-\boldsymbol{P}_s$. Analogously, there will be a remanent polarization $-\boldsymbol{P}_r$ when the new electric field goes to zero.

Different hysteresis loop shapes (Fig. 2.8) determine different properties, dividing piezoceramic materials in two categories: soft and hard piezoelectrics. The first ones exhibit high saturation point $\boldsymbol{P}_s$ and low coercive electric field $\boldsymbol{E}_{co}$, conversely, the latter is characterized by lower saturation point, but higher coercive electric field, as shown in Fig. 2.9. Soft piezoelectric materials perform better for wider frequency bands but have lower transduction efficiency and suffer more easily from depolarization and deterioration. Moreover, they exhibit low Curie temperatures (<300 °C), and thus they can be used only in low temperature applications. Finally, a low coercive field value means need for low field to be polarized initially, with lower energy consumption for the production, but makes soft materials easy to depolarize, and thus not useful in applications in which electric fields are involved. Hard piezoelectrics have opposite characteristics: high curie temperature, higher transduction efficiency for narrow frequency bands in the neighbourhood of resonance frequencies. Furthermore, having higher coercive field value, they keep the residual polarization longer than soft materials. For the previous reasons, hard piezoelectrics are typically used in energy harvesting from sources characterized by certain frequencies, while soft ones are more suitable for random excitation spectra sensing.

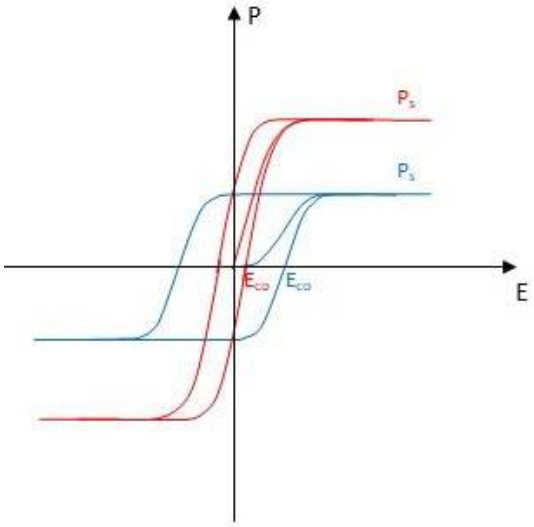

Figure 2.9: Hysteresis loop for a soft (red) and hard (blue) piezoelectric materials.

In Fig. 2.10 a typical strain curve in function of an external electric field $\boldsymbol{E}$ is shown. During polarization, the material stretches in $\boldsymbol{E}$ direction, due to converse piezoelectric effect. Usually polarization (cycle in dashed line) occurs for electric field values at which the induced strain is almost linear.

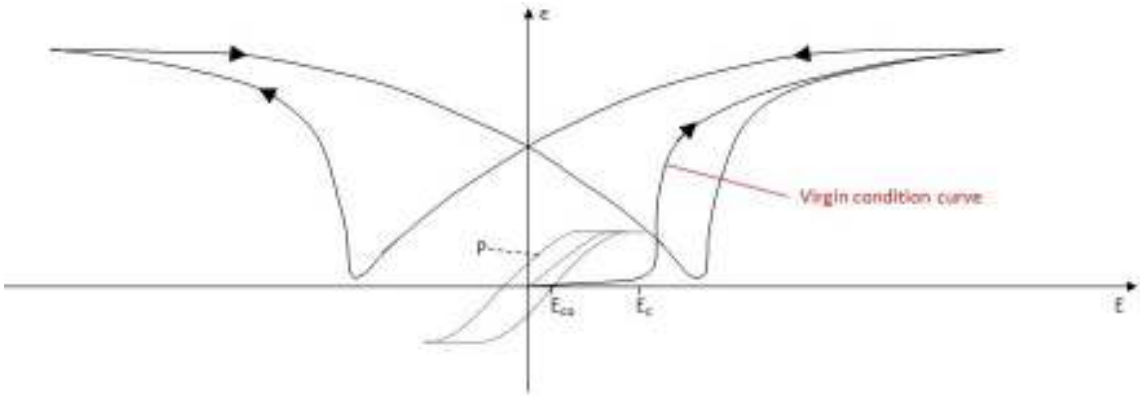

Figure 2.10: Strain - electric field diagram for polarization process.

Nonetheless, when the electric field overcomes a critic value $\boldsymbol{E}_c$, the strain assumes a non-linear behaviour, with a butterfly-shaped symmetric trend. This change is due to internal domains polarization inversion, as better explained in Fig. 2.11.

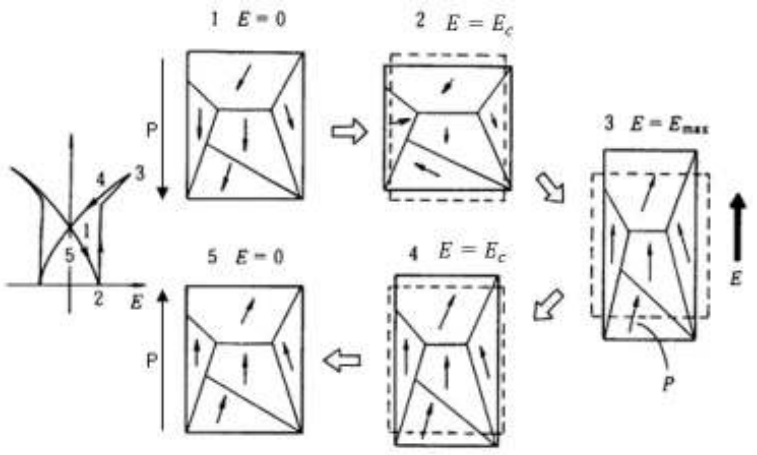

Figure 2.11: Domains polarization inversion and effect on strain for a piezoceramic material.

Indeed, if a piezoelectric material undergoes to an electric field opposite in direction with respect to its polarization, firstly it experiences a contraction due to internal domains resistance, until the minimum strain is reached for critical value $\boldsymbol{E}_c$. Then, a polarization inversion happens, determining a more and more consistent and fast expansion till the electric field maximum value $\boldsymbol{E}_{max}$. After all domains being in the new orientation, the crystal experiences a strain decreasing until the electric field goes to zero. This bipolar field application can induce mechanical damage inside the material. Once polarization is obtained, it can be lost because of three different phenomena: electric, mechanical, and thermal depolarization. The first occurs when a static external electric field is applied in the opposite direction with respect to the internal polarization, in particular if at the material coercive value $\boldsymbol{E}_{co}$. For this reason $\boldsymbol{E}_{co}$ is a measure of the resistance to depolarization: the higher it is, the higher electric fields the piezoelectric material can undergo without being damaged (hard materials). Electric depolarization can also occur with a sinusoidal electric field during the period in which $\boldsymbol{E}$ direction is opposite to the polarization one. In this situation, frequency is a fundamental parameter since the higher it is, the less and easier to be fixed in the following half period polarization damages are. Mechanical depolarization occurs when the material undergoes to high stress, disturbing domains and dipoles orientation. This limit varies a lot depending on material and dopants used, so it must be verified for every different case. Finally, thermal depolarization occurs when the piezoelectric works at a temperature higher than T_c: due to thermal excitation, domains regain random orientations. Moreover, a phase shift occurs and, even going back to the original phase, the material be back at virgin state. An empiric rule to avoid thermal depolarization is to always work at temperatures lower than $T_c/2$, at which thermal depolarization is negligible.

2.2 Constitutive equations

In this section, variables and coefficients involved in piezoelectric effect will be first defined and then used to express the material constitutive equations.

External forces in equilibrium condition are applied to a generic continuum body and induce internal forces inside the material. Considering an internal surface element $\Delta\boldsymbol{A}$, a generic point P in it, with $\boldsymbol{n}$

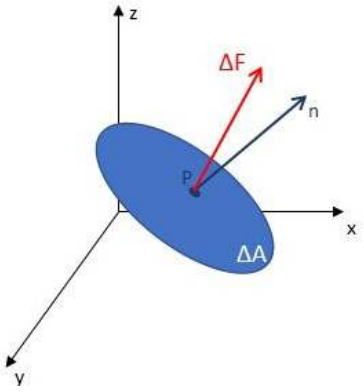

Figure 2.12: Force acting on a generic surface.

denoting the normal to the surface in P, and the external force $\Delta \boldsymbol{F}$ acting on the surface $\Delta \boldsymbol{A}$ (Fig. 5.1), the stress vector is defined as

$$\boldsymbol{\sigma} = \lim_{\Delta A \to 0} \frac{\Delta \boldsymbol{F}}{\Delta A} \tag{2.3}$$

with force and normal having different directions.

If now a body with surfaces parallel to the $[x, y]$, $[x, z]$, and $[y, z]$ planes is considered, the stress can be expressed as a second order tensor measured in $[N/m^2]$. Each component is denoted as σ_{ij}, with the first index $i = 1, 2, 3$ referring to the surface normal and the second index $j = 1, 2, 3$ denoting the component of the force in the j-th direction, as shown in Fig. 2.13.

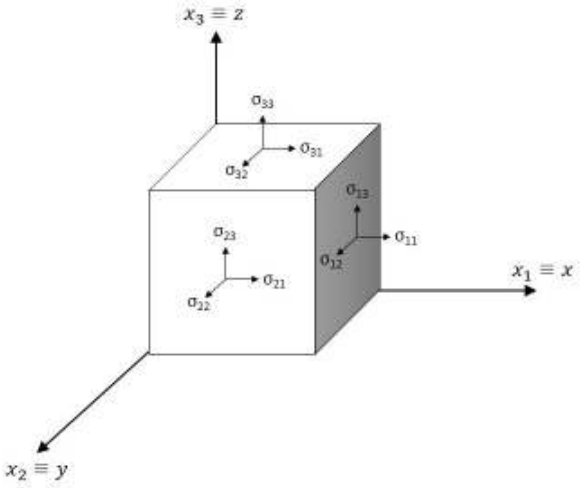

Figure 2.13: Mechanical stress tensor components acting on a solid body.

A stress field in a continuous body induces deformation, the transition from a non-deformed configuration (reference configuration) to a new configuration (current configuration) with deformation or distortion effects. The strain represents the measure of deformation in terms of relative displacements of the body's particles. Thus, considering two particles in their initial positions Q and P in the reference configuration and in their final positions Q' and P' in the current configuration, as shown in Fig. 5.2, the strain is defined

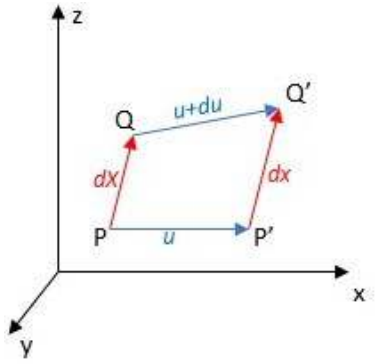

Figure 2.14: Transition form reference to current configuration for points P and Q.

as the relative change of the vector dX.

$$\varepsilon = \lim_{dX \to 0} \frac{|dx| - |dX|}{|dX|} \tag{2.4}$$

As for the stress, the strain can be expressed as a non-dimensional second order tensor, whose components are ε_{ij}, with index following the same stress tensor components logic.

Stress and strain are connected to each other by the following relation.

$$\sigma_{ij} = s_{ijmn}\, \varepsilon_{mn} \tag{2.5}$$

where s_{ijmn} is the stiffness or elasticity fourth-order tensor component, depending on material properties. Eq. 2.5 can also be written as

$$\varepsilon_{mn} = c_{ijmn}\, \sigma_{ij} \tag{2.6}$$

with c_{ijmn} the compliance fourth-order tensor component.

The dielectric permittivity represents the electric polarization response of a material to an external electric field and can be defined as the electric displacement $\boldsymbol{D}$ resulting from an applied electric field $\boldsymbol{E}$.

$$D_i = \epsilon_{ij} E_j \tag{2.7}$$

Since the electric displacement $\boldsymbol{D}$ and the electric field $\boldsymbol{E}$ are both vectors, the dielectric permittivity is a second order tensor measured in [F/m].

The piezoelectric charge or strain coefficient represents, for the direct piezoelectric effect, the polarization produced in the material due to a mechanical stress applied.

$$P_k = d_{ijk} \sigma_{ij} \tag{2.8}$$

For the converse effect it can be defined as the generated strain per unit of applied electric field:

$$\varepsilon_{ij} = d_{ijk} E_k \tag{2.9}$$

So the subscript k refers to the electric quantity, P and E having the same direction, and ij to the mechanical one, σ and ε having the same direction. d_{ijk}. The piezoelectric coefficient is a a third order tensor and it is measured in $[C/N]$ or $[m/V]$.

Finally, the stress or charge coefficient represents, for the direct piezoelectric effect, the charge produced due to a strain in the material

$$D_k = -\hat{e}_{ijk}\varepsilon_{ij} \tag{2.10}$$

For the converse piezoelectric effect, it can be expressed as the stress produced for an external electric field applied

$$\sigma_{ij} = -\hat{e}_{ijk}E_k \tag{2.11}$$

with same use of subscripts as for d_{ijk}. The charge coefficient is a third order tensor measured in $[C/m^2]$ or $[V \cdot m/N]$.

Despite using the piezoelectric constants, in order to have a global estimation of the material behaviour, the electromechanical coupling coefficient K^2_{eff}, ratio between energy converted and energy in input, can be used. K^2_{eff} is always lower than 1, and typically varies among 0.5 and 0.7 for PZT ceramics. This quantity though is not always a precise efficiency indicator since the energy converted does not always correspond to the useful one. A good piezoelectric material at its resonance frequency could reach an efficiency higher than 90 $\%$, that unluckly drops quickly out of the resonance point.

Other piezoelectric coefficients, not used in our problems, are reported in Tab. 2.2.

Table 2.2: Piezoelectric coefficients [Damjanovic 1998].

Name	Symbol	Unit	Definition
Dielectric lost coefficient	$\tan\delta_e$	[-]	$P_{e,loss}/Q_e$
Strain or voltage coefficient	g_{ijk}	$[V \cdot m/N]$	$E_k/\sigma_{ij} \equiv \varepsilon_{ij}/D_k$
Stress or voltage coefficient	e_{ijk}	$[N/C]$ or $[V/m]$	$-E_k/\varepsilon_{ij} \equiv -\sigma_{ij}/D_k$

The constitutive equations for direct and converse piezoelectric effect can be defined, respectively, in tensorial form.

$$D_l = d_{mnl}\,\sigma_{mn} + \epsilon^{\sigma}_{lk}\,E_k \tag{2.12}$$

$$\varepsilon_{ij} = c^{E}_{ijmn}\,\sigma_{mn} + d_{ijk}\,E_k \tag{2.13}$$

where the superscript is a quantity kept constant during the coefficient identification, with the piezoelectric elastic quantities having a different value for DC current (E constant) or AC current (D constant).

A tensorial analysis could help in understanding how all the quantities influence each other. Remembering their definitions at the beginning of the chapter, both strain and stress are second-order tensors. So, the elasticity and compliance (Eqs. 2.5 and 2.6) must be fourth-order tensors, with 81 components. Then, being electric displacement and electric field vectors, the permittivity is necessarily a second-order tensor (9 components) and the piezoelectric coefficients third-order tensors (27 components).

Recalling Cauchy's second law of motion, we can assume the stress tensor to be symmetric, *i.e.*, $\sigma_{23} = \sigma_{32}$, $\sigma_{12} = \sigma_{21}$, $\sigma_{13} = \sigma_{31}$, and the compliance tensor c_{ijmn} independent components be reduced from 81 to 36. Moreover, being the force system conservative, the compliance tensor has to be symmetric, so

components further decrease to 21. Thus strain and stress relevant components are 6 and, for sake of simplicity, the two tensors can be written in engineering notation, *i.e.*, as vectors:

$$[\sigma_{11}, \sigma_{22}, \sigma_{33}, \sigma_{23}, \sigma_{13}, \sigma_{12}] = [\sigma_1, \sigma_2, \sigma_3, \sigma_4, \sigma_5, \sigma_6]$$

$$[\varepsilon_{11}, \varepsilon_{22}, \varepsilon_{33}, \varepsilon_{23}, \varepsilon_{13}, \varepsilon_{12}] = [\varepsilon_1, \varepsilon_2, \varepsilon_3, \varepsilon_4, \varepsilon_5, \varepsilon_6]$$

with subscripts $[1, 2, 3]$ and $[4, 5, 6]$ corresponding now respectively to relative rotations and shear actions.

Moreover, only 18 piezoelectric constant and 6 permittivity constant components happen to be independent and, being the material isotropic only in the plane orthogonal to the global dipole direction due to polarization, the cylindrical symmetry further reduces the independent components to 10 [Fabbri 1998].

So now the constitutive Eqs. 2.12 and 2.13 for direct and converse piezoelectric effect can be defined in linear form respectively as.

$$D_l = d_{jl}\,\sigma_j + \epsilon^{\sigma}_{lk}\,E_k \tag{2.14}$$

$$\varepsilon_i = \boldsymbol{c}^{E}_{ij}\,\sigma_j + d_{ik}\,E_k \tag{2.15}$$

with $l, k = 1, 2, 3$ and $i, j = 1, 2, ..., 6$.

Thus, Eqs. 2.14 and can be written for each component as

$$D_1 = \epsilon_{11}\,E_1 + d_{15}\,\sigma_5 \tag{2.16a}$$

$$D_2 = \epsilon_{11}\,E_2 + d_{15}\,\sigma_4 \tag{2.16b}$$

$$D_3 = \epsilon_{33}\,E_3 + d_{31}\,(\sigma_1 + \sigma_2) + d_{33}\,\sigma_3 \tag{2.16c}$$

And, analogously, Eqs. 2.15 can be written as

$$\varepsilon_1 = \boldsymbol{c}^{E}_{11}\,\sigma_1 + \boldsymbol{c}^{E}_{12}\,\sigma_2 + \boldsymbol{c}^{E}_{13}\,\sigma_3 + d_{31}\,E_3 \tag{2.17a}$$

$$\varepsilon_2 = \boldsymbol{c}^{E}_{11}\,\sigma_2 + \boldsymbol{c}^{E}_{12}\,\sigma_1 + \boldsymbol{c}^{E}_{13}\,\sigma_3 + d_{31}\,E_3 \tag{2.17b}$$

$$\varepsilon_3 = \boldsymbol{c}^{E}_{13}\,(\sigma_1 + \sigma_2) + \boldsymbol{c}^{E}_{33}\,\sigma_3 + d_{33}\,E_3 \tag{2.17c}$$

$$\varepsilon_4 = \boldsymbol{c}^{E}_{44}\,\sigma_4 + d_{15}\,E_1 \tag{2.17d}$$

$$\varepsilon_5 = \boldsymbol{c}^{E}_{44}\,\sigma_5 + d_{15}\,E_1 \tag{2.17e}$$

$$(\varepsilon_6 = \boldsymbol{c}^{E}_{66}\,\sigma_6) \tag{2.17f}$$

with Eq. 2.17f defining the shear strain ε_6 (in $\{x, y\}$ direction) not showing any piezoelectric effect and thus being neglected, since the material is polarized in z direction.

Eqs. 2.16 and 2.17 are thus expressed in matrix form as

$$\begin{bmatrix} \boldsymbol{\varepsilon} \\ \boldsymbol{D} \end{bmatrix} = \begin{bmatrix} \boldsymbol{c}^{E} & \boldsymbol{d}^{t} \\ \boldsymbol{d} & \boldsymbol{\epsilon}^{\sigma} \end{bmatrix} \begin{bmatrix} \boldsymbol{\sigma} \\ \boldsymbol{E} \end{bmatrix} \tag{2.18}$$

where the superscript t stands for matrix transposition, the compliance matrix is

$$\boldsymbol{c} = \begin{bmatrix} \boldsymbol{c}_{11}^E & \boldsymbol{c}_{12}^E & \boldsymbol{c}_{13}^E & 0 & 0 & 0 \\ \boldsymbol{c}_{12}^E & \boldsymbol{c}_{11}^E & \boldsymbol{c}_{13}^E & 0 & 0 & 0 \\ \boldsymbol{c}_{13}^E & \boldsymbol{c}_{13}^E & \boldsymbol{c}_{33}^E & 0 & 0 & 0 \\ 0 & 0 & 0 & \boldsymbol{c}_{44}^E & 0 & 0 \\ 0 & 0 & 0 & 0 & \boldsymbol{c}_{44}^E & 0 \\ 0 & 0 & 0 & 0 & 0 & 2\left(\boldsymbol{c}_{11}^E - \boldsymbol{c}_{21}^E\right) \end{bmatrix}$$

the piezoelectric matrix is

$$\boldsymbol{d} = \begin{bmatrix} 0 & 0 & 0 & 0 & d_{15} & 0 \\ 0 & 0 & 0 & d_{15} & 0 & 0 \\ d_{31} & d_{31} & d_{33} & 0 & 0 & 0 \end{bmatrix}$$

and the permittivity matrix is

$$\boldsymbol{\epsilon} = \begin{bmatrix} \epsilon_{11}^\sigma & 0 & 0 \\ 0 & \epsilon_{11}^\sigma & 0 \\ 0 & 0 & \epsilon_{33}^\sigma \end{bmatrix}$$

from which its clear which are the 10 independent coefficients.

Chapter 3

Electromechanical modelling of piezoelectric cantilevered beams

In recent years, researchers from different engineering fields (materials, mechanical, and electric) have addressed piezoelectric energy harvester (PEH) modelling, although frequently using oversimplified hypothesis to reach compact formulations and thus leading to inaccurate results [Erturk and Daniel J. Inman 2008b].

The most simple representation of a PEH is the Single Degree of Freedom (SDOF) model, usually suffering from incorrect representation of the electromechanical coupling. Following this approach, some researchers [Jeon et al. 2005] [Hua-Bin et al. 2006] modelled the energy conversion due to piezoelectric effect with a viscous damping term, as also done for energy harvesters exploiting an electromagnetic principle (although exploiting a completely different physics). However, change in resonance frequency due to resistive load variation demonstrate that the piezoelectric effect is more complex than a viscous damping, the latter depending on rapidity of oscillations. The piezoelectric can be also modelled as a transformer [Goldfarb et al. 1999], with capacitance, inductance and resistance representing, respectively, spring, mass, and damper at the primary winding. This representation allows for a more accurate representation of the electromechanical coupling, since a variation of the resistive load results in a consequent change in the resonance frequency of the structure. However, considering the tip mass as unique responsible of inertia forces leads to acceptable results only if the distributed beam mass is comparatively small, otherwise both oscillation amplitude and power output are underestimated. Finally, SDOF representation lacks of useful details like strain distribution, multi-modal behaviour, and electrodes position, and can be mainly used for describing simple features of the mechanical response.

Although more accurate than the SDOF models, also Single-mode Distributed Parameter (SDP) models exhibit some issues. They are developed considering the PEH working only at its fundamental resonance frequency, typically the first bending mode one. However, this hypothesis guarantees accurate results only in the neighbourhood of the considered resonance frequency [Lu et al. 2003] [S.-N. Chen et al. 2006]. Moreover, as for the SDOF, the piezoelectric effect is sometimes oversimplified by representing it as a viscous damping [S.-N. Chen et al. 2006] or by not considering the influence of the electric circuit on the structural response [Lu et al. 2003] [JH Lin et al. 2007] [Ajitsaria et al. 2007]. If then the backward piezoelectric effect is

not taken into account, in addition to missing the correct resonance frequency, the predicted power output for the optimal resistive load is not accurate.

Erturk and Inman [Erturk and Daniel J. Inman 2008a] [Erturk; Hoffmann, et al. 2009] [Stanton; Erturk, et al. 2010] [Erturk 2012] and other research groups [M. Kim et al. 2010] [Tang et al. 2017] proposed a Multimode Distributed Parameter (MDP) model, with two-way coupling in the piezoelectric model. Being more accurate than the previous models, they employ exact modes for modal solution of the governing equations of multilayer uniform beams. Moreover, in case of linear response, an analytical expression of the transfer function from the imposed acceleration to the system response is found, providing the voltage output for harmonic excitation.

From the above literature review, it emerges that an accurate prediction of the harvester electromechanical behaviour is strictly required to match its natural frequencies with the spectrum peaks of the excitation; this is a simple but not easy requirement for maximizing the energy conversion. More in general, the availability of reduced-order models (ROMs), encompassing the coupling between the mechanical and piezoelectric models, as well as the AC/DC electrical conversion system downstream, allows for a balanced and computationally affordable optimization of the device.

In the following sections a MDP model of a non-uniform PEH is presented. Its numerical solution is found and compared before with analytical results proposed in [Erturk and Daniel J. Inman 2008a] and then with 3D COMSOL Multiphysics simulations.

3.1 Device configuration

3.1.1 Cantilevered plate configuration with proof mass

The investigated energy harvester converts ambient vibrations into electric energy by exploiting the piezoelectric effect of its piezoceramic layer. The cantilevered configuration, shown in Fig. 3.1, is excited by basement vibrations through its clamped side and exhibits significant flapping amplitudes at resonance. This configuration combines efficiency and simplicity, the latter feature favoring the possibility of a precise prediction of the bending natural frequencies. In Fig. 3.1, a Cartesian coordinate system is defined with origin O at the midpoint of the clamped edge of width b, x-axis lying on bottom face of the beam, y-axis on its clamped edge, and z-axis pointing upward.

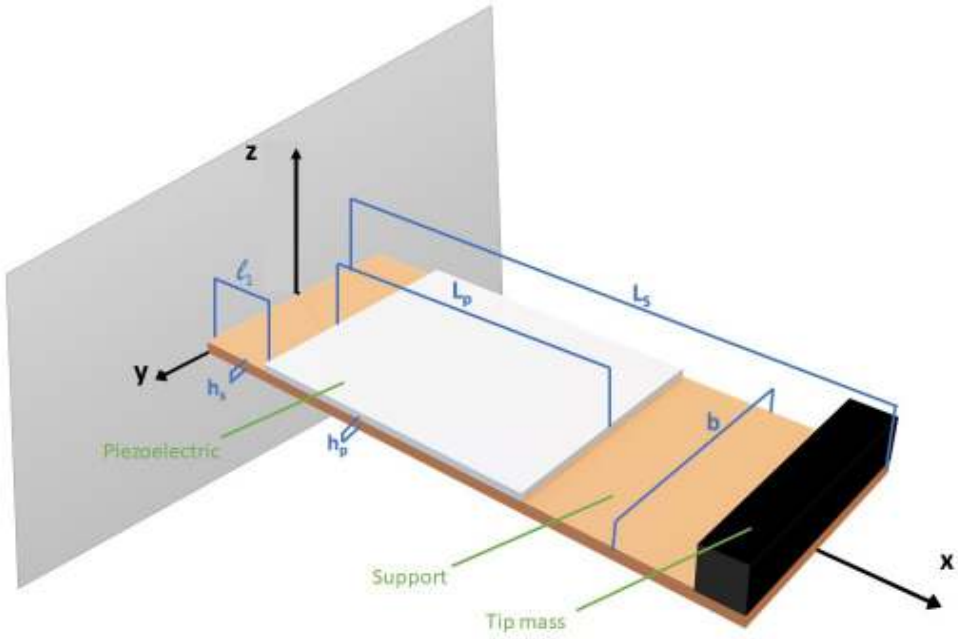

Figure 3.1: 3D view and main dimensions of the PEH.

A unimorph configuration is adopted, with a thin piezoelectric lamina of length L_p and width b glued on the top side of the supporting plate at a distance l_1 from the clamped edge, and covering partially the support layer up to $x = l_2$, such as $L_p = l_2 - l_1 < L_s$, with L_s the overall length of the supporting plate. Though the piezoelectric patch should be placed toward the clamped edge as much as possible to harvest more energy, this geometrical layout describes a generic configuration of the piezoelectric layer, making the model able to easily reproduce different devices. Moreover, in the following chapters, the importance of the piezoelectric patch length will be studied, taking into account the compromise between material use and energy production, and analysing different modes exploitation through electrode segmentation. The connection between support layer and piezoelectric lamina is supposed to be perfect, without any loss in mechanical energy transmission. For sake of clarity, in the following the letter 'p' will be used to indicate variables or coefficients related to the piezoelectric layer, the letter 's' for the support layer instead. Figure 3.2 highlights the thicknesses h_s and h_p for support and piezoelectric layers, respectively.

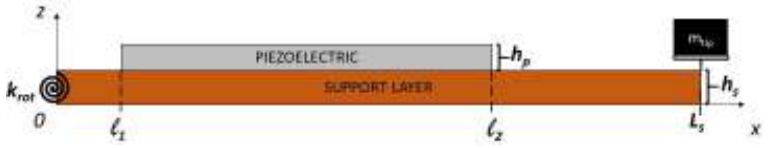

Figure 3.2: Lateral view of the PEH (dimensions do not scale real values of the device considered later).

Apart from providing the necessary structural strength, one of the benefits of the support layer is avoiding the charge cancellation phenomenon when the circuit is connected to electrical loads. Indeed, in case of passing from fiber compression to tension through the piezoelectric material, opposing charge is generated

because of polarization. To keep strain in the same direction through the piezoelectric layer, the thickness of support plate must be chosen to contain the neutral axis of the overall structure. This choice guarantees that the piezoelectric material is subjected to mechanical stress in just one direction through its thickness.

As shown in Fig. 3.2, a tip mass is positioned on the free edge to tune harvester's natural frequency with the excitation frequency, if the latter is lower than the natural frequencies of the device, and to enhance oscillations. For sake of simplicity, the mass is initially supposed to have negligible extension and rotational inertia. The clamping can be also supposed to be yielding in rotation and consequently a torsional spring of coefficient k_{rot} is added at $x = 0$ to take this effect into account. Typically, the elastic constant k_{rot} will be assigned by matching the eigenfrequencies of the structure, numerically found, with those measured during experiments.

3.1.2 Multilayer Euler-Bernoulli beam model

Assuming perfect connection between the piezoelectric and support layers as well as small thickness of both and considering the cantilevered configuration, the system can be modelled as a 2D multi-layer thin plate in plain-stress conditions ($\sigma_3 = \sigma_4 = \sigma_5 = 0$), where the engineering notation, introduced in the previous chapter, is used ($[\sigma_{11}, \sigma_{22}, \sigma_{33}, \sigma_{23}, \sigma_{13}, \sigma_{12}] = [\sigma_1, \sigma_2, \sigma_3, \sigma_4, \sigma_5, \sigma_6]$). Since both materials are mechanically isotropic and homogeneous, the stress-strain relation (neglecting now the piezoelectric effect for sake of simplicity) is expressed as:

$$\begin{bmatrix} \sigma_1 \\ \sigma_2 \\ \sigma_6 \end{bmatrix} = \frac{Y}{1-\nu^2} \begin{bmatrix} 1 & \nu & 0 \\ \nu & 1 & 0 \\ 0 & 0 & 1-\nu \end{bmatrix} \begin{bmatrix} \varepsilon_1 \\ \varepsilon_2 \\ \varepsilon_6 \end{bmatrix} \tag{3.1}$$

Nevertheless, considering seismic excitation in the z-direction at the applied in $x = 0$, the device symmetry, and the tip mass layout in Fig. 3.2, the main phenomena to be evaluated are expected to live only in the $[x, z]$ plane. Thus, even though the general condition $b/L_s >> 1$ is not satisfied, we can suppose that the plate deflection does not depend on y and consequently adopt an Euler - Bernoulli beam theory, for which the only non-zero stress component is σ_1, acting in x direction. Moreover, since electrodes cover the piezoelectric surfaces perpendicular to z direction (polarization direction), the only relevant electric field component inside the material is E_3. Therefore, based on the previous assumptions, the constitutive equations of piezoelectric materials Eqs. 2.18, relating mechanical stress $\boldsymbol{\sigma}$ and mechanical strain $\boldsymbol{\varepsilon}$ to electric field $\boldsymbol{E}$ and displacements $\boldsymbol{D}$, can be reduced to the following scalar equations in stress / electric displacement form:

$$\begin{bmatrix} \sigma_1 \\ D_3 \end{bmatrix} = \begin{bmatrix} s_{11} & -\bar{e}_{31} \\ \bar{e}_{31} & \bar{\epsilon}_{33} \end{bmatrix} \begin{bmatrix} \varepsilon_1 \\ E_3 \end{bmatrix}, \tag{3.2}$$

where σ_1 and ε_1 are the stress and strain in x direction, respectively, D_3 and E_3 are the electric displacement and electric field components in z-direction, respectively. Equation 3.2 further simplifies for the support layer as

$$\sigma_1 = s_{11}\varepsilon_1 \tag{3.3}$$

because of absence of piezoelectric properties.

Recalling the generic definition of voltage as electric potential representing the work of an electric charge to move from a point A to another point B

$$V = -\int_A^B \boldsymbol{E}(\boldsymbol{P}) \cdot d\overrightarrow{\boldsymbol{OP}} \tag{3.4}$$

where P is a generic point, and defining formally the flux linkage as

$$\lambda = \int V dt\,, \tag{3.5}$$

it is convenient to express the electric field E_3 as a function of the electric flux linkage λ derivative with respect to time:

$$E_3 = -\dot{\lambda}\,/\,h_p. \tag{3.6}$$

This expression of the electric field will allow for expressing the piezoelectric electromechanical coupling as a current source (see later).

The coefficients of Eq. 3.2 can be further detailed. The elastic stiffness component at constant electric field, denoted as s_{11}^E, the piezoelectric constant $\bar{e}_{31}$, and the permittivity component at constant strain, denoted as $\bar{\epsilon}_{33}^{\varepsilon}$ are

$$s_{11,p}^E = \frac{1}{c_{11}^E}, \qquad \bar{e}_{31} = \frac{d_{31}}{c_{11}^E}, \qquad \bar{\epsilon}_{33}^{\varepsilon} = \epsilon_{33}^{\sigma} - \frac{d_{31}^2}{c_{11}^E}, \tag{3.7}$$

where ϵ_{33}^{σ} is the permittivity at constant stress, d_{31} piezoelectric coefficient, and, according to the plain stress hypothesis, it is set:

$$s_{11,p} = \frac{1}{c_{11}^E} = Y_p/(1-\nu_p^2), \qquad s_{11,s} = Y_s/(1-\nu_s^2) \tag{3.8}$$

with Y_s and Y_p Young's moduli, and ν_s and ν_p Poisson's ratios.

Finally, the strain ε_1, representing the stretch in the longitudinal direction, can be expressed as:

$$\varepsilon_1 = e_0 - z_1\kappa \tag{3.9}$$

where e_0 is the strain along the neutral axis, z_1 is the vertical distance from the neutral axis (see next section), and κ is the curvature in the x-direction. Since only one edge of the beam is constrained, there is no stretch of the neutral axis and the latter can be considered inextensible, *i.e.*, $e_0 = 0$. Moreover, small displacements are assumed, and consequently linear behaviour of the system. Thus, the curvature is

$$\kappa = w''(x,t) \tag{3.10}$$

with $w(x,t)$ with $w(x,t)$ the time-dependent vertical beam displacement at any point x, relative to the frame of reference fixed to the clamping. However, since the clamping itself experiences an oscillating vertical motion $w_b(t)$, the absolute transverse displacement at any point x takes the expression:

$$w_a(x,t) = w(x,t) + w_b(t). \tag{3.11}$$

3.1.3 Neutral axis position

As mentioned before, in designing the device one has to avoid occurrence of charge cancellation. To reach this goal, the support plate thickness must be chosen to contain the neutral axis of the overall structure, located at z_0 from the bottom. This choice guarantees that the piezoelectric material is subjected to stress distribution through its thickness (Fig. 3.3) pointing in the same direction. Indeed, if the piezoelectric experiences stress in opposite directions, there would be also opposite polarized layers through the lamina, leading to partial or even total cancellation of charge produced when the circuit is connected to the electric load.

The neutral axis is defined as intersection of the neutral plane (where $\sigma_1 = 0$) with the xz-plane, located at a distance z_0 from the beam bottom. To determinate the position z_0 of the neutral axis (see *e.g.*, [**ballas:2007**]), the equilibrium of internal forces through the section of the beam is imposed:

$$\int_0^{h_s+h_p} \sigma_1(x, z - z_0)\, dz = 0 \tag{3.12}$$

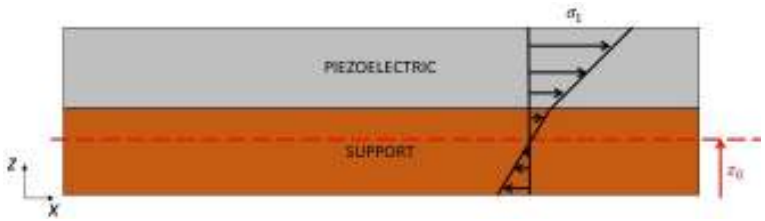

Figure 3.3: Sketch of the mechanical configuration. The neutral axis z_0 is positioned inside the support plate and the piezoelectric undergoes tension σ_1 in the same direction.

and z_0 is chosen to satisfy the previous relation. As mentioned previously, in order to take into account the neutral axis influence on the behaviour of the device, a new vertical coordinate z_1, referred to z_0, will be defined as

$$z_1 = z - z_0 \tag{3.13}$$

The neutral axis identification will also be fundamental to express the equivalent bending stiffness $\bar{D}$ and the electromechanical coupling coefficient θ for the piezoelectric region in mechanical equations (obtained in the following sections).

Considering the change of material in the thickness direction, the compliance $s_{11}(x, z)$ for $x \in (l_1, l_2)$ can be expressed in function of z as

$$s_{11}(x,z) = \begin{cases} s_{11}^{(s)} = \dfrac{Y_s}{1-\nu_s^2}, & 0 < z \leq h_s \\ \\ s_{11}^{(p)} = \dfrac{Y_p}{1-\nu_p^2}, & h_s < z \leq h_p + h_s \end{cases} \tag{3.14}$$

with $s_{11}(x, z) = s_{11}^{(s)}$ for $x \leq l_1$ and $x \geq l_2$. By substituting Eqs. 3.2, 3.3, 3.9, and 3.10, Eq. 3.12 becomes for

$x \in (l_1, l_2)$

$$\int_0^{h_p+h_s} -s_{11}(x,z)\,(z-z_0)\,w''(x)\,dz = 0 \tag{3.15}$$

where the dependence of the different variables on the local coordinates is highlighted once for the sake of clarity. Next, by substituting the compliance expressions (Eq. 3.14), it yields

$$\int_0^{h_s} \frac{Y_s}{1-\nu_s^2}(z-z_0)w''dz + \int_{h_s}^{h_p+h_s} \frac{Y_p}{1-\nu_p^2}(z-z_0)w''dz = 0 \tag{3.16}$$

which, after evaluation of the integrals, becomes

$$\frac{Y_s}{1-\nu_s^2}\Big(\frac{h_s^2}{2} - h_s z_0\Big) + \frac{Y_p}{1-\nu_p^2}\Big(\frac{h_p^2}{2} - h_p z_0 + h_p h_s\Big) = 0\,. \tag{3.17}$$

Solving the previous equation with respect to z_0, the expression of the neutral axis position with respect to the material properties is determined:

$$z_0 = \frac{\dfrac{Y_s}{1-\nu_s^2}h_s^2 + \dfrac{Y_p}{1-\nu_p^2}(h_p^2 + 2h_p h_s)}{2\Big(\dfrac{Y_s}{1-\nu_s^2}h_s + \dfrac{Y_p}{1-\nu_p^2}h_p\Big)} \tag{3.18}$$

If $x \leq l_1$ or $x \geq l_2$, we can assume $h_p = 0$ and the neutral axis position becomes $z_0 = h_s/2$. Thus, combining the previous results, the neutral axis expression over the total length of the beam is

$$z_0(x) = \begin{cases} \dfrac{\dfrac{Y_s}{1-\nu_s^2}h_s^2 + \dfrac{Y_p}{1-\nu_p^2}(h_p^2 + 2h_p h_s)}{2\Big(\dfrac{Y_s}{1-\nu_s^2}h_s + \dfrac{Y_p}{1-\nu_p^2}h_p\Big)}, & l_1 < x < l_2 \\ \dfrac{h_s}{2}, & 0 \leq x \leq l_1 \text{ and } l_2 \leq x \leq L_s \end{cases} \tag{3.19}$$

The position z_0 of the neutral axis is a weighted mean of the layer thicknesses, with weights related to the Young moduli of the different layers.

3.2 Governing equations from extended Hamilton principle

The electromechanical model has been developed by using the Lagrangian equations with an energetic approach derived from the Extended Hamilton's Principle for continuous systems [Gupta 1988], which is expressed as:

$$\delta I = \int_{t_1}^{t_2} (\delta\mathcal{L} + \delta W_{nc})\; dt = 0 \tag{3.20}$$

where δ denotes variation, I stands globally for the integral term on the right. Hamilton's principle states that for a time interval t_1 and t_2 the integral is stationary when taken along the dynamical path in the

state space defined by the set $\boldsymbol{u}$ of the independent parameters of the dynamical system, with $\mathcal{L}$ the Lagrangian function also known as kinetic potential in mechanical problems. W_{nc} is the virtual work of non-conservative forces and $\mathcal{L}$ the Lagrangian function, which includes three different contributions, one distributed $\mathcal{L}_1$ and two concentrated $\mathcal{L}_2$ and $\mathcal{L}_3$, of tip mass and yielding clamp, respectively:

$$\mathcal{L}_1 = T - U_m + U_e = \int_0^{L_s} \ell dx \tag{3.21}$$

$$\mathcal{L}_2 = \frac{1}{2} m_{tip} \dot{w}_a^2(L_s, t) \tag{3.22}$$

$$\mathcal{L}_3 = \frac{1}{2} k_{rot} \gamma^2 \tag{3.23}$$

The term $\mathcal{L}_2$ represents the kinetic energy of the tip mass in $x = L_s$ [Meirovitch 2001]. $\mathcal{L}_3$ is the potential elastic energy related to the rigid body rotation [Laura et al. 1975], (γ angle of rotation) at the yielding clamp at $x = 0$ (Fig. 3.4).

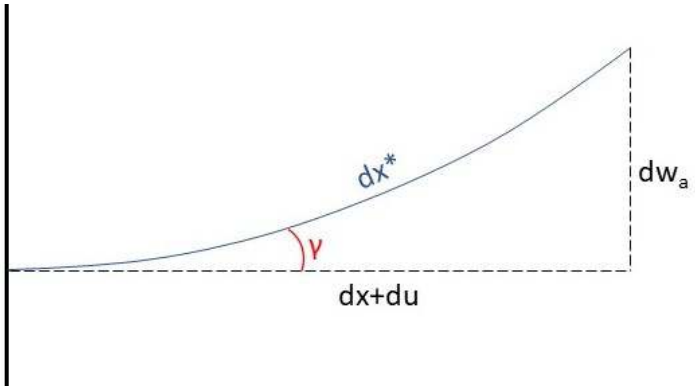

Figure 3.4: Yielding clamp: configuration and variables definition. γ, dx, dx^*, du, and dw_a are respectively angle of rotation, initial configuration, deformed configuration, horizontal displacement, and vertical displacement.

Thus, the global displacement of the beam can be expressed as

$$w_a = w_{rb} + w_e \tag{3.24}$$

with w_{rb} the rigid body displacement and w_e the elastic displacement, satisfying the condition $w_e = 0$. Therefore,

$$w_a = \gamma x + w_e \tag{3.25}$$

and, by differentiating with respect to x and calculating at $x = 0$

$$w_a'(0) = \gamma \tag{3.26}$$

Substituting (3.24), the Lagrangian term of elastic potential energy $\mathcal{L}_3$ can be written as

$$\mathcal{L}_3 = \frac{1}{2} k_{rot} w_a'^2(0) \tag{3.27}$$

$\mathcal{L}_1$ is given by the kinetic energy T, the mechanical potential energy U_m, and the electric internal energy U_e of the piezoelectric beam, expressed in terms of their energy density per unit volume.

The mechanical potential energy is given by

$$\begin{aligned} U_m = \frac{1}{2}\int_V \sigma_1\varepsilon_1 dV = \frac{1}{2}\Bigg\{ \int_{-b/2}^{b/2}\int_0^{l_1}\left[\int_0^{h_s}\sigma_1^s\varepsilon_1 dz\right]dxdy + \\ + \int_{-b/2}^{b/2}\int_{l_1}^{l_2}\left[\int_0^{h_s}\sigma_1^s\varepsilon_1 dz + \int_{h_s}^{h_p+h_s}\sigma_1^p\varepsilon_1 dz\right]dxdy + \int_{-b/2}^{b/2}\int_{l_2}^{L_s}\left[\int_0^{h_s}\sigma_1^s\varepsilon_1 dz\right]dxdy\Bigg\} \end{aligned} \tag{3.28}$$

in which the integral is split in three parts on x direction due to the inhomogeneity in the device material. Substituting the strain (Eq. 3.9) and stress (Eq. 3.3) expressions for the support material, the explicit integrations through its thicknesses h_s yields

$$\int_0^{h_s}\sigma_1^s\varepsilon_1 dz = \int_0^{h_s}\frac{Y_s}{1-\nu_s^2}(z-z_0)^2\kappa^2 dz = \frac{Y_s}{1-\nu_s^2}\kappa^2\int_0^{h_s} z^2 - 2zz_0 + z_0^2 dz = \frac{Y_s}{1-\nu_s^2}\kappa^2\left[\frac{h_s^3}{3} - z_0h_s^2 + h_sz_0^2\right] \tag{3.29}$$

Analogously, substituting the strain (Eq. 3.9) and stress (Eq. 3.2) expressions for the piezoelectric material, the explicit integrations through its thicknesses h_p gives

$$\int_{h_s}^{h_p+h_s}\sigma_1^p\varepsilon_1 dz = \frac{Y_p}{1-\nu_p^2}\int_{h_s}^{h_p+h_s}\kappa^2(z^2-2zz_0+z_0^2) - \frac{d_{31}\dot{\lambda}\kappa}{h_p}(z-z_0)dz \tag{3.30}$$

and, after some algebric manupulation,

$$\begin{aligned} &\frac{Y_p}{1-\nu_p^2}\kappa\Bigg\{\kappa\left[\left(\frac{h_p^3}{3}+\frac{h_s^3}{3}+h_p^2h_s+h_s^2h_p-\frac{h_s^3}{3}\right) - z_0\left(h_p^2+h_s^2+2h_ph_s-h_s^2\right) + z_0^2\left(h_p+h_s-h_s\right)\right] + \\ &\quad -\frac{d_{31}\dot{\lambda}}{h_p}\left[\frac{1}{2}\left(h_p^2+h_s^2+2h_ph_s-h_s^2\right) - z_0\left(h_p+h_s-h_s\right)\right]\Bigg\} = \\ &= \frac{Y_p}{1-\nu_p^2}\kappa^2\left[\frac{h_p^3}{3}+h_p^2h_s+h_s^2h_p - z_0\left(h_p^2+2h_ph_s\right)+z_0^2h_p\right] - \frac{Y_p\dot{\lambda}d_{31}\kappa}{1-\nu_p^2}\left[\frac{h_p}{2}+h_s-z_0\right] \end{aligned} \tag{3.31}$$

Then, substituting Eqs. 3.29 and 3.31 in the potential energy expression 3.28, we obtain the final expression of the mechanical potential energy of the system.

$$\begin{aligned} U_m = \frac{b}{2}\Bigg\{ &\int_0^{l_1}\frac{Y_s}{1-\nu_s^2}\kappa^2\left[\frac{h_s^3}{3}-z_0h_s^2+h_sz_0^2\right]dx + \int_{l_1}^{l_2}\frac{Y_s}{1-\nu_s^2}\kappa^2\left[\frac{h_s^3}{3}-z_0h_s^2+h_sz_0^2\right] + \\ &+\frac{Y_p}{1-\nu_p^2}\kappa^2\left[\frac{h_p^3}{3}+h_p^2h_s+h_s^2h_p - z_0\left(h_p^2+2h_ph_s\right)+z_0^2h_p\right] - \frac{Y_p\dot{\lambda}d_{31}\kappa}{1-\nu_p^2}\left[\frac{h_p}{2}+h_s-z_0\right]dx + \\ &+\int_{l_2}^{L_s}\frac{Y_s}{1-\nu_s^2}\kappa^2\left[\frac{h_s^3}{3}-z_0h_s^2+h_sz_0^2\right]dx\Bigg\} \end{aligned} \tag{3.32}$$

The electric potential energy is present only in the piezoelectric domain V_p, for $x \in (l_1, l_2)$, and is given

by

$$U_e = \frac{1}{2}\int_{V_p} \boldsymbol{E}\cdot\boldsymbol{D}\, dV = \frac{1}{2}\int_{V_p} E_3 D_3\, dV = \frac{1}{2}\int_{V_p} -\frac{\dot{\lambda}}{h_p}\left(\varepsilon_{11}\bar{e}_{31} - \epsilon_{33}\frac{\dot{\lambda}}{h_p}\right) dV \tag{3.33}$$

with $\boldsymbol{E}$ and $\boldsymbol{D}$ the electric field and electric displacement vectors, respectively. With E_3 the only component in z direction not vanishing, remembering Eqs. 3.2, and decomposing the volume V_p, the latter equation becomes

$$\begin{aligned} U_e &= -\frac{\dot{\lambda}}{2h_p}\iint_{A_p}\int_{h_s}^{h_p+h_s} -\kappa(z-z_0)\bar{e}_{31} - \epsilon_{33}\frac{\dot{\lambda}}{h_p} dz dA = \\ &= \frac{b\dot{\lambda}}{2h_p}\int_{l_1}^{l_2} \bar{e}_{31}\left[\frac{\kappa}{2}\left(h_p^2 + h_s^2 + 2h_p h_s - h_s^2\right) - \kappa z_0\left(h_p + h_s - h_s\right)\right] + \epsilon_{33}\frac{\dot{\lambda}}{h_p}\left(h_p + h_s - h_s\right)dx = \\ &= \int_{l_1}^{l_2} \frac{d_{31}Y_p b}{2(1-\nu_p^2)}\left(\frac{h_p}{2} + h_s - z_0\right)\kappa\dot{\lambda} + \epsilon_{33}\frac{b}{2h_p}\dot{\lambda}^2 dx \end{aligned} \tag{3.34}$$

Finally, the kinetic energy is given by

$$T = \frac{1}{2}\int_0^{L_s} \mu(x)\dot{w}_a^2\, dx \tag{3.35}$$

where the kinetic energy term due to the horizontal displacement u can be neglected because of the small displacement hypothesis and μ is the beam mass per unit of length, defined along the beam as

$$\mu(x) = \begin{cases} \rho_p h_p b + \rho_s h_s b, & l_1 < x < l_2 \\ \\ \rho_s h_s b, & 0 \le x \le l_1 \text{ and } l_2 \le x \le L_s \end{cases} \tag{3.36}$$

Substituting the expression for kinetic energy T (Eq. 3.35), mechanical potential energy U_m (Eq. 3.32), and electric potential energy U_e (Eq. 3.34), finally we can define $\mathcal{L}_1$ by means of the density Lagrangian function ℓ in the form

$$\begin{aligned} \ell =& \frac{1}{2}\left\{\mu\dot{w}_a^2 - \frac{bY_p}{1-\nu_p^2}\kappa^2\left[\frac{h_p^3}{3} + h_p^2 h_s + h_p h_s^2 - z_0\left(h_p^2 + 2h_p h_s\right) + h_p z_0^2\right] - \frac{bY_s}{1-\nu_s^2}\kappa^2\left[\frac{h_s^3}{3} - h_s^2 z_0 + h_s z_0^2\right] + \right. \\ &\left. + \frac{bd_{31}Y_p}{1-\nu_p^2}\kappa\dot{\lambda}\left[\frac{h_p}{2} + h_s - z_0\right] + \frac{bd_{31}Y_p}{1-\nu_p^2}\kappa\dot{\lambda}\left[\frac{h_p}{2} + h_s - z_0\right] + \frac{b\epsilon_{33}}{h_p}\dot{\lambda}^2\right\} \end{aligned} \tag{3.37}$$

and further collecting together the terms multiplying κ^2, $\kappa\dot{\lambda}$, and $\dot{\lambda}^2$, Eq. 3.37becomes:

$$\begin{aligned} \ell =& \frac{1}{2}\left\{\mu\dot{w}^2 - \kappa^2\left[\frac{bY_p}{1-\nu_p^2}\left(\frac{h_p^3}{3} + h_p^2 h_s + h_p h_s^2 - z_0\left(h_p^2 + 2h_p h_s\right) + h_p z_0^2\right) + \frac{bY_s}{1-\nu_s^2}\kappa^2\left(\frac{h_s^3}{3} - h_s^2 z_0 + h_s z_0^2\right)\right] + \right. \\ &\left. + 2\kappa\dot{\lambda}\left[\frac{bd_{31}Y_p}{1-\nu_p^2}\left(\frac{h_p}{2} + h_s - z_0\right)\right] + \dot{\lambda}^2\left(\frac{b\epsilon_{33}}{h_p}\right)\right\} \end{aligned} \tag{3.38}$$

Thus, introducing the following coefficients:

- Equivalent bending stiffness of the system

$$\bar{D}(x) = \begin{cases} \dfrac{Y_s b}{1-\nu_s^2}\left[\dfrac{h_s^3}{3} - z_0 h_s^2 + h_s z_0^2\right] + \dfrac{Y_p b}{1-\nu_p^2}\left[\dfrac{h_p^3}{3} + h_p^2 h_s + h_s^2 h_p - z_0\left(h_p^2 + 2h_p h_s\right) + z_0^2 h_p\right], & l_1 < x < l_2 \\ \dfrac{Y_s b h_s^3}{12(1-\nu_s^2)}, \qquad 0 \le x \le l_1 \text{ and } l_2 \le x \le L_s \end{cases} \tag{3.39}$$

- Electromechanical coupling coefficient

$$\theta = \frac{Y_p b d_{31}}{1-\nu_p^2}\left(\frac{h_p}{2} + h_s - z_0\right) \tag{3.40}$$

- Equivalent piezoelectric capacity per unit of length

$$C_{p,L} = \epsilon_{33}\frac{b}{h_p} \tag{3.41}$$

and the Heaviside function, defined as

$$H(x) = \begin{cases} 1, & x \ge 0 \\ 0, & x < 0 \end{cases} \tag{3.42}$$

Substituting the above expressions in Eq. 3.38,

$$\ell = \frac{1}{2}\left\{\mu \dot{w}_a^2 - \bar{D} w''^2 + 2\theta w'' \dot{\lambda}[H(x-l_1) - H(x-l_2)] + C_{p,L}\dot{\lambda}^2[H(x-l_1) - H(x-l_2)]\right\} \tag{3.43}$$

It is worth noting that the Heaviside function $H(x)$ has been used to consider the contribution of the piezoelectric lamina only on its length.

Finally, the external work of non-conservative forces is:

$$\begin{aligned} \delta W_{nc} &= -\frac{1}{R}\ddot{\lambda}\,\delta\lambda - \int_0^{L_s} c_a \dot{w}_a\,\delta w_a\,dx - \int_0^{L_s} c_s \dot{\varepsilon}\,\delta\varepsilon\,dV = \\ &= \frac{1}{R}\ddot{\lambda}\,\delta\lambda + \int_0^{L_s} c_a \dot{w}_a\,\delta w_a\,dx + \int_0^{L_s} c_s J\,\dot{w}''\,\delta w''\,dx \end{aligned} \tag{3.44}$$

with $\ddot{\lambda}/R\,\delta\lambda = I_c$ the current powering the electric load (represented by a resistance R), $(c_s J \dot{w}'')''$ the Kelvin-Voigt (or strain-rate) damping term, expressing the internal energy dissipation of the beam, and $c_a \dot{w}_a$ the viscous air damping.

Focusing on the specific form of the Lagrangian function, which includes continuous ℓ and lumped

contributions $\mathcal{L}_k$ (see *e.g.*, [Gupta 1988]),

$$\delta\mathcal{L}(\boldsymbol{u}) = \int_0^{L_s} \delta\ell(\boldsymbol{u})\ dx + \delta\mathcal{L}_2(\boldsymbol{u}) + \delta\mathcal{L}_3(\boldsymbol{u}), \tag{3.45}$$

the set of independent parameters is provided for the piezoelectric cantilever by functions $p_1 = w_a(x,t)$ and $p_2 = \lambda(t)$ along with their time and space derivatives. Thus, setting $\mathbf{p} = \{p_1, p_2\}$, the Lagrangian from Eq. A.7 can be expressed in general form as:

$$\delta\mathcal{L}(\mathbf{p}, \mathbf{p}', \mathbf{p}'', \dot{\mathbf{p}}, \dot{\mathbf{p}}') = \int_0^{L_s} \left(\sum_{j=1}^{2} \sum_{i=0}^{4} \frac{\partial \ell}{\partial {p_j}^{(i)}} \delta {p_j}^{(i)} \right) dx + \sum_{k=2}^{3} \sum_{j=1}^{2} \sum_{i=0}^{4} \frac{\partial \mathcal{L}_k}{\partial {p_j}^{(i)}} \delta {p_j}^{(i)} \tag{3.46}$$

where, for the sake of conciseness, it is set $p_j^{(0)} = p_j$, $p_j^{(1)} = p_j'$, $p_j^{(2)} = p_j''$, and $p_j^{(3)} = \dot{p_j}$. Each term of the expansion with respect to the virtual displacements $\delta p_j^{(i)}$ needs to be separately evaluated, using the condition $\delta\mathbf{p}(t_1) = \delta\mathbf{p}(t_2) = 0$. In the following, only not vanishing derivatives will be taken into account relatively to the summations in the r.h.s of Eq. A.8. Thus, remembering the Extended Hamilton's Principle (Eq. 3.20), and considering the order reversibility of integrals and the commutativity of the operators $\delta(\cdot)$ and $\partial/\partial x(\cdot)$, the derivative of ℓ with respect to $\dot{p_j}$ can be integrated by parts over time, as follows

$$\int_0^{L_s} \int_{t_1}^{t_2} \frac{\partial \ell}{\partial \dot{p_j}} \delta \dot{p_j}\ dt\, dx = \int_0^{L_s} \left[\frac{\partial \ell}{\partial \dot{p_j}} \delta p_j \bigg|_{t_1}^{t_2} - \int_{t_1}^{t_2} \frac{\partial}{\partial t} \left(\frac{\partial \ell}{\partial \dot{p_j}} \right) \delta p_j\ dt \right] dx = - \int_0^{L_s} \int_{t_1}^{t_2} \frac{\partial}{\partial t} \left(\frac{\partial \ell}{\partial \dot{p_j}} \right) \delta p_j\ dt\, dx. \tag{3.47}$$

Analogously, the derivative with respect to $\dot{p_j}$ relative to $\mathcal{L}_2$ can be integrated by parts over time

$$\int_{t_1}^{t_2} \frac{\partial \mathcal{L}_2}{\partial \dot{p_j}} \delta \dot{p_j}\ dt = \frac{\partial \mathcal{L}_2}{\partial \dot{p_j}} \delta p_j \bigg|_{t_1}^{t_2} - \int_{t_1}^{t_2} \frac{\partial}{\partial t} \left(\frac{\partial \mathcal{L}_2}{\partial \dot{p_j}} \right) \delta p_j\ dt = - \int_{t_1}^{t_2} \frac{\partial}{\partial t} \left(\frac{\partial \mathcal{L}_2}{\partial \dot{p_j}} \right) \delta p_j\ dt \tag{3.48}$$

and the integral over the beam length not taken into account since $\mathcal{L}_2$ is defined only at the free edge.

Regarding the term $\mathcal{L}_3$ associated to the yielding clamp, one obtains,

$$\int_{t_1}^{t_2} \frac{\partial \mathcal{L}_3}{\partial p_j'} \delta p_j'\ dt = \frac{\partial \mathcal{L}_3}{\partial p_j'} \delta p_j \bigg|_{t_1}^{t_2} - \int_{t_1}^{t_2} \frac{\partial}{\partial x} \left(\frac{\partial \mathcal{L}_3}{\partial p_j'} \right) \delta p_j\ dt = - \int_{t_1}^{t_2} \frac{\partial}{\partial x} \left(\frac{\partial \mathcal{L}_3}{\partial p_j'} \right) \delta p_j\ dt \tag{3.49}$$

Finally, the derivative of $\mathcal{L}_3$ with respect to $\dot{p_j}$ is equal to zero, since this lagrangian term is not time dependent.

A similar calculation can be performed for derivatives with respect to p_j' and p_j''. Since both $\mathcal{L}_2$ and $\mathcal{L}_3$ are defined only at the boundaries, their integral over the beam length is zero. Thus, integrals of ℓ over x of the derivative with respect to p_j' can be integrated by parts:

$$\int_{t_1}^{t_2} \int_0^{L_s} \frac{\partial \ell}{\partial p_j'} \delta p_j'\ dx\, dt = \int_{t_1}^{t_2} \left[\frac{\partial \ell}{\partial p_j'} \delta p_j \bigg|_0^{L_s} - \int_0^{L_s} \frac{\partial}{\partial x} \left(\frac{\partial \ell}{\partial p_j'} \right) \delta p_j\ dx \right] dt \tag{3.50}$$

and, analogously, for the derivative of ℓ with respect to p_j'' we obtain

$$\int_{t_1}^{t_2}\int_0^{L_s}\frac{\partial \ell}{\partial p_j''}\,\delta p_j''\;dx\,dt=\int_{t_1}^{t_2}\left[\frac{\partial \ell}{\partial p_j''}\,\delta p_j'\Big|_0^{L_s}-\frac{\partial}{\partial x}\left(\frac{\partial \ell}{\partial p_j''}\right)\delta p_j\Big|_0^{L_s}+\int_0^{L_s}\frac{\partial^2}{\partial x^2}\left(\frac{\partial \ell}{\partial p_j''}\right)\delta p_j\;dx\right]dt \tag{3.51}$$

Recalling also the expression of external work of non-conservative forces leading to mechanical damping and electrical dissipation terms,

$$\delta W_{nc}=\int_0^{L_s}(\bar{Q}_{11}\,\delta p_1+\bar{Q}_{12}\,\delta p_1'')dx+Q_2\,\delta p_2 \tag{3.52}$$

As seen before for the Lagrangian function, exploiting the order reversibility of time and space integrals, the $Q_{12}\delta p_1''$ term can be integrated by parts:

$$\begin{aligned}\int_0^{L_s}Q_{12}\delta p_1''\,dx&=Q_{12}\delta p_1'\Big|_0^{L_s}-\int_0^{L_s}\frac{\partial Q_{12}}{\partial x}\delta p_1'\,dx=\\ =&Q_{12}\delta p_1'\Big|_0^{L_s}-\frac{\partial Q_{12}}{\partial x}\delta p_1\Big|_0^{L_s}+\int_0^{L_s}\frac{\partial^2 Q_{12}}{\partial x^2}\delta p_1\,dx\end{aligned} \tag{3.53}$$

Substituting the expressions 3.47, 3.48, 3.50, 3.51, and 3.53 in the Eq. A.8, we can rewrite the Extended Hamilton Principle 3.20 as

$$\begin{aligned}&\int_{t_1}^{t_2}\Bigg\{\int_0^{L_s}\left[\frac{\partial \ell}{\partial p_j}-\frac{\partial}{\partial x}\left(\frac{\partial \ell}{\partial p_j'}\right)+\frac{\partial^2}{\partial x^2}\left(\frac{\partial \ell}{\partial p_j''}\right)-\frac{\partial}{\partial t}\left(\frac{\partial \ell}{\partial p_j}\right)+Q_j\right]\delta p_j\,dx+\\ &\left[\frac{\partial \ell}{\partial p_j'}-\frac{\partial}{\partial x}\frac{\partial \ell}{\partial p_j''}-\frac{\partial Q_{12}}{\partial x}-\frac{\partial}{\partial t}\frac{\partial \mathcal{L}_2}{\partial \dot{p}_j}\right]\delta p_j\Big|_0^{L_s}+\left[\frac{\partial \ell}{\partial p_j''}+Q_{12}+\frac{\partial \mathcal{L}_3}{\partial p_j'}-\frac{\partial}{\partial t}\frac{\partial \mathcal{L}_2}{\partial \dot{p}_j'}\right]\delta p_j'\Big|_0^{L_s}\Bigg\}dt=0\end{aligned} \tag{3.54}$$

where the terms involving $\mathcal{L}_2$ and $\mathcal{L}_3$ are considered equal to zero in 0 and L_s, respectively, and where Q_1 includes the resulting term from integration by parts of the integral term in Eq. 3.52. Usually, Eq. 3.54 leads to separately setting the terms associated to virtual displacements equal to zero because of principle of virtual work, directly providing in this way the governing equation and the BCs. However, in the present case it would lead to time dependent BCs due to the presence of imposed excitation w_b inside the total displacement w_a, and this suggest to rearranging terms in Eq. 3.54 before setting them equal to zero.

Thus, for $p_1=w_a$ we have

$$\begin{aligned}&\int_0^{L_s}\left[\frac{\partial \ell}{\partial w_a}-\frac{\partial}{\partial x}\left(\frac{\partial \ell}{\partial w_a'}\right)+\frac{\partial^2}{\partial x^2}\left(\frac{\partial \ell}{\partial w_a''}\right)-\frac{\partial}{\partial t}\left(\frac{\partial \ell}{\partial \dot{w}_a}\right)+Q_{11}+\frac{\partial^2 Q_{12}}{\partial x^2}\right]\delta w_a\,dx+\\ &+\left[\frac{\partial \ell}{\partial w_a'}-\frac{\partial}{\partial x}\frac{\partial \ell}{\partial w_a''}-\frac{\partial Q_{12}}{\partial x}-\frac{\partial}{\partial t}\frac{\partial \mathcal{L}_2}{\partial \dot{w}_a}\right]\delta w_a\Big|_0^{L_s}+\left[\frac{\partial \ell}{\partial w_a''}+Q_{12}+\frac{\partial \mathcal{L}_3}{\partial w_a'}-\frac{\partial}{\partial t}\frac{\partial \mathcal{L}_2}{\partial \dot{w}_a'}\right]\delta w_a'\Big|_0^{L_s}=0\end{aligned} \tag{3.55}$$

in which, recalling that the space derivatives of w_a contain only the elastic contribution w, the terms are

$$\frac{\partial \ell}{\partial w_a}=\frac{\partial \ell}{\partial w_a'}=0,\qquad \frac{\partial \ell}{\partial w_a''}=-\bar{D}w''+\theta\dot{\lambda}\big[H(x-l_1)-H(x-l_2)\big],\qquad \frac{\partial \ell}{\partial \dot{w}_a}=\mu\dot{w}_a$$

Then, by substituting in Eq. 3.55 we obtain

$$\begin{aligned}&\int_0^{L_s} \frac{\partial^2}{\partial x^2}\left\{-\bar{D}w'' + \theta\dot{\lambda}\Big[H(x-l_1) - H(x-l_2)\Big]\right\} - \frac{\partial}{\partial t}\Big(\mu\dot{w}_a\Big) - c_a\dot{w}_a - \frac{\partial^2}{\partial x^2}\Big(c_sJ\dot{w}''\Big)dx + \\ &+ \left\{-\frac{\partial}{\partial x}\left[-\bar{D}w'' - c_sJ\dot{w}'' + \theta\dot{\lambda}\Big(H(x-l_1) - H(x-l_2)\Big)\right] - \frac{\partial}{\partial t}\Big(m_{tip}\dot{w}_a(L_s)\Big)\right\}\delta w_a\Big|_0^{L_s} + \\ &+ \Big\{-\bar{D}w'' - c_sJ\dot{w}'' + \theta\dot{\lambda}\Big[H(x-l_1) - H(x-l_2)\Big] + k_{rot}w'\Big\}\delta w'\Big|_0^{L_s} = 0\end{aligned} \tag{3.56}$$

Considering the term depending from θ vanished since, thanks to the Heaviside function, the piezoelectric does not act in 0 and L_s, by performing derivatives in Eq. 3.56 the following equation can be obtained.

$$\begin{aligned}&\int_0^{L_s} -\mu\ddot{w}_a - (\bar{D}w'')'' + \theta\dot{\lambda}\Big[H''(x-l_1) - H''(x-l_2)\Big] - c_a\dot{w}_a - (c_sJ\dot{w}'')''dx + \\ &+ \Big[(\bar{D}w'')' + (c_sJ\dot{w}'')' - m_{tip}\dot{w}_a\Big]\delta w_a\Big|_0^{L_s} + \Big(-\bar{D}w'' - c_sJ\dot{w}'' + k_{rot}w'\Big)\delta w'\Big|_0^{L_s} = 0\end{aligned} \tag{3.57}$$

Where the second derivative of the Heaviside function is equal to the first derivative of the Dirac delta function δ, defined as.

$$\delta(x) = \begin{cases} +\infty, & x = 0 \\ \\ 0, & x \neq 0 \end{cases} \tag{3.58}$$

It is convenient splitting w_a into the elastic and rigid body contribution, and then grouping the terms both depending on w_b and associated to δp_1 with the continuous term (δ-Dirac symbols are introduced for that). Thus, the following equation is obtained:

$$\begin{aligned}&\int_0^{L_s}\left\{-\mu\ddot{w} - (\bar{D}w'')'' + \theta\Big[\delta'(x-l_1) - \delta'(x-l_2)\Big]\dot{\lambda} - c_a\dot{w} - (c_sJ\dot{w}'')'' - \Big[\mu + m_{tip}\delta(x-L_s)\Big]\ddot{w}_b - c_a\dot{w}_b\right\}dx + \\ &+ \Big[(\bar{D}w'')' + (c_sJ\dot{w}'')' - m_{tip}\dot{w}\Big]\delta w\Big|_0^{L_s} + \Big(-\bar{D}w'' - c_sJ\dot{w}'' + k_{rot}w'\Big)\delta w'\Big|_0^{L_s} = 0\end{aligned} \tag{3.59}$$

Considering $\delta\boldsymbol{p}(0,t) = \delta\boldsymbol{p}(L_s,t) = \delta\boldsymbol{p}'(0,t) = \delta\boldsymbol{p}'(L_s,t) = 0$, according to the fundamental lemma of calculus of variations and thanks to the arbitrariness of virtual displacements $\delta\boldsymbol{p}$, Eq. 3.59 is satisfied $\forall\delta p$ and $\forall(x,t) \in (0,L_s)\times[0,+\infty)$ only if the terms inside and outside the integral are equal to zero. Thus, the following equation is obtained.

$$\mu\ddot{w} + c_a\dot{w} + (\bar{D}w'' + c_sJ\dot{w}'')'' - \theta\Big[\delta'(x-l_1) - \delta'(x-l_2)\Big]\dot{\lambda} = f(x,t) \tag{3.60}$$

with $f(x,t)$ expressed as:

$$f(x,t) = -\left[\mu + m_{tip}\delta(x-l_r)\right]\ddot{w}_b - c_a\dot{w}_b \tag{3.61}$$

The natural and geometric boundary conditions are obtained by setting to zero arbitrarily $\delta \boldsymbol{p}(0,t)$ and $\delta \boldsymbol{p}'(0,t)$ or their coefficients of the terms out of the integral in Eq. 3.59.

For $p_2 = \lambda$, the derivatives in Eq. 3.54 take the form:

$$\frac{\partial \ell}{\partial \lambda'} = \frac{\partial \ell}{\partial \lambda''} = \frac{\partial \ell}{\partial \lambda} = 0, \qquad \frac{\partial \ell}{\partial \dot{\lambda}} = \theta w''[H(x-l_1) - H(x-l_2)] + C_{p,L}\dot{\lambda}[H(x-l_1) - H(x-l_2)]$$

Recalling that $Q_2 = -I_c$, and setting equal to zero the first term in r.h.s. of Eq. 3.54, the following equation is obtained:

$$\int_0^{L_s} \left[\frac{\partial \ell}{\partial \lambda} - \frac{\partial}{\partial x}\left(\frac{\partial \ell}{\partial \lambda'}\right) + \frac{\partial^2}{\partial x^2}\left(\frac{\partial \ell}{\partial \lambda''}\right) - \frac{\partial}{\partial t}\left(\frac{\partial \ell}{\partial \dot{\lambda}}\right) - I_c^{(L_s)} \right] dx = 0 \tag{3.62}$$

Substituting the above derivatives expressions, the following equation is obtained

$$\begin{aligned} &\int_0^{L_s} \left\{ -\frac{\partial}{\partial t}\left[\theta w'' \Big[H(x-l_1) - H(x-l_2) \Big] + C_{p,L}\dot{\lambda}[H(x-l_1) - H(x-l_2)] \right] - I_c^{(L_s)} \right\} dx = 0 \Rightarrow \\ \Rightarrow &- \int_0^{L_s} \theta \dot{w}'' \Big[H(x-l_1) - H(x-l_2) \Big] dx - C_p \ddot{\lambda} - I_c = 0 \end{aligned} \tag{3.63}$$

where $C_p = C_{p,L} \cdot L_p$ is the equivalent piezoelectric capacity, including the length of the piezo lamina.

Thus, the final system is

$$\begin{cases} \mu \ddot{w} + c_a \dot{w} + (c_s J \dot{w}'' + \bar{D} w'')'' - \theta \big[\delta'(x-l_1) - \delta'(x-l_2) \big] \dot{\lambda} = f(x,t) \\ C_p \ddot{\lambda} + \int_0^{L_s} \theta \Big[H(x-l_1) - H(x-l_2) \Big] \dot{w}'' \, dx = -I_c \end{cases} \tag{3.64}$$

with boundary conditions in $x = 0$

$$w(0) = 0 \tag{3.65}$$

$$-\bar{D} w''(0) - c_s J \dot{w}''(0) + k_{rot} w'(0) = 0 \tag{3.66}$$

and in $x = L_s$

$$\bar{D} w''(L_s) + c_s J \dot{w}''(L_s) = 0 \tag{3.67}$$

$$[\bar{D} w''(L_s) + c_s J \dot{w}''(L_s)]' - m_{tip} \ddot{w}(L_s) = 0. \tag{3.68}$$

3.3 Electromechanical reduced-order model

3.3.1 Analytical beam modes including tip mass and yielding clamp effects

As known from several authors, the contribution of higher-order modes to voltage and then power production is negligible. Fot this reason, it is convenient to find a solution of Eqs. 3.64 by modal superposition. Thus, the displacement w can be expressed as a linear combination of the product of a time and space function:

$$w(x,t) = \sum_{j=1}^{N_w} q_j(t) \phi_j(x) \tag{3.69}$$

with q_j the generalized coordinate depending on time, $\phi_j(x)$ the linear normal modes of the multi-layer beam, satisfying the geometric and natural boundary conditions at the beam edges, and N_w number of modes taken into account. The flux linkage λ is constant along the length of the piezoelectric patch and, consequently, has the unit constant as shape function:

$$\lambda(x,t) = \lambda(t) \cdot C \tag{3.70}$$

where can be set directly $C = 1$.

To solve the system equations and obtain the most accurate solution, the exact modes ϕ_j of the considered structure can be calculated. First, the external force $f(x,t)$ is set to zero to obtain the free vibration condition. Moreover, the system is considered undamped to avoid complex modes. Finally, to uncouple electrical and mechanical equations, the short circuit condition, *i.e.*, $\dot{\lambda} = 0$, is imposed. With the previous hypothesis, Eqs. **??** are reduced to

$$\mu\ddot{w} + (\bar{D}w'')'' = 0 \tag{3.71}$$

and, substituting the modal expansion (Eq. 3.69) into Eq. 3.71, the equation for the j-th mode is

$$\mu\ddot{q}_j(t)\phi_j(x) + (\bar{D}\phi_j'')''q_j(t) = 0 \quad or \quad -\frac{\ddot{q}_j}{q_j} = \frac{(\bar{D}\phi_j'')''}{\mu\phi_j} \tag{3.72}$$

Since the left-hand side is time dependent and the right-hand side is not, Eq. 3.72 is verified only if both sides are equal to a positive constant, *i.e.*,

$$-\frac{\ddot{q}_j}{q_j} = \frac{(\bar{D}\phi_j'')''}{\mu\phi_j} = cost = \omega_j^2 \tag{3.73}$$

where the constant ω_j^2 is the eigenvalue referred to the eigenfunction j, expressed as the ratio of the modal stiffness and the modal mass. Thus, the following equations can be defined

$$\begin{cases} \ddot{q}_j + \omega_j^2 q_j = 0 \\ (\bar{D}\phi_j'')'' - \mu\phi_j = 0 \end{cases} \tag{3.74}$$

The second equation can be solved easily only for a beam with uniform stiffness $\bar{D}$ over the length, providing

$$\bar{D}\phi_j^{IV} - \mu\omega_j^2\phi_j = 0 \tag{3.75}$$

For the piezoelectric structure under consideration has non-uniform distribution of stiffness and mass, the calculation of the exact bending modes, which allows for modal decoupling, requires some mathematical developments (a similar problem is addressed in [Dessi et al. 2015]). First, in order to refer to Eq. 3.75, a piecewise definition of $w(x,t)$ in space is introduced and consequently three different displacement func-

tions can be locally defined along the beam axis as:

$$w(x,t) = \begin{cases} w_1(x_1), & for\, 0 \le x_1 \le l_1 \\ w_2(x_2), & for\, 0 \le x_2 \le L_p = l_2 - l_1 \\ w_3(x_3), & for\, 0 \le x_3 \le L_s - l_2 \end{cases} \tag{3.76}$$

where local coordinate systems have been defined for the three parts of the beam, as shown in Fig. 3.5.

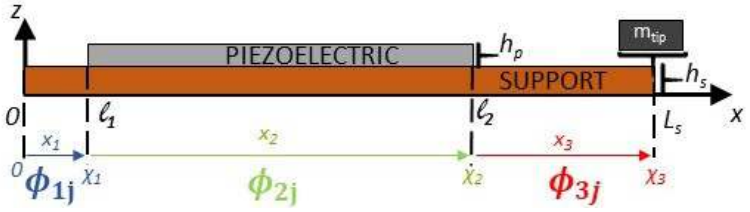

Figure 3.5: Definition of local coordinate systems for exact mode calculation.

Each local displacement function w_i can be expanded with respect to the local modes relative to the i-th portion as $w_i = \sum q_j \phi_{ij}$. Each set of shape functions $\{\phi_{1j}, \phi_{2j}, \phi_{3j}\}$ represents the global mode ϕ_j and satisfies the proper BCs at the beam ends and the continuity conditions at the piezoelectric layer edges up to 3-rd order spatial derivative [Dessi et al. 2015]. Each function ϕ_{ij} satisfies the following eigenvalue problem:

$$\phi_{ij}^{IV} - \alpha_{ij}^4 \phi_{ij} = 0 \tag{3.77}$$

with $\alpha_{ij}^4 = \mu\omega_j^2/\bar{D}$, where μ and $\bar{D}$ are constant in each subproblem, and ω_j is the natural frequency of the vibration modes. Next, given the shape functions ϕ_{ij} in the form:

$$\phi_{ij}(x_i) = A_{ij}^{(1)} \sin(\alpha_{ij} x_i) + A_{ij}^{(2)} \cos(\alpha_{ij} x_i) + A_{ij}^{(3)} \sinh(\alpha_{ij} x_i) + A_{ij}^{(4)} \cosh(\alpha_{ij} x_i) \tag{3.78}$$

where $i = 1, 2, 3$ correspond respectively to the three parts of the beam. To determinate the $A_{ij}^{(k)}$ coefficients, the following boundary conditions are rewritten in terms of ϕ_{ij}.

At the beam clamping, in $x_1 = 0$:

$$w_1(0) = 0 \Rightarrow \phi_{1j}(0) = A_{1j}^{(2)} + A_{1j}^{(4)} = 0 \tag{3.79}$$

$$\bar{D} w''(0) = k_{rot} w'(0) \Rightarrow \phi'_{1j}(0) = \frac{\bar{D}}{k_{rot}} \phi''_{1j}(0) \Rightarrow A_{1j}^{(1)} + A_{1j}^{(3)} = \frac{\bar{D}\alpha_{1j}}{k_{rot}} (-A_{1j}^{(2)} + A_{1j}^{(4)}) \tag{3.80}$$

At the discontinuity interfaces same displacement, slope, shear stress and bending moment are imposed. For $x_1 = l_1$ and $x_2 = 0$:

- displacement

$$\begin{aligned} &w_1(l_1) = w_2(0) \Rightarrow \phi_{1j}(l_1) = \phi_{2j}(0) \Rightarrow \\ &A_{1j}^{(1)} \Big[\sin(\alpha_{1j} l_1) - \sinh(\alpha_{1j} l_1)\Big] + A_{1j}^{(2)} \Big[\cos(\alpha_{1j} l_1) - \cosh(\alpha_{1j} l_1)\Big] = A_{2j}^{(2)} + A_{2j}^{(4)} \end{aligned} \tag{3.81}$$

- slope

$$w_1'(l_1) = w_2'(0) \Rightarrow \phi_{1j}'(l_1) = \phi_{2j}'(0) \Rightarrow$$
$$\alpha_{1j}\, A_{1j}^{(1)}\Big[\cos(\alpha_{1j}l_1) - \cosh(\alpha_{1j}l_1)\Big] + \alpha_{1j}\, A_{1j}^{(2)}\Big[-\sin(\alpha_{1j}l_1) - \sinh(\alpha_{1j}l_1)\Big] = \alpha_{2j}\, A_{2j}^{(1)} + \alpha_{2j}\, A_{2j}^{(3)} \tag{3.82}$$

- bending moment

$$\begin{aligned}&\bar{D}(l_1)w_1''(l_1) = \bar{D}(L_p)w_2''(0) \Rightarrow \phi_{1j}''(l_1) = D_{21}\phi_{2j}''(0) \Rightarrow \\ &\alpha_{1j}^2\, A_{1j}^{(1)}\Big[-\sin(\alpha_{1j}l_1) - \sinh(\alpha_{1j}l_1)\Big] + \alpha_{1j}^2\, A_{1j}^{(2)}\Big[-\cos(\alpha_{j1}l_1) - \cosh(\alpha_{1j}l_1)\Big] = \\ &D_{21}(\alpha_{2j}^2\, A_{2j}^{(4)} - \alpha_{2j}^2\, A_{2j}^{(2)})\end{aligned} \tag{3.83}$$

- shear stress

$$\bar{D}(l_1)w_1'''(l_1) = \bar{D}(L_p)w_2'''(0) \Rightarrow \phi_{1j}'''(l_1) = D_{21}\phi_{2j}'''(0) \Rightarrow$$
$$\alpha_{1j}^3\, A_{1j}^{(1)}\Big[-\cos(\alpha_{1j}l_1) - \cosh(\alpha_{1j}l_1)\Big] + \alpha_{1j}^3\, A_{1j}^{(2)}\Big[\sin(\alpha_{1j}l_1) - \sinh(\alpha_{1j}l_1)\Big] = D_{21}(\alpha_{2j}^3\, A_{2j}^{(3)} - \alpha_{2j}^3\, A_{2j}^{(1)}) \tag{3.84}$$

For $x_2 = L_p$ and $x_3 = 0$:

- displacement

$$\begin{aligned}&w_2(L_p) = w_3(0) \Rightarrow \phi_{2j}(L_p) = \phi_{3j}(0) \Rightarrow \\ &A_{2j}^{(1)}\Big[\sin(\alpha_{2j}L_p) - \sinh(\alpha_{2j}L_p)\Big] + A_{2j}^{(2)}\Big[\cos(\alpha_{2j}L_p) - \cosh(\alpha_{2j}L_p)\Big] = A_{3j}^{(2)} + A_{3j}^{(4)}\end{aligned} \tag{3.85}$$

- slope

$$w_2'(L_p) = w_3'(0) \Rightarrow \phi_{2j}'(L_p) = \phi_{3j}'(0) \Rightarrow$$
$$\alpha_{2j}\, A_{2j}^{(1)}\Big[\cos(\alpha_{2j}L_p) - \cosh(\alpha_{2j}L_p)\Big] + \alpha_{2j}\, A_{2j}^{(2)}\Big[-\sin(\alpha_{2j}L_p) - \sinh(\alpha_{2j}L_p)\Big] = \alpha_{3j}\, A_{3j}^{(1)} + \alpha_{3j}\, A_{3j}^{(3)} \tag{3.86}$$

- bending moment

$$\bar{D}(L_p)w_2''(L_p) = \bar{D}(L_s)w_3''(0) \Rightarrow \phi_{2j}''(L_p) = \phi_{3j}''(0)/D_{21} \Rightarrow$$
$$\alpha_{2j}^2\, A_{2j}^{(1)}\Big[-\sin(\alpha_{2j}L_p) - \sinh(\alpha_{2j}L_p)\Big] + \alpha_{2j}^2\, A_{2j}^{(2)}\Big[-\cos(\alpha_{2j}L_p) - \cosh(\alpha_{2j}L_p)\Big] = \frac{\alpha_{3j}^2\, A_{3j}^{(4)} - \alpha_{3j}^2\, A_{3j}^{(2)}}{D_{21}} \tag{3.87}$$

- shear stress

$$\bar{D}(L_p)w_2'''(L_p) = \bar{D}(L_s)w_3'''(0) \Rightarrow \phi_{2j}'''(L_p) = \phi_{3j}'''(0)/D_{21} \Rightarrow$$
$$\alpha_{2j}^3 A_{2j}^{(1)}\Big[-\cos(\alpha_{2j}L_p) - \cosh(\alpha_{2j}L_p)\Big] + \alpha_{2j}^3 A_{2j}^{(2)}\Big[\sin(\alpha_{2j}L_p) - \sinh(\alpha_{2j}L_p)\Big] = \frac{\alpha_{3j}^3 A_{3j}^{(3)} - \alpha_{3j}^3 A_{3j}^{(1)}}{D_{21}} \tag{3.88}$$

where

$$\alpha_{1j}^4 = \frac{\mu(0)\,\omega_j^2}{\bar{D}(0)} \tag{3.89}$$

$$\alpha_{2j}^4 = \frac{\mu(L_p)\bar{D}(0)}{\mu(0)\bar{D}(L_p)}\alpha_{1j}^4 = \frac{\mu_{21}}{D_{21}}\alpha_{1j}^4 \tag{3.90}$$

$$\alpha_{3j}^4 = \alpha_{1j}^4 \tag{3.91}$$

Finally, for $x_3 = L_s - l_2 = \chi_3$ the boundary conditions are:

$$\begin{aligned}&\bar{D}w_3'''(\chi_3) - m_{tip}\ddot{w}_3(\chi_3) = 0 \Rightarrow \phi_{3j}'''(\chi_3) = -\frac{m_{tip}}{\bar{D}}\omega_j^2\phi_{3j}(\chi_3) \Rightarrow \\ &{\phi_{3j}}'''(\chi_3) = -\mu_t\alpha_{1j}^4\phi_{3j}(\chi_3)\end{aligned} \tag{3.92}$$

$$\bar{D}w''(\chi_3) = 0 \Rightarrow \phi_{3j}''(\chi_3) = 0 \tag{3.93}$$

where $\mu_t = m_{tip}/\mu(0)$. Boundary and continuity conditions together form a system of equations from the associated eigenproblem in the unknown eigenvalues α_{ij} and coefficients $A_{ij}^{(k)}$ is solved, and the modal shape functions ϕ_{ij} and pulsation ω_j are then obtained for each beam portion thanks to the MATLAB numerical solvers. Thus, the shape of the j-th mode is reconstructed according to modal representation introduced above.

3.3.2 Modal projection

Taking now into account the damped equations, by substituting Eq. 3.69 into the first equation of (3.64), and projecting the first equation over the mode $\phi_m(x)$, one has:

$$\begin{aligned}&\sum_{j=1}^{N_w}\ddot{q}_j < \mu\phi_j, \phi_m > + \sum_{j=1}^{N_w}\dot{q}_j\,(c_a < \mu\phi_j, \phi_m > + c_s < (J\phi_j'')'', \phi_m >) + \\ &+ \sum_{j=1}^{N_w} q_j < (\bar{D}\phi_j'')'', \phi_m > - \theta\dot{\lambda} < \big[\delta'(x-l_1) - \delta'(x-l_2)\big], \phi_m > = < f(x,t), \phi_m > = F_m(t)\end{aligned} \tag{3.94}$$

where the inner product between generic functions g_1 and g_2 in the interval $[0, l_r]$ is introduced as $< g_1, g_2 > = \int_0^{l_r} g_1 g_2\, dx$. In Eq. 3.94 it is convenient to group terms sharing the same inner product.

$$\begin{aligned}&\sum_{j=1}^{N_w}(\ddot{q}_j+\frac{c_a}{\mu}\dot{q}_j)<\mu\phi_j,\phi_m>+\sum_{j=1}^{N_w}\dot{q}_j<(c_sJ\phi_j'')'',\phi_m>+\\&+\sum_{j=1}^{N_w}q_j<(\bar{D}\phi_j'')'',\phi_m>-\theta\dot{\lambda}<\left[\delta'(x-l_1)-\delta'(x-l_2)\right],\phi_m>=F_m(t)\end{aligned}\tag{3.95}$$

Moreover, considering the following properties of the Dirac distributions δ for a generic function $f(x)$

$$\int_0^L \delta'(x)\,f(x)\,dx=-\int_0^L \delta(x)\,f'(x)\,dx\tag{3.96}$$

$$\int_0^L \delta(x-x_0)\,f(x)\,dx=f(x_0)\tag{3.97}$$

the term including the Dirac function δ derivatives becomes:

$$<\delta'(x-l_1)-\delta'(x-l_2),\phi_m>=-\phi_{1m}'(l_1)+\phi_{2m}'(L_p)\tag{3.98}$$

Defining then $M_{jm}=<\mu\phi_j,\phi_m>$ and $\tilde{K}_{jm}=<(\bar{D}\phi_j'')'',\phi_m>$, Eq. 3.95 can be written as:

$$\begin{aligned}&\sum_{j=1}^{N_w}(\ddot{q}_j+\frac{c_a}{\mu}\dot{q}_j)M_{jm}+\sum_{j=1}^{N_w}\dot{q}_j<(c_sJ\phi_j'')'',\phi_m>+\\&+\sum_{j=1}^{N_w}q_jK_{jm}-\theta\dot{\lambda}\left[\phi_{2m}'(L_p)-\phi_{1m}'(l_1)\right]=F_m(t)\end{aligned}\tag{3.99}$$

Moreover, by using integration by parts, and recalling the boundary conditions in Eqs. 3.79, 3.80, 3.92, and 3.93, the damping and stiffness terms in Eq. 3.92 can be written as:

$$<(c_sJ\phi_j'')'',\phi_m>=(c_sJ\phi_{ij}'')'\phi_{im}\Big|_0^{L_s}-c_sJ\phi_{ij}''\phi_{im}'\Big|_0^{L_s}+\int_0^{L_s}c_sJ\phi_j''\phi_m''dx\Rightarrow\tag{3.100}$$

$$<(\bar{D}\phi_j'')'',\phi_m>=(\bar{D}\phi_{ij}'')'\phi_{im}\Big|_0^{L_s}-\bar{D}\phi_{ij}''\phi_{im}'\Big|_0^{L_s}+\int_0^{L_s}\bar{D}\phi_j''\phi_m''dx\Rightarrow\tag{3.101}$$

Substituting Eqs. 3.100 and 3.101 into Eq. 3.95

$$\begin{aligned}&\sum_{j=1}^{N_w}(\ddot{q}_j+\frac{c_a}{\mu}\dot{q}_j)<\mu\phi_j,\phi_m>+\sum_{j=1}^{N_w}\dot{q}_j(<c_sJ\phi_j'',\phi_m''>+\phi_{3m}(L_s)(c_sJ\phi_{3j}'')'|_{x=L_s}+\phi_{1m}'(0)c_sJ_0\phi_{1j}''(0))+\\&+\sum_{j=1}^{N_w}q_j(<\bar{D}\phi_j'',\phi_m''>+\phi_{3m}(L_s)(\bar{D}\phi_{3j}'')'|_{x=L_s}+\phi_{1m}'(0)\bar{D}_0\phi_{1j}''(0))-\theta\dot{\lambda}\left[\phi_{2m}'(L_p)-\phi_{1m}'(l_1)\right]=F_m(t)\end{aligned}\tag{3.102}$$

where, for the sake of conciseness, $\bar{D}_0 = \bar{D}(0)$ and $J_0 = J(0)$. Equation 3.102 can be rearranged as

$$\begin{aligned}
&\sum_{j=1}^{N_w}(\ddot{q}_j + \frac{c_a}{\mu}\dot{q}_j) < \mu\phi_j, \phi_m > + \sum_{j=1}^{N_w}\dot{q}_j < c_s J\phi_j'', \phi_m'' > + \sum_{j=1}^{N_w} q_j < \bar{D}\phi_j'', \phi_m'' > + \\
&+ \sum_{j=1}^{N_w}\dot{q}_j\phi_{3m}(L_s)(c_s J\phi_{3j}'')'|_{x=L_s} + \sum_{j=1}^{N_w} q_j\phi_{3m}(L_s)(\bar{D}\phi_{3j}'')'|_{x=L_s} + \\
&+ \sum_{j=1}^{N_w}\dot{q}_j\phi_{1m}'(0)c_s J_0\phi_{1j}''(0) + \sum_{j=1}^{N_w} q_j\phi_{1m}'(0)\bar{D}_0\phi_{1j}''(0) - \theta\dot{\lambda}\Big[\phi_{2m}'(L_p) - \phi_{1m}'(l_1)\Big] = F_m(t)
\end{aligned} \tag{3.103}$$

Substituting Eq. 3.69 into the expression of the boundary condition at $x = L_s$ (*i.e.*, $[c_s J\dot{w}'' + \bar{D}w'']'|_{x=L_s} = m_{tip}\ddot{w}|_{x=L_s}$) yields:

$$[\sum_{j=1}^{N_w}\dot{q}_j(c_s J\phi_{3j}'') + \sum_{j=1}^{N_w} q_j(\bar{D}\phi_{3j}'')]'|_{x=L_s} = m_{tip}\sum_{j=1}^{N_w}\ddot{q}_j\phi_{3j}(L_s). \tag{3.104}$$

Similarly, substituting Eq. 3.69 into the expression of the boundary condition at $x = 0$ (*i.e.*, $[\bar{D}w''(0) + c_s J\dot{w}''(0)]|_{x=0} = k_{rot}w'(0)|_{x=0}$) yields:

$$\sum_{j=1}^{N_w} q_j\bar{D}_0\phi_{1j}''(0) + \sum_{j=1}^{N_w}\dot{q}_j c_s J_0\phi_{1j}''(0) = k_{rot}\sum_{j=1}^{N_w} q_j\phi_{1j}'(0) \tag{3.105}$$

Taking into account relations 3.104 and 3.105, one can write Eq. 3.102 as:

$$\begin{aligned}
&\sum_{j=1}^{N_w}\Big(M_{jm} + m_{tip}\,\phi_{3j}(L_s)\phi_{3m}(L_s)\Big)\ddot{q}_j + \sum_{j=1}^{N_w}\left(\frac{c_a}{\mu}M_{jm} + \frac{c_s J}{\bar{D}}K_{jm}\right)\dot{q}_j + \\
&+ \sum_{j=1}^{N_w}\Big(K_{jm} + k_{rot}\phi_{1j}'(0)\phi_{1m}'(0)\Big)q_j - \theta\,(\phi_{2m}'(L_p) - \phi_{1m}'(l_1))\dot{\lambda} = F_m(t),
\end{aligned} \tag{3.106}$$

with $K_{jm} =< \bar{D}\phi_j'', \phi_m'' >$. Introducing the normalization condition *i.e.*, $M_{jm} + m_{tip}\phi_{3j}(L_s)\phi_{3m}(L_s) = \delta_{jm}$ (δ_{jm} is a Kronecker delta), the overall mass matrix is diagonal with unit elements and consequently we have also an overall diagonal stiffness matrix $K_{jm} + k_{rot}\phi_{1j}'(0)\phi_{1m}'(0) = \delta_{jm}\omega_m^2$. Thus the previous equation becomes:

$$\ddot{q}_m + 2\,\zeta_m\omega_m\dot{q}_m + \omega_m^2 q_m - \theta\,(\phi_{2m}'(L_p) - \phi_{1m}'(l_1))\dot{\lambda} = F_m(t), \tag{3.107}$$

where the damping ratio is $\zeta_m = 1/2\,\big[c_s J\omega_m/\bar{D} + c_a/(\mu\omega_m)\big]$.

Recalling the second equation of Eqs. 3.64,

$$C_p\ddot{\lambda} + \int_0^{L_s}\theta\big[H(x - l_1) - H(x - l_2)\big]\dot{w}''\,dx = -I_c$$

where θ is constant over the piezoelectric patch, and substituting Eq. 3.69, one has for the integral term:

$$\theta\sum_{j=1}^{N_w}\dot{q}_j\int_0^{L_s}\big[H(x - l_1) - H(x - l_2)\big]\phi_j''\,dx = \theta\sum_{j=1}^{N_w}\dot{q}_j\int_{l_1}^{l_2}\phi_j''\,dx, \tag{3.108}$$

where the effect of the Heaviside function is just to limit the integration domain between l_1 and l_2. Denoting then with χ_j the integral term the right hand side of Eq. 3.108, the second equation of the system takes the form:

$$C_p\ddot{\lambda} + \theta \sum_{j=1}^{N_w} \chi_j \dot{q}_j = -I_c \tag{3.109}$$

The final system of equations is:

$$\ddot{q}_m + 2\zeta_m \omega_m \dot{q}_m + \omega_m^2 q_m - \theta(\phi'_{2m}(L_p) - \phi'_{1m}(l_1))\dot{\lambda} = F_m(t) \tag{3.110}$$

$$C_p\ddot{\lambda} + \theta \sum_{j=1}^{N_w} \chi_j \dot{q}_j = -I_c \tag{3.111}$$

where $m = 1, 2, ..., N_w$.

The hypothesis of lumped tip mass can be inaccurate if its extension l_{tip} covers a significant part of the beam, *i.e.*, $l_{tip}/L_s << 1$ is not verified, as also intuitively shown in Fig. 3.6. The tip mass, positioned on the support layer, affects the vibration modes differently with respect to a concentrated proof mass because is featured by a moment of inertia as well. For this reason, an extended tip mass model is adopted, following several authors [M. Kim et al. 2010] [Tang et al. 2017] [Magrab 2012]. This model describes closely what happens in real-life applications where a more stable adhesion of proof mass to the cantilever is guaranteed via a sufficiently large contact surface. To fit into the 1D representation, a mass per unit of length μ_{tip} is defined over its length l_{tip}.

Figure 3.6: Lateral view of the PEH with extended tip mass (dimensions do not scale real values of the device considered later).

For the sake of simplicity, supposing the support layer as part of the tip mass above for $l_r \leq x \leq L_s$ and since the overall mass per unit of length keeps constant in the same interval, it follows for the total tip mass m_{tip} and moment of inertia J_{tip}:

$$m_{tip} = \mu_{tip} l_{tip} + \mu(l_r) l_{tip} \tag{3.112}$$

$$J_{tip} = \frac{\mu_{tip} l_{tip}}{3}\left(h_{tip}^2 + \frac{l_{tip}^2}{4} - \frac{h_s}{8h_{tip}} l_{tip}^2\right) + \frac{\mu(l_r) l_{tip}^3}{12} \tag{3.113}$$

where the point T with coordinates $x = l_r$, $z = h_s/2$ is assumed as pole to calculate the moment of inertia and terms of order higher than $O(h_s)$ are neglected since $h_s << h_{tip}$. Following this hypothesis, $x = l_r$ becomes the effective beam length for which the beam modes are calculated.

The new boundary conditions at the free end $x = l_r$ become

$$\bar{D}w''(l_r) + c_s J\dot{w}''(l_r) + \frac{m_{tip} l_{tip}}{2}\left(\ddot{w}(l_r) + \frac{l_{tip}}{2}\ddot{w}'(l_r)\right) + J_{tip}\ddot{w}'(l_r) = 0 \tag{3.114}$$

$$[\bar{D}w''(l_r) + c_s J\dot{w}''(l_r)]' - m_{tip}\left(\ddot{w}(l_r) + \frac{l_{tip}}{2}\ddot{w}'(l_r)\right) = 0. \tag{3.115}$$

and the the normalization condition is now

$$M_{jm}+m_{tip}\phi_{3j}(l_r)\phi_{3m}(l_r)+\frac{m_{tip}l_{tip}}{2}[\phi'_{3j}(l_r)\phi_{3m}(l_r)+\phi_{3j}(l_r)\phi'_{3m}(l_r)]+\left(J_{tip}+m_{tip}\frac{l_{tip}^2}{4}\right)\phi'_{3j}(l_r)\phi'_{3m}(l_r) = \delta_{jm}. \tag{3.116}$$

The modal forcing term $F_m(t)$ is defined as the component of the excitation over the m-th mode, and, introducing $\beta_m = \int_0^{l_r} \mu\phi_m\, dx$ and $\gamma_m = \int_0^{l_r} \phi_m\, dx$, Eq. **??** can be written as:

$$F_m(t) = -\ddot{w}_b\left[\beta_m + m_{tip}\phi_{3m}(l_r) + m_{tip}\frac{l_{tip}}{2}\phi'_{3m}(l_r)\right] - c_a\gamma_m\dot{w}_b \tag{3.117}$$

For more details on extended tip mass theory, see Appendix A.

3.3.3 Comparison of beam analytical modes with existing results

In order to validate the theory developed in the previous section, the calculation of exact modes first is compare with numerical results found by Laura *et al.* [Laura et al. 1975], who have studied a beam with uniform mass and stiffness distribution for different mass ($m_{tip}/(\mu \cdot L_s)$) and stiffness ($\bar{D}/k_{rot} \cdot L_s$) non-dimensional ratios, without any piezoelectric effect involved. The beam is considered to be uniform and made of the only support layer (piezoelectric effect is not involved in resonance frequency calculation). Moreover, the tip mass is considered to be concentrated in $x = L_s$ and its rotational inertia neglected. In Figs. 3.7a, 3.7b, and 3.7c the solutions obtained by Laura (squares), expressed as the non-dimensional spatial frequency $\alpha_{j1}L_s$, for the first three modes are plotted as function of different tip mass ratios for different spring/stiffness ratios and compared with those relative to the analytical modes obtained with the present model implemented in MATLAB (dots), showing a complete agreement. By maintaining the segmented mode model, both correct definition of boundary conditions (Eqs. 3.79, 3.105, 3.93, 3.104) and effectiveness of interface conditions (Eqs. 3.81 to 3.88) are thus verified.

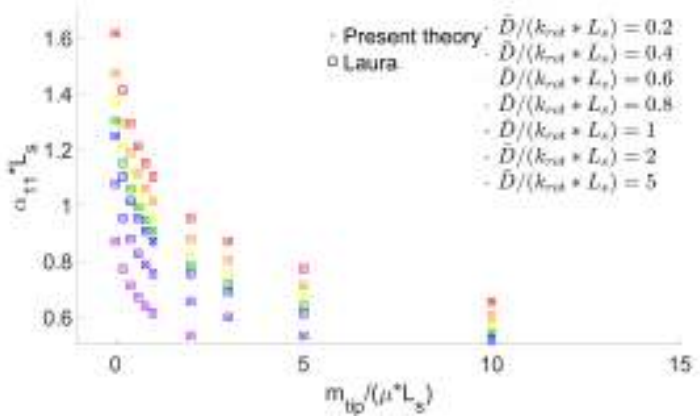

(a) *First mode.*

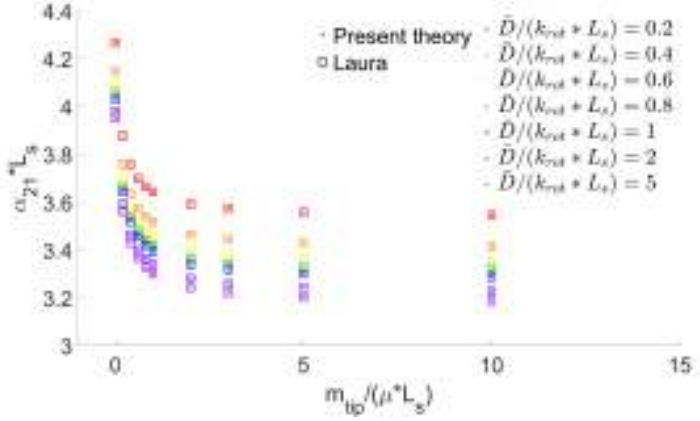

(b) *Second mode.*

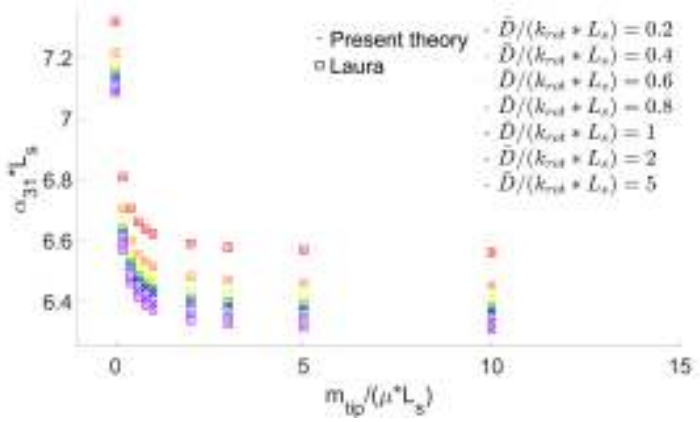

(c) *Third mode.*

Figure 3.7: Comparison between Laura *et al.* [Laura et al. 1975] and present theory results for a uniform cantilevered beam with torsional spring at the clamping and concentrated mass at the free end.

From the analysis of the previous plots, it emerges that adding even a small tip mass on the free end of the beam has a great impact on the structure resonance frequencies. However, if this mass is increased

above a certain value its effect on reducing the beam frequency reaches a horizontal asymptote for $m_{tip}/(\mu \cdot L_s) > 3$. This implies that frequency estimation is more sensitive to model or parameters errors for lower tip mass ratios.

The dependence of the frequency on the stiffness/spring ratio needs to be clarified as well. An 'infinite' value of K determines that the ratio tends to zero, which is equivalent to constrain the beam slope and then impose clamping BC. A finite value of this ratio has a significant effect on frequencies, and as the spring coefficient gets lower, the BC resembles more and more to simply supported BC, where only vertical displacement are constrained.

Finally, the extended tip mass model (not lumped as in previous cases) has been validated by comparing results obtained with the present theory with those reported by Kim *et al.* [M. Kim et al. 2010]. The main parameters of the investigated device are reported in Tab. 3.1 and in Tab. 3.2 resonance frequencies for the first bending mode and different tip masses, found with the present theory, are compared with those by Kim *et al.* , showing good agreement.

Table 3.1: Kim *et al.* [M. Kim et al. 2010] energy harvester parameters.

Parameter	Unit	Value
Support layer		
Length L_s	m	0.053
Thickness h_s	m	0.000126
Width b	m	0.0317
Young's modulus Y_s	Pa	$100 \cdot 10^9$
Density ρ_s	kg/m^3	7630
Piezoelectric layer		
Length L_p	m	0.053
Thickness h_p	m	0.000275
Young's modulus Y_p	Pa	$61 \cdot 10^9$
Density ρ_p	kg/m^3	7750
Tip mass 1		
Length l_{tip}	m	0.0104
Thickness h_{tip}	m	0.00661
Mass m_{tip}	kg	0.0167
Tip mass 2		
Length l_{tip}	m	0.0216
Thickness h_{tip}	m	0.00666
Mass m_{tip}	kg	0.0347

Table 3.2: Frequency comparison between Kim *et al.* [M. Kim et al. 2010] and present theory.

Tip mass	Kim *et al.* [Hz]	Present theory [Hz]	Concentrated mass [Hz]
0	109.45	109.45	109.45
$m_{tip}1$	41.44	41.64	36.86
$m_{tip}2$	34.85	34.87	26.34

3.4 Numerical solution validation via COMSOL Multiphysics plate solution

COMSOL Multiphysics™ is the commercial solver chosen to generate a 3D model of the device to which compare the developed analytical model, and consequently evaluate if the ROM introduces errors in describing the bending plate behaviour. It is a software able to solve PDEs systems through a finite element method (FEM) for space variables, providing stationary, time-dependent, frequency-domain, and eigenfrequency studies. To run the simulation, the system is defined through geometry (thanks to an integrated CAD tool), material properties, and different physics involved.

To model a piezoelectric energy harvester two physics are needed: Solid Mechanics and Electrostatics. The first one describes the mechanical behaviour and boundary conditions of the system. A fixed constraint with zero displacements and rotation is imposed at one edge of the support layer to simulate the clamping. To evaluate the eigenfrequencies, the following system of equation is solved

$$\begin{cases} -\rho_j \omega^2 \boldsymbol{u} = \nabla \cdot \boldsymbol{\sigma} \\ -i\omega = \lambda \end{cases}, \tag{3.118}$$

where the subscript j refers to the different layer. The stress matrix $\boldsymbol{\sigma}$ is defined according to the constitutive equations of piezoelectric and isotropic linear elastic materials, respectively reported below

$$\boldsymbol{\sigma} = \boldsymbol{s\varepsilon} - \bar{e}_{31}\boldsymbol{E} \tag{3.119}$$

$$\boldsymbol{\sigma} = \boldsymbol{s\varepsilon} \tag{3.120}$$

In the Electrostatics section, the charge conservation relation is imposed

$$\nabla \cdot \boldsymbol{D} = \rho_v \tag{3.121}$$

where ρ_v is the charge density of the material and the electrical displacement D is defined according to the electrical permittivity through the materials, taking into account the internal polarization for the piezoelectric. Finally, the Multiphysics section couples the Solid Mechanics and Electrostatics equations with a segregated approach to simulate the piezoelectric behaviour of the device. The eigenvalues problem is then solved by using the ARPACK FORTRAN routines, suitable for large-scale problems and based on the implicitly restarted Arnoldi method (IRAM).

Thus, to prove the 2D reduced order model assumption is not effecting the final results, a 3D model of the energy harvesting device was created in COMSOL using parameters in Tab. 3.3, the same of the device investigated experimentally in following sections.

Table 3.3: Energy harvester parameters.

Parameter	Unit	Value
Support layer		
Length L_s	m	0.0633
Thickness h_s	m	0.000274
Width b	m	0.04
Young's modulus Y_s	Pa	$190 \cdot 10^9$
Density ρ_s	kg/m^3	7850
Poisson's ratio ν_s	-	0.3
Piezoelectric layer		
Length L_p	m	0.04
Thickness h_p	m	0.000184
Width b	m	0.04
Distance from clamping l_1	m	0.0023
Young's modulus Y_p	Pa	$90 \cdot 10^9$
Density ρ_p	kg/m^3	7800
Poisson's ratio ν_p	-	0.34
Relative electric permittivity ϵ_{33}	F/m	2400
Piezoelectric coefficient d_{31}	C/N	$-2.1 \cdot 10^{-10}$
Stiff matrix component s_{11}	1/Pa	$15 \cdot 10^{-12}$
Stiff matrix component $s_{12} = s_{33}$	1/Pa	$19 \cdot 10^{-12}$
Stiff matrix component s_{12}	1/Pa	$-4.5 \cdot 10^{-12}$
Stiff matrix component $s_{13} = s_{23}$	1/Pa	$-5.7 \cdot 10^{-12}$
Stiff matrix component $s_{44} = s_{55}$	1/Pa	$39 \cdot 10^{-12}$
Stiff matrix component s_{66}	1/Pa	$49.4 \cdot 10^{-12}$

In the Geometry and Materials sections two main blocks have been defined and modelled as piezoelectric and harmonic steel lamina glued together with the Form Union command, and then setting the relative physics to the layers.

The mesh is defined with the Physics-controlled option, as shown in Fig. 3.8, choosing automatically the best shape for physic interface settings imposed and normal size of the elements. As seen in Fig. 3.8, the support lamina has three holes close to the free edge, previously inserted to allow for different clamping layouts. The ROM takes into account the missing mass due to the holes by reducing the mass per unit of length μ in the final portion of the beam (this reduction has not been reported in Eq. 3.36 for the sake of simplicity).

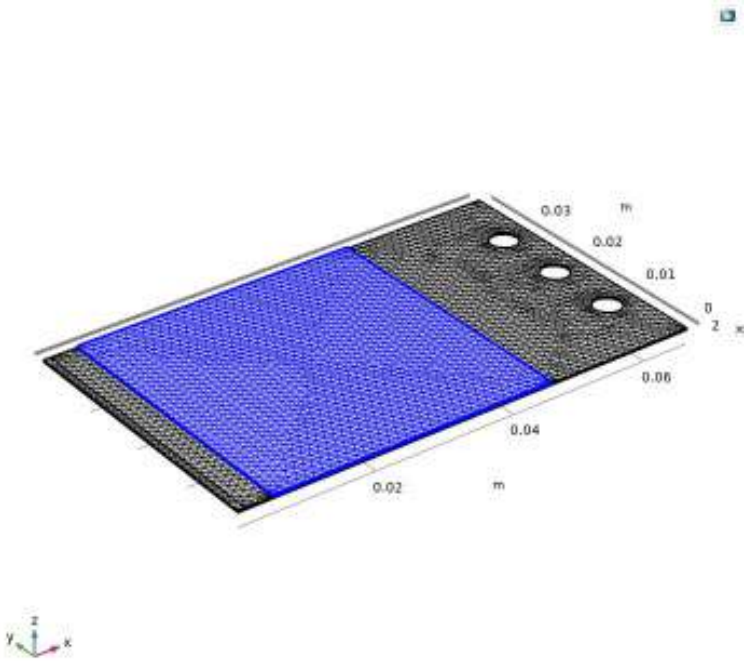

Figure 3.8: Finite element discretization of the support and piezoelectric layers.

The torsional spring BC has been simulated and compared with the ROM results with no tip on the free end. The reproduction of yielding clamp condition requires some care to guarantee its equivalence with the torsional spring model adopted in the ROM. A small area (see Fig. 3.9) is reserved at the constrained edge of the PEH to impose numerically the BCs. Along line A the vertical displacement is set to zero, while at the side connected with the device, *i.e.*, line B in Fig. 3.9, a linear spring system, exerting its restoring force in the transverse (z-axis) direction, is defined.

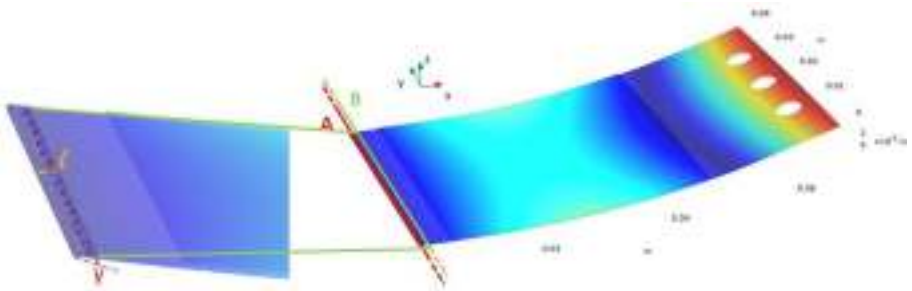

Figure 3.9: Schematic representation of the spring system for the yielding clamp as modelled in COMSOL.

To identify the value of the linear spring coefficient to be set in COMSOL™, a criterion based on the equivalence of the moment exerted by the constraint in both 1D and 3D models is adopted. This moment can be expressed as:

$$M = k_{rot}^{(3D)} \cdot b \cdot l \cdot l \, \sin\gamma = k_{rot}^{(1D)} \cdot \arccos\gamma \tag{3.122}$$

with $k_{rot}^{(3D)}$ and $k_{rot}^{(1D)}$ spring constants for, respectively, the distributed linear spring system (3D model) and the lumped torsional spring (1D model), γ the allowed rotation at the clamping, and l the distance between the spring attachment (line B) and the points where displacement is set to zero (line A). Thus, for small rotation angles the spring coefficients are related to each other by this relation:

$$k_{rot}^{(1D)} = k_{rot}^{(3D)} \cdot b \cdot l^2 \tag{3.123}$$

allowing for the equivalence between the 1D and 3D models. In Fig. 3.10 the natural frequencies associated to the considered bending modes are compared, showing that 3D and 1D results do not differ for more than 6 %, and thus demonstrating that the Euler-Bernoulli beam model well represents the considered problem. The difference tends to lower as the BC approximates the perfect clamping condition, with an error which becomes negligible for the first mode. Moreover, a decrease in spring coefficient value, *i.e.*, a yielding clamp, affects in a relevant way the resonance frequency, as also demonstrated in Sec. 3.3.3.

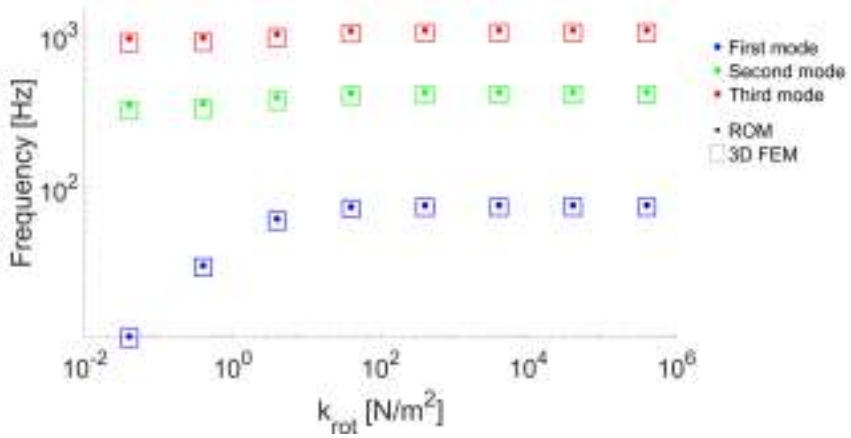

Figure 3.10: Comparison of the frequency prediction for different values of the torsional spring k_{rot} at the yielding clamping in logarithmic scale.

A tip mass can be modelled in COMSOL as a body placed at the free end, as shown in Fig. 3.11, assuming this time ideal clamping conditions at the opposite side.

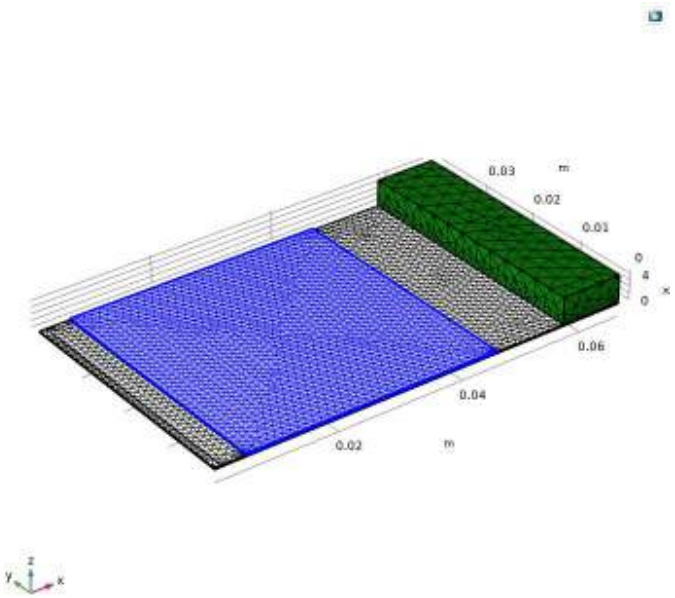

Figure 3.11: COMSOL model of the PEH with extended tip mass on the free edge.

Table 3.4: Tip mass parameters.

Tip mass	Dimensions LxWxh [mmxmmxmm]	Weight [g]
$m_{tip}1$	8.1 x 40 x 5.15	2.6
$m_{tip}2$	9.6 x 40 x 4.1	3.72

As shown in Fig. 3.12, both extended and concentrated tip mass theories show good agreement with the 3D model results in terms of resonance frequency for the first mode, the most relevant for energy harvesting, but slightly different results for second and third modes. Although both are close to the 3D FEM results, the extended mass theory difference with the 3D model is always less than 5 %, while the concentrated tip mass model reaches even 7.7 %. Moreover, Laura conclusions on tip mass are confirmed, with a relevant but limited decrement of the system resonance frequencies for the two different tip masses studied.

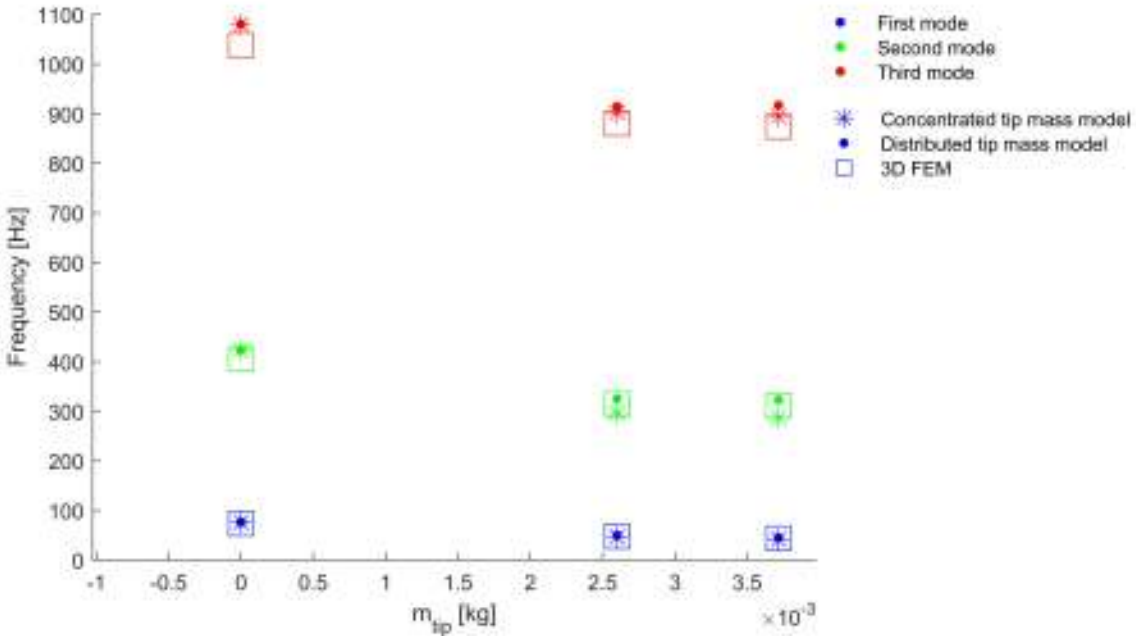

Figure 3.12: Comparison between resonance frequencies of 3D FEM model (squares) and present theory with concentrated (stars) or extended (dots) tip mass conditions.

Finally, Fig. 3.13 shows, through a comparison with the 3D model in COMSOL, how the exact mode calculations significantly improves the structural representation provided by the modal decomposition. In one case, the exact modes of the stepped beam are employed as in the developed theory, while in the other case the mode shapes of the uniform structure are used for projecting the PDE and obtaining a system of ODEs. Using the exact modes, the relative difference with the 3D FE model reduces from 17.5 % to 5 %. Moreover, expanding the displacement field with respect to the exact (undamped) vibration modes (or system eigenfunctions) provides diagonal mass and stiffness matrices of the ODE, which allows full-decoupling of the ODE equations.

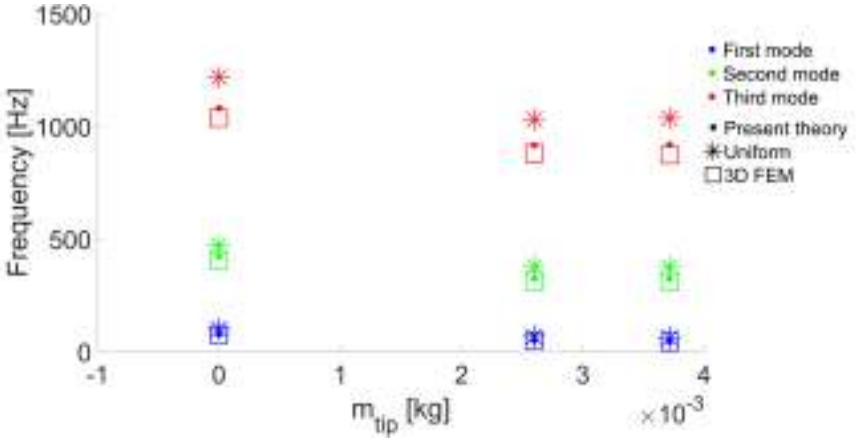

Figure 3.13: Comparison between resonance frequencies of 3D FE model (squares) and present theory for different tip mass conditions, using both approximated (stars) or exact (dots) modes for the modal solution.

3.5 Analytical transfer function vs time marching solution of ROM

To evaluate the energy harvester voltage output under harmonic excitation conditions, Erturk's analytical solution [Erturk and Daniel J. Inman 2008a] of forced response under sinusoidal input of Eq. 3.110 has been implemented in MATLAB, taking into account the first three modes of the system. The PEH considered is a uniform cantilevered beam with support and piezoelectric layers having the same length and width, but different thickness, as shown in Fig. 3.14.

Figure 3.14: Erturk unimorph PEH.

Main characteristics of the piezoelectric energy harvester are listed in Tab. 3.5

Erturk obtained analytically the ratio of the voltage amplitude with respect to the basement acceleration amplitude F in the frequency domain as:

$$\frac{\dot{\lambda}(\omega)}{-\omega^2 f(x,t)} = \frac{\sum_{r=1}^{3} \frac{-j\mu\omega\varphi_r\gamma_r}{\omega_r^2 - \omega^2 + j2\zeta_r\omega_r\omega}}{\sum_{r=1}^{3} \frac{j\omega\psi_r\varphi_r}{\omega_r^2 - \omega^2 + j2\zeta_r\omega_r\omega} + \frac{1 + j\omega\tau_c}{\tau_c}} \tag{3.124}$$

where ω_r is the circular eigenfrequency of the system, ω is the circular frequency of the seismic excitation, $\varphi_r = \theta/C_p \cdot d\phi_r/dx|_{L_s}$ is the modal projection of the ratio between the coupling term in the electrical equation and the equivalent piezoelectric capacitance, $\gamma_r = \int_0^{L_s} \phi_r dx$ is the modal projection of the base excitation, $\psi_r = \theta d\phi_r/dx|_{L_s}$ is the modal projection of the coupling term in mechanical equations, and

Table 3.5: Erturk energy harvester parameters.

Parameter	Unit	Value
Support layer		
Length L_s	m	0.1
Thickness h_s	m	0.0005
Width b	m	0.02
Young's modulus Y_s	Pa	$100 \cdot 10^9$
Density ρ_s	kg/m^3	7165
Piezoelectric layer		
Length L_p	m	0.1
Thickness h_p	m	0.0004
Width b	m	0.02
Young's modulus Y_p	Pa	$66 \cdot 10^9$
Density ρ_p	kg/m^3	7800
Permittivity ϵ_{33}	nF/m	15.93
Piezoelectric coefficient d_{31}	pm/V	-190

$\tau_c = R \cdot C_p$ (with R electric load) is the time constant of the circuit.

In Fig. 3.15 Erturk analytical solution (continuous lines) for different resistive loads are compared with the voltage output of Eq. 3.110 (dashed lines) solved in MATLAB with a Runge-Kutta algorithm.

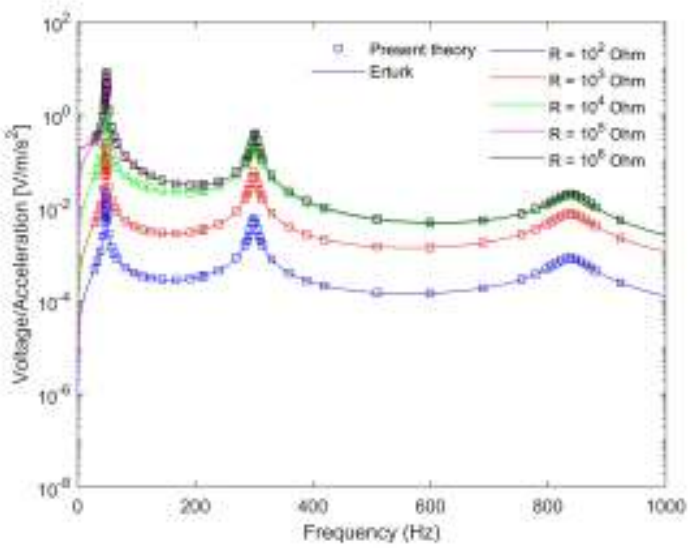

Figure 3.15: Comparison between analytical (continuous lines) and numerical (dashed lines) voltage FRFs calculated in MATLAB for different resistive loads.

Results obtained with the two different methods are in accordance to each other. Voltage increases with the resistive load, varying from short circuit ($R = 100\,\Omega$) until open circuit ($R = 10^6\,\Omega$). First and second modes are more relevant then the third one, for a unique electrode configuration. Moreover, resistive load variation causes a slight change in resonance frequency of the system (approximately 1-2 Hz from short circuit to open circuit conditions).

3.6 Concluding remarks

In this chapter a multi-layer composite cantilevered Euler – Bernoulli beam model of a piezoelectric energy harvester has been developed, with non-uniform mass and stiffness distribution through its length. The electromechanical coupling has been introduced in the mechanical description by using the linear piezoelectric constitutive equations. A tip mass is positioned on the free edge to tune harvester's natural frequencies with lower excitation frequencies and to enhance oscillations. Although a concentrated mass model is considered initially, a more accurate description is introduced, taking into account the not negligible extension and rotational inertia effect. Finally, to simulate a non-perfect clamping, yielding in rotation, a torsional spring is added at $x = 0$. By analytically developing Lagrange equations from Hamilton's principle, a partial differential equation system is found and then projected on the exact non-uniform beam modes (determined in MATLAB). Thus, the developed ROM allows mechanically decoupling oscillators and then easily neglecting those modes not contributing to energy production. The set of ordinary differential equations is integrated in MATLAB.

Numerical results are compared first with those by Kim et al. [M. Kim et al. 2010] and Laura et al. [Laura et al. 1975], validating the effectiveness of boundary conditions, and then with a 3D high-fidelity model of the harvester for the non-uniform configuration developed in Comsol Multiphysics, to show that geometrical and mechanical hypothesis do not undermine the overall consistency of the ROM. Finding the yielding influencing in a relevant way the resonance frequencies of the device, tests on the clamping reliability must be carried out along with piezoelectric energy harvester characterization, as further explained in Sec. 5.3.2. Moreover, the influence of tip mass position and weight on the device power output will be further investigated in Chap. 6, as design variables for one of the optimization problems.

Finally, numerical results in terms of voltage output for different resistive loads have been compared with the analytical solution proposed by Erturk et al. [Erturk and Daniel J. Inman 2008a] for a uniform configuration without tip mass, finding perfect agreement. If ones considers the φ_r and ψ_r terms calculated not for the total length L_s, but in $[l_1, l_2]$ instead, the analytical solution (Eq. 3.124) also solves the configuration with piezoelectric patch shorter than the support layer.

Chapter 4

Energy conversion system and storage

4.1 Introduction

As seen in previous chapters, the voltage output from a piezoelectric device is not constant, but varies in time and spectrum depending on the external excitation. Thus, to make energy produced by the harvester usable and available at any time for powering electronic device a critical component is a proper electric conversion system. At first stage, this goal can be simply obtained with a Full Bridge Rectifier (FBR) and/or storage capacitance to increase global performances.

Research studies focused on electric conversion systems for Piezoelectric Energy Harvesters (PEHs) oversimplify the usually electromechanical behaviour by modelling the device as a current source in parallel with a capacitance and considering the output signal only for sinusoidal excitation conditions. Others, like Goldfarb et al. [Goldfarb et al. 1999], model the PEH as a transformer, with mass, stiffness, damping and external force represented, respectively, by inductance, capacitance, resistance, and voltage source. Within this approach, the transformer turns ratio represents the piezoelectric coupling θ. Although better than modelling the PEH as a real current source, the previous 1-dof model suffers from inaccurate results and lack of information on strain distribution and modes shape identification, as seen in Chap. 3.

In the following section the full bridge rectifier will be described and studied, considering proper sizing, coupled behaviour and critical issues in interfacing with a PEH. The integration with the electromechanical model of Chap. 3 will be shown, along with the conversion circuit model. A deeper understanding of the system will be also useful to properly develop the electrode segmentation, to improving the system performances and in provide solutions to limits for both electric and mechanical issues, such as FBR and loads voltage threshold and charge cancellation.

4.2 Full bridge rectifier and capacity storage

4.2.1 Electric circuit model

A piezoelectric energy harvester alone undergoing to seismic excitation would produce a sinusoidal AC current. To power electronic devices anyway a DC current is needed, and for this reason a Full Bridge Rec-

tifier (FBR) is employed. This component is chosen for its stability and simplicity, despite issues connected to voltage activation threshold. Other kind of rectifiers can be found in literature for energy harvesting applications, like for instance MEMS. In this case, as usually MEMS PEHs cannot reach easily the activation voltage threshold required by FBRs and have low conversion efficiency with FBRs, synchronized switch harvesting on inductor (SSHI) [Lallart et al. 2008] [Liang et al. 2011] [Du; Amaratunga, et al. 2018][Fu et al. 2018] or synchronous electric charge extraction (SECE) [Romani et al. 2013] have been used. Although generally allowing an higher power transmission than a FBR, they have limits in real-life applications. SSHI shows a good performance only for a limited excitation level range, making applications at variable excitation source difficult. Both SSHI and SECE need power to work, thus, at the very beginning or after a long time without any input, they prevent the AC/DC conversion to happen (cold-startup issue). For this reason higher excitation levels are needed to first activate the system. Moreover, SSHI and SECE are suitable only for low piezoelectric coupling conditions, since, at resonance, the Synchronized Switch Damping phenomenon occurs, for which the charge extracted (SECE) or the pulse current applied (SSHI) induce an actuation effect on the piezoelectric, damping its oscillations and thus cancelling the resonance effect. [Badel et al. 2006] [Ji et al. 2016].

Before considering PEH and FBR connected, the rectifier behaviour is explained. A single-phase full bridge rectifier is a passive AC/DC converter made by four diodes and a polarized capacitor (Fig. 4.1).

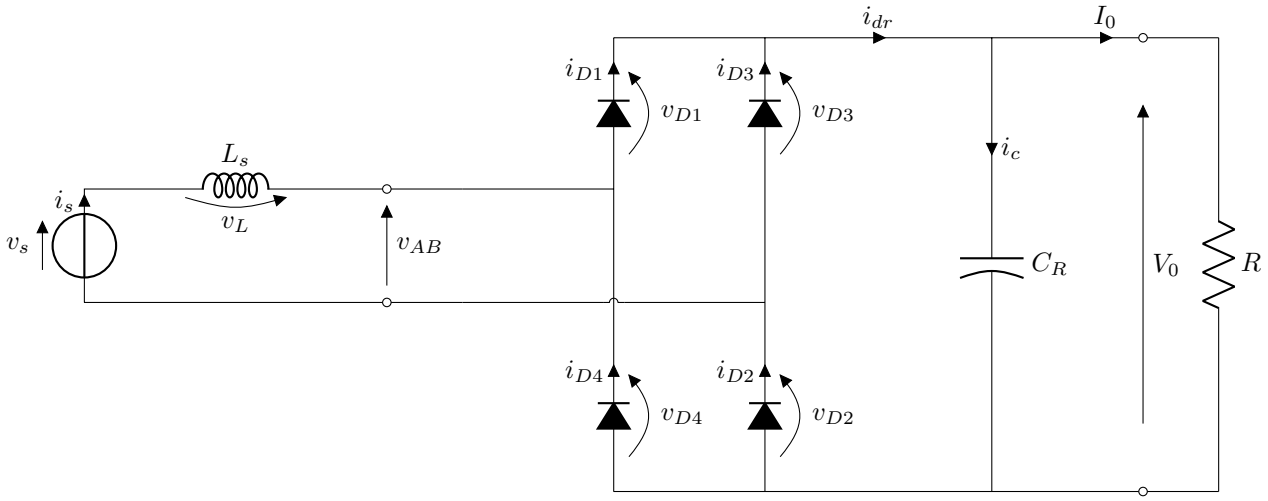

Figure 4.1: Generic full bridge rectifier connected to a voltage generator in input and a resistive load in output.

To explain its behaviour, the FBR is considered connected to a utility supply in input (voltage generator v_s in series with an inductance L_s) and a resistive load R in output [Mohan 2011a]. Steady state conditions (inductance voltage and capacitor current mean values equal to zero) are assumed, decomposing the signal into a mean value and ripple [1], and evaluating separately their effect. The following circuit equations can

[1]The ripple is a periodic variation of a signal on its DC value, by applying the superposition principle. Usually it is recommanded to reduce it to allow for electronics correct functioning.

be then written by applying Kirchhoff's laws to the circuit in Fig. 4.1.

$$v_s = L_s \frac{di_s}{dt} + v_{AB} \tag{4.1a}$$

$$v_0 = v_{D1} + v_{D2} + v_{AB} \tag{4.1b}$$

$$v_0 = v_{D3} - v_{AB} + v_{D4} \tag{4.1c}$$

$$v_0 = v_{D1} + v_{D4} \tag{4.1d}$$

$$v_0 = v_{D2} + v_{D3} \tag{4.1e}$$

$$i_{dr} = i_{D1} + i_{D3} \tag{4.1f}$$

$$i_{dr} = i_c + I_0 \tag{4.1g}$$

where, in general, v is a voltage, i is a current, subscripts are referred to source output (AB), FBR output (0), $i-th$ diode (D_i), and capacitor C_R (c), as shown in Fig. 4.1, and the uppercase denotes system coefficients (later also used to indicate variables).

In steady state conditions Eq. 4.1g becomes

$$\bar{i}_{dr} = \bar{i}_c + I_0 = I_0 \tag{4.2}$$

since the mean value of the capacitor current is zero on the period. Thus I_0 represents the i_{dr} DC component and i_c its ripple, *i.e.*, the voltage ripple in output from diodes will impact only on the capacitor.

To understand the FBR behaviour, voltage and current trend have to be studied on one period (steady state conditions), as shown in Fig. 4.2.

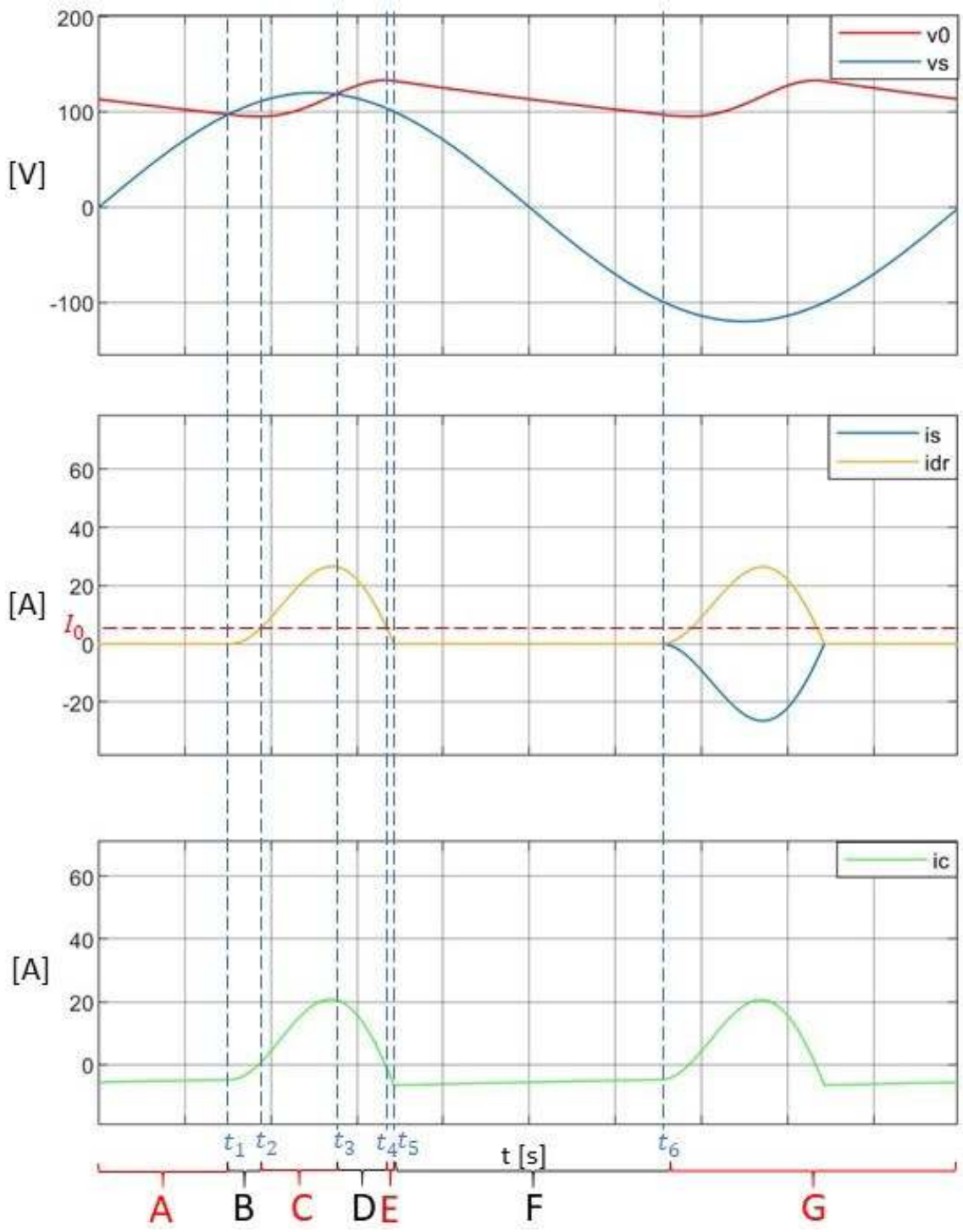

Figure 4.2: Voltage and current waveforms for a full bridge rectifier.

By choosing appropriate time intervals, the behaviour of the system can be split into different phases and described as follows, where the letters refer to Fig. 4.2:

A) Considering $v_s = v_{AB} = 0$ and $v_0 > v_{AB}$ at $t = 0$, it can be proved by contradiction that all the four diodes are reverse biased[2]. For example, from Eq. 4.1b, $v_{D1} + v_{D2} > 0$ necessarily. Assuming them v_{D1} to be zero, Eqs. 4.1 would become

$$v_{D1} = 0 \tag{4.3a}$$

$$v_{D4} = v_0 \tag{4.3b}$$

$$v_0 = v_{D3} + v_0 - v_{AB} \Rightarrow v_{D3} = v_{AB} = 0 \tag{4.3c}$$

$$v_{D2} + v_{D3} = v_0 \Rightarrow v_{D2} = v_0 \tag{4.3d}$$

meaning that diodes D1 and D3 are in conduction mode (voltage equal to zero). However, this configuration would not allow any closed circuit, so the initial condition on D1 voltage has to be impossible. Analogously, D2 cannot conduct either and, following similar logic paths for Eqs. 4.1c, 4.1d, and 4.1e, it is found that there is no diodes combination at $t = 0$ that can be in conduction mode (Fig. 4.3). Consequently, the rectifier current i_{dr} is zero and the capacitor current has to be equal to $-I_0$ (Eq. 4.1g). Being C_R a finite value and considering $i_c = C_R\, dv_0/dt < 0$, v_0 has to decrease linearly.

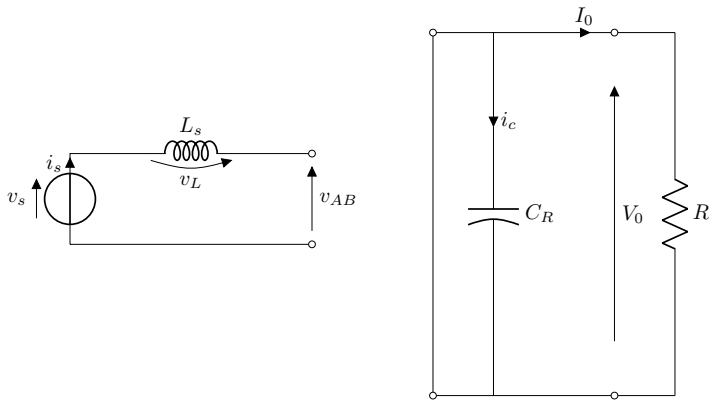

Figure 4.3: Equivalent circuit for the FBR system in phase A) (it applies also to phase F)).

B) At $t = t_1$, the external sinusoidal generator and FBR output voltages reach the same value $v_s = v_{AB} = v_0$, so, for Eq. 4.1b, both v_{D1} and v_{D2} have to be zero, meaning diodes D1 and D2 conduct (Fig. 4.4). Then, the FBR current $i_s = i_{dr} = i_{D1}$ increases, since input voltage keeps growing and the voltage on the inductance becomes $L_s\, di_s/dt = v_s - v_0 > 0$. Being though constant the output current I_0, i_c on the capacitor has to decrease (Eq. 4.1g).

[2]A diode can work in *forward biased* condition, conducting currents and acting like a short circuit, or in *reverse biased* condition, not conducting and acting like an open circuit.

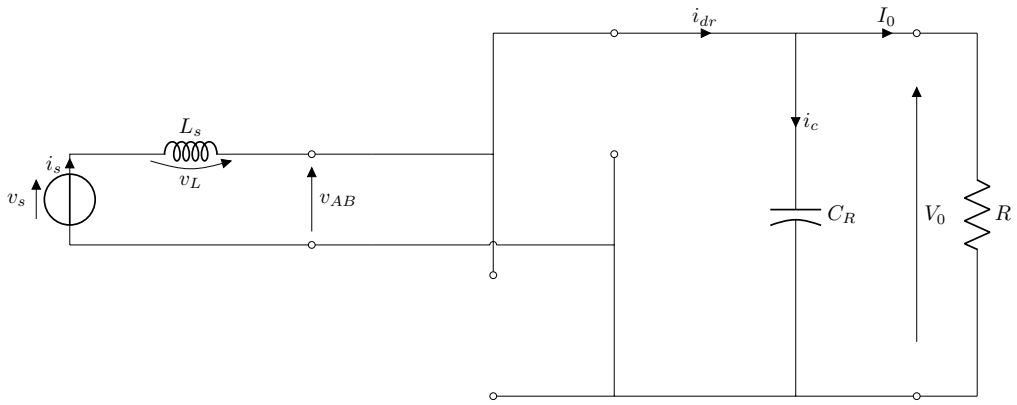

Figure 4.4: Equivalent circuit for the FBR system in phase B), C), D), and E).

C) When i_{dr} reaches a mean value equal to I_0 ($t = t_2$), and consequently i_c goes to zero, v_0 reaches a minimum. However, since v_L is still positive, i_s keeps growing, overcoming I_0 mean value, charging the capacitor but decreasing v_L. The equivalent circuit is still the one shown in Fig. 4.4

D) When v_L goes to zero ($t = t_3$), $v_0 = v_s$ and both i_s and i_c reach a maximum. Being the capacitor current still positive, its voltage overcomes again the generator one ($v_0 > v_s$ as for $t = 0$), but diodes do not go reverse biased because $i_{dr} > 0$.

E) When i_{dr} reaches I_0 and consequently the capacitor current goes to zero ($t = t_4$), a maximum for v_0 occurs.

F) Then, being now $v_L < 0$, the FBR current keeps decreasing until zero ($t = t_5$), and so do both i_{D1} and i_{D2}, while still $v_0 > v_s$. Consequently, diodes D1 and D2 go reverse biased and again all four diodes do not conduct (Fig. 4.3).

G) At $t = t_6$, again $|v_s| = v_0$ and diodes D3 and D4 are activated (due to the reverse sign of the input voltage). In the remaining time interval the rectifier acts analogously to D1-D2 conduction mode.

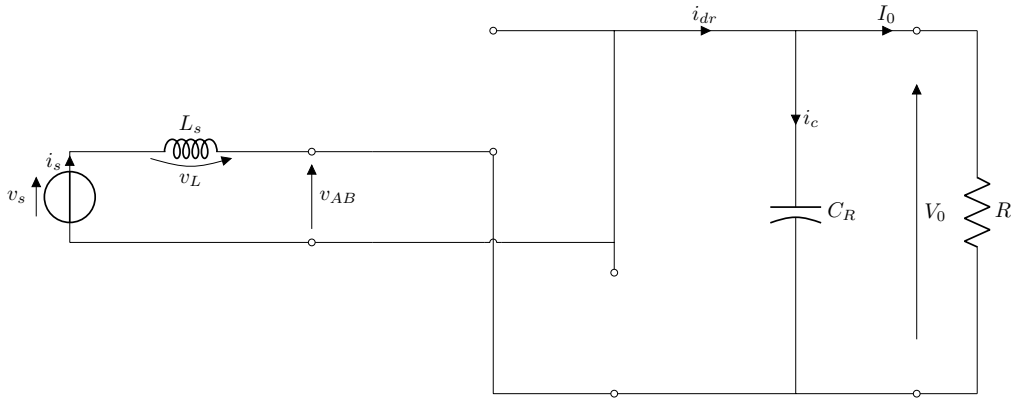

Figure 4.5: Equivalent circuit for the FBR system in phase G).

Having clarified how the rectifier behaves, in the following the FBR is connected to the PEH in order to rectify and filter its output signal. From an electrical point of view, a piezoelectric energy harvesters can be modelled as a current source in parallel with a capacitance C_p and a resistance R_p (usually not taken into account because negligible). The resulting circuit powering a resistive load is reported in Fig. 4.6

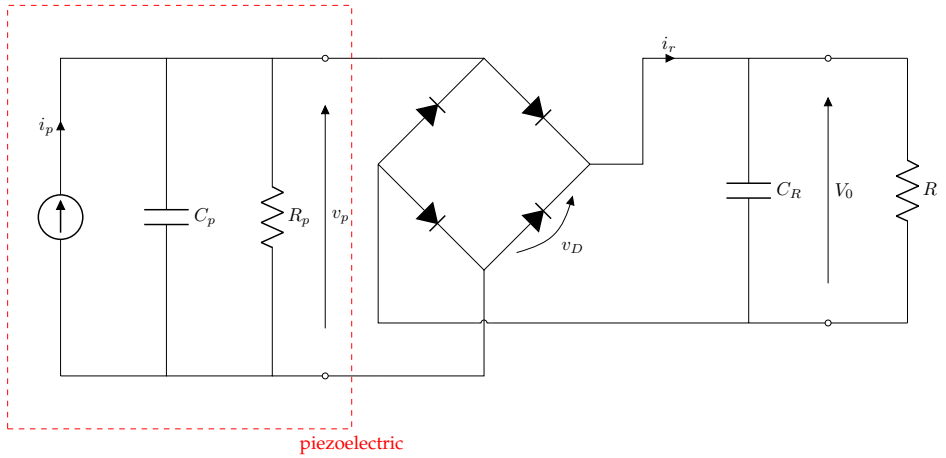

Figure 4.6: Piezoelectric energy harvester connected to FBR and external resistive load.

To power R, the harvester has to reach a threshold voltage value imposed by the storage capacitance C_R of the FBR. Indeed, as explained previously in Fig. 4.2, the FBR is activated only when the input and output voltage reach the same value. Then, the threshold can be defined as

$$V_{th} = V_0 + 2 \cdot V_D \tag{4.4}$$

where V_0 is the voltage imposed by the FBR capacitor and V_D is the voltage drop on each diode (previously neglected for sake of simplicity, being a constant value over the time). Until V_{th} is reached, the energy produced is lost in charging the piezoelectric internal capacitance C_p. Being C_p negligible during FBR conduction, the output current i_0 can be expressed as follows:

$$i_0 = \begin{cases} 0, & |\dot{\lambda}| < V_{th} \\ \dfrac{R \cdot \frac{1}{j\omega C_R}}{R + \frac{1}{j\omega C_R}}(|\dot{\lambda}| - 2V_D), & |\dot{\lambda}| > V_{th} \end{cases}, \tag{4.5}$$

where j is the imaginary unit and ω is the current pulsation.

Finally, considering that the voltage ripple ΔV_0 usually should be kept under 5 % of V_0 DC value

$$\Delta V_0 \leq 0.05 V_0 \,, \tag{4.6}$$

the capacitance of the FBR could be sized considering

$$i_0 = C_R \frac{\partial V_0}{\partial t} = C_R \frac{\Delta V_0}{T} \Rightarrow C_R = \frac{V_0 T}{R \Delta V_0} \tag{4.7}$$

4.2.2 Numerical solution via Simulink/Simscape

In order to obtain a complete model of the Piezoelectric Energy Harvester (PEH) from both mechanical and electrical points of view, in the next sections all the circuits being part of the conversion system will be modelled using Simscape blocks in Simulink (version R2020b), making them compatible with the numerical electromechanical model developed in section 3.5.

Full bridge rectifier response

The FBR circuit has been modelled in Simulink, as shown in Fig. 4.7, to confirm its behaviour under a sinusoidal ideal current source in parallel with a capacitance and a resistance. Reference values for all quantities have been used (i_p of 10^{-5} A at 60 Hz, $C_p = 10\,nF$, $C_R = 500\,\mu F$, $R = 100\,\Omega$. $R_p = 10\,M\Omega$), being consistent with the expected current output and equivalent capacitance of the piezoelectric from mechanical modelling.

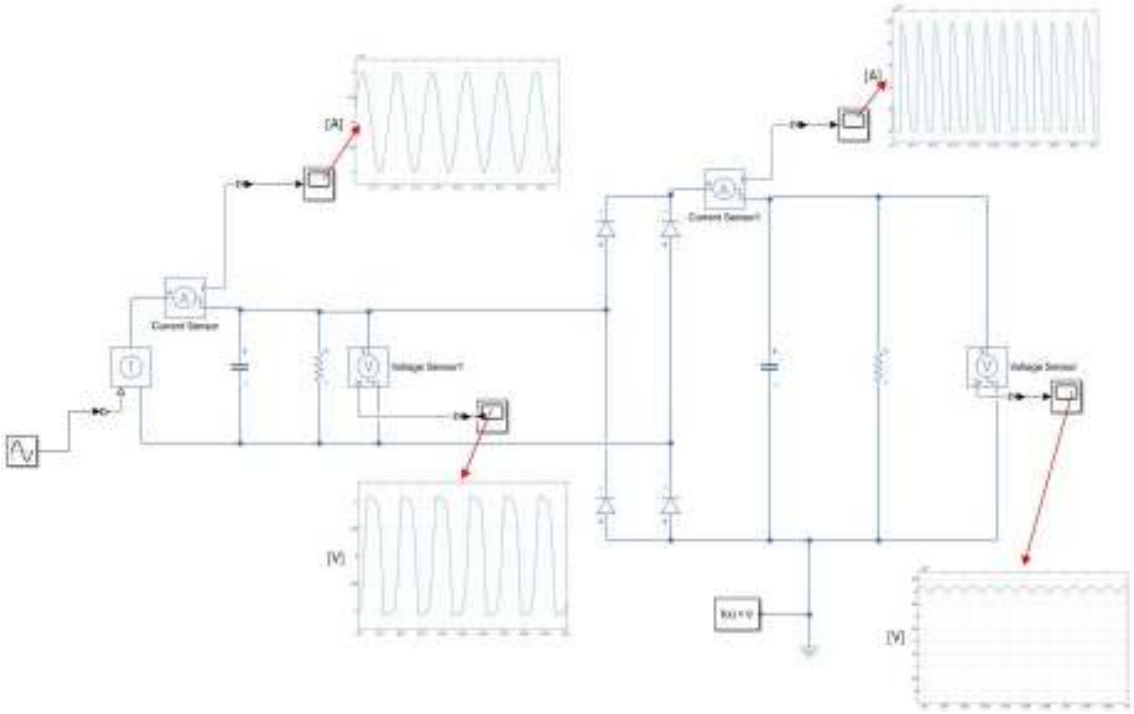

Figure 4.7: Simulink/Simscape model of PEH and FBR.

The output, shown in Fig. 4.8, is obtained in agreement with the behaviour expected for this circuit configuration.

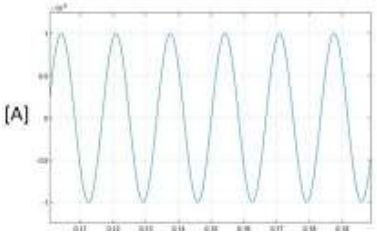

(a) i_p *is imposed by the electromechanical equations.*

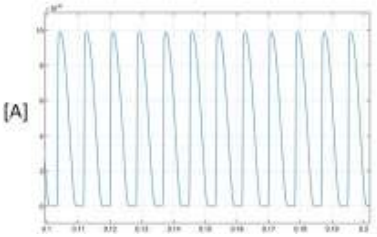

(b) i_0 *is non-zero only when the input voltage overcomes the threshold.*

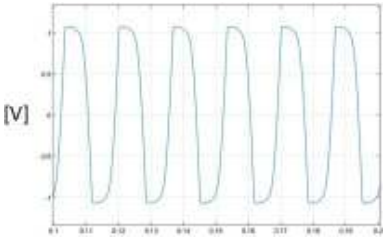

(c) $v_p = \dot{\lambda}$ *grows while charging* C_p *and keeps constant once reached* V_{th}.

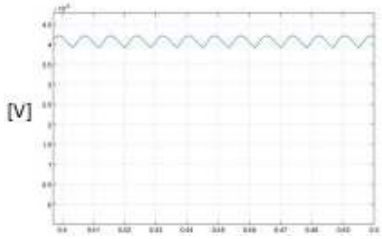

(d) V_0 *showing a ripple that has to be low compared to the mean value.*

Figure 4.8: Simulink output of the FBR simulation.

Analysis of full bridge rectifier and energy harvester coupled behaviour for different resistive loads

To achieve a full simulation of both PEH and FBR and provide a proper and accurate model of the conversion system, as anticipated in the previous paragraph, Simscape was used to model the electric components. In this way, also the mechanical equation of the PEH, previously developed in MATLAB, must be recast into Simulink blocks. The ordinary differential equation solver used is *ode15s*, a variable step method for stiff problems. Indeed, even though the piezoelectric problem itself is not stiff, diodes and switches introduces non-linearities in the system, making necessary the choice of an appropriate solver to ensure both simulation efficiency and speed. The maximum step size chosen for the simulations is $10^{-4}\,s$. The adopted PEH configuration for the following simulations is the simplest among all considered in Chap. 3, with no tip mass and perfect clamping, in order to focus only on the relationship between the device and the conversion system. For the excitation, an acceleration amplitude of 0.06 g was proposed as reference, being representative of different vibration sources such as home devices, vehicles, wind and traffic on bridges [Khan 2016]. Since the main purpose of this chapter is understanding the conversion circuit behaviour, for sake of simplicity, the excitation frequency is set equal to the first mode resonance one of the device (76.1 Hz).

The capacitance was sized considering the current voltage characteristic (Fig. 4.14) of a temperature sensor with operating range of -25/85 °C (LM61BIM3, National Semiconductor). Thus, considering the current almost constant equal to $82\,\mu A$, taking as reference voltage 3 V, and considering a voltage ripple desired of 5 %, the capacitance value for the full bridge rectifier is $7.2\,\mu F$.

The simulation was carried out for different resistive loads, ranging from short circuit (assumed as $100\,\Omega$) to open circuit ($10^{10}\,\Omega$), to study the behaviour of the FBR in both conditions of correct and incorrect sizing of C_R. Results shown in Figs. 4.9 and 4.10 refer to two resistive loads, $R = 1.5{\cdot}10^3\,\Omega$ and $R = 6{\cdot}10^3\,\Omega$,

respectively. For the first case, during the transient and when the FBR is in conduction, a small rise in PEH voltage can be seen, as a consequence of the electromechanical coupling. Indeed, remembering Eq. 3.111

$$C_p\ddot{\lambda} = -\theta \sum_{j=1}^{N_w} \chi_j \dot{q}_j - I_c,$$

the piezoelectric voltage output $\dot{\lambda}$ is due to both the electromechanical coupling term and the current of the electric circuit connected.

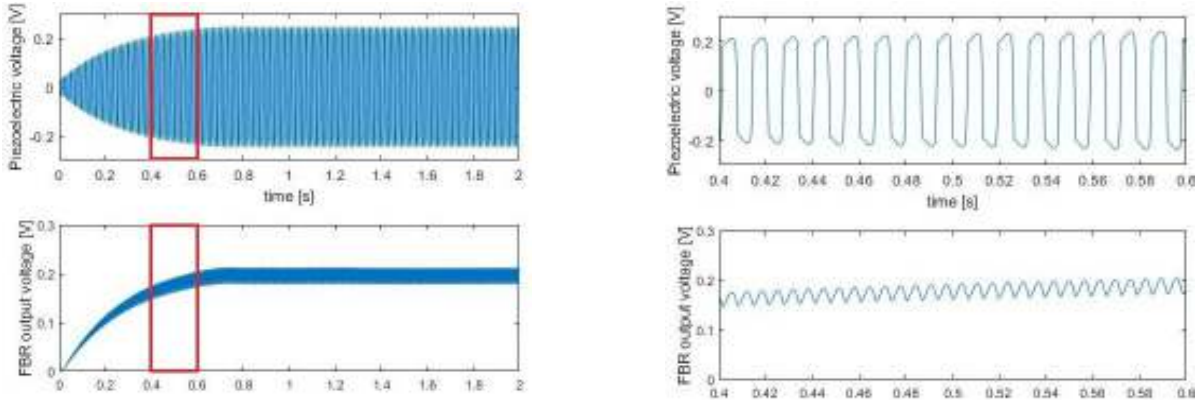

(a) *Time histories.* (b) *Zoom of the signals.*

Figure 4.9: Piezoelectric (top) and FBR (bottom) output voltage for $R = 1.5 \cdot 10^3\,\Omega$.

The $R = 6 \cdot 10^3\,\Omega$ shows a more efficient behaviour of the capacitance, with a smaller voltage ripple when the complete charge is reached.

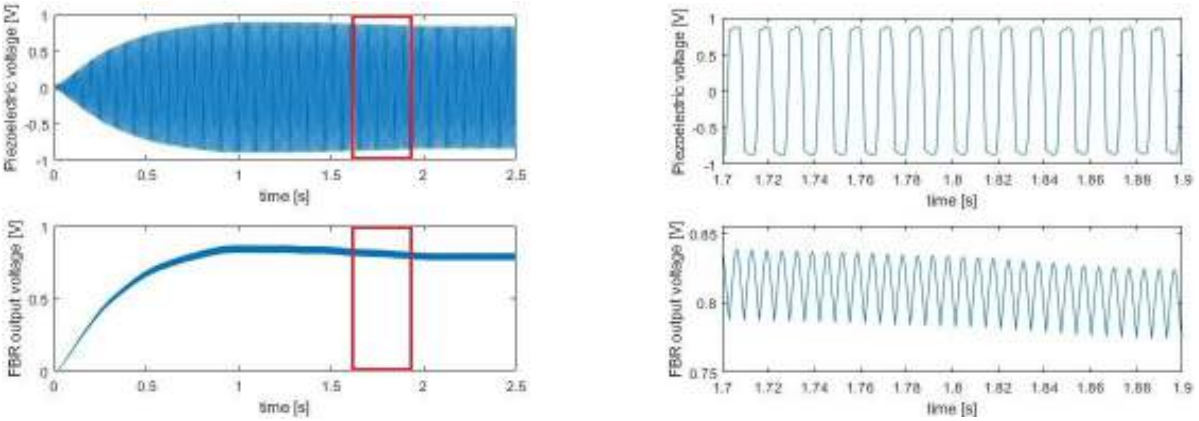

(a) *Time histories.* (b) *Zoom of the signals.*

Figure 4.10: Piezoelectric (top) and FBR (bottom) output voltage for $R = 6 \cdot 10^3\,\Omega$.

This phenomenon of reciprocal excitation keeps increasing with the resistive load, as can be seen in Fig. 4.11 for $R = 2.5 \cdot 10^4\,\Omega$, leading to a relevant periodic voltage amplitude oscillation in both piezoelectric harvester and FBR. However, when a maximum voltage is reached, due to internal damping of the PEH,

the piezoelectric voltage drops and returns, with a transient, to the open circuit conditions. In this period of time, the capacitance of the full bridge rectifier has to provide power to the load and thus its voltage decreases, resulting in an high amplitude oscillation, as shown in Fig. 4.11. When the capacitance voltage reaches again the PEH voltage in open circuit condition, the charge starts again. The capacitance voltage oscillation during PEH disconnection is due to C_R being sized for signal frequency, but not for energy storage. Thus, a long off - condition in the FBR results in a deep discharge as it attempts to provide the power required by the load. In any case, the maximum voltage level reached (1 V) would not be enough to power the temperature sensor taken as reference at this excitation level.

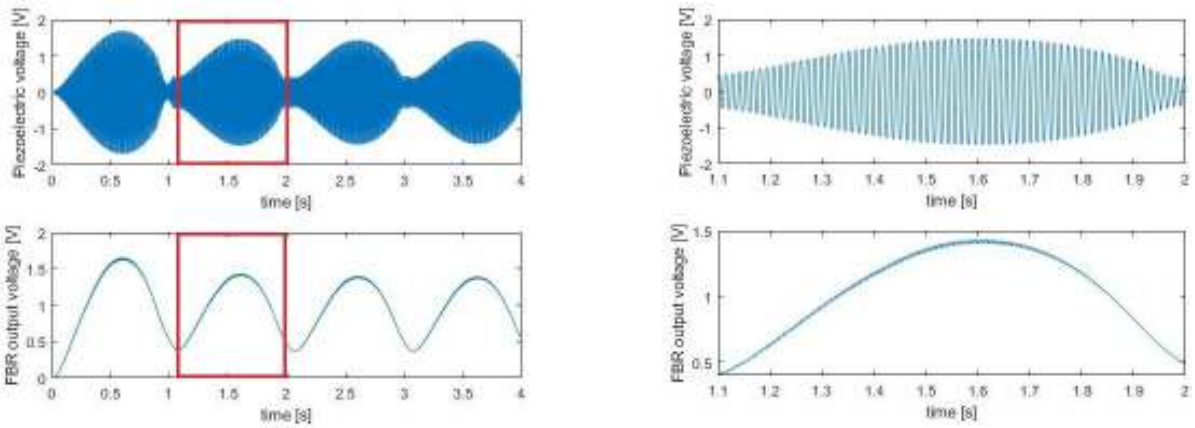

(a) *Time histories.* (b) *Zoom of the signals.*

Figure 4.11: Piezoelectric (top) and FBR (bottom) output voltage for $R = 2.5 \cdot 10^4\,\Omega$.

In the open circuit condition, simulated with $R = 10^{10}\,\Omega$ (Fig. 4.12), the amplification phenomenon is still present, but once the transitory phase ends and the capacitance is charged, it does not power any electric load and thus its voltage has no drop (apart from self discharge, not taken into account for sake of simplicity). Thus, the piezoelectric keeps working at its open circuit conditions.

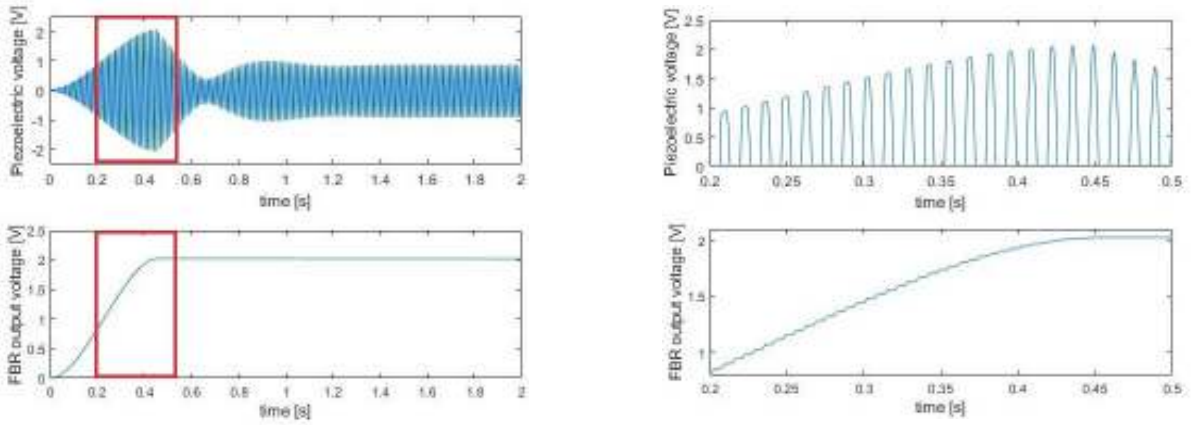

(a) *Time histories.* (b) *Zoom of the signals.*

Figure 4.12: Piezoelectric (top) and FBR (bottom) output voltage for the open circuit condition ($R = 10^{10}\,\Omega$).

In Fig. 4.13 the root mean square (rms) values of power and voltage of the whole system (PEH and FBR), considered after transient and thus for signals with constant spectral characteristics, are plotted in function of different resistive loads. The voltage also shows error bars representing the standard deviation, expressed as

$$\sigma^2 = \sqrt{\frac{\sum_{i=1}^{A} |\dot{\lambda}(t_i) - \bar{\dot{\lambda}}(t)|^2}{A-1}} \tag{4.8}$$

where A is the number of element of the voltage output and $\bar{\dot{\lambda}}(t)$ is the mean value of the voltage. The standard deviation expresses the ripple of the signal, giving a measure of the FBR capacitance filtering action for different resistive loads. A resonant piezoelectric energy harvester connected to a Full Bridge Rectifier and an electric resistive load constitute an RC circuit, in which the equivalent capacitance is the parallel of C_p and C_R. The power output of the device (PEH and FBR), considered after transient, is formally expressed as

$$P = \frac{V_0^2}{R}\,, \tag{4.9}$$

and depends not only on the amplitude of the external excitation but also on the load R value, reaching a maximum condition known as impedance matching *i.e.*, maximum power transfer theorem for AC circuits[3]. In the studied configuration, the maximum power occurs for an electric load of $6 \cdot 10^3\,\Omega$. There is a second peak at $R = 2.5 \cdot 10^4\,\Omega$, that, as seen previously, corresponds to the amplification phenomenon. However, this condition produces an high ripple of voltage, that can be seen both on the voltage curve and its standard deviation in Fig. 4.13b. This behaviour could potentially damage an electronic device and thus should be avoided. As expected, the voltage keeps growing with the resistive load, reaching the maximum for the open circuit condition. Comparing the two graphs it can be highlighted that the best condition occurs in the flat-slope region of the voltage curve, for which the FBR behaviour is constant, a safe working condition for electronic devices. In the power output curve, this area corresponds to the descending branch, starting from the maximum point until 0.02 mW. After the flat-slope region, the open circuit conditions are almost reached and, indeed, the power output goes to zero.

[3] An AC circuit exhibits maximum power transfer when the load impedance is equal to the complex conjugate of the power source impedance

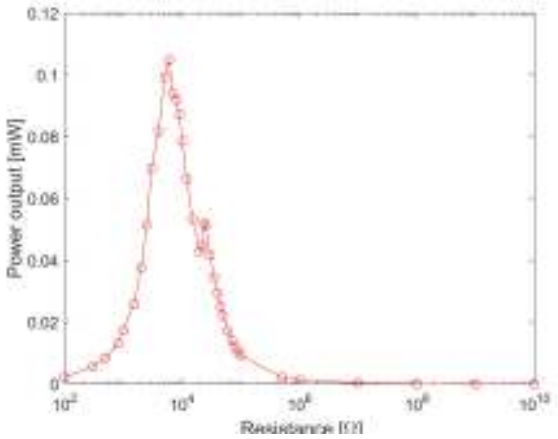

(a) *Power output for different resistive loads.*

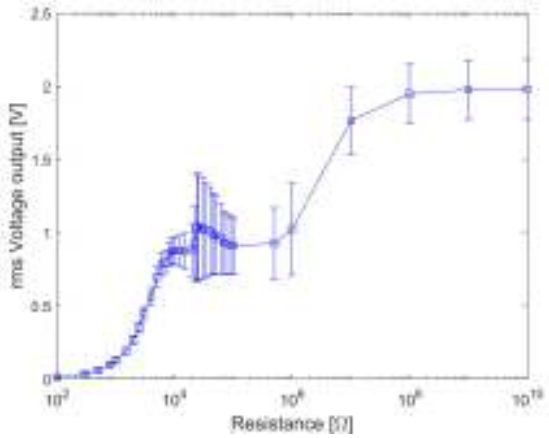

(b) *FBR rms voltage output and standard deviation for different resistive loads.*

Figure 4.13: Power (left) and voltage (right) output from the conversion system for different resistive loads, from short circuit till open circuit conditions.

Analysis of full bridge rectifier and energy harvester coupled behaviour for a variable resistive load

The Full Bridge Rectifier and the resistance modelled in the previous section does not take into account limits of the capacitance C_R and of a real load. For this reason, an electronic device, such as a typical temperature sensor (LM61BIM3, National Semiconductor) is taken into account. Indeed, its voltage working range and impedance vary, as shown in its I-V curve (Fig. 4.14).

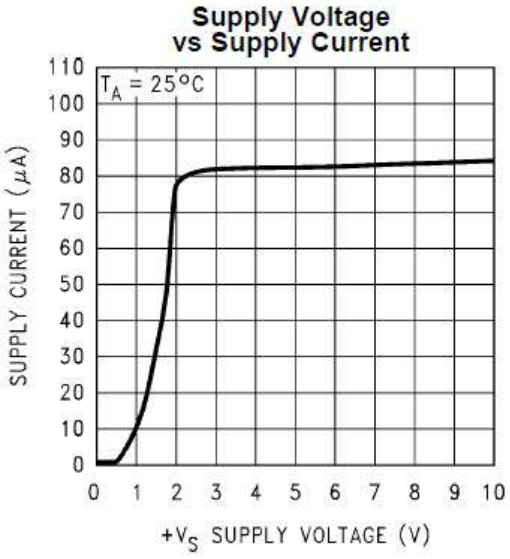

Figure 4.14: I-V curve of the temperature sensor LM61BIM3 produced by National Semiconductor.

Thus, if the supply voltage is lower than a certain threshold, the device will not work at all, while if an overvoltage is applied, it will be damaged. The capacitance has a limit voltage (surge voltage) too, over

which it breaks or even explodes. For this reason a new Simulink model was developed, with two switches and a variable load. The first switch disconnects the capacitor in case of overvoltage. Taking into account the capacitance value used in the previous section ($7.2\,\mu F$), a real tantalums capacitor produced by AVX is taken as reference: the TAJB685*006NJ, with $6.8\,\mu F$ capacitance, 6.3 V rated voltage, and 8 V surge voltage. The second switch disconnects the load when the voltage is whether too low (not working for $V_0 < 3V$) or too high (damage for $V_0 > 10V$).

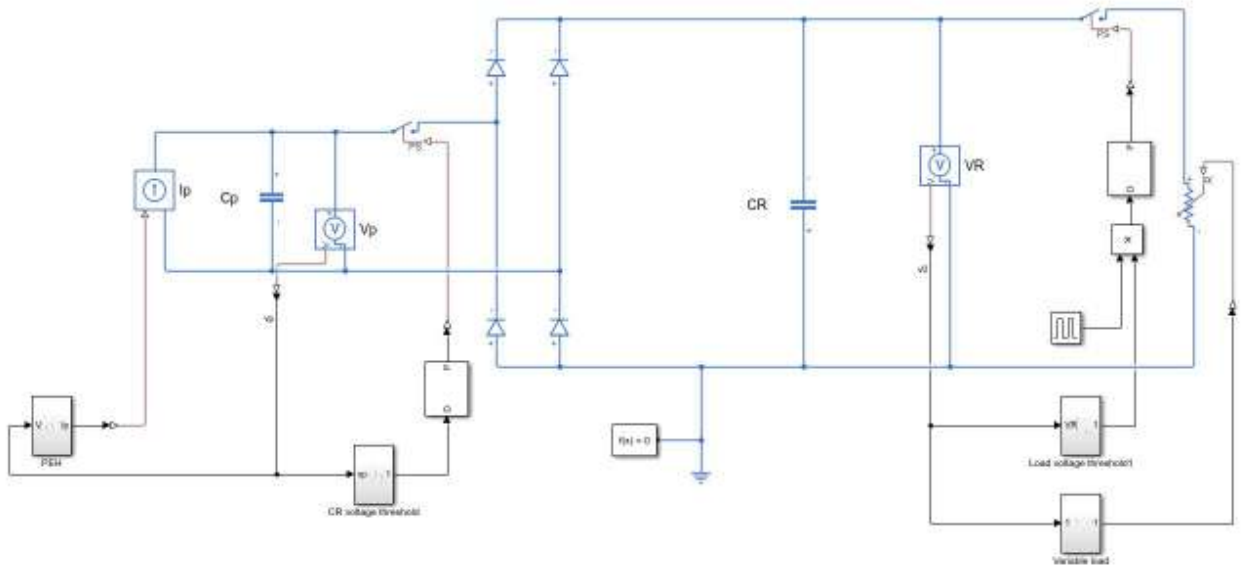

Figure 4.15: Simulink model of PEH and FBR with conditions on capacitance and variable load voltage.

The minimum voltage required by the temperature sensor is then higher than the open circuit voltage output (2 V) of the PEH and FBR configuration taken into account. Thus, the acceleration level taken previously as reference is not sufficient to power the load. For this reason te simulation was run for different acceleration amplitudes, in order to find the minimum and maximum values allowed for the circuit. Results are shown in Fig. 4.16. It must be pointed out that the variable resistance was defined as a piecewise function, which explains why the curve slope seems to have some discontinuity points. As expected, at the acceleration amplitude used in the previous simulations (0.06 g) the PEH does not power the load, although this condition is close to the minimum acceleration requirement (0.18 g). The load damage occurs for acceleration amplitude higher than 0.6 g and, since close to this condition small changes in acceleration can lead out of the safe working area, a lower value should be used.

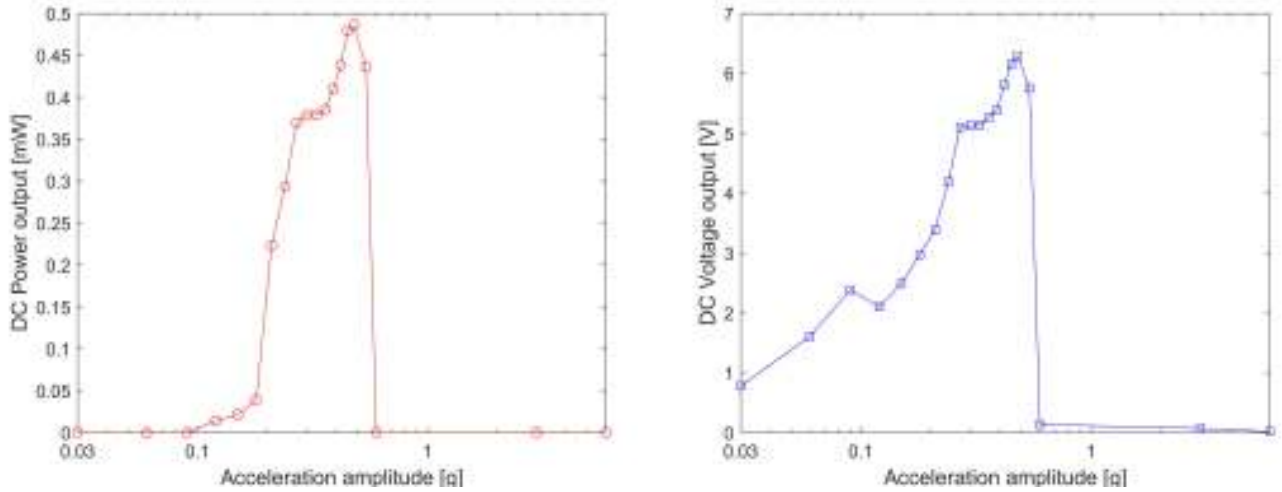

(a) *Power.* (b) *Voltage.*

Figure 4.16: Power and voltage output from the conversion system for different acceleration amplitudes.

The developed model gives a full representation of the behaviour of a device completely equipped to manage real operating conditions. This model allows also for a preliminary design of an experimental campaign, minimizing the risk of failures and malfunctioning of components.

4.3 Segmented electrode technique for voltage amplification

4.3.1 Conceptual development

In this section the electrode segmentation in width and length will be investigated to underline its effectiveness in voltage amplification and avoiding charge cancellation for higher order modes, respectively. The development of a new set of electromechanical coupled equations will show how the segmentation has an influence on the electrical equation of the system, but does not change the mechanical model.

As seen in the previous section, instead of looking for higher accelerations to meet the load requirements, one should try to properly design both the PEH and the conversion system, so they can efficiently work together. In particular, since the voltage threshold V_{th} could be hard to reach for low seismic excitation levels, a step-up converter is needed. Anyway this solution could lead to relevant losses, affecting significantly the total amount of power generated. Du *et al.* [Du; Jia, and Seshia 2017] proposed the width segmented electrodes, demonstrating their effectiveness as voltage amplifier, with piezoelectric as a current source in parallel with a capacitance. To implement this approach, in Sec. 4.3.2 the electromechanical model of the PEH with segmented electrode is presented. To overcome this issue, the device electrodes can be divided into n_w regions connected to each other in series, in order to obtain a voltage input at the FBR n_w times higher and so overcoming more easily the V_{th} issue. In Fig. 4.17 the actual PEH configuration is shown, with segmented electrodes in width connected to a FBR, whose equivalent circuit can be seen in Fig. 4.18.

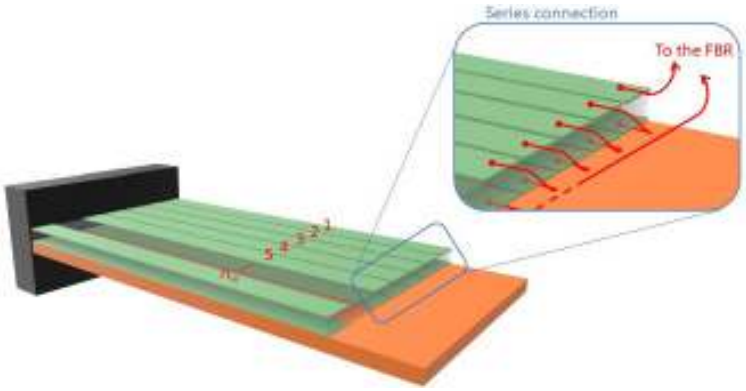

Figure 4.17: Representation of a PEH with electrodes segmented in width. The electrodes are connected in series.

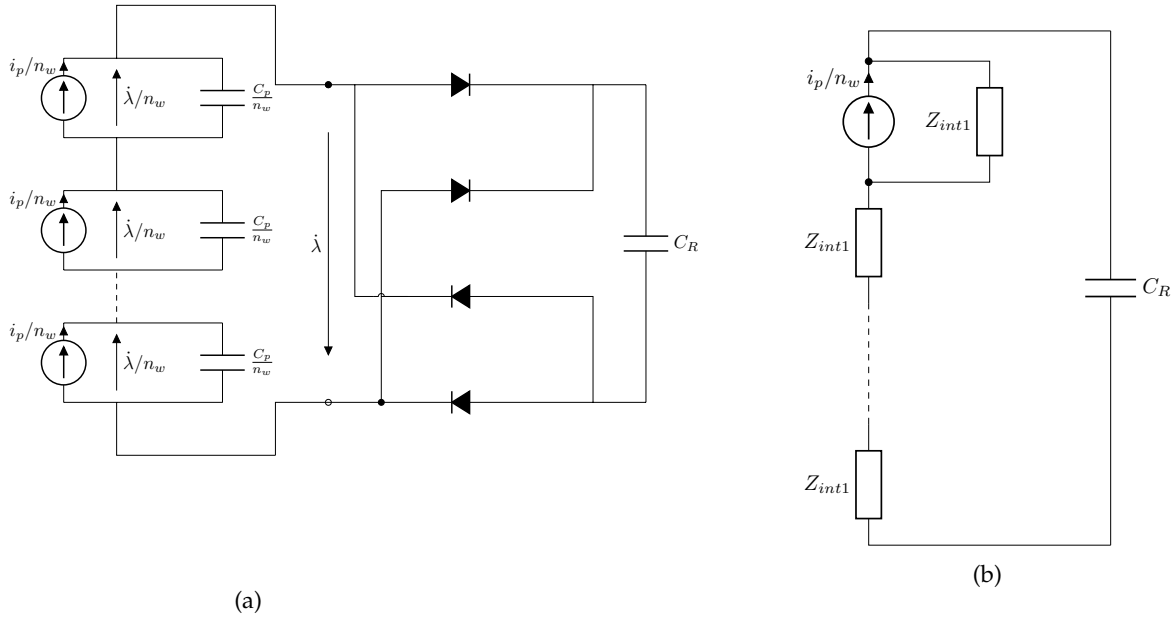

Figure 4.18: Actual (a) and equivalent (b) circuit of a FBR and a PEH with electrodes segmentation in width connected in series and main electric quantities.

Moreover, the electrode segmentation technique can be useful also to avoid charge cancellation through the piezoelectric length, allowing an increase in energy production and higher modes power recovery. Du *et al.* [Du; Jia; S.-T. Chen, et al. 2017] proposed a similar idea, with electrodes segment in width connected gradually to find the electrode area harvesting the maximum power. They demonstrate that a distribution from the maximum strain point (clamping) to about a half the maximum strain would be optimal. Since this result are due to charge cancellation, a further improvement in optimal electrode positioning in length could be done by studying the structure nodes and finding an optimal configuration of electrode segmentation in length. Moreover, to actually avoid charge cancellation, the output voltage from each segment of the piezoelectric patch must be first rectified and then can be connected to the others to power a unique load.

In Fig. 4.20 the PEH configuration with segmented electrodes in length is shown and its equivalent circuit is presented and in Fig. 4.19.

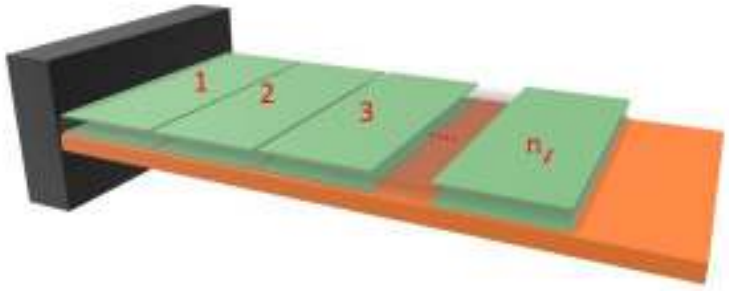

Figure 4.19: Representation of a PEH with electrodes segmented in width.

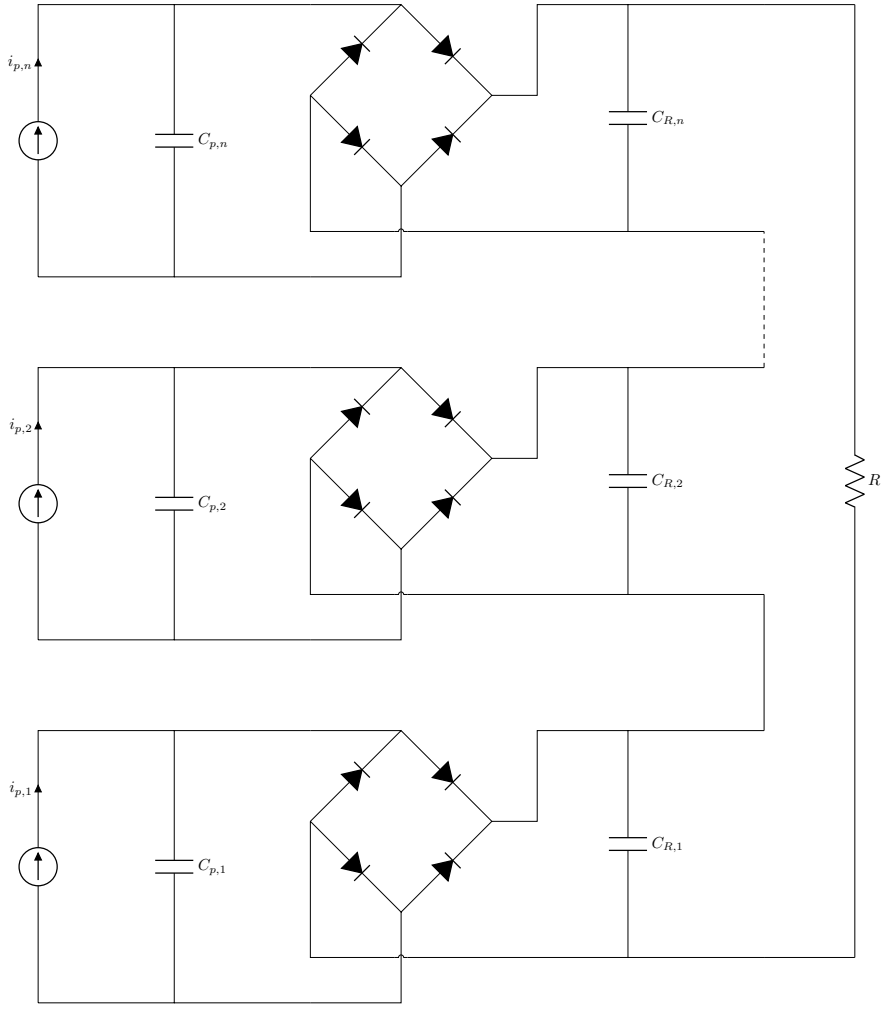

Figure 4.20: Actual (a) and equivalent (b) circuit of a FBR and a PEH with electrodes segmentation in length.

4.3.2 Segmentation in width

As mentioned before, the electrode segmentation in width is helpful to overcome the voltage threshold set by the FBR capacitor C_R. In order to find the effect of electrode segmentation, the Lagrange equations will be developed again taking into account the discontinuity introduced in electrical behaviour.

Electromechanical reduced-order model

Despite the electrode segmentation in width in n_w parts, the electric field in z direction E_3 is still defined as

$$E_3 = -\frac{\dot{\lambda}}{h_p} = -\frac{\sigma}{2\epsilon_{33}} \tag{4.10}$$

where $\dot{\lambda}$ is the voltage measured between terminals of all segmented parts connected in series, σ is the superficial charge, and ϵ_{33} is the permittivity of the material. The first definition has not changed, since it depends on the material characteristics rather than on how electrodes are positioned. However a second definition is given, being convenient to express the series connection in the following. Although the mechanical potential energy calculations remain the same, it is convenient to express the integral over width as sum of the n_w intervals in which electrodes divide the surface. Consequently, the mechanical potential energy becomes

$$\begin{aligned} U_m = \frac{1}{2}\Bigg\{ & b\int_0^{l_1} \frac{Y_s}{1-\nu_s^2}\kappa^2\left[\frac{h_s^3}{3} - z_0 h_s^2 + h_s z_0^2\right]dx + \sum_{i=1}^{n_w}\left[b_i\int_{l_1}^{l_2}\frac{Y_s}{1-\nu_s^2}\kappa^2\left[\frac{h_s^3}{3} - z_0 h_s^2 + h_s z_0^2\right] + \right. \\ & + \frac{Y_p}{1-\nu_p^2}\kappa^2\left[\frac{h_p^3}{3} + h_p^2 h_s + h_s^2 h_p - z_0\left(h_p^2 + 2h_p h_s\right) + z_0^2 h_p\right] - \frac{Y_p d_{31}\kappa}{1-\nu_p^2}\left[\frac{h_p}{2} + h_s - z_0\right]\dot{\lambda}dx\Bigg] + \\ & \left. + b\int_{l_2}^{L_s}\frac{Y_s}{1-\nu_s^2}\kappa^2\left[\frac{h_s^3}{3} - z_0 h_s^2 + h_s z_0^2\right]dx\right\} \end{aligned} \tag{4.11}$$

with b_i width of the $i-th$ electrode and $\sum_{i=1}^{n_w} b_i = b$. The new n_w contributions from segmented electrodes takes into account the electric discontinuity in y direction. Since this discontinuity does not occur from a mechanical point of view, it is not considered in the areas where piezoelectric material is not present.

Similarly, the electric internal energy is given by

$$U_e = \frac{1}{2}\int\int_{A_p}\int_{h_s}^{h_p+h_s} E_3\left(\varepsilon_1\bar{e}_{31} - \epsilon_{33}E_3\right)dzdxdy \tag{4.12}$$

where it is convenient to express the electric field as function of the charge density for the capacitive part of the energy expression. Thus,

$$\begin{aligned} U_e &= \frac{1}{2}\iint_{A_p}\int_{h_s}^{h_p+h_s}\left(-\frac{\dot{\lambda}}{h_p}\varepsilon_1\bar{e}_{31} - \epsilon_{33}\frac{\sigma^2}{2\epsilon_{33}^2}\right)dz\,dx\,dy = \\ &= \left(\frac{1}{2}\iint_{A_p}\int_{h_s}^{h_p+h_s} -\frac{\dot{\lambda}}{h_p}\varepsilon_1\bar{e}_{31} - \epsilon_{33}\frac{Q^2}{2\,S_p^2\epsilon_{33}^2}\right)dz\,dx\,dy. \end{aligned} \tag{4.13}$$

substituting then in the previous equation the strain ε_1 expression and integrating over the width and thickness of the piezoelectric, the following expression of electric potential energy is obtained:

$$U_e = \int_{l_1}^{l_2} \sum_{i=1}^{n_w} \left[b_i \frac{d_{31} Y_p}{2(1-\nu_p^2)} \left(\frac{h_p}{2} + h_s - z_0 \right) \kappa \dot{\lambda} + \epsilon_{33} b_i h_p \frac{Q_i^2}{2\, S_{p,i}^2 \epsilon_{33}^2} \right] dx \tag{4.14}$$

where Q_i is the superficial charge produced by the piezoelectric effect and $S_{p,i}$ is the surface on which the charge is distributed. Since all the electrodes are considered to be equal in width $b_i = b/n_w$, each element has the same surface and equivalent capacitance and, thus, equal superficial charge $Q_i = \pm \overline{Q}$. Considering now that the connection among the different parts of the piezoelectric is in series, the sum of the superficial charges on the electrodes results in only $\overline{Q}$ on those on the terminal electrodes since all the others cancel, as schematically shown in Fig. 4.21.

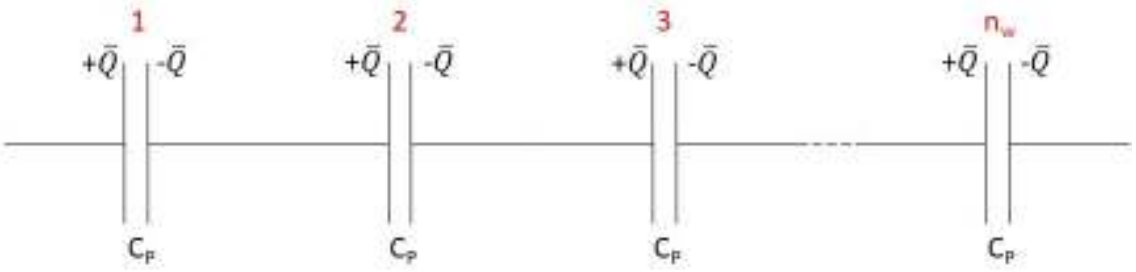

Figure 4.21: Series connection of the $i-th$ capacitances.

Thus, the term relative to the charge can be now written in terms of PEH series voltage $\dot{\lambda}$, obtaining

$$\begin{aligned} U_e &= \int_{l_1}^{l_2} \left[b \frac{d_{31} Y_p}{2(1-\nu_p^2)} \left(\frac{h_p}{2} + h_s - z_0 \right) \kappa \dot{\lambda} \right] + \epsilon_{33} \frac{b h_p}{2 n_w} \frac{\dot{\lambda}^2}{h_p^2} dx \\ &= \int_{l_1}^{l_2} \left[b \frac{d_{31} Y_p}{2(1-\nu_p^2)} \left(\frac{h_p}{2} + h_s - z_0 \right) \kappa \dot{\lambda} \right] + \epsilon_{33} \frac{b}{2 n_w} \frac{\dot{\lambda}^2}{h_p} dx \end{aligned} \tag{4.15}$$

By substitution of Eqs. 4.11, 4.13, and 3.35 in Eq. 3.22, the specific Lagrangian ℓ can be written as

$$\begin{aligned} \ell = \frac{1}{2} \Big\{ & \mu \dot{w}_a^2 - \bar{D} w''^2 + 2\theta [H(x-l_1) - H(x-l_2)] w'' \dot{\lambda} + \\ & C_{p,i}^L [H(x-l_1) - H(x-l_2)] \dot{\lambda}^2 \Big\} \end{aligned} \tag{4.16}$$

With respect to the single electrode configuration the electromechanical coupling coefficient θ does not change,

$$\theta = \frac{Y_p b d_{31}}{1-\nu_p^2} \left(\frac{h_p}{2} + h_s - z_0 \right) \tag{4.17}$$

while the equivalent piezoelectric capacity per unit of length $C^L_{p,i}$ of the single $i-th$ element becomes

$$C^L_{p,i} = \epsilon_{33}\frac{b}{n_w h_p}. \tag{4.18}$$

Thus, again the relation 3.54 is used to derive the electric equation of the system. For λ we have

$$\begin{aligned}
&\frac{\partial \ell}{\partial \lambda'} = \frac{\partial \ell}{\partial \lambda''} = \frac{\partial \ell}{\partial \lambda} = 0 \\
&\frac{\partial \ell}{\partial \dot{\lambda}} = C^L_{p,i}[H(x-l_1) - H(x-l_2)]\dot{\lambda} + \theta[H(x-l_1) - H(x-l_2)]w''
\end{aligned}$$

from which, by applying the 3.54 the following equation is obtained

$$-C_{p,i}\ddot{\lambda} - \int_0^{L_s} \theta\Big[H(x-l_1) - H(x-l_2)\Big]\dot{w}''\,dx - I_c = 0 \tag{4.19}$$

where $C_{p,i} = C^L_{p,i} \cdot L_p$ is the equivalent piezoelectric capacity of each electrode element. This equation corresponds to apply the Kirchhoff's current law to one of the nodes of connection with the conversion circuit.

Being the sum over n_w only virtual for the electromechanical coupling term, mechanical equations of the PEH do not change. Thus, the final global equation system, also taking into account a Kelvin-Voigt (or strain-rate) damping term and a viscous air damping one, becomes

$$\begin{cases}
\mu\ddot{w} + c_a\dot{w} + (c_s J\dot{w}'' + \bar{D}w'')'' - \theta\Big[\delta'(x-l_1) - \delta'(x-l_2)\Big]\dot{\lambda} = f(x,t) \\
C_{p,i}\ddot{\lambda} + \displaystyle\int_0^{L_s} \theta\Big[H(x-l_1) - H(x-l_2)\Big]\dot{w}''\,dx = -I_c
\end{cases}, \tag{4.20}$$

Both damping terms introduced are not affected by the electrode segmentation, since they are not electric variable dependent.

Finally, by projecting equations 4.20 on the modes of the structure, the following system of equations is obtained:

$$\ddot{q}_m + 2\zeta_m\omega_m\dot{q}_m + \omega_m^2 q_m - \theta(\phi'_{2m}(L_p) - \phi'_{1m}(l_1))\dot{\lambda} = F_m(t) \tag{4.21}$$

$$C_{p,i}\ddot{\lambda} + \theta\sum_{j=1}^{N_w}\chi_j\dot{q}_j = -i_R \tag{4.22}$$

Numerical solution via Simulink

The electrode segmentation in width was simulated in the same conditions (excitation amplitude and FBR capacitance) adopted for the single electrode configuration. As seen before, the electrode segmentation in width do not change the superficial charge produced, and thus, if one neglects the electromechanical coupling effect, the expected output voltage is n_w times the voltage from a single electrode. Considering that in Sec. 4.2.2, for the simple resistive load, the acceleration amplitude of 0.06 g (about 1 V in maximum power condition) was found too low for the PEH to produce a typical 3 V minimum voltage required by

electronic devices, an $n_w = 3$ segmentation is chosen to overcome the threshold value.

To obtain the electrical outputs shown in Fig. 4.22, the system is solved using the joint Simscape-Simulink formulation introduced before in this Chapter. It can be observed that the voltage corresponding to the optimal working conditions is close to 3 V, as desired, and the open circuit voltage is three time the single electrode configuration one, reaching 6 V. It is then worth noting that these conditions potentially match the powering requirements seen in Sec. 4.2.2 on the temperature sensor for both minimum voltage and overvoltage thresholds. The maximum power occurs for a different value of resistance with respect the single electrode condition. This is due to the change of the equivalent capacitance of the system, that requires a different impedance matching. Indeed, the piezoelectric series capacitance is n_w^2 times smaller than the one for a single electrode, and thus, considering the frequency does not change, the impedance of the PEH grows. The peak power of the segmented electrode configuration (0.09 mW) is slightly lower than the one of the single electrode (0.1 mW), due to a more dissipative optimal resistance ($5 \cdot 10^4\,\Omega$).

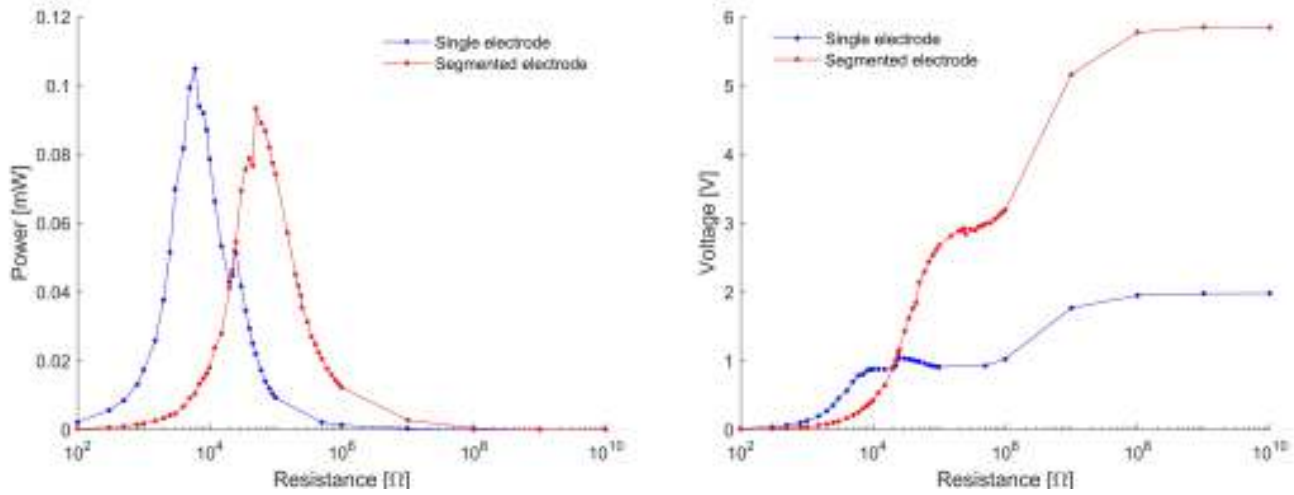

(a) *Power.* (b) *Voltage.*

Figure 4.22: Power and voltage output from the conversion system for different resistive loads for the single electrode configuration (blue) and for the segmented electrode with $n_w = 3$ (red).

4.3.3 Segmentation in length

Electromechanical reduced-order model

As for the previous configuration, electrode segmentation in length will not affect the mechanical behaviour of the structure if only longitudinal bending modes are involved in the structural response. However, n_l different voltage variables $\dot{\lambda}_i$ ($i = 1, ..., n_l$) have to be introduced, because different longitudinal portions experience different strain and so produce different amounts of superficial charge. Thus, a no

more uniform but piecewise voltage function can be defined as

$$\dot{\lambda}(x) = \begin{cases} \dot{\lambda}_1, & l_1 < x \leq l_2 \\ \dot{\lambda}_2, & l_2 < x \leq L_3 \\ \dots & \\ \dot{\lambda}_{n_l}, & L_{n_l} < x \leq L_{n_l+1} \end{cases} \tag{4.23}$$

A schematic representation of the electrode segmentation the new reference length used in the following is reported in Fig. 4.23.

Obviously, all the n_l parts have to be connected to as many FBRs, to completely avoid signal destructive interference. After the signals are rectified, they can be mixed together to jointly supply the same electric load, as shown in Fig. 4.20.

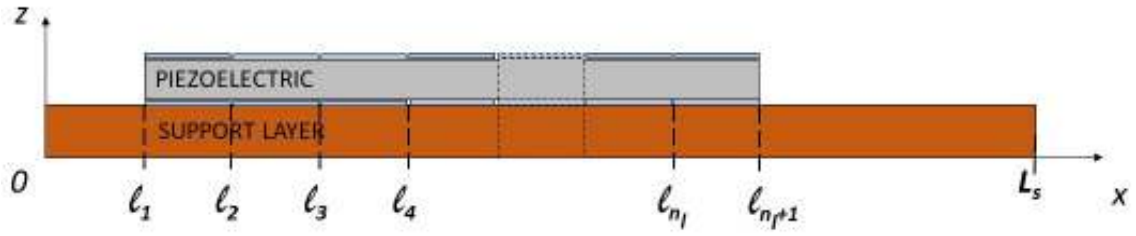

Figure 4.23: Schematic representation of the PEH with electrode segmented in n_l parts.

The voltage $\dot{\lambda}_i$ is then referred to terminals of each segmented part. Consequently, the piezoelectric stress 3.2 and electric field expressions 3.6 change as follow

$$E_3 = -\frac{\dot{\lambda}(x)}{h_p} \tag{4.24}$$

$$\sigma_1^p = -\frac{Y_p}{1-\nu_p^2}(z-z_0)w'' + d_{31}\frac{Y_p}{1-\nu_p^2}\frac{\dot{\lambda}(x)}{h_p}. \tag{4.25}$$

and mechanical potential energy becomes

$$\begin{aligned} U_m = \frac{1}{2}\Bigg\{ & b\int_0^{l_1} \frac{Y_s}{1-\nu_s^2}\kappa^2\left[\frac{h_s^3}{3} - z_0h_s^2 + h_sz_0^2\right]dx + \sum_{i=1}^{n_l}\left[b\int_{l_i}^{l_{i+1}} \frac{Y_s}{1-\nu_s^2}\kappa^2\left[\frac{h_s^3}{3} - z_0h_s^2 + h_sz_0^2\right] + \right. \\ & + \frac{Y_p}{1-\nu_p^2}\kappa^2\left[\frac{h_p^3}{3} + h_p^2h_s + h_s^2h_p - z_0\left(h_p^2 + 2h_ph_s\right) + z_0^2h_p\right] - \frac{Y_pd_{31}\kappa}{1-\nu_p^2}\left[\frac{h_p}{2} + h_s - z_0\right]\dot{\lambda}_i dx\Bigg] + \\ & \left. + b\int_{l_{n_l+1}}^{L_s} \frac{Y_s}{1-\nu_s^2}\kappa^2\left[\frac{h_s^3}{3} - z_0h_s^2 + h_sz_0^2\right]dx\right\} \end{aligned} \tag{4.26}$$

Indeed, the sum to n_l term represents the contribution of each element in x direction. Since this discontinuity does not occur from a mechanical point of view, it have not been taken into account in the areas where

piezoelectric material is not present. Thus, the previous relation can be rewritten as

$$U_m = \frac{1}{2}\Bigg\{ b\int_0^{L_s} \frac{Y_s}{1-\nu_s^2}\kappa^2\left[\frac{h_s^3}{3} - z_0 h_s^2 + h_s z_0^2\right]dx + b\int_{l_1}^{l_{n_l+1}} \frac{Y_p}{1-\nu_p^2}\kappa^2\left[\frac{h_p^3}{3} + h_p^2 h_s + h_s^2 h_p - z_0\left(h_p^2 + 2h_p h_s\right) + z_0^2 h_p\right] + \\ + \sum_{i=1}^{n_l}\left[b\int_{l_i}^{l_{i+1}} - \frac{Y_p d_{31}\kappa}{1-\nu_p^2}\left[\frac{h_p}{2} + h_s - z_0\right]\dot{\lambda}_i dx\right] \tag{4.27}$$

Similarly, the electric internal energy is given by

$$U_e = \frac{1}{2}\iint_{A_p}\int_{h_s}^{h_p+h_s} -\frac{\dot{\lambda}(x)}{h_p}\left(\varepsilon_1\bar{e}_{31} - \epsilon_{33}\frac{\dot{\lambda}(x)}{h_p}\right)dzdxdy \tag{4.28}$$

which, by substituting the local expression of the voltage and integrating over width and thickness, taking into account Eq. 4.25, becomes

$$U_e = \sum_{i=1}^{n_l}\int_{l_i}^{l_{i+1}}\left[b\frac{d_{31}Y_p}{2(1-\nu_p^2)}\left(\frac{h_p}{2} + h_s - z_0\right)\kappa\dot{\lambda}_i + \epsilon_{33}\frac{b}{2h_p}\dot{\lambda}_i^2\right]dx \tag{4.29}$$

By substitution of Eqs. 4.26, 4.28, and 3.35 the specific Lagrangian ℓ can be written as

$$\begin{aligned}\ell =& \frac{1}{2}\Bigg\{\mu\dot{w}_a^2 - \bar{D}w''^2 + 2\sum_{i=1}^{n_l}\Big[\theta[H(x-l_i) - H(x-l_{i+1})]w''\dot{\lambda}_i\Big] + \\ & \sum_{i=1}^{n_l}\Big[C_{p,L}[H(x-l_i) - H(x-l_{i+1})]\dot{\lambda}_i^2\Big]\Bigg\}\end{aligned} \tag{4.30}$$

With respect to the single electrode configuration, the equivalent mass and bending stiffness do not change, being only dependent on mechanical quantities. The electromechanical coupling coefficient θ and capacitance per unit of length $C_{p,L}$ do not change either, because they have no dependency on the length.

Thus, once again Eq. 3.54 is used to derive system equations and its boundary conditions.

For each λ_i we have

$$\begin{aligned}&\frac{\partial\ell}{\partial\lambda_i'} = \frac{\partial\ell}{\partial\lambda_i''} = \frac{\partial\ell}{\partial\lambda_i} = 0\\ &\frac{\partial\ell}{\partial\dot{\lambda}_i} = C_{p,L}[H(x-l_i) - H(x-l_{i+1})]\dot{\lambda}_i + \theta[H(x-l_i) - H(x-l_{i+1})]w''\end{aligned}$$

from which, by applying the 3.54 the following equation is obtained

$$-C_p^{(i)}\ddot{\lambda}_i - \int_0^{L_s}\theta\Big[H(x-l_i) - H(x-l_{i+1})\Big]\dot{w}''\,dx - I_c = 0 \tag{4.31}$$

where $C_p^{(i)}$ is the equivalent piezoelectric capacity for the $i-th$ segment of electrode and $I_{c,i}$ is the current to the $i-th$ FBR. The equation represents the current balance at the connection node considered for the $i-th$ segment.

For w_a we have

$$\frac{\partial \ell}{\partial w_a} = \frac{\partial \ell}{\partial w_a'} = 0 \qquad \frac{\partial \ell}{\partial w_a''} = -\bar{D}w'' + \sum_{i=1}^{n_l} \left\{ \theta\big[H(x-l_i) - H(x-l_{i+1})\big]\dot{\lambda}_i \right\} \qquad \frac{\partial \ell}{\partial \dot{w}_a} = \mu \dot{w}_a$$

from which, referring to the 3.54, substituting and deriving, the following equation can be obtained

$$\begin{cases} \mu\ddot{w} + c_a\dot{w} + (c_s J\dot{w}'' + \bar{D}w'')'' - \sum_{i=1}^{n_l} \left\{ \theta\Big[\delta'(x-l_i) - \delta'(x-l_{i+1})\Big]\dot{\lambda}_i \right\} = f(x,t) \\ C_p^{(i)}\ddot{\lambda}_i + \int_0^{L_s} \theta\Big[H(x-l_i) - H(x-l_{i+1})\Big]\dot{w}''\,dx = -I_c \end{cases}, \tag{4.32}$$

Both damping terms introduced are not affected by the electrode segmentation, since they are not electric variable dependent.

Finally, by projecting equations 4.32 on the modes of the structure, the following system of equations is obtained:

$$\ddot{q}_m + 2\zeta_m\omega_m\dot{q}_m + \omega_m^2 q_m - \sum_{i=1}^{n_l} \left[\theta(\phi_m'(l_{i+1}) - \phi_m'(l_i))\dot{\lambda}_i \right] = F_m(t) \tag{4.33}$$

$$C_p^{(i)}\ddot{\lambda}_i + \theta \sum_{j=1}^{N_w} \chi_{j,i}\dot{q}_j = -i_R \tag{4.34}$$

Numerical solution via Simulink

In order to avoid charge cancellation phenomenon, piezoelectric areas with opposite curvatures should be electrically disconnected to each other. For this reason, the electrode segmentation has to be performed taking into account the position of the nodes of the relevant bending modes. For a cantilever beam, thus, a test case with segmented electrode in length must consider the curvatures of the second derivative of second and third bending modes. Once the curvature zeroes have been calculated with a Newton Raphson method, the second mode is found to be not suitable for electrode segmentation in the considered configuration, being too close to the piezoelectric edge. Conversely, for the third mode a change in curvature was found for $x = 0.03$, close to the centre of the piezoelectric patch. Indeed, in Section 3.5 the third mode contribution to power production was negligible if compared with those of first and second modes, with an open voltage of 0.02 V in open circuit conditions for 0.1 g acceleration amplitude. This is due to charge cancellation phenomenon, being the node almost in the centre of the patch and, thus, having a relevant opposite charge production on the same side of the lamina. However, with length segmentation of electrodes, this issue is overcame. The $n_l = 2$ configuration has then one electrode of 2.6 cm and the other of 1.4 cm, as shown in Fig. 4.24. As in the previous sections, the device was simulated with acceleration amplitude of 0.06 g, but the excitation frequency is set equal to the third mode one (1080.2 Hz). Consequently, the capacitance size is adjusted in frequency (keeping constant all the other parameters), obtaining $C_R = 2.5mF$.

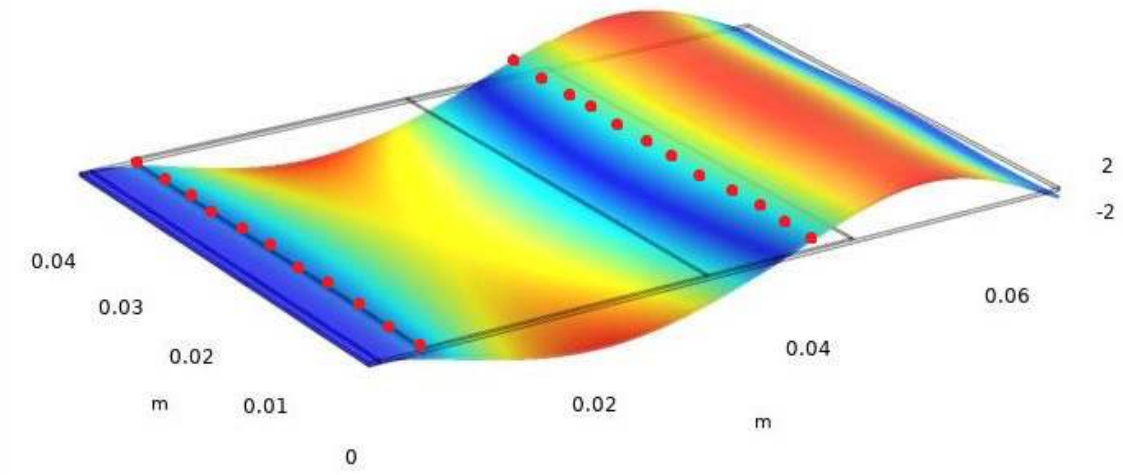

Figure 4.24: Segmented electrode in length configuration with third mode shape.

In Fig. 4.25 a comparison of the two configurations is shown. The single electrode does not produce any power, since the voltage output cannot even overcome the drop due to diodes. On the opposite, the segmented electrode configuration provides a power output not completely negligible, although small if compared to the one obtained for the first mode resonance frequency, with a peak occurring for $R = 9 \cdot 10^3\,\Omega$. Similarly, the voltage output is very low. Thus, this configuration if excited on the third mode frequency alone could not supply an electronic device, but shows the potential effectiveness of the electrode segmentation in length. In fact, for a configuration with the piezoelectric patch properly positioned, the second bending mode could benefit of the electrode segmentation as well, being then more relevant as a contribution with respect to the third mode.

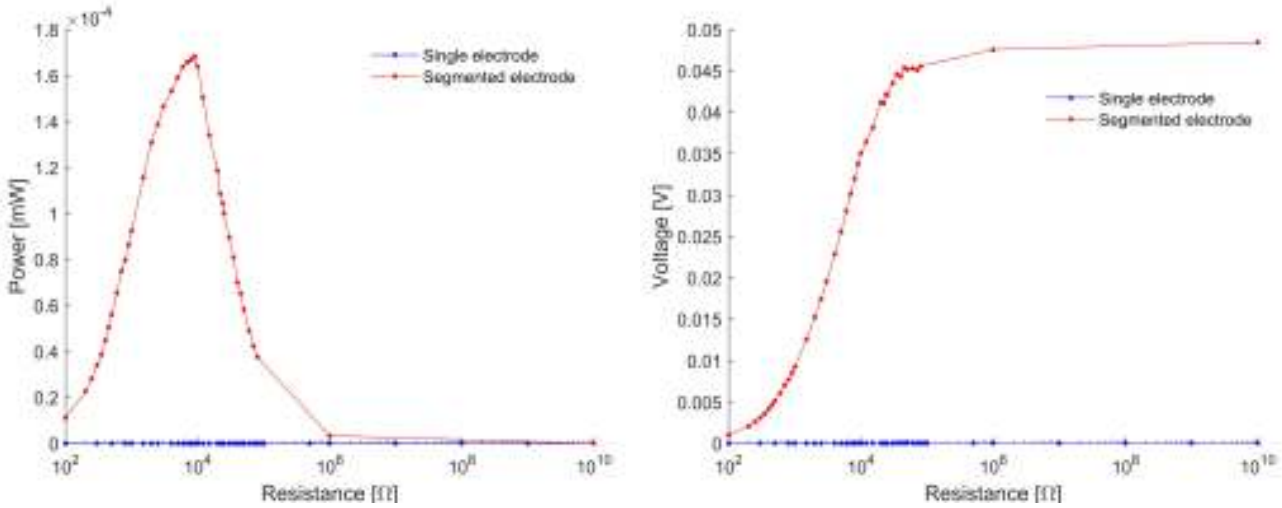

(a) *Power.* (b) *Voltage.*

Figure 4.25: Power and voltage output from the conversion system for different resistive loads for the single electrode configuration (blue) and for the segmented electrode with $n_w = 2$ (red).

Chapter 5

Experimental analysis and model validation

In this chapter the piezoelectric harvester is investigated experimentally, also providing data to validate the mathematical models introduced in the previous chapters. The experiments were carried out at the Structural Dynamics and Diagnostic Laboratory (SDDLab) at Institute of Marine Engineering of the National Research Council (CNR-INM) facility in Rome.

First, a brief account of piezoelectric patch realization is described, from material production, through cutting techniques, till polarization process. Then, a comparative analysis of four custom piezoelectric energy harvesters (same piezoelectric material but different support layer) is performed to select in open circuit condition the best device, which is further investigated under both sinusoidal and random excitations, analysing its performances and power output with respect to a commercial PEH. Finally, the chosen custom device is taken as reference configuration for the theoretical model validation. The clamping condition and the structural and air damping coefficients are first identified for different tip mass conditions (no tip mass, $m_{tip,1}$, and $m_{tip,2}$). The device is then tested for the three tip mass configurations with different resistive loads under sinusoidal excitations (different frequencies but constant acceleration amplitude). Finally, numerical results of the present theory are compared with the obtained voltage - acceleration transfer function.

5.1 Remarks on piezoelectric patch production

In order to create a PEH performing at low frequencies, a piezoelectric lamina was made at the CNR-ISTEC laboratory. The material is produced with a tape casting process, particularly useful when a thin thickness (220 μm) needs to be reached. To create the ceramic material, a suspension of ceramic powder dispersed in an organic liquid is prepared [Gardini et al. 2010]. The powder is lead-zirconate-titanate doped with niobium and lanthanum (PLZTN):

$$(Pb_{0.93}\ La_{0.07})\ [(Zr_{0.60}\ Ti_{0.40})_{0.9825}\ Nb_{0.0175}]\ O_3. \tag{5.1}$$

and has been synthesized through a solid state reaction of the single elements oxides: PbO, ZrO_2, TiO_2, Nb_2O_3, and La_2O_3. The powder synthesis happens in consecutive stages. First, the oxides are mixed in water with zirconia spheres for 48 hours. The suspension is lyophilized and sieved at 250 μm, to then undergo to calcination at 850 °C for 4 hours. After this process, the product is subjected to grinding for 100 hours, drying and again sieving.

Knowing form empirical experiences that the sintering process induces a linear shortening of about 21% and willing for a 220 μm thickness, a 278 μm tape should be produced. The suspension is made by powder, solvent and additives. The solvent is an azeotropic mixture of methylethylketone (MEK) (or 2-butanone), 67% by weight, and ethanol (EtOH). The additives are a dispersant, stabilizing colloidally the suspension and so avoiding agglomerates formation, a plasticizer, making tapes flexible and so possible to be bended, and a binder, binding together the particles.

Table 5.1: Suspension components.

Component	Acronym	Name
Powder	PLZTN	lead-zirconate-titanate doped with niobium and lanthanum
Solvent	MEK-EtOH	Methylethylketone (2-butanone)-Ethanol (azeotropic mixture)
Dispersant	GTO	Trioleate glycerol
Binder	PVB	polyvinyl butyral
Plasticizer 1	ABP	Alkyl (C7-C9) benzyl phthalate
Plasticizer 2	PEG400	Polyethylene glycol (molecular weight 400)

To properly prepare the suspension, components must be added at different moments and with specific intervals of time between two consecutive additions for mixing/grinding with small zirconia spheres (ball milling technique). First dispersant, part of the binder and part of the powder are added in the solvent, with 4 hours for grinding. Then, respectively the remaining powder, binder, and plasticizers are added, each addition being followed by 24 hours for grinding. The whole process takes 4 days to be completed.

To be ready for casting, the suspension must undergo to filtering, to remove any lumps due to a non efficient mix/grinding, and degassing, to eliminate possible air bubbles. The latter process is performed in atmosphere saturated in solvent to avoid suspension properties changes due to evaporation.

To level the layers thickness to 278 μm, the suspension moves on a belt at a 62 cm/min speed and passes under a blade positioned at the desired high (Fig. 5.1). After the casting process, the tape is kept in atmosphere saturated with solvent at 22 °C for 24 hours to dry, with a ventilation system aspirating the steams produced. This phase is one of the most critical since the solvent evaporation induces mechanical stress inside the tape, consequently producing macroscopic defects in the final product. The flexible solid tape can be punched or cut to obtain different shapes, taking into account the shorten during sintering

Figure 5.1: Casting bench.

process when choosing dimensions (Fig. 5.2).

Figure 5.2: Casting samples after the cutting process.

In order to eliminate all organic components, the material obtained undergoes to debonding by slow temperature increase (4 °C/h) till 600 °C, taking 5 days. Then, to consolidate the extremely fragile sample obtained, the sintering process is performed at 1200 °C for 2 hours in PLZTN powder, to avoid changes in stoichiometry due to lead and other elements evaporation. Finally, silver paste-made electrodes are deposited on the sample surfaces by screen printing and the polarization process to induce piezoelectric properties in the ferroelectric material is performed, by applying an external 3 kV/mm electric field for 40 minutes in a silicon oil bath at 120 °C.

5.2 Selection of the supporting plate material

5.2.1 Experimental setup

The selection of the device configuration is based on comparing performances among four cantilevers sharing the same piezoelectric patch but different support materials. To assess the energy harvester performance under variable conditions, an experimental setup is required. For the following tests, the PEHs lie on a metallic plate, simulating a real-life installation (e.g. floor or walls), clamped along the contour between a metal frame and a backframe, as shown in Fig. 5.3. The plate transfers to the piezoelectric device the force excitation applied via a shaker. In order to understand how the applied ideal force was transmitted to the energy harvester, the frequency transfer function (FRF), defined as ratio between the Fourier transform of the acceleration of the free edge of the piezoelectric and that relative to the exciting force, was identified. The FRF can be split as the product of two transfer functions: the transfer function between the exciting system and the plate (FRF1), and the one between the support and the piezoelectric device (FRF2). By the knowledge of FRF, it is possible to reproduce the required acceleration on the piezoelectric element by controlling the shaker with the proper input signal. Nonetheless, an accelerometer (PCB Piezotronic 333B32),

placed on the piezoelectric clamping, allows for empirical verification of the excitation actually transmitted, making sure the devices are tested under same excitation levels, an accelerometer. The LMS acquisition system collects voltage data from the piezoelectric harvester and acceleration data from the accelerometer at the clamp.

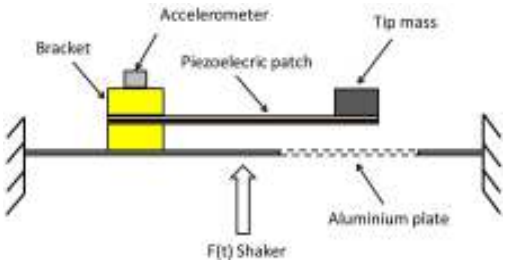

(a) *Setup schematic representation of the setup.*

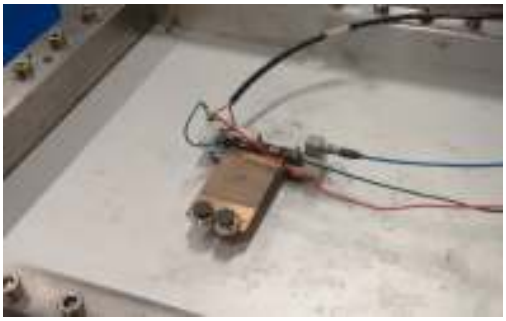

(b) *Close view of the setup at SDDLab.*

Figure 5.3: Configuration of the experimental setup.

5.2.2 Comparison of the devices in open circuit condition

The four piezoelectric energy harvesters (Fig. 5.4) were built by using identical piezoelectric patches (PLZTN produced at CNR-ISTEC) but different materials as support plates: Steel, Brass, Aluminium and PLA (Polylactic Acid, obtained by 3D printing) [Passacantilli et al. 2018]. Each support layer thickness, reported in Tab. 5.2, has been chosen in order to keep the beam neutral axis outside the piezoelectric material, and thus avoiding charge cancellation phenomenon.

Figure 5.4: Custom energy harvesters with same piezoelectric material (PLZTN) but different support layer materials (Steel, Brass, PLA, Alluminium).

Table 5.2: Thickness and materials of ISTEC piezoelectric energy harvester support layers and the bending resonance frequency.

Short name	Material	Thickness [mm]	Bending frequency [Hz]
ISTEC-Al	Aluminium	0.5	72.3
ISTEC-Br	Brass	0.3	42.3
ISTEC-PLA	PLA	0.8	65.4
ISTEC-St	Harmonic Steel	0.3	76.1

To investigate the electromechanical performances of the four piezoelectric devices, a test was carried out with harmonic excitation at the first bending mode frequency (different for each device). The results, summarized in Tab. 5.3, show that in resonance condition (optimal working point) ISTEC-St produces the highest outputs in terms of open circuit voltage relatively to the given excitation.

A second kind of test was carried out by comparing the most performing in-house built device (ISTEC-St), without tip mass, and the commercial piezoelectric harvester, equipped with tip mass in order to bring the frequency of the second device at the same value of the first one (44.1 Hz). The two PEH dimensions are reported in Table 5.4. Since the MIDE PPA 1012 was provided with its clamping structure, a custom one was 3D-printed in PLA for the ISTEC-St as well, in order to test both devices in similar BCs (Fig. 5.5). Despite the tip mass enhancing oscillation amplitude, for the commercial device, ISTEC-St still exhibits a better performance in voltage than MIDE PPA 1012, as shown in the last column of Table 5.3.

Table 5.3: Comparison among the four ISTEC PEH and the commercial PEH MIDE PPA 1012 in term of open circuit output voltage.

Test type	Signal		Output	
	Type	Frequency [Hz]	Device	RMS OC Voltage $[V \cdot s^2/m]$
1	Sinusoidal	44.1	ISTEC-St	3.64
	Sinusoidal	42.3	ISTEC-Br	2.11
	Sinusoidal	72.3	ISTEC-Al	1.14
	Sinusoidal	65.4	ISTEC-PLA	0.30
2	Sinusoidal	44.1	ISTEC-St	3.64
	Sinusoidal	44.1	PPA 1012	2.62

Table 5.4: Piezoelectric material patch dimensions.

Device	LxWxT [mm]	Area $[mm^2]$	Volume $[mm^3]$
ISTEC-St	40x40x0.2	1600	320
MIDE PPA 1012	46x38x0.25	1766	442

Furthermore, device sensitivity to perturbation of optimal excitation frequency was analysed too. Both ISTEC-St and MIDE PPA 1012 have been equipped with a tip mass to lower their natural frequency f_n till (Fig. 5.5). Thus, five test conditions with sinusoidal excitation were carried out at $0.6\,m/s^2$ amplitude, varying the excitation frequency f_e of $\pm 5\%$ and $\pm 10\%$ with respect to the initial resonance frequency value f_n.

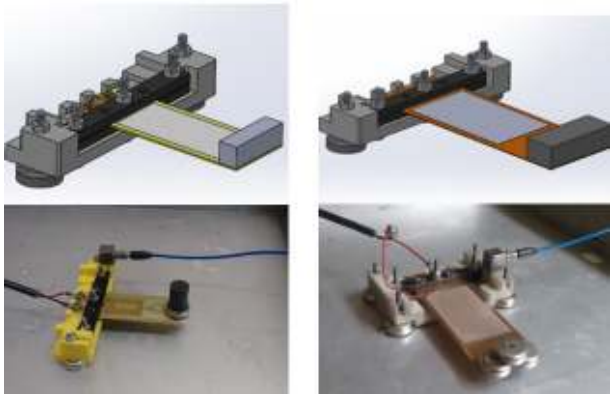

Figure 5.5: Schematic configuration (top) and picture (bottom) of the commercial (left) and in-house assembled device (right).

Results in Fig. 5.6 show in the y axis the root mean square (rms) value of the voltage harmonic time history. It is evident the expected drop in the voltage output for both devices out of the resonant frequency ($f_e \neq f_n$). However, ISTEC-St still provides a slightly better performance at the resonant excitation and for $f_e > f_n$, but this difference becomes negligible for $f_e < f_n$.

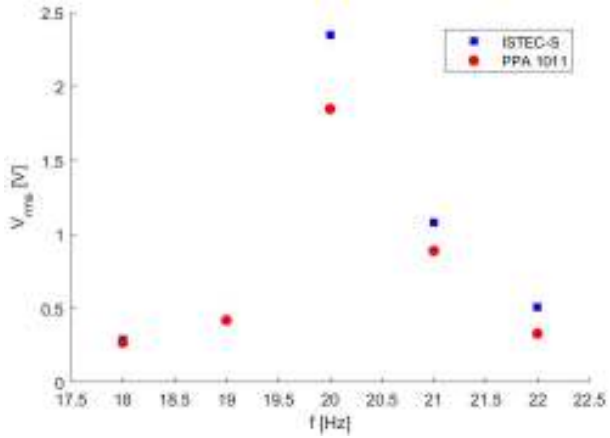

Figure 5.6: Comparison between the commercial and in-house assembled device output voltage for harmonic excitation at different frequencies.

5.2.3 Comparison in terms of power output

Recalling Table 5.4, ISTEC-St and MIDE PPA 1012 have similar values of piezoelectric areas and volumes, thus a comparison in terms of power depends also not only on active material quantity, but also on the configuration adopted.

The two devices were tested for different resistive loads, varying from $0.82\,k\Omega$ to $90\,k\Omega$ (Figs. 5.7 and 5.8). The shift in optimal load condition ($70\,k\Omega$ for ISTEC-St and at $50\,k\Omega$ for the PPA 1012) reflects the change in electrical behaviour due to different piezoelectric capacitance C_p, which depends on material characteristics and patch dimensions. Both absolute (Fig. 5.7) and per unit volume (Fig. 5.8) power output

data point out a better performance for ISTEC-St, confirming previous results also when the circuit is closed on an electric load.

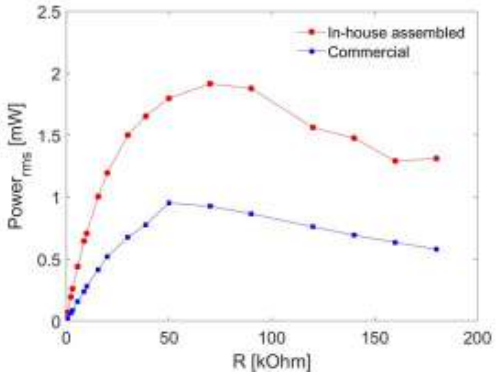

Figure 5.7: Comparison between the commercial and in-house assembled device output power for different resistive loads.

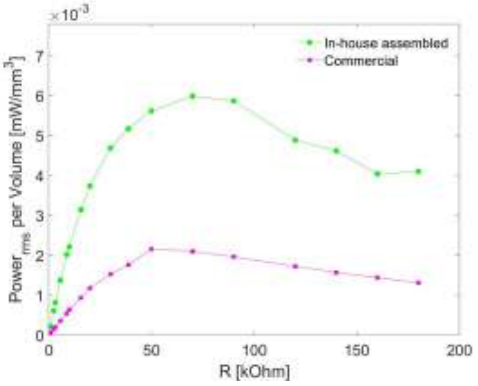

Figure 5.8: Comparison between the commercial and in-house assembled device output power per unit of volume for different resistive loads.

Finally, the two devices performances are experimentally compared through their response to a realistic working case, with a resistive temperature sensor (TMP36 by Analog Devices) as load and a voltage amplifier connected to a commercial charge regulator (BOB 09946) as conversion circuit, shown in Fig. 5.9. Having six steps made by Schottky diodes and tantalum capacitors, the multiplier gives an output voltage up to 6 times the input one, allowing the PEH to reach the minimum threshold needed to activate the charge regulator. A storage capacitor (1500 mF) is connected to the BOB 09946 to ensure constant power flow for a time interval sufficient to perform the temperature measurement. The sensor indeed is activated by an enable signal from BOB 09946 controlling a MOSFET: the circuit is *on* only when the capacitor reaches 3.3 V, but it goes *off* when the voltage drops again under 3 V.

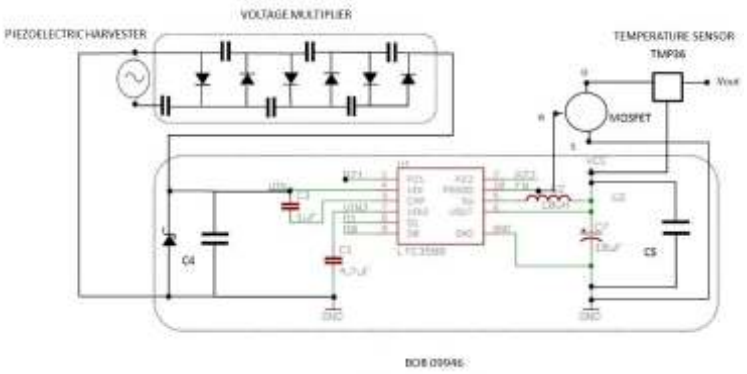

Figure 5.9: PEH, commercial conversion system, and temperature sensor schematic representation.

The test were carried out under harmonic seismic excitation with acceleration amplitude and frequency equal to $0.1\ m/s^2$ and 20 Hz, respectively. The first charge of the capacitance to reach 3.3 V from zero takes a few minutes for both devices. Despite this, since the MOSFET opens only when the voltage drops from 3.3

V to 3 V, and the storage capacitor voltage has then to regain only 0.3 V, the subsequent charges are operated in a shorter period. In Tab. 5.5 the intermediate charges and the charge from scratch are compared in time. Both devices power successfully the load, but recharge time is 27 s for ISTEC-St against 48 s for MIDE PPA 1012, as shown in Tab. 5.5.

Table 5.5: Storage capacitor recharge intervals.

Device	First charge [min]	Temperature data sample [s]
ISTEC-St	5	27
MIDE PPA 1012	9	48

5.3 Piezoelectric structure identification

5.3.1 Experimental setup

After identifying a preliminary prototype, as seen in the previous section, the most performing device ISTEC-St was elected as reference device for modelling purposes and, consequently, underwent a systematic series of tests to provide data for validating the theoretical models developed in the previous chapters. However, considering some limitations of the clamping block used in the previous experiments (too low stiffness and screws too small to use a torque wrench and thus to have an easily reproducible tightening condition), in the following a new clamping structure is employed to ensure a clamping condition is as ideal as possible. Indeed, in the following tests the PEH is clamped on a custom steel block, shown in Fig. 5.10. Thus, to overcome limitations of the previous constraint system, three central screws passing through holes in the support layer ensure clamping and do not allow any rotation of the lamina, and other two side screws make the clamp more tight. One of the side screw also is used as a terminal for piezoelectric output voltage measurement.

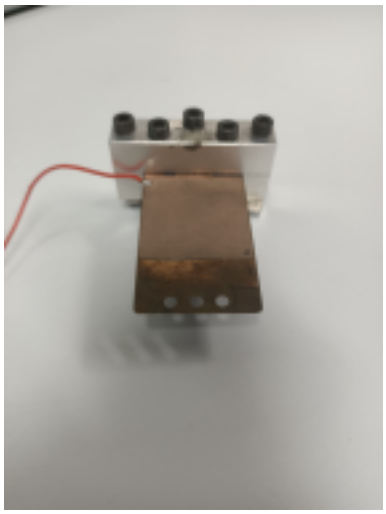

Figure 5.10: Custom clamping structure for the piezoelectric energy harvester.

The device (clamping block plus PEH) is provided with a thread at the vice to directly place it on the head of a shaker (Fig. 5.11), used to produce seismic excitations. The shaker The Modal Shop 2100E11 is controlled through LMS Simcenter Testlab via an amplifier.

Figure 5.11: Experimental setup: PEH with clamping structure positioned on the shaker head. The accelerometer is placed on the clamping end.

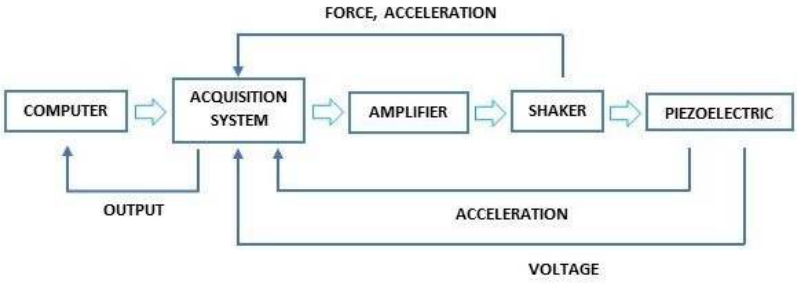

Figure 5.12: Experimental setup block diagram.

The LMS acquisition system collects acceleration and voltage signals, provided by an accelerometer PCB PIEZOTRONICS Model M352C68, placed at the clamping (Fig. 5.11), and by the PEH, respectively. Indeed, being the piezoelectric device directly positioned on the shaker prevents from using a sensing head, that would measure applied force and acceleration output and allow for direct control on the seismic excitation. Thus, to ensure the tests are carried out under the same amplitude, the acceleration measurement is taken as reference, since, though giving as input the same voltage with the amplifier, the shaker excitation varies with frequency. In diagram 5.12 the experimental set-up chain is shown.

5.3.2 Analysis of the yielding clamp

Before comparing experimental data and simulation results, a more accurate characterization of the PEH needed to be done. First, layer characteristics were verified by measuring their weight and dimensions, taking also into account the silver electrodes and the epoxy resins, glueing together piezoelectric and support material. In Tab. 5.6 deduced thicknesses and densities are reported for each layer.

Table 5.6: Experimentally verified thickness and density for each layer of the PEH.

Layer	Material	Thickness $[mm]$	Density $[kg/m^3]$
Support	Harmonic steel	0.27	7850
Piezoelectric	PLZTN	0.18	7800
Electrodes	Silver	0.005	10490
Glue	Epoxy resins	0.19	2000

Other characteristics of the piezoelectric energy harvester are reported in Tab. 5.7.

Table 5.7: Energy harvester parameters.

Parameter	Unit	Value
Support layer		
Length L_s	m	0.0633
Width b	m	0.04
Young's modulus Y_s	Pa	$190 \cdot 10^9$
Poisson's ratio ν_s	-	0.3
Piezoelectric layer		
Length L_p	m	0.04
Width b	m	0.04
Distance from clamping l_1	m	0.0023
Young's modulus Y_p	Pa	$9 \cdot 10^{10}$
Poisson's ratio ν_p	-	0.34
Relative electric permittivity ϵ_{33}	F/m	2400
Piezoelectric coefficient d_{31}	C/N	$-2.1 \cdot 10^{-10}$

In order to provide a better clamping system than the one presented in Sec. 5.2.2, a steel block made of a lower and upper side was build. The screws used are suited to be tightened with a torque wrench, in order to ensure equal and repeatable tightening torques. The clamping was tested to evaluate its effectiveness and possible corrections to describe non ideal boundary conditions in the model (e.g., a yielding clamp), as seen in section 3.2. The device is positioned on the shaker head (Fig. 5.13) and, by randomly tipping on the plate edge, modal frequencies in open circuit conditions (in order to avoid short circuit, that could damage the acquisition system) are measured by recording the voltage output for different clamping torques.

Figure 5.13: Experimental setup for boundary condition test.

A torque wrench was used to know exactly the screws tightness level. Tests were repeated (Table 5.8) for several torque values (1.5, 2.5, and 3.5 $\mathrm{N} \cdot \mathrm{m}$) using different tightening sequences for screw (345, 543, and 453) with screws numbered as shown in Fig. 5.14. The screws 1 and 2 are only used as electric terminals. To reduce uncertainty, each individual test was repeated 3 times. Indeed, by measuring the voltage output during transient vibrations following a small hit on the support layer, resonance frequencies of the first two bending modes are found to vary slightly from one condition to the other, as shown in Figs. 5.15a and 5.15b.

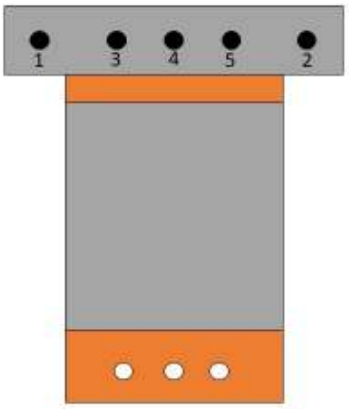

Figure 5.14: Schematic representation of PEH clamping and screws identification by numbers.

Table 5.8: Test matrix for clamping effectiveness verification.

Tightening torque $[\mathrm{N} \cdot \mathrm{m}]$	Tightening sequence	Number of test repetition for each torque value
1.5		3
2.5	345	3
3.5		3
1.5		3
2.5	453	3
3.5		3
1.5		3
2.5	543	3
3.5		3

The mean values (Fig. 5.15) and the max-min oscillation (Table 5.9) of first and second bending modes resonance frequencies, calculated over the data from three repetitions, are reported for different tightening sequences and torques. It can be seen that for a torque value higher than 1.5 $\mathrm{N} \cdot \mathrm{m}$ the clamping effect is the same and one can conclude that perfect clamping BC is closely approximated. However, constraint relaxation in terms of frequency reduction appears for 1.5 $\mathrm{N} \cdot \mathrm{m}$, proving that attention to clamping effectiveness is requested in this case to make results repeatable.

Moreover, data in Table 5.5 confirm that, for higher torques, the tightening sequence has no influence on the measured resonance frequency, while for 1.5 $\mathrm{N} \cdot \mathrm{m}$ there is one sequence (453) providing less repeatable results. The frequency variation is always within the 1.5 % of the mean frequency, proving that the value of applied torque is anyway more relevant than the tightening sequence in affecting the experimental frequency value.

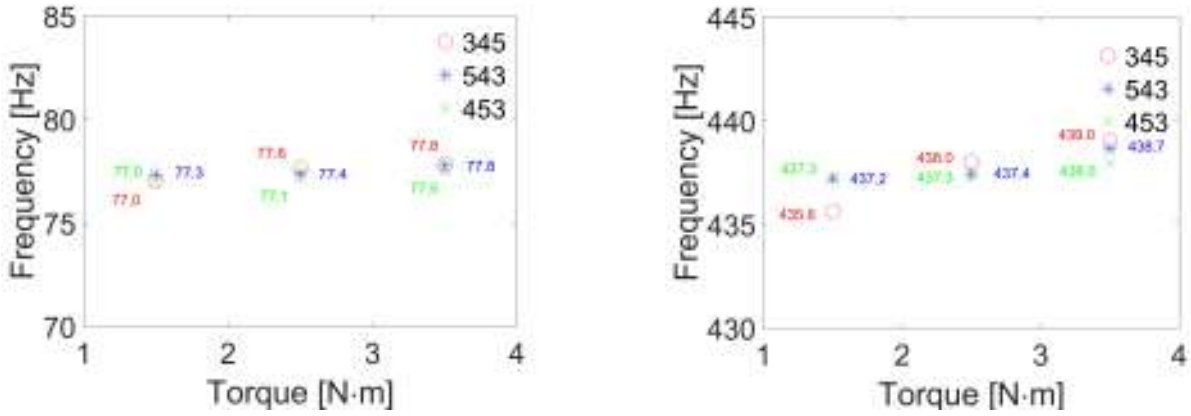

(a) *Mean frequencies for the first bending mode.* (b) *Mean frequencies for the second bending mode.*

Figure 5.15: Resonance frequencies for three different torques (1.5, 2.5 and 3.5 $\mathrm{N} \cdot \mathrm{m}$) for different screw tightening sequence.

Table 5.9: Frequency variation around its mean value for three different torques (1.5, 2.5 and 3.5 $\mathrm{N} \cdot \mathrm{m}$) and for different screw tightening sequences.

Tightening torque $[N \cdot m]$	Tightening sequence	$\Delta f_{1,mean}$ [Hz]	$\Delta f_{2,mean}$ [Hz]
1.5	345	0.1	0.9
2.5		0.7	1.5
3.5		0.5	1.3
1.5	453	2.0	3.3
2.5		0.5	2.1
3.5		0.9	1.2
1.5	543	0.7	2.3
2.5		0.8	1.4
3.5		0.7	1.4

5.3.3 Identification of the structural damping

As the PEH response in resonance conditions is strongly dependent on damping, it is necessary to update these values in the mathematical model. Thus, the PEH damping is experimentally identified and expressed as modal critical damping coefficient ζ_m using the logarithmic decrement method [Daniel J. Inman 2008]. Limiting the analysis to the first two modes, the investigation is carried out also considering the effect of the tip mass, whose dimension and weight are reported in Tab. 5.10.

Table 5.10: Parameters of the three tip mass conditions tested.

Tip mass	Dimensions LxWxh [mmxmmxmm]	Weight [g]
no m_{tip}	-	-
$m_{tip}1$	8.1 x 40 x 5.15	2.6
$m_{tip}2$	9.6 x 40 x 4.1	3.72

The natural frequencies of the structure are first identified by analysing the power spectral density peaks of voltage produced by randomly hitting the support layer. These frequencies are then used to generate a sinusoidal seismic excitation, exerted with the shaker, which was suddenly stopped to induce transient decaying oscillations at the desired frequency. An example of the signal obtained for the first resonance frequency is shown in Fig. 5.16. The logarithmic decrement method, implemented in MATLAB, is then used to calculate the damping ratio, expressed as

$$\zeta_m = \frac{\delta_m}{\sqrt{4\,\pi^2 + \delta_m^2}} \tag{5.2}$$

where the logarithmic decrement δ_m is defined as [Daniel J. Inman 2008]

$$\delta_m = ln \frac{\dot{\lambda}(t)}{\dot{\lambda}(t+T)} \tag{5.3}$$

where, in our case, $\dot{\lambda}$ is filtered voltage signal relative to a certain mode of the structure.

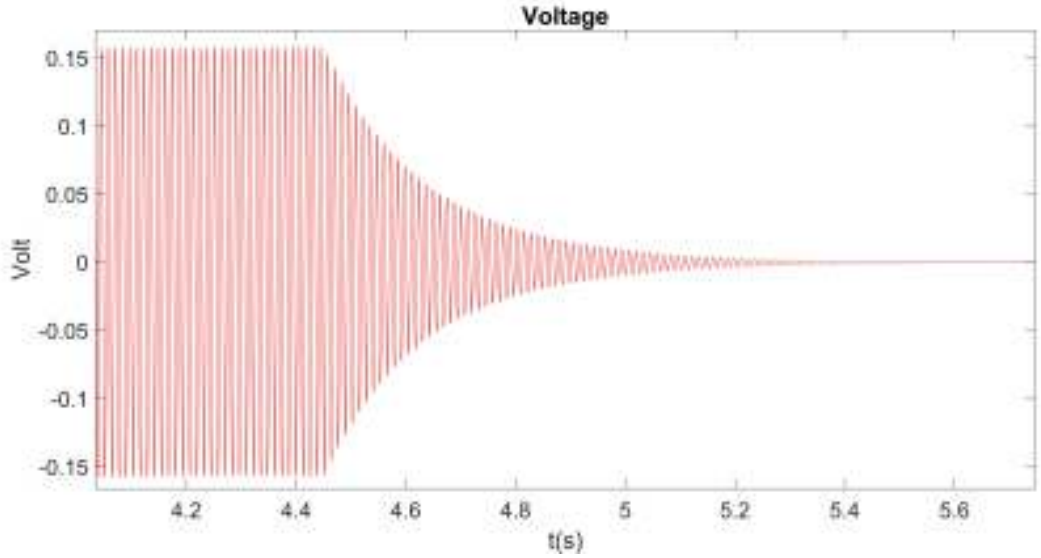

Figure 5.16: Voltage time history for logarithmic decrement method application.

In Tab. 5.11 the natural frequencies, damping rations for the first and second bending modes, and damping coefficients are reported for the three tip mass conditions. For instance, considering the configuration without tip mass, the two damping ratios for the first (76.09 Hz) and second (437 Hz) resonance frequencies are respectively $\zeta_1 = 0.0101$ and $\zeta_2 = 0.0045$. Thus, recalling the generic expression in function of air and structure damping coefficients (Eq. 3.3.2), used in the governing Eq. 3.111 as

$$\zeta_m = 1/2 \left(c_s J \omega_m / \bar{D} + c_a / \mu \omega_m \right), \tag{5.4}$$

it can be found that $c_s J/\bar{D} = 2.2754 \cdot 10^{(-6)}\ s/rad$ and $c_a/\mu = 8.1856\, rad/s$. In the previous equation $c_s J$, $\bar{D}$, ω_m, c_a, and μ are, respectively, the Kelvin-Voigt damping term, the equivalent stiffness, the eigenvalue of the m-th mode, the viscous air damping term, and the equivalent mass per unit of length. In this way, the damping coefficient ratios allow the determination of damping ratios ζ_m for $m > 2$ as well. Analogously, the damping coefficients are found for the first and second tip mass conditions.

Table 5.11: Modal parameters and damping coefficient ratios relative to the considered tip mass conditions.

Tip mass condition	$f_{r,1}$ [Hz]	$f_{r,2}$ [Hz]	ζ_1	ζ_2	$c_s J/\bar{D}$ [s/rad]	c_a/μ [rad/s]
no m_{tip}	76.09	437.0	0.0101	0.0045	$2.2754 \cdot 10^{-6}$	8.1856
$m_{tip,1}$	49.57	325.1	0.0118	0.0069	$5.1310 \cdot 10^{-6}$	6.8569
$m_{tip,2}$	44.88	323.1	0.0243	0.0049	$1.5780 \cdot 10^{-6}$	13.5654

5.4 Linear model validation

In this sections results from tests carried out to validate the numerical model for different resistive load and tip mass conditions are presented. The coefficients of the theoretical model have been updated here with experimental results obtained in the previous section. Thus, a perfect clamping BC and different damping coefficients depending on the tip mass are used. Experiments are set up, as described in Sec. 5.3.2, with the clamping block directly screwed on the shaker head, as shown in Fig. 5.13. An accelerometer is positioned on the clamping to measure the actual acceleration the piezoelectric energy harvester (PEH) is subjected to. Data acquisition for both excitation input and voltage output are collected as described in Sec. 5.3.1.

Tests have been carried out under sinusoidal excitation, with acceleration amplitude kept equal to $5 \cdot 10^{-3}\, g$ in order to avoid non linear piezoelectric behaviour [Erturk and Daniel J. Inman 2011c]. To acquire the transfer function of the PEH, the device was tested for different forcing frequencies. Moreover, voltage output has been measured in open circuit conditions and with two resistive loads of respectively $10^4\,\Omega$ and $10^5\,\Omega$. To better compare numerical and experimental data, results are presented in voltage per unit of acceleration amplitude.

5.4.1 Response analysis without tip mass

In Fig. 5.17 numerical results (lines) and experimental data (squares) for open circuit (OC) condition are shown. In MATLAB, the OC is simulated with high resistive load, $R = 10^6\,\Omega$.

Focusing on the comparison of FRF peaks, the relative difference in resonance frequencies between numerical and experimental results, defined as $\Delta f_j / f_j^{(exp)}$ and shown as a percentage in Table 5.12, is only 0.3 % for the first mode and 1.8 % for the second one. The numerical value of first peak amplitude matches quite exactly the experimental one while the second peak is slightly underestimated ($\Delta A_m / A_m^{(exp)} \simeq -15\%$). The agreement keeps good also outside the FRF peaks, especially for the first mode, highlighting the possibility to evaluate the sensitivity of the response to off-design conditions. As expected, the second mode peak is far lower than that of the first mode, due to charge cancellation phenomenon. Thus, in the case of broad-band excitation, the contribution of the second mode can be disregarded as first approximation. This issue can be solved by electrode segmentation in length, as seen in Sec. 4.3.3, that could thus make the second mode relevant for power production as well.

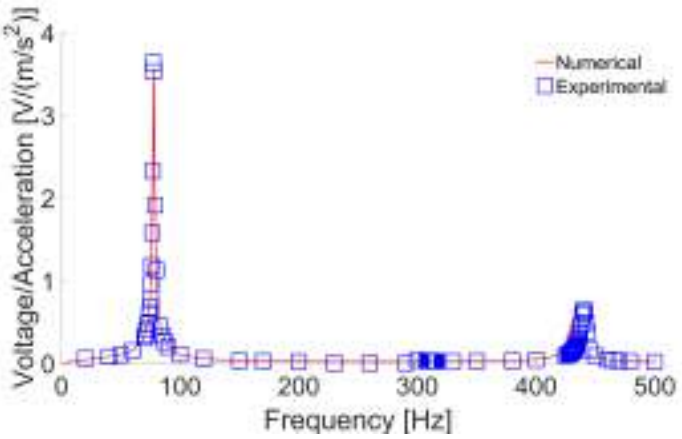

Figure 5.17: Voltage per unit acceleration amplitude for the configuration without tip mass in open circuit conditions.

In Figs. 5.18b and 5.18a similar results have been achieved for closed circuit conditions, for resistive loads of respectively $10^4\ \Omega$ and $10^5\ \Omega$. The first mode peak amplitude is slightly overestimated ($\Delta A_m/A_m^{(exp)} \simeq 15\%$) but the second peak is almost exactly captured. As in the OC condition, the difference between numerical and experimental resonance frequency keeps quite small (1 % for the first mode, 1.8 % for the second mode). This confirms the model as a useful tool to estimate performances of the device, calculated in terms of power in closed circuit conditions. As expected, the load causes a voltage drop with respect to the open circuit condition value. As seen also in Sec. 3.5, resonance frequencies experience a small decrease (up to 0.5 Hz), passing from OC conditions to closed circuit conditions for $R = 10^4\ \Omega$.

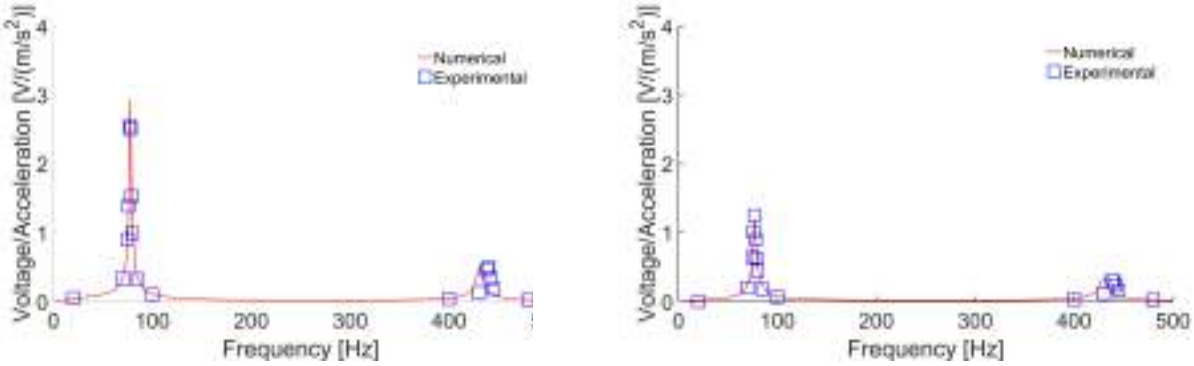

(a) $R = 10^5\ \Omega$.

(b) $R = 10^4\ \Omega$.

Figure 5.18: Voltage per acceleration amplitude for the configuration without tip mass for two different resistive loads.

5.4.2 Response analysis with different tip masses

As seen in previous chapters, a tip mass on the free edge can be useful to tune the resonance frequency of the device with the excitation frequency. For this reason the PEH has been studied with two different tip mass (different from those used in Sec. 5.2.3), whose features are reported in Tab. 5.10. The experimental

setup is the same of the previous tests, but a tip mass is placed at the free end of the device, covering part of the support layer, as shown in Fig. 5.19 for $m_{tip,2}$. Three different circuit conditions were investigated: open circuit ($R = 10^6\,\Omega$), $R = 10^5\,\Omega$, and $R = 10^4\,\Omega$. These numerical results are compared with experimental data and the no-tip mass condition, already analysed of the previous paragraph.

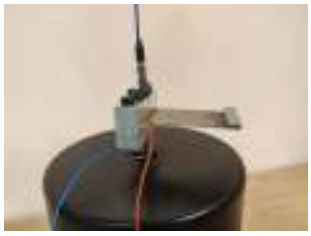

Figure 5.19: Experimental setup with tip mass on the free edge.

In Fig. 5.19 the open circuit condition results are shown. There is a satisfactory agreement between predicted and experimental resonance frequencies, with differences of less than 5 % for the first mode and of 2 % for the second mode with reference to both mass values. Moreover, the agreement with experimental results in terms of FRF amplitudes can be considered satisfactory as well. As expected, the tip mass lowers in a relevant way both first and second mode resonance frequency, but, as previously underlined in Sec. 3.3.3, its effect has a limited frequency range. Indeed, when passing from $m_{tip,1}$ (16 % of PEH mass) to $m_{tip,2}$ (38 % of PEH mass), the resonance frequency decrease is not as relevant as it is from no-tip mass to $m_{tip,1}$ configuration, as expected from simulation results [Laura et al. 1975]. Moreover, although a tip mass is commonly considered enhancing oscillation amplitude, results show this is not necessarily true. Indeed, when a certain threshold is reached, the total mass of the system increases and, consequently, the damping too (Tab. 5.11), but without a correspondent rise in oscillation amplitude. In this condition the voltage output drops, as shown for the $m_{tip,2}$ configuration. Finally, it is worth noting that the frequency decrease for the second mode is more relevant in absolute terms than for the first one. This fact suggests the tip mass could also be useful to create a wider band gap for a device with initial first and second modes sufficiently close to each other.

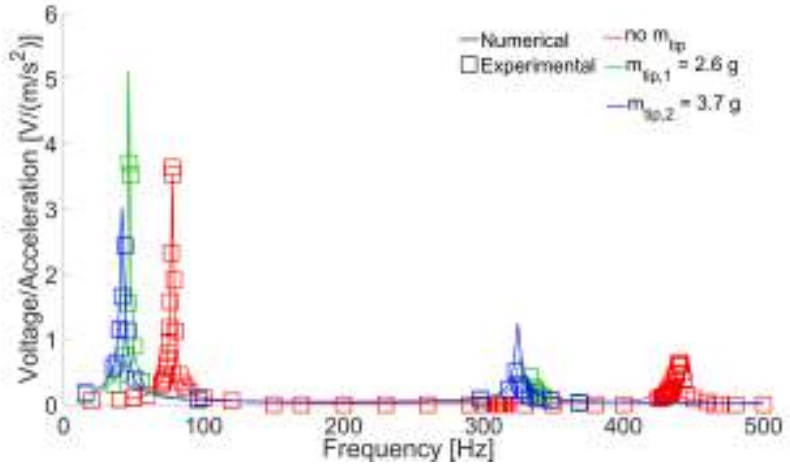

Figure 5.20: Voltage per acceleration amplitude with (2 cases) and without tip mass in open circuit condition.

As for the no-tip mass configuration, closed circuit conditions have been investigated for two different resistive loads: $R = 10^5\,\Omega$, shown in Fig. 5.21a, and $R = 10^4\,\Omega$, shown in Fig. 5.21b. The enhanced oscillation amplitude, caused by a proper tip mass condition $m_{tip,1}$, brings to a first mode voltage output almost twice the one of the two other configurations (Fig. 5.21a). Conversely, it is obvious that $m_{tip,2}$ does not produce any oscillation enhancement, having higher damping and thus providing a power output even lower than the no-tip mass configuration. For this reason it is evident that the only advantage of adding $m_{tip,2}$ over the no-tip mass condition could be in frequency tuning for a specific vibration excitation, in case any other parameter of the device (*i.e.*, length, thickness, width, materials) could not be changed.

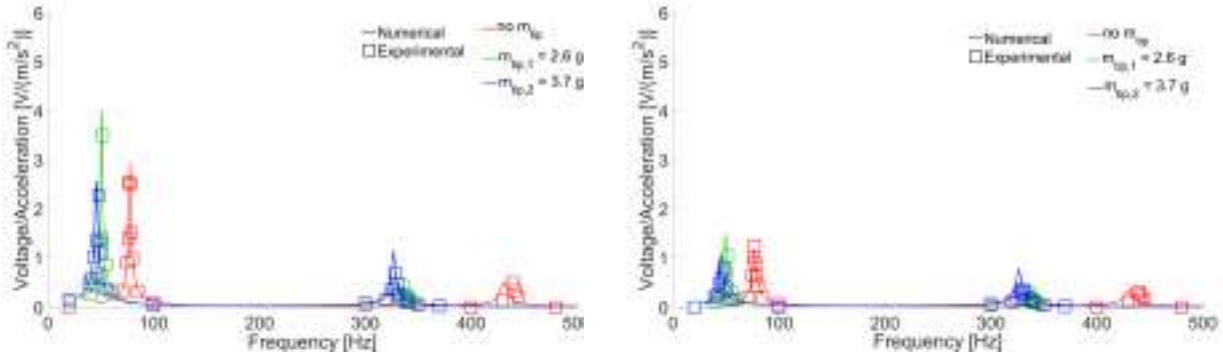

(a) $R = 10^5\,\Omega$.

(b) $R = 10^4\,\Omega$.

Figure 5.21: Voltage per acceleration amplitude with (2 cases) and without tip mass for two different resistive loads.

Table 5.12: Percentage difference between numerical results and experimental data in terms of resonance frequency for different tip mass and resistive load conditions.

Tip mass condition	$R = 10^6\,\Omega$		$R = 10^5\,\Omega$		$R = 10^4\,\Omega$	
	$\Delta f_1/f_1\%$	$\Delta f_2/f_2\%$	$\Delta f_1/f_1\%$	$\Delta f_2/f_2\%$	$\Delta f_1/f_1\%$	$\Delta f_2/f_2\%$
no m_{tip}	0.3	-1.8	1.0	-1.8	0.3	-1.8
$m_{tip,1}$	-0.9	-1.9	-2.7	-1.9	-3.6	-1.9
$m_{tip,2}$	-4.7	0.5	-4.7	-0.4	-6.6	-1.0

Table 5.13: Comparison of predicted and experimental resonance frequencies for different tip mass and resistive load conditions.

Tip mass	$R = 10^6\,\Omega$				$R = 10^5\,\Omega$				$R = 10^4\,\Omega$			
	f_1		f_2		f_1		f_2		f_1		f_2	
	num	exp	num	exp	num	exp	num	exp	num	exp	num	exp
no m_{tip}	77.7	77.5	431.9	440.0	77.7	77.0	431.9	440.0	77.0	77.0	431.9	440.0
$m_{tip,1}$	50.6	51.0	328.6	335.0	50.6	52.0	328.6	335.0	50.0	52.0	328.6	335.0
$m_{tip,2}$	45.8	48.0	326.7	325	45.8	48.0	326.7	328.0	44.9	48.0	326.7	330.0

Following the previous experimental validation, the ROM is finally used to predict the power performance of device. In Fig. 5.22 the power output for acceleration amplitude of 1 $\mathrm{m/s^2}$ is shown for several values of the resistive load. The maximum performance of the device occurs at the resonance frequency of the first mode for $R = 10^4\,\Omega$, a value close to the impedance matching condition, generating 0.2 mW. For the second resonance frequency, the peak value of 0.03 mW is obtained for $R = 10^3\,\Omega$. It is worth noting that the resonance frequencies vary depending on the resistance, with differences of about 1 Hz for the first mode and 3 Hz for the second mode passing from OC and low-resistance circuit condition. The shown dependence of both power output and mechanical behaviour on the electric load confirms how relevant a proper description of the electromechanical coupling is.

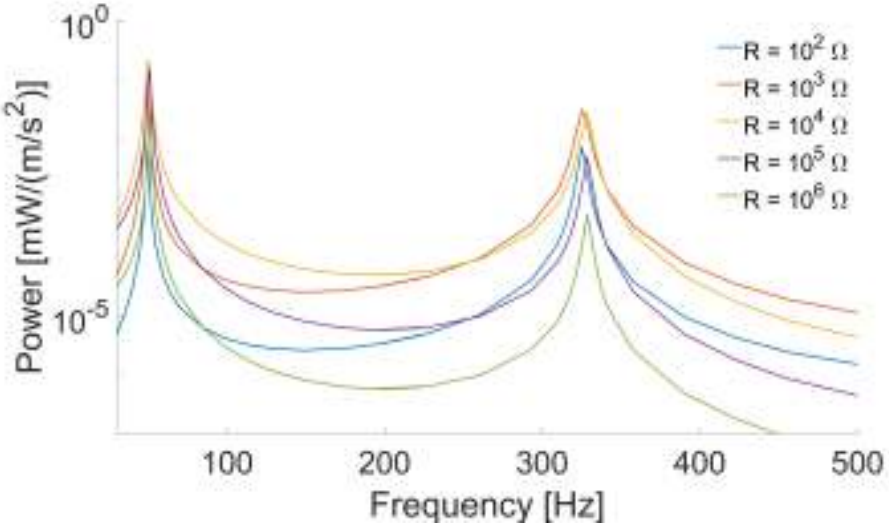

Figure 5.22: Power per acceleration amplitude for $m_{tip} = m_{tip,1}$ for different electric loads.

Chapter 6

Device optimization for performance improvement

6.1 Introduction

In this chapter an overview of the extent at which some mechanical and electrical parameters influence the power output of the piezoelectric energy harvester is given. This goal is not reached directly performing a sensitivity analysis; it is obtained as a by-product of the attempt of optimizing the device leveraging the mechanical configuration and electric system features. The PEH electromechanical system subjected to optimization is considered in two configurations: the one taken into account in Chapter 3, with only a resistive load connected, and the one with the FBR interposed between the PEH and the load (Chapter 4). Considering both configurations will show how different equivalent impedances affect the optimization results. As design parameters, the distance of the piezoelectric patch from the clamping and its length are assumed.

Thus, the FBR capacitance is considered, finding the best sizing to perform signal filtering, and showing how minimizing the voltage ripple leads to better performance of the converter. Moreover, the active control for impedance matching with a Buck-Boost (BB) converter is performed, comparing the optimized duty cycle with the one calculated with Maximum Power Point Tracking (MPPT) logic. In order to improve the control circuit performance, the capacitance sizing will be studied again to provide a storage function besides the filtering one considered previously, and, thus, allowing for a better coupling with the BB inductor.

Finally the distance from the clamping and the capacitance will be taken into account jointly, proving that a coupled optimization is fundamental to improve the overall performance of the PEH system, and thus proving the effectiveness of the holistic approach presented in this work.

6.2 Constrained optimization and *Patternsearch* solver

An optimization process aims to improve a merit function (*objective function*), by changing some of the problem parameters (*design variable*). Indeed, the optimization goal is to maximize or minimize the objective function inside a defined domain A, called *search space* or the *choice set*, in which the feasible solution of the problem will be found. To define the search space A a series of conditions on the design variables are imposed, defined as *inequality constraints* (inequality conditions, such as material limits or device dimensions) or *equality constraints* (equality conditions, such as balance of forces or energy).

In general, a minimization problem can be defined as [Haftaka et al. 1992]

$$\begin{aligned} &minimize && f(\boldsymbol{x}) \\ &such\,that && g_i(\boldsymbol{x}) \geq 0, \quad i = 1, ..., n_g \\ & && h_k(\boldsymbol{x}) = 0, \quad k = 1, ..., n_e \end{aligned} \tag{6.1}$$

where $\boldsymbol{x}$ is the vector of design variables, $f(\boldsymbol{x})$ is the objective function, $g_i(\boldsymbol{x})$ are the inequality constraints, and $h_k(\boldsymbol{x})$ the equality constraints. Usually an optimization is defined as a minimization problem, since the maximization can be obtained by minimizing the negative of the function. If the design variables are only subjected to bounds and are not related to each other in other ways, a more simple constraint definition can be used in the form of parameter bounds

$$\boldsymbol{x_l} \leq \boldsymbol{x} \leq \boldsymbol{x_u} \tag{6.2}$$

where $\boldsymbol{x_l}$ and $\boldsymbol{x_u}$ are respectively the upper and lower bound vectors.

When both objective function and constraints are defined as linear functions, the problem is known as *Linear Programming* problem, but if non-linearities are present then the *Nonlinear Programming* problem should be addressed. Moreover, the optimization can be carried out on a *local* or *global* basis, finding respectively local or global minima of the objective function. Indeed, the objective function could have more *basins of attraction*, regions in which for any given initial condition a unique minimum is found, as shown in Fig. 6.1.

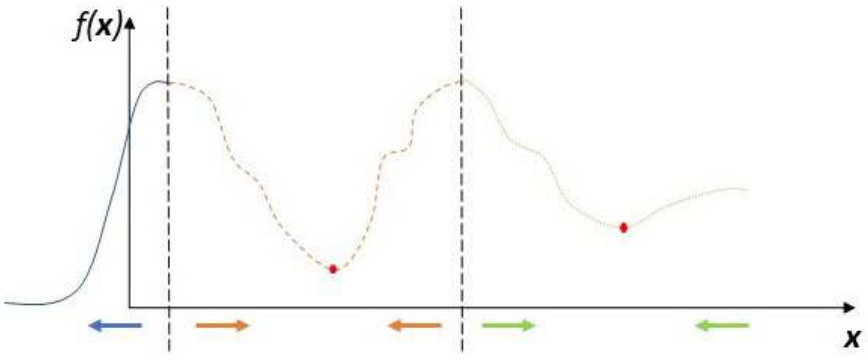

Figure 6.1: Basins of attraction for a generic objective function $f(\boldsymbol{x})$.

Thus, depending on the initial condition given to the solver, a different solution can be found, being

a local minimum, but not necessarily the global minimum of the problem. If one wants to search for the global minimum, then the starting point condition has to be investigated first, running the optimization problem with a regular grid of initial points inside the boundaries defined for the design variables.

Thus, depending on what the optimization goal is, a different solver should be chosen depending on non-linearities and variables constraints. Considering that our problem is non-linear and stiff due to the presence of time varying circuit elements (diodes and switches), the Matlab Global Optimization Toolbox guide suggests the *patternsearch* algorithm, suitable for non-smooth problems. Although less efficient than gradient-based solvers, *patternsearch* is provably converging on a wide range of problems, and thus reliable. At the beginning, *patternsearch* runs for a certain number of points in the neighbourhood of the initial condition given and, if some of them are found to belong to different basins, it looks in more basins at the same time, although not ensuring that no other minima exist outside that area. Thus, if interested in a global solution, *patternsearch* has to be run initially with multiple starting points distributed on the design variable domain.

To find the solution, the optimization algorithm defines a set of fixed-direction vectors (*pattern*), depending on the design-space dimension, usually coinciding with unit basis vectors [Audet et al. 2002] [Conn et al. 1997] [Lewis et al. 2006]. At each step, those vectors are multiplied by a scalar (*mesh size*), evaluating the objective function in the new positions and comparing their values to the current point. If a new minimum is found, the *poll* is called *successful*, becoming the point for the next iteration, and the mesh size is doubled. Otherwise the poll is *unsuccesful* and at the next iteration the point stays the same, but the mesh size is reduced to a half. Although the mesh size is treated as previously described, *patternsearch* modifies the point to always stay inside the constrained boundaries. The run stops when, after a successful poll, the change in both objective function and mesh size is less then the tolerance set.

The objective function that will be used in the following simulations is the power output, expressed in mW and found by making the resistive load vary from a minimum of $100\,\Omega$ to a maximum of $10^6\,\Omega$. Obviously, this can lead to different maximum resistive loads for different design variables values, and this will be evaluated in the following.

6.3 Optimization on tructural parameters

First, the device performances are improved by modifying the mechanical layout, that is, the value of two geometrical parameters of the PEH: the distance from the clamping l_1 and the piezoelectric patch length L_p, shown in Fig. 6.2.

Figure 6.2: PEH configuration with its geometrical parameters.

The investigated configuration does not include a tip mass. The harmonic acceleration amplitude con-

sidered to calculate the power output is the same used in Chap. 4, equal to 0.06 g, and its frequency is the natural frequency of the PEH first bending mode. As said before, the *patternsearch* algorithm is employed to find their optimum value. Regarding the electric circuit downstream the piezoelectric, two configurations are studied:

- PEH connected to a resistive load, denoted as S1 in the following. The power output is calculated as ratio between the square of the peak voltage over the resistive load

$$P_{S1} = \frac{\dot{\lambda}_{peak}^2}{R} \tag{6.3}$$

  which gives an indication of the possible output in DC.

- PEH connected to the full bridge rectifier, named S2 in the following. The power output is calculated as root mean square of the instantaneous power $p(t_n)$ sampled at t_n time instants over the resistive load

$$P_{S2} = P_{rms} = \sqrt{\frac{1}{N}\sum_{n=1}^{N} |p(t_n)|^2} \tag{6.4}$$

  where N is the number of time steps. This power definition will be used also for the MPPT optimization.

In both configurations the power is calculated in stationary conditions, after the transient phase is over. The power is calculated in mW and thus the maximum tolerance set for *patternsearch* is 10^{-4}, considering a difference of less than μW not significant. Moreover, the FBR capacitance sized as

$$i_0 = C_R \frac{\partial V_0}{\partial t} = C_R \frac{\Delta V_0}{T} \Rightarrow C_R = \frac{V_0}{R \Delta V_0 f_r} \tag{6.5}$$

were R is the resistive load, V_0 and ΔV_0 are the required voltage and the admissible ripple and f_r is the frequency of the circuit, provided by the excitation source. Thus, the capacitance depends on the PEH resonance frequencies, and, consequently, the impedance matching point is expected to change too. It is worth to underline that the FBR is likely to produce enhancement of the model instability, because of the strong non-linearity of the circuit. This instabilities may appear only for particular combinations of the piezoelectric parameters, unpredictably chosen by the *patternsearch* algorithm. This behaviour is well known in technical literature, as also underlined for instance by Manzoor *et al.* [Manzoor et al. 2017]. A remedy is setting a one-way coupling between the mechanical system and the conversion circuit, *i.e.*, imposing the FBR current not participating in the piezoelectric effect on the structure; even if underestimating the output power, as shown in Fig. 6.3. Moreover, a shift in the optimal resistive load occurs, since the structure behaves as the equivalent capacitance relevant for the matching is only the piezoelectric one C_p. Although the peak is underestimated and shifted, the optimization in S2 configuration will show comparatively different results with respect to the resistive load configuration, underlying the importance of a realistic description of the problem.

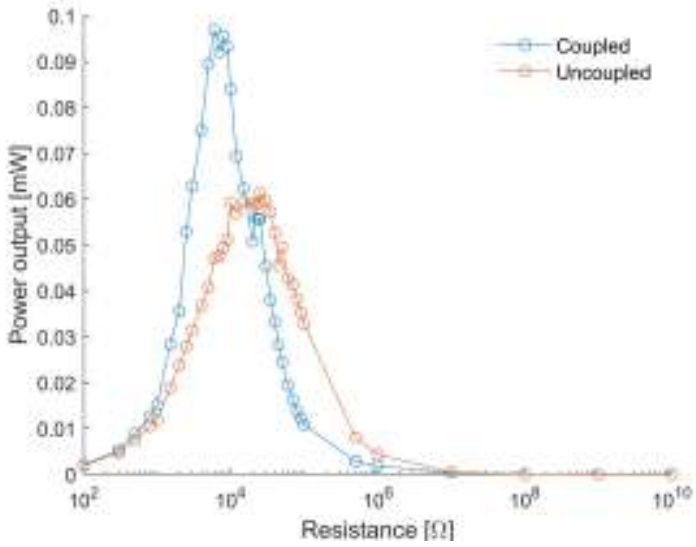

Figure 6.3: Power output comparison between the coupled and uncoupled model of the PEH and FBR system.

First, with the only resistive load connected to the PEH, the convergence of *patternsearch* is investigated for different initial conditions, showing how the algorithm gives reliable solutions. Then the best initial condition is used to perform an optimization of the parameter in the FBR configuration and results are compared with the previous ones.

6.3.1 Piezoelectric patch distance from clamping

The influence of distance l_1 from the clamping is investigated in the following. To avoid the patch is moved with one edge beyond the supporting structure, the design variable l_1 is constrained by upper and lower boundaries of 25 mm (piezoelectric patch reaching the free end) and 0 mm (piezoelectric patch attached to the clamping point), respectively. In the *patternsearch* call, the mesh tolerance imposed is 10^{-4} considering values under 0.1 mm not relevant in a real life design.

To avoid stopping the search at local minima the *patternsearch* routine, running on S1 case, is started for a set of different initial conditions, distributed between the limits. In Fig. 6.4 the final objective function maximum is plotted in function of the optimized design variable. Different initial conditions lead to similar output power values, but some difference exists in the optimal points, with $3.7\,mm < l_1 < 4.6\,mm$ ($l_1 = 3.7\,mm$ in the original configuration), showing that the curve has a flat behaviour around the maximum. At first glance, this result seems to point out we can get almost the maximum power output even with a not precise technique for piezoelectric patch positioning on the support layer.

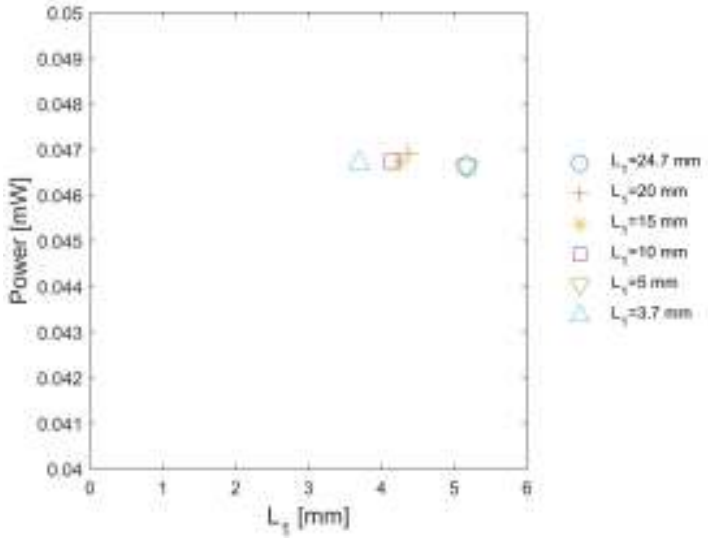

Figure 6.4: Dependence of the optimum patch distance on initial conditions imposed to the *patternsearch* algorithm.

In Fig. 6.5 the intermediate optimization steps for the S1 (circles) and S2 (squares) configuration are compared, with *patternsearch* starting from the same initial condition of 20 mm. It is evident how the two configurations reach the optimum power condition for different resistive loads. Indeed, by introducing the FBR, the total equivalent capacitance of the circuit decreases and thus the impedance matching occurs for an higher resistive load. Moreover, the optimal distance from the clamping changes too, reaching almost zero for the FBR configuration. Thus, optimizing the PEH parameters without taking into account the correct circuit ahead leads to relevant changes in results.

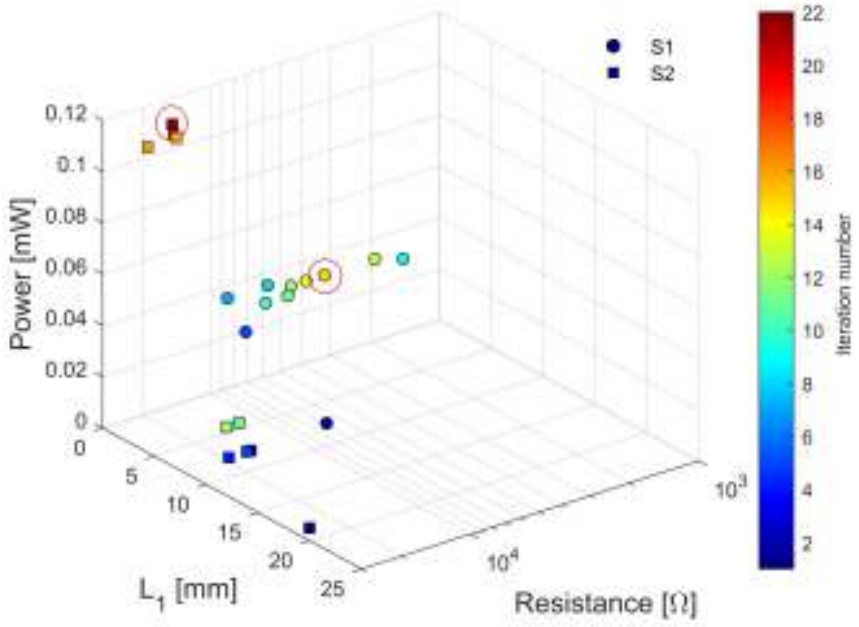

Figure 6.5: Power output comparison for optimization of the distance from the clamping with the PEH connected to a resistive load (circles) or to the FBR (squares).

Table 6.1 summarizes input and output for optimization of both S1 and S2 configurations.

Table 6.1: Summary Table of the l_1 optimization.

Configuration	Fixed parameters	Design variable	Design variable constraints [mm]	Optimized design variable [mm]	Objective function P_{Si} [mW]	Correspondent resistance $[k\Omega]$
S1	L_p, C_R	l_1	0 - 25	4.3	0.047	5
S2	L_p, C_R	l_1	0 - 25	0.4	0.11	15

6.3.2 Length of the piezoelectric patch

This time fixing the parameter l_1, the length L_p of the piezoelectric patch which maximizes the power is investigated as well. Upper and lower limits need to be also set for L_p. These are set equal, respectively, to 10 mm, considered as minimum value to make a comparison with the initial length of 40 mm, and 61 mm, representing the piezoelectric patch covering the entire support layer except for the distance from the clamping (3.7 mm). The mesh tolerance imposed is 10^{-4} considering values under 0.1 mm not relevant in a real life design.

As in the previous section, the algorithm reliability and the presence of possible local minima are investigated by running *patternsearch* on the S1 configuration for a set of different initial conditions, spanning the interval of admissible values. In Table 6.2 the final objective function maxima are reported along with the design variable. The optimal condition is found close to the upper boundary as expected; more piezo-

electric material is used, more charge is produced. Small differences in the final values of the design and objective variable depend on the imposed algorithm tolerances.

Table 6.2: Study of *patternsearch* output for different initial conditions.

Initial L_p mm	P_{S1} mW	Optimal L_p mm
10	0.0541	60.7
20	0.0538	60.0
30	0.0539	60.3
40	0.0541	60.5
50	0.0541	60.7
61	0.0540	60.1

In Fig. 6.6 the optimization steps for the S1 (circles) and S2 (squares) configuration are compared, with *patternsearch* starting from the same initial condition of 40 mm. As also seen in the previous section, it is evident how the two configurations have optimum power for different combinations of the resistive load and piezoelectric patch length. Indeed, by introducing the FBR, the total equivalent capacitance of the circuit decreases and thus the impedance matching occurs for a higher resistive load. However, at the same time, the impedance matching criterion forces the optimization algorithm to find the most suitable C_p for the circuit rather then the maximum charge production, resulting in a final length of 36 mm. Thus, also in this problem, optimizing the PEH parameters with different conversion circuits ahead leads to relevant changes in results, and the more realistic solution (S2) should be preferably considered.

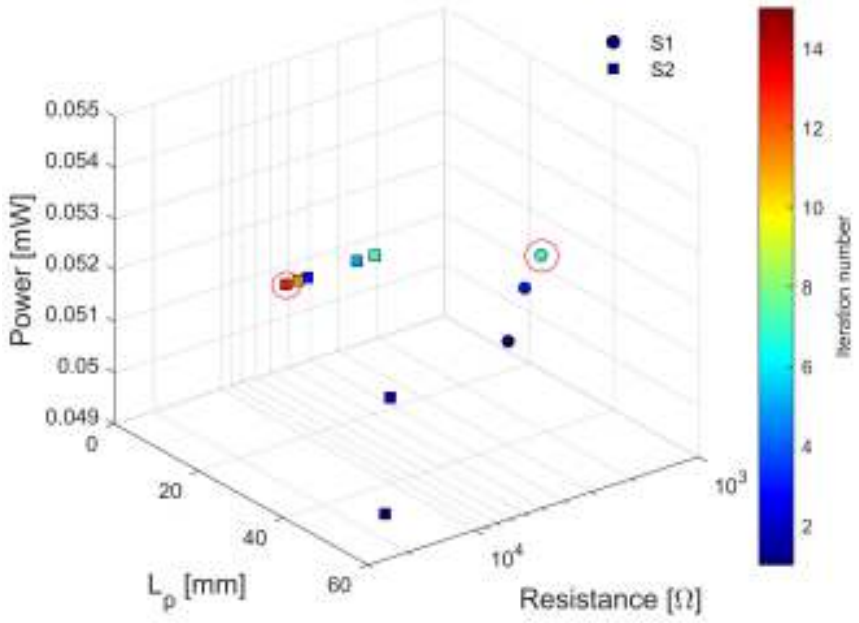

Figure 6.6: Power output comparison for optimization of the piezoelectric patch length with the PEH connected to a resistive load (circles) or to the FBR (squares).

Table 6.3 summarizes input and output for optimization of both S1 and S2 configurations.

Table 6.3: Summary Table of the L_p optimization.

Configuration	Fixed parameters	Design variable	Design variable constraints [mm]	Optimized design variable [mm]	Objective function P_{Si} [mW]	Correspondent resistance [$k\Omega$]
S1	l_1, C_R	L_p	0.1 - 61	60.7	0.054	5
S2	l_1, C_R	L_p	0.1 - 61	36.3	0.053	25

6.4 Optimization on full bridge rectified capacitance

A correct sizing of the FBR capacitance C_R is fundamental for system performance and output DC signal filtering. Although an approximated sizing can be done with Eq. 6.5, in Chap. 4 C_R inefficiency in providing adequate power output to higher loads was reported. Thus, the optimization can be useful to find a suitable value of the capacitance for a PEH device, as a compromise between short charge time and required power output. Therefore, the capacitance is assumed as unique design variable. For this reason the simulation time is set to 20 s, sufficient to not only overcome the transient, but also large enough to allow for charging of higher capacitances. In order to be consistent with the previous section, the simulation is run with the one-way piezoelectric coupling, although the model is less sensitive to FBR capacitance changes rather than to structural parameters variation. The harmonic acceleration amplitude is equal to 0.06 g, with

excitation frequency set to the resonance one of the PEH first bending mode. The objective function is the power output calculated in mW as rms value of the instantaneous power, as reported in Eq. 6.4.

Two PEH configurations are investigated: the first (S2) is the one used in the previous section, comprehensive of PEH and FBR, the second ($S2_{opt}$) is equal to S2, but has a distance from the clamping l_1 equal to the optimum value found in Sec. 6.3.1 (0.4 mm). By sizing the capacitance according to Eq. 6.5, S2 and $S2_{opt}$ would have C_R values equal to 7 μF and 6 μF, respectively, very close to each other. The first of these value is set as initial conditions for the iterations. Both simulations are run limiting the capacitance between 10^{-1} and 10^4 the initial C_R values.

In Fig. 6.7 the optimization steps for the S2 (circles) and $S2_{opt}$ (squares) configuration are compared, with initial condition of $C_R = 7\,\mu F$. It can be noted that $S2_{opt}$ has a power output almost double the S2 one, although its optimal capacitance is one orders of magnitude smaller. Thus, not only a complete model of the energy harvesting circuit provides more accurate optimization of structural parameters, but it is also fundamental to properly size the circuital elements, improving efficiency with lower capacitance and, consequently, sizes.

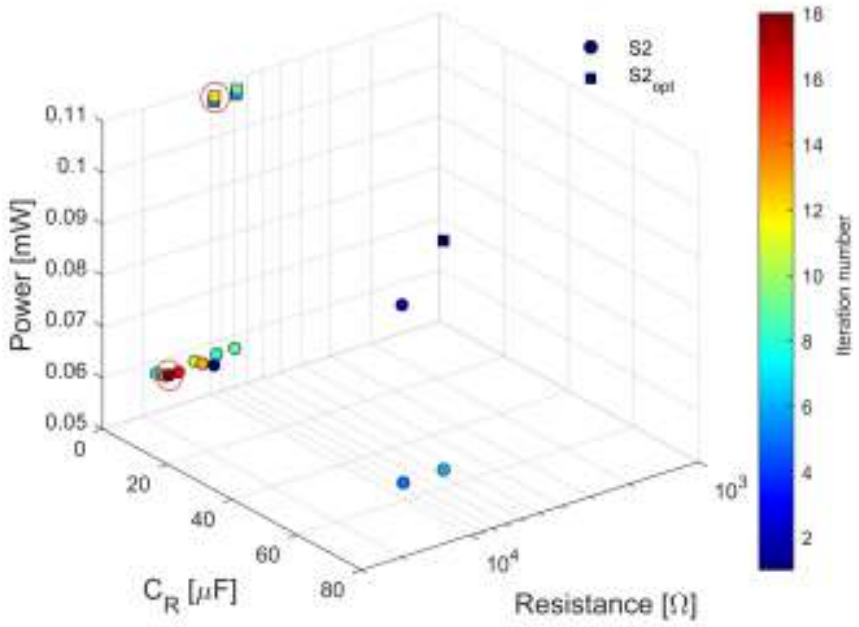

Figure 6.7: Power output comparison for optimization of the FBR capacitance with the distance from the clamping being 3.7 mm (circles) or to 0.4 mm (squares).

Although until now the FBR capacitance was only considered for filtering purposes, in Section 4.2.2 it was pointed out that the PEH cannot efficiently supply higher power-demanding loads, and, thus, the capacitance exhibit a periodic deep charge-discharge cycle, with consequent increase in voltage ripple. For this reason it is important to investigate the role of the FBR capacitance also as storage element. Therefore, a new optimization was performed ($S2_{storage}$), with the same S2 configuration, but for longer simulation time (100 s instead of 20 s), to reach full charge even for higher capacitance values. In Fig. 6.8 is shown that

the optimized storage capacitance can provide an higher amount of energy instantaneously, with a power output double the one of the optimal capacitance for a charging time of 20 s. However, it must be taken into account that higher capacitance values mean also higher volumes of the device. Moreover, the maximum charging time should be set also considering the sample time of the powered electronic device.

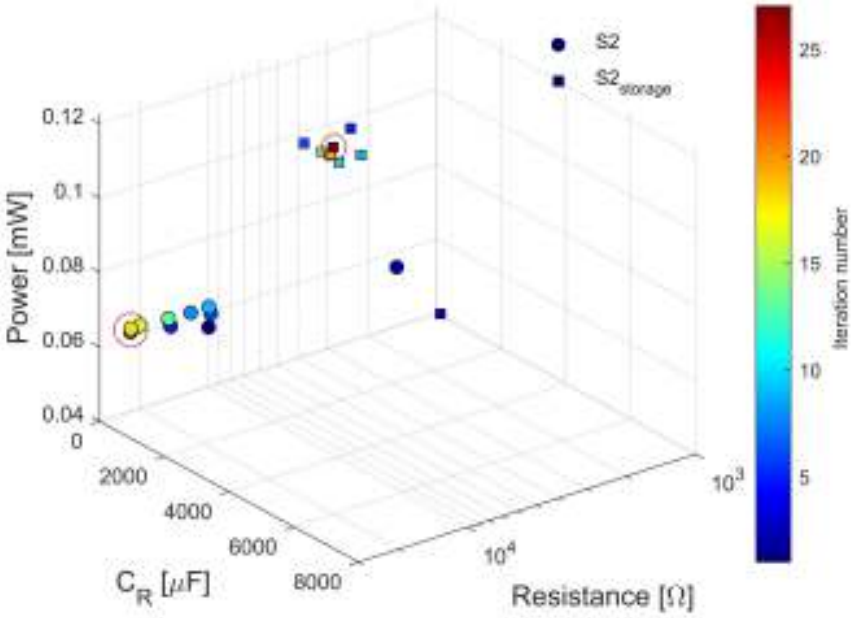

Figure 6.8: Power output comparison for optimization of the FBR capacitance for a charging time of 20 s (circles) and 100 s (squares).

Table 6.4 summarizes input and output for all the performed optimization of the FBR capacitance.

Table 6.4: Summary Table of the C_R optimization.

Configuration	Fixed parameters	Design variable	Design variable constraints $[\mu F]$	Optimized design variable $[\mu F]$	Objective function P_{Si} [mW]	Correspondent resistance $[k\Omega]$
S2	l_1, L_p	C_R	0.7 - 7 · 10^4	11.0	0.06	22
$S2_{opt}$	l_1, L_p	C_R	0.6 - 6 · 10^4	0.96	0.11	10
$S2_{storage}$	l_1, L_p	C_R	0.7 - 7 · 10^4	3.8·10^3	0.12	10

6.5 Final remarks on optimization results

In Table 6.5 all the optimization cases are summarized. The first important result is how the system performance is improved if the conversion circuit model is included. Indeed, although the one-way coupling hypothesis has been introduced, the power output is doubled by the conversion circuit for both l_1

and L_p optimization cases, the latter with an S2 configuration performing as S1 but with half the patch length. Thus, designing a PEH without taking into account the FBR interaction leads to underestimate power output. Moreover, the optimal resistance, for which the impedance matching occurs, changes too, reaching higher values due to a different equivalent capacitance of the system. This means that if the PEH was designed in configuration S1, then the real impedance matching conditions would be missed in the application, resulting in far lower power outputs. Therefore, the structural parameters optimization highlights that the comprehensive model is fundamental to understand the PEH efficiency and to predict the future optimal working conditions of the device. In general, the capacitance should be sized by taking into account the required power and the space and time constraints (maximum volume of the device, load sample time). However, by jointly optimize the PEH design variables and the FBR capacitance, a compromise between energy storage and size can be found. Indeed, cases 4 and 6 point out that the holistic approach can lead to more efficient material use for both piezoelectric patch and FBR capacitance, showing that size reduction is possible without compromising on power output.

Table 6.5: Summary Table of all optimization problems.

Case	Configuration	Fixed parameters	Design variable	Optimized design variable	Objective function P_{Si}	Correspondent resistance
1	S1	L_p, C_R	l_1	4.3 mm	0.047 mW	5 $k\Omega$
2		l_1, C_R	L_p	60.7 mm	0.054 mW	5 $k\Omega$
3	S2	L_p, C_R	l_1	0.4 mm	0.11 mW	15 $k\Omega$
4		l_1, C_R	L_p	36.3 mm	0.053 mW	25 $k\Omega$
5	S2	l_1, L_p	C_R	11.0 μF	0.06 mW	22 $k\Omega$
6	$S2_{opt}$	l_1, L_p	C_R	0.96 μF	0.11 mW	10 $k\Omega$
7	$S2_{storage}$	l_1, L_p	C_R	3.8 mF	0.12 mW	10 $k\Omega$

6.6 Active circuits for load-adapting energy production

6.6.1 Introduction

As previously mentioned, the impedance matching phenomenon can be exploited to maximize the efficiency of the device, varying R (*i.e.*, the voltage required by the load) during the energy harvesting process. To reach this optimum efficiency condition, a DC/DC converter, with duty cycle d provided by a Maximum Power Point Tracking logic unit (MPPT), must be added to the power conversion system as shown in Fig. 6.9.

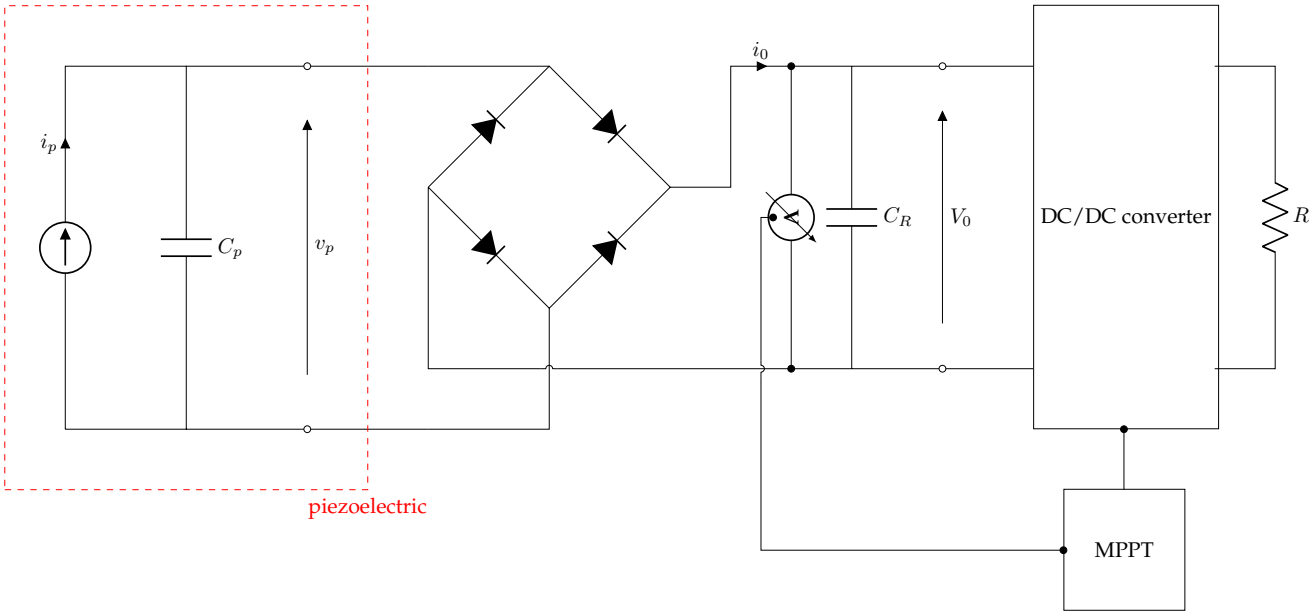

Figure 6.9: Maximum Power Point Tracking system.

The logic unit detects the condition at which the piezoelectric device works, due to the external excitation, and adjusts it thanks to the DC/DC converter, setting the voltage at the maximum power point condition. The DC/DC converter is supposed to be a buck - boost converter and will be presented in the next section.

6.6.2 DC/DC converter: Buck-Boost theory

Electrical model

The buck - boost converter is a DC/DC converter able to both increase and decrease a DC input voltage, while keeping the overall power constant (despite small internal losses). The circuit, shown in Fig. 6.10, is constituted by a switch, a diode, an inductor, and a capacitance. The switch is controlled by an external logic signal imposing a duty cycle or switching signal d.

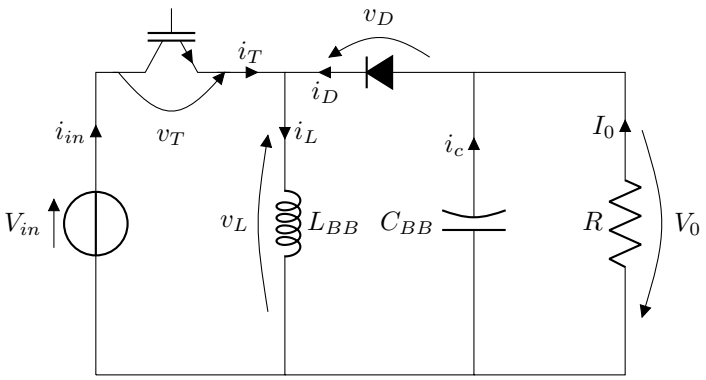

Figure 6.10: Buck - boost converter circuit.

In order to understand its behaviour, mesh and nodes equations can be written by applying Kirchhoff's laws.

$$V_{in} = v_T + v_L \tag{6.6}$$

$$V_0 + v_L = v_D \tag{6.7}$$

$$i_T + i_D = i_L \tag{6.8}$$

$$i_D = i_c + I_0 \tag{6.9}$$

where subscripts refer to parameters relative to the voltage source (in), the transistor (T), the inductance (L), the output (0), and the diode (D). When the switch is in *on* condition (Fig. 6.11), the previous equations become

$$v_T = 0 \tag{6.10}$$

$$v_L = V_{in} \tag{6.11}$$

$$v_D = V_{in} + V_0 \tag{6.12}$$

$$i_L = i_T = i_{in} \tag{6.13}$$

$$i_D = 0 \Rightarrow i_c = -I_0 \tag{6.14}$$

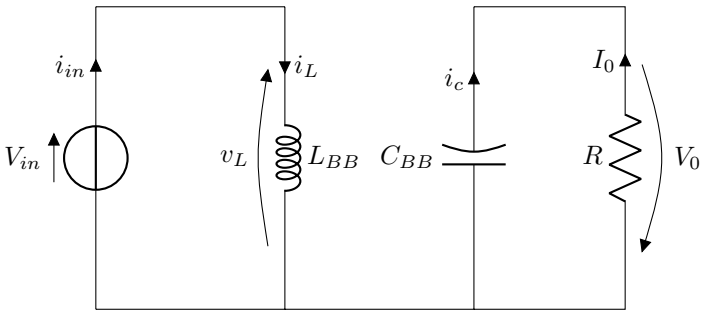

Figure 6.11: Buck - boost converter circuit with switch ON.

Equation 6.12 shows that the diode is reverse biased, and so it is equivalent to an open circuit. The load is completely powered by the capacitance (6.14) and the input voltage charges the inductance (6.13).

During the *off* state of the switch (Fig. 6.12), circuit equations become:

$$i_T = 0 \tag{6.15}$$

$$v_D = 0 \tag{6.16}$$

$$v_T = V_{in} + V_0 \tag{6.17}$$

$$v_L = -V_0 \tag{6.18}$$

$$i_D = i_L > 0 \tag{6.19}$$

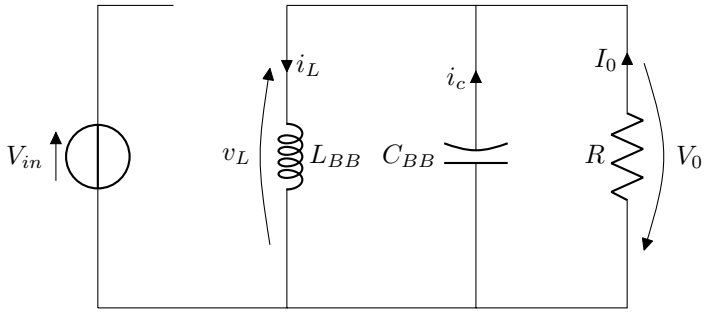

Figure 6.12: Buck - boost converter circuit with switch OFF.

The diode now conducts (Eq. 6.19), then it is equivalent to a short circuit. The inductance powers the load and charges the capacitance. In the following graphs, the main voltage and current trends are reported in function of the switching signal d.

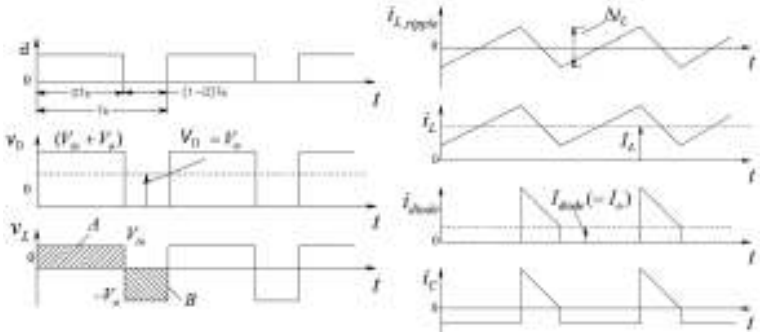

Figure 6.13: Buck - boost converter voltage and currents[Mohan 2011b].

To understand how the duty cycle sets V_0 value, the mean value of the voltage over the inductance $\bar{v}_L$ is studied. Being equal to zero for the Continuous Conduction Mode hypothesis and recalling Eqs. 6.11 and 6.18, $\bar{v}_L$ can be written as

$$\begin{aligned}\bar{v}_L &= \frac{1}{T_s}\left[\int_0^{t_{on}} V_{in}dt + \int_{t_{on}}^{T_s} -V_0 dt\right] = \frac{1}{T_s}\left[V_{in}t_{on} - V_0(T_s - t_{on})\right] = dV_{in} - V_0(1-d) = 0 \Rightarrow \\ \Rightarrow V_0 &= \frac{d}{1-d}V_{in}\end{aligned} \tag{6.20}$$

The previous equation gives then the relation between V_0 and V_{in}:

- if $d = 0.5$, then $V_0 = V_{in}$;
- if $d < 0.5$, then $V_0 < V_{in}$;
- if $d > 0.5$, then $V_0 > V_{in}$.

The inductor can be sized from the *on*-state equation of the inductor voltage (eq. 6.11):

$$v_L = V_{in} \Rightarrow L_{BB}\frac{\partial i_L}{\partial t} = V_{in} \Rightarrow L_{BB} = \frac{V_{in}T_s d}{\Delta i_L} \tag{6.21}$$

where Δi_L is the inductor current ripple amplitude, usually kept between 10 % and 20 % of i_L mean value in order to obtain a wide range of operating conditions.

To size the capacitor, the output voltage ripple must be taken into account.

$$i_c = C_{BB}\frac{\partial V_0}{\partial t} = I_0 \Rightarrow C_{BB} = \frac{I_0\, T_s\, d}{\Delta V_0} \tag{6.22}$$

where the ripple of the output voltage ΔV_0 is usually small (1-2 % of V_0).

Finally, the power flowing through the buck - boost converter can be expressed as

$$P = \frac{1}{d(1-d)} V_0 I_0 \tag{6.23}$$

Obviously, P has a maximum for $d = 0.5$, condition that determines the switch choice.

6.6.3 Maximum Power Point Tracking logic unit

MPPT methods

The most widely used MPPT techniques for piezoelectric resonant energy harvesters are the Perturb & Observe technique and the Open Circuit Voltage (OCV) technique [Balato et al. 2018]. The first one (fig. 6.14) is based on voltage perturbation to find the maximum power point with a trial and error mechanism. After changing V, the new voltage and current are measured and the calculated power is compared with the old value, determining if voltage perturbation brought to higher or lower energy production. Depending on the comparison, a further voltage perturbation is decided for the following time step until the optimum power condition is reached ($\Delta P = 0$). The variation of $V_{0,ref}$ must induce a variation in P_0 greater than the one caused by the maximum variation of the vibration amplitude [Balato et al. 2018]. Although simple to be implemented, P&O technique can fail easily under excitation fast changing condition [Tung et al. 2006], so it could be not suitable for a noisy spectrum vibration condition.

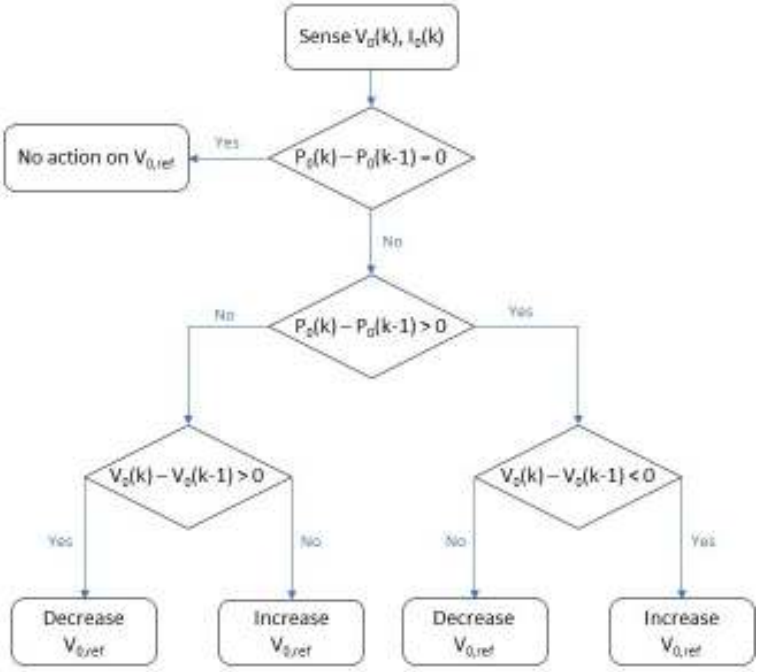

Figure 6.14: Perturb & Observe MPPT logic.

The Open Circuit Voltage technique relies on the principle according to which the maximum power point voltage of the device is always a fraction of the open circuit voltage $V_{opt} = \alpha V_{oc}$, with α a constant related to the working conditions. At every cycle, the open circuit voltage is measured and the new optimal condition is found. Then V_{opt} is compared with the operating voltage and an increment or decrement is considered to reach the optimal working conditions [Sharma et al. 2016] (Fig. 6.15).

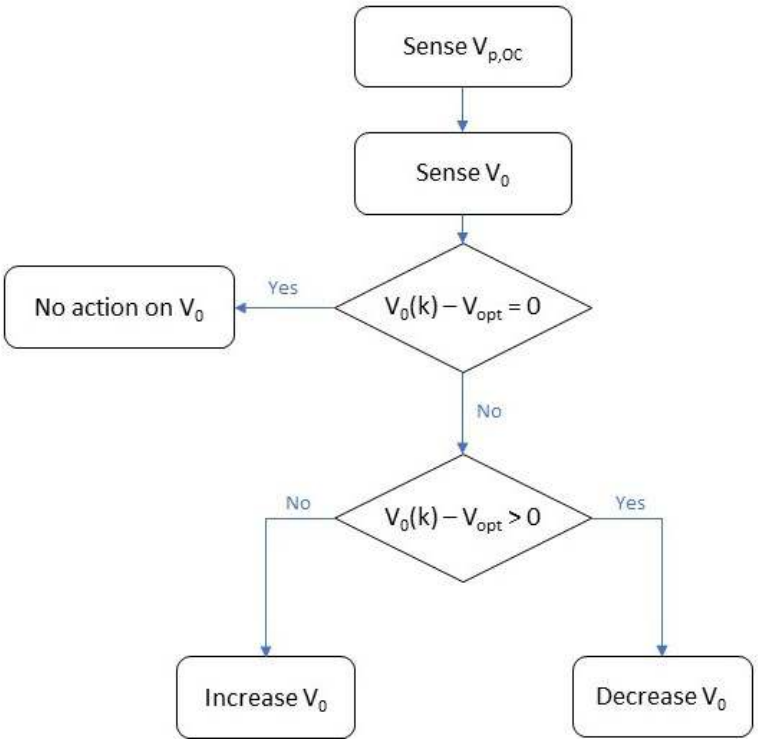

Figure 6.15: Open Circuit Voltage MPPT logic.

Ottman *et al.* [Ottman; Hofmann; Bhatt, et al. 2002] considered the MPPT with buck-boost converter only for the sinusoidal case, a rather ideal condition far from real life applications, demonstrating its effectiveness, although for high excitation amplitudes. Moreover, the same research group [Ottman; Hofmann, and Lesieutre 2003] studied the optimal duty cycle in relationship with the external force amplitude, finding that control becomes easier (duty cycle constant) for higher acceleration amplitude.

A new upcoming technique in the MPPT field is based on Machine Learning (ML) [Memaya et al. 2019]. Providing a faster convergence towards the optimum point with respect to the previous methods, ML could be useful in the energy harvesting application field, since a variable and noisy excitation (fast changing conditions) requires an equally fast control. However, to implement this MPPT logic a training set is needed, with data on the PEH system behaviour for different excitation and load conditions, with optimum duty cycle found with optimization algorithms. Following the last point, an holistic, robust and accurate model, providing the acceleration-voltage transfer function, is still fundamental, showing once again the benefits of a comprehensive approach to this problem.

In the following, first the OCV method will be presented for piezoelectric device under sinusoidal excitations, and then results will be compared with those of the duty cycle found with the *patternsearch* algorithm.

MPPT logic for piezoelectric harvesters with sinusoidal excitation

As mentioned previously, Ottman *et al.* [Ottman; Hofmann; Bhatt, et al. 2002] presented a MPPT logic for a piezoelectric device producing a sinusoidal current output, deriving the V_0 optimal value in function of open circuit voltage (OCV technique) from the average power output expression.

Knowing that

$$I_p sin(\omega t) = C_p \frac{\partial v_p}{\partial t} = \omega C_p \frac{\partial v_p}{\partial(\omega t)} \tag{6.24}$$

and integrating the previous relation from 0 to the instant t_1 at which C_p is fully charged,

$$cos(\omega t_1) = 1 - \frac{2V_0 \omega C_p}{I_p} \tag{6.25}$$

is obtained.

So the FBR output current DC component is expressed as mean value of the signal, that is

$$< i_0(t) >= \frac{1}{\pi}\Big(0 + \int_{t_1}^{T} I_p sin(\omega t) dt\Big) = \frac{I_p}{\pi}\big(- cos(\pi) + cos(\omega t_1)\big) = \frac{2I_p}{\pi} - \frac{2\omega C_p V_0}{\pi} \tag{6.26}$$

Considering the output voltage kept almost constant by C_R, the system average power output is

$$< P_0 >= V_0 < i_0(t) >= V_0\Big(\frac{2I_p}{\pi} - \frac{2\omega C_p V_0}{\pi}\Big) \tag{6.27}$$

from which, the voltage at maximum power production can be determined:

$$(V_0)_{opt} = \frac{I_p}{2\omega C_p} \tag{6.28}$$

corresponding to half the open circuit voltage, measured during the off-condition period of the DC/DC converter switch.

6.6.4 OCV MPPT technique versus duty cycle optimization

To find the results of the power output produced with the OCV MPPT control, a new configuration ($S3_{OCV}$) is used, comprehensive of PEH, FBR and DC/DC converter. The optimization problem with duty cycle d as design variable runs with the same configuration of the OCV, but denoted as $S3_{opt}$ for the sake of clarity. The FBR capacitance is set equal to the optimized one to provide a storage function ($C_R = 3.8\,mF$), since the inductor charge otherwise could cause high voltage ripples. From Eqs. 6.21 and 6.22, the inductance and capacitance of the buck-boost converter are set equal to $L_{BB} = 1.2\,kH$ and $C_{BB} = 5.7\,\mu F$, respectively.

The two control techniques are tested for a set of resistive load values. In Fig. 6.16 a comparison between $S3_{OCV}$ and $S3_{opt}$ results is shown in function of resistance and duty cycle. The optimization algorithm provides better performances than OCV for all load conditions, overcoming it in particular for low R values and keeping the mean power to a higher average level. Indeed the OCV technique shows a low capability to cover on the duty cycle interval ([0,1]), limiting its effectiveness for low voltage conditions occurring at low impedances. On the contrary the optimized duty cycle is more flexible, proving to be a better strategy to obtain a condition of maximum power.

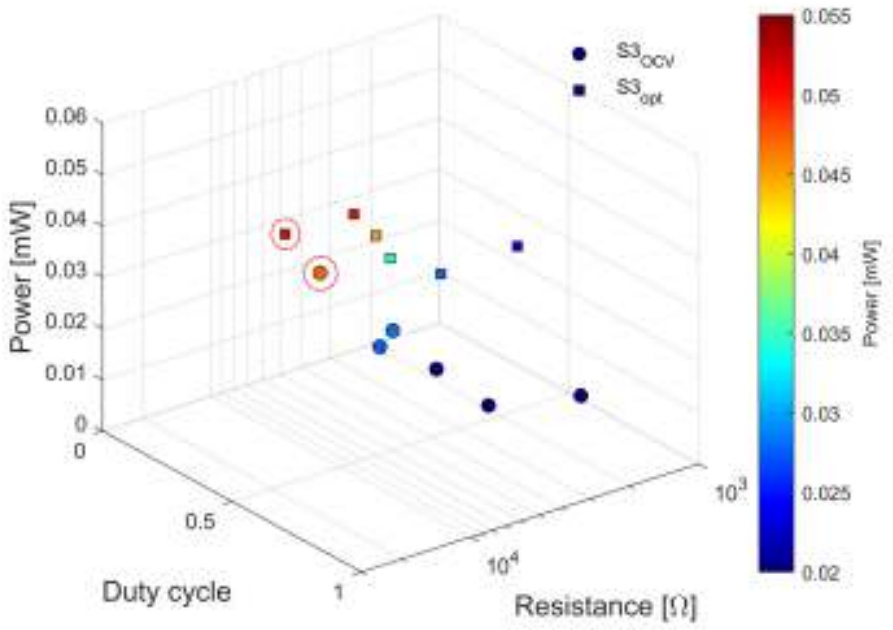

Figure 6.16: Power output comparison of MPPT results with duty cycle obtained with the OCV technique (circles) and with the optimization algorithm (squares).

Since the optimized duty cycle has been proved to be more efficient than the OCV method by running the present model under different load and excitation conditions, this technique can create a set of data to train the ML algorithm under a supervised learning approach. This provides a ML-MPPT technique capable to perform for any kind of excitation (harmonic, stochastic) and electric load.

Chapter 7

Conclusions

In the present work a piezoelectric energy harvester has been studied with an holistic approach to achieve a deeper understanding of its behaviour, to predict more accurately and efficiently the response and to provide potential enhancement to design. The PEH is described as a multi-layer composite cantilevered Euler – Bernoulli beam with not uniform material distribution along its length. The electromechanical coupling is introduced in the structural model by adding the linear piezoelectric constitutive equations. A finite dimension tip mass, taking into account the not negligible extension and rotational inertia effect, is positioned on the free edge to tune harvester's natural frequencies on (lower) external excitation frequencies and to enhance oscillations. By analytically developing Lagrange equations from extended Hamilton's principle, also including electrical potential energy and electric load interactions, a partial differential equation system is obtained and then projected on the exact bending modes of the structure. Thanks to the analytical determination of the modes of the not-uniform beam (obtained in MATLAB), the developed ROM allows mechanically decoupling modal oscillators and then easily neglecting those modes not contributing to energy production, simplifying the problem and saving computational time. The electric conversion system is developed in Simulink by Simscape's blocks, allowing for a simple simulation of voltage rectifier, storage capacitance, Maximum Power Point Tracking system, and resistive load, with an easy data exchange with the ROM model in Simulink environment. To enhance the accuracy of the theory, an experimental identification of torsional spring and modal damping coefficients is carried out. A PEH prototype is tested under sinusoidal excitation, imposed by a shaker, for different frequencies, but constant acceleration amplitude to provide data for validation of the developed ROM. Though approximated, the model captures the system response, being in agreement with experimental evaluation of the acceleration - voltage frequency transfer function for different resistive load and tip mass conditions. Finally, mechanical and electrical key parameters of the system are optimized to maximise the power output with the *patternsearch* algorithm in MATLAB, investigating their influence on the device and underlying the crucial co-dependency of mechanical and electrical behaviour, connected by means of the piezoelectric effect.

The presented holistic procedure fills a gap in past literature, in which usually mechanical and electrical description are addressed separately for this kind of devices, thus preventing from a global comprehension and optimization, and limiting the possibility of introducing technological improvements for PEH efficiency. Interfacing the ROM with the conversion system in Simulink/Simscape allows for a deep un-

derstanding of dynamic coupled behaviour of PEH and FBR; as an example, the developed tool helps in sizing correctly the capacitance not only as signal filter but also as a storage element to ensure the electronic device powering. First, by considering the exact modes of a not uniform multi-layer structure, new design opportunities are introduced, allowing for more flexibility in piezoelectric material use and positioning. Indeed, an accurate simulation of the model behaviour is fundamental for accurate tuning with the main excitation frequencies. Moreover, by studying the node position of the bending modes, an electrode segmentation in length can be performed to avoid charge cancellation and, thus, increase power production. Furthermore, the introduction of electrode segmentation in width shows how the device could comply with voltage requirement of both FBR and loads (typically 3 V) also for very low excitation levels (0.06 g), opening to possible IoT applications for low vibration sources.

The integrated multi-physics approach used in the developed ROM overcomes issues related to interfacing computationally expensive models and shows how few parameters are sufficient to carry out effective sensitivity analysis and optimization of the PEH. Indeed, the sensitivity study underlines which design variables are more relevant in terms of power production and how they influence each other, and that an integrated approach is fundamental to reach an efficient device. Finally, the optimization problem with duty cycle as design variable is addressed, achieving a more efficient behaviour than that obtained with the Open Circuit Voltage MPPT method. This approach can produce more valuable data to build training datasets for the supervised ML techniques increasingly used in MPPT implementation. Hence, the combination of a multi-physics efficient and robust ROM with an optimization approach constitutes a novelty proposed in this thesis to provide a useful tool for improving the design of piezoelectric energy harvesters for real life applications, paving the way for a significant increase in the device performances.

Experimental testing has been systematically used for validating the developed theoretical and numerical models as far as time constraints has allowed for, leaving some work to do in an ideal continuation of the present efforts beyond the PhD thesis. First, the device performance should be tested also under multi-frequency or stochastic excitations. Indeed, the off-design conditions analysis is useful to understand the weaknesses of the device and then design, thanks to the optimization technique, a more robust configuration. Non-linearities could also taken into account in the model, both neglecting the small displacement hypothesis and introducing the not linear piezoelectric constitutive equations. This allows for model validation at higher excitation levels, representing real-life vibration sources characterized by high energy densities. Then, a further experimental campaign should be carried out to test the complete PEH - conversion circuit system model, since both diodes and capacitance blocks need for experimental characterization and validation. Moreover, comparing different capacitor technologies and sizes, and measuring the initial full-charge time is fundamental for data comparison with simulation results and could highlight the need for some improvement in the model. The real load model could be validated too by testing different sensors and data transmitters, thus assessing more specific applications for the PEHs. Finally, the MPPT control module could be added, with the ML logic unit working remotely from an online server, in order to validate the fully coupled model provided in this thesis and give an estimation on the power consumption of the MPPT unit. Moreover, tests under stochastic excitations could bring to the development of a dynamic MPPT logic, based on the correlation between input excitation and optimal duty cycle in a feasible range of acceleration amplitudes and frequencies. As underlined before, the Machine Learning MPPT logic can be more fruitfully trained with simulation data employing the duty cycle optimized under different excitation

and load conditions.

An investigation, both numerical and experimental, of more complex PEH configurations derived from the present ones is also worthwhile, and further exploring the electrode segmentation technique and considering a bimorph configuration to improve device power output. As part of the fundamental tuning process, sensitivity analysis on the tip mass position and weight can be fruitfully performed too, developing a new empirical model that correlates tip mass and damping coefficients.

Moreover, the energy flow, from the vibration source (mechanical energy) till the electronic device (electric energy), could be investigated, offering a quick evaluation of the device efficiency and giving a new simplified model to be used in possible PEH multi-array applications.

Finally, the optimization process should be refined and extended to a multi-objective analysis, testing at the same time the performance of different algorithms provided by the Matlab Optimization Tool to reduce the computational time. Indeed, optimization techniques are expected to provide the perfect match among piezoelectric patch dimensions and position, and the best electrode segmentation both in length and width, coupling it with the search for a new optimum FBR capacitance. Moreover, following the identification of the best configuration for ideal conditions, optimization can lead to address efficiently the presence of a real load, as seen in Chapter 4, and to adjust the PEH system parameters for quasi-periodic and stochastic excitations, more likely in real life applications.

Appendices

Appendix A

Governing equations with extended tip mass

A.1 Device configuration

As shown in Fig. A.1, the studied piezoelectric energy harvesting (PEH) has a tip mass covering part of the support layer.

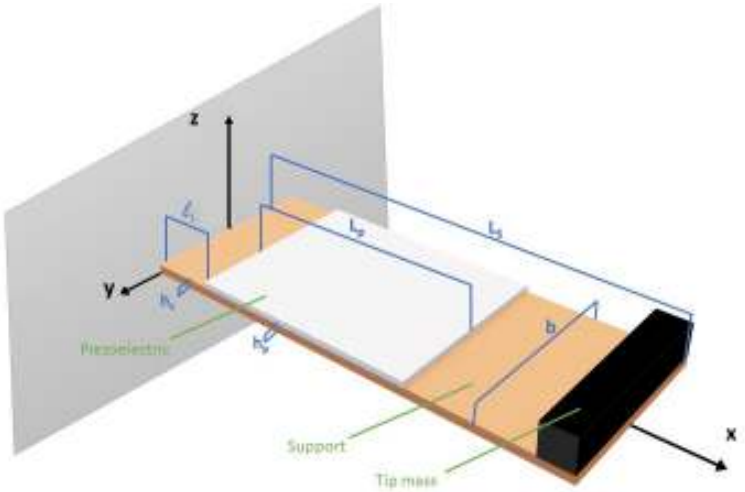

Figure A.1: Configuration of the piezoelectric cantilevered harvester with geometrical characteristics.

Thus, in order to better describe the proof mass effect on resonance frequencies and power output, the extended mass model proposed by several authors [Tang et al. 2017] [Magrab 2012] is adopted, with not negligible extension nor rotational inertia. The tip mass is then defined with a mass per unit of length μ_{tip}, a length l_{tip}, and a thickness h_{tip}, as shown in Fig. A.2.

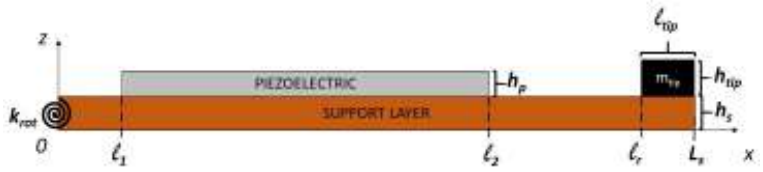

Figure A.2: Lateral view of the PEH with extended tip mass (dimensions do not scale real values of the device considered later).

For the sake of simplicity, supposing the support layer as part of the tip mass above for $l_r \leq x \leq L_s$ and since the overall mass per unit of length keeps constant in the same interval, it follows for the total tip mass m_{tip} and moment of inertia J_{tip}:

$$m_{tip} = \mu_{tip} l_{tip} + \mu(l_r) l_{tip} \tag{A.1}$$

$$J_{tip} = \frac{\mu_{tip} l_{tip}}{3}\left(h_{tip}^2 + \frac{l_{tip}^2}{4} - \frac{h_s}{8h_{tip}} l_{tip}^2\right) + \frac{\mu(l_r) l_{tip}^3}{12} \tag{A.2}$$

where the point T with coordinates $x = l_r$, $z = h_s/2$ is assumed as pole to calculate the moment of inertia and terms of order higher than $O(h_s)$ are neglected since $h_s << h_{tip}$. Following this hypothesis, $x = l_r$ becomes the effective beam length for which the beam modes are calculated.

A.2 Electromechanical PDE model

As in Chapter 3, to obtain the equations describing the behaviour of the piezoelectric bender with an extended tip mass, the Hamilton's principle for continuous systems [Gupta 1988] is written in the form:

$$\delta I = \int_{t_1}^{t_2} (\delta \mathcal{L} + \delta W_{nc})\ dt = 0 \tag{A.3}$$

with W_{nc} the virtual work of non-conservative forces and $\mathcal{L}$ the Lagrangian function, which includes three different contributions,

$$\mathcal{L}_1 = T - U_m + U_e = \int_0^{L_s} \ell dx \tag{A.4}$$

$$\mathcal{L}_2 = T_{tip} = \frac{1}{2} m_{tip}\left[\dot{w}_a(l_r,t) + \frac{l_{tip}}{2}\dot{w}_a'(l_r,t)\right]^2 + \frac{1}{2} J_{tip}\dot{w}_a'^2(l_r,t) \tag{A.5}$$

$$\mathcal{L}_3 = \frac{1}{2} k_{rot}\gamma^2 \tag{A.6}$$

The term $\mathcal{L}_2$ represents the kinetic energy of the extended tip mass placed on the free edge of the beam ($x = l_r$).

Focusing on the specific form of the Lagrangian function, which includes continuous ℓ and lumped contributions $\mathcal{L}_k$ (see *e.g.*, [Gupta 1988]),

$$\delta\mathcal{L}(\boldsymbol{u}) = \int_0^{L_s} \delta\ell(\boldsymbol{u})\ dx + \delta\mathcal{L}_2(\boldsymbol{u}) + \delta\mathcal{L}_3(\boldsymbol{u}), \tag{A.7}$$

the set of independent parameters is provided for the piezoelectric cantilever by functions $p_1 = w_a(x,t)$ and $p_2 = \lambda(t)$ along with their time and space derivatives. Thus, setting $\mathbf{p} = \{p_1, p_2\}$, the Lagrangian from Eq. A.7 can be expressed in general form as:

$$\delta\mathcal{L}(\mathbf{p}, \mathbf{p}', \mathbf{p}'', \dot{\mathbf{p}}, \dot{\mathbf{p}}') = \int_0^{L_s} \left(\sum_{j=1}^{2} \sum_{i=0}^{4} \frac{\partial \ell}{\partial {p_j}^{(i)}} \delta {p_j}^{(i)} \right) dx + \sum_{k=2}^{3} \sum_{j=1}^{2} \sum_{i=0}^{4} \frac{\partial \mathcal{L}_k}{\partial {p_j}^{(i)}} \delta {p_j}^{(i)} \tag{A.8}$$

where, for the sake of conciseness, it is set $p_j^{(0)} = p_j$, $p_j^{(1)} = p_j'$, $p_j^{(2)} = p_j''$, $p_j^{(3)} = \dot{p}_j$, and $p_j^{(4)} = \dot{p}_j{}'$. Each term of the expansion with respect to the virtual displacements $\delta p_j^{(i)}$ needs to be separately evaluated, using the condition $\delta\mathbf{p}(t_1) = \delta\mathbf{p}(t_2) = 0$. In the following, only not vanishing derivatives will be taken into account relatively to the summations in the r.h.s of Eq. A.8. Thus, remembering the Extended Hamilton's Principle (Eq. 3.20), and considering the order reversibility of integrals and the commutativity of the operators $\delta(\cdot)$ and $\partial/\partial x(\cdot)$, the derivative with respect to $\dot{p}_j$ relative to $\mathcal{L}_2$ can be integrated by parts over time

$$\int_{t_1}^{t_2} \frac{\partial \mathcal{L}_2}{\partial \dot{p}_j} \delta \dot{p}_j \, dt = \frac{\partial \mathcal{L}_2}{\partial \dot{p}_j} \delta p_j \Big|_{t_1}^{t_2} - \int_{t_1}^{t_2} \frac{\partial}{\partial t} \left(\frac{\partial \mathcal{L}_2}{\partial \dot{p}_j} \right) \delta p_j \, dt = - \int_{t_1}^{t_2} \frac{\partial}{\partial t} \left(\frac{\partial \mathcal{L}_2}{\partial \dot{p}_j} \right) \delta p_j \, dt \tag{A.9}$$

with the integral over the beam length not taken into account since $\mathcal{L}_2$ is defined only at the free edge.

Analogously, the derivative with respect to $\dot{p}_j'$ relative to $\mathcal{L}_2$ can be integrated by parts over time

$$\int_{t_1}^{t_2} \frac{\partial \mathcal{L}_2}{\partial \dot{p}_j'} \delta \dot{p}_j' \, dt = \frac{\partial \mathcal{L}_2}{\partial \dot{p}_j'} \delta p_j' \Big|_{t_1}^{t_2} - \int_{t_1}^{t_2} \frac{\partial}{\partial t} \left(\frac{\partial \mathcal{L}_2}{\partial \dot{p}_j'} \right) \delta p_j' \, dt = - \int_{t_1}^{t_2} \frac{\partial}{\partial t} \left(\frac{\partial \mathcal{L}_2}{\partial \dot{p}_j'} \right) \delta p_j' \, dt \tag{A.10}$$

Substituting the expressions 3.47, A.9, A.10, 3.50, and 3.51 in the Eq. A.8, we can rewrite the Extended Hamilton Princile 3.20 as

$$\begin{aligned} \int_{t_1}^{t_2} \Bigg\{ \int_0^{L_s} \left[\frac{\partial \ell}{\partial p_j} - \frac{\partial}{\partial x} \left(\frac{\partial \ell}{\partial p_j'} \right) + \frac{\partial^2}{\partial x^2} \left(\frac{\partial \ell}{\partial p_j''} \right) - \frac{\partial}{\partial t} \left(\frac{\partial \ell}{\partial \dot{p}_j} \right) + Q_j \right] \delta p_j \, dx + \\ \left[\frac{\partial \ell}{\partial p_j'} - \frac{\partial}{\partial x} \frac{\partial \ell}{\partial p_j''} - \frac{\partial Q_{12}}{\partial x} - \frac{\partial}{\partial t} \frac{\partial \mathcal{L}_2}{\partial \dot{p}_j} \right] \delta p_j \Big|_0^{L_s} + \left[\frac{\partial \ell}{\partial p_j''} + Q_{12} + \frac{\partial \mathcal{L}_3}{\partial p_j'} - \frac{\partial}{\partial t} \frac{\partial \mathcal{L}_2}{\partial \dot{p}_j'} \right] \delta p_j' \Big|_0^{L_s} \Bigg\} dt = 0 \end{aligned} \tag{A.11}$$

where the terms involving $\mathcal{L}_2$ and $\mathcal{L}_3$ are considered equal to zero in 0 and l_r, respectively. Usually, Eq. A.11 leads to separately setting the terms associated to virtual displacements equal to zero because of principle of virtual work, directly providing in this way the governing equation and the BCs. However, in the present case it would lead to time dependent BCs due to the presence of imposed excitation w_b inside the total displacement w_a, and this suggest to rearranging terms in Eq. A.11 before setting them equal to zero.

For $p_1 = w_a$, one has:

$$\frac{\partial \ell}{\partial w_a} = \frac{\partial \ell}{\partial w_a'} = \frac{\partial \ell}{\partial \dot{w}_a{}'} = 0, \qquad \frac{\partial \ell}{\partial w_a''} = -\bar{D} w'' + \theta \left[H(x - l_1) - H(x - l_2) \right] \dot{\lambda}, \qquad \frac{\partial \ell}{\partial \dot{w}_a} = \mu \dot{w}_a$$

recalling that the space derivatives of w_a contain only the elastic contribution w. After substitution of the above relations into Eq. A.11, it si convenient splitting w_a into the elastic and rigid body contribution, and then grouping the terms both depending on w_b and associated to δp_1 with the continuous term (δ-Dirac

symbols are introduced for that). Thus, the following equation is obtained:

$$\int_0^{l_r} \{\mu\ddot{w} + (\bar{D}w'')''\} - \theta\left[\delta'(x-l_1) - \delta'(x-l_2)\right]\dot{\lambda} + c_a\dot{w} + (c_sJ\dot{w}'')'' + \\ + [\mu + m_{tip}\delta(x-l_r) + \frac{m_{tip}}{2}\delta'(x-l_r)]\,\ddot{w}_b + c_a\dot{w}_b\}\,dx = 0 \tag{A.12}$$

where the second derivative of the Heaviside function $H(x)$ is replaced with the first derivative of the Dirac delta function δ. Equation A.12 is then satisfied if the integrated function vanishes, obtaining Eq. A.14 in Sec. 3.3.2.

For the BCs, considering that only elastic terms are retained after splitting of w_a in Eq. A.12, it yields:

$$\left[(\bar{D}w'')' + c_s(J_r\dot{w}'')' - m_{tip}\left(\ddot{w} + \frac{l_{tip}}{2}\ddot{w}'\right)\right]\delta w\Bigg|_0^{l_r} + \\ \left[-\bar{D}w'' + c_sJ_r\dot{w}'' + k_{rot}w' - \frac{m_{tip}l_{tip}}{2}\left(\ddot{w} + \frac{l_{tip}}{2}\ddot{w}'\right) - J_{tip}\ddot{w}'\right]\delta w'\Bigg|_0^{l_r} = 0 \tag{A.13}$$

where the term depending on θ has vanished as the piezoelectric effect occurs only in (l_1, l_2). Tthe system governing equations are then obtained as:

$$\begin{cases} \mu\ddot{w} + c_a\dot{w} + (c_sJ\dot{w}'' + \bar{D}w'')'' - \theta\left[\delta'(x-l_1) - \delta'(x-l_2)\right]\dot{\lambda} = f(x,t) \\ C_p\ddot{\lambda} + \int_0^{L_s}\theta\left[H(x-l_1) - H(x-l_2)\right]\dot{w}''\,dx = -I_c \end{cases}, \tag{A.14}$$

with δ the Dirac-delta distribution and $f(x,t)$ expressed as:

$$f(x,t) = -[\mu + m_{tip}\delta(x-l_r) + \frac{m_{tip}l_{tip}}{2}\delta'(x-l_r)]\,\ddot{w}_b - c_a\dot{w}_b \tag{A.15}$$

The boundary conditions in $x = 0$ are:

$$w(0) = 0, \quad -\bar{D}(0)w''(0) - c_sJ\dot{w}''(0) + k_{rot}w'(0) = 0 \tag{A.16}$$

and in $x = l_r$:

$$\bar{D}(l_r)w''(l_r) + c_sJ\dot{w}''(l_r) + \frac{m_{tip}l_{tip}}{2}\left(\ddot{w}(l_r) + \frac{l_{tip}}{2}\ddot{w}'(l_r)\right) + J_{tip}\ddot{w}'(l_r) = 0 \tag{A.17}$$

$$[\bar{D}(l_r)w''(l_r) + c_sJ\dot{w}''(l_r)]' - m_{tip}\left(\ddot{w}(l_r) + \frac{l_{tip}}{2}\ddot{w}'(l_r)\right) = 0. \tag{A.18}$$

A.3 Electromechanical reduced-order model

As previously mentioned, the piezoelectric structure under consideration is modelled as a beam with non uniform distribution of stiffness and mass. Thus, in order to refer to Eq. 3.75, a piecewise definition of $w(x,t)$ in space is introduced [Dessi et al. 2015] and three different displacement functions can be locally

defined along the beam length as

$$w(x,t) = \begin{cases} w_1(x_1), & for\, 0 \le x_1 \le l_1 \\ w_2(x_2), & for\, 0 \le x_2 \le L_p = l_2 - l_1 \\ w_3(x_3), & for\, 0 \le x_3 \le L_s - l_2 \end{cases} \tag{A.19}$$

where local coordinate systems are defined for the three parts of the beam, as shown in Fig. A.3.

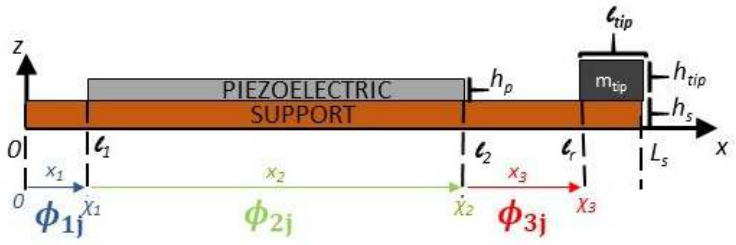

Figure A.3: Definition of local coordinate systems for exact mode calculation.

Each local displacement function w_i can be expanded with respect to the local modes relative to the i-th portion as $w_i = \sum q_j \phi_{ij}$. Each set of shape functions $\{\phi_{1j}, \phi_{2j}, \phi_{3j}\}$ represents the global mode ϕ_j and satisfies the proper BCs at the beam ends and the continuity conditions at the piezoelectric layer edges up to 3-rd order spatial derivative [Dessi et al. 2015]. Each function ϕ_{ij} satisfies the following eigenvalue problem:

$$\phi_{ij}^{IV} - \alpha_{ij}^4 \phi_{ij} = 0 \tag{A.20}$$

with $\alpha_{ij}^4 = \mu\omega_j^2/\bar{D}$, where μ and $\bar{D}$ are constant in each subproblem, and ω_j is the natural frequency of the vibration modes. Next, given the shape functions ϕ_{ij} in the form:

$$\phi_{ij}(x_i) = A_{ij}^{(1)} \sin(\alpha_{ij} x_i) + A_{ij}^{(2)} \cos(\alpha_{ij} x_i) + A_{ij}^{(3)} \sinh(\alpha_{ij} x_i) + A_{ij}^{(4)} \cosh(\alpha_{ij} x_i) \tag{A.21}$$

where $i = 1, 2, 3$ correspond respectively to the three parts of the beam. To determinate the $A_{ij}^{(k)}$ coefficients, the following boundary conditions are rewritten in terms of ϕ_{ij}.

$$\alpha_{j3}^4 = \alpha_{j1}^4 \tag{A.22}$$

Indeed, for $x_3 = l_r - l_2 = \chi_3$ the boundary conditions are:

- $$\begin{aligned} &[\bar{D} w_3''(\chi_3)]' - m_{tip}\left(\ddot{w}_3(\chi_3) + \frac{l_{tip}}{2}\ddot{w}_3'(\chi_3)\right) = 0 \Rightarrow \\ &{\phi_{3j}}'''(\chi_3) = -\frac{m_{tip}}{\bar{D}}\omega_j^2\left(\phi_{3j}(\chi_3) + \frac{l_{tip}}{2}\phi_{3j}'(\chi_3)\right) \Rightarrow \\ &{\phi_{3j}}'''(\chi_3) = -\mu_t \alpha_{1j}^4\left(\phi_{3j}(\chi_3) + \frac{l_{tip}}{2}\phi_{3j}'(\chi_3)\right) \end{aligned} \tag{A.23}$$

•

$$\begin{aligned}
&\bar{D}w_3''(\chi_3) + \frac{m_{tip}l_{tip}}{2}\left(\ddot{w}_3(\chi_3)+\frac{l_{tip}}{2}\ddot{w}_3'(\chi_3)\right) + J_{tip}\ddot{w}_3'(\chi_3) = 0 \Rightarrow \\
&{\phi_{3j}}''(\chi_3) = \frac{1}{2}\frac{m_{tip}l_{tip}}{\bar{D}}\omega_j^2\left(\phi_{3j}(\chi_3)+\frac{l_{tip}}{2}\phi_{3j}'(\chi_3)\right) + \frac{J_{tip}}{\bar{D}}\omega_j^2\phi_{3j}'(\chi_3) \Rightarrow \\
&{\phi_{3j}}''(\chi_3) = \frac{\mu_t}{2}\alpha_{1j}^4\left(\phi_{3j}(\chi_3)+\frac{l_{tip}}{2}\phi_{3j}'(\chi_3)\right) + \frac{J_{tip}}{\mu}\alpha_{1j}^4\phi_{3j}'(\chi_3)
\end{aligned} \tag{A.24}$$

where $\mu_t = m_{tip}/\mu(0)$. Boundary and continuity conditions together form a system of equations from which the 12 $A_{ij}^{(k)}$ coefficients for each mode, and thus the exact modes ϕ_{ij}, are determined thanks to the MATLAB numerical solvers.

Taking now into account the damped equations, by substituting Eq. 3.69 into the first equation of (3.64), and projecting the first equation over the mode $\phi_m(x)$, one has:

$$\begin{aligned}
&\sum_{j=1}^{N_w}\ddot{q}_j < \mu\phi_j, \phi_m > + \sum_{j=1}^{N_w}\dot{q}_j\left(c_a < \mu\phi_j, \phi_m > + c_s < (J\phi_j'')'', \phi_m >\right) + \\
&+ \sum_{j=1}^{N_w} q_j < (\bar{D}\phi_j'')'', \phi_m > - \theta\dot{\lambda} < \left[\delta'(x-l_1) - \delta'(x-l_2)\right], \phi_m > = < f(x,t), \phi_m > = F_m(t)
\end{aligned} \tag{A.25}$$

wwhere the inner product between generic functions g_1 and g_2 in the interval $[0, l_r]$ is introduced as $< g_1, g_2 > = \int_0^{l_r} g_1 g_2\, dx$ for sake of conciseness.

Moreover, by using integration by parts, and recalling the boundary conditions 3.79, 3.80, 3.92, and 3.93, the damping and stiffness terms in Eq. 3.92 can be written as:

$$< (c_s J\phi_j'')'', \phi_m > = (c_s J\phi_{ij}'')'\phi_{im}\Big|_0^{l_r} - c_s J\phi_{ij}''\phi_{im}'\Big|_0^{l_r} + \int_0^{l_r} c_s J\phi_j''\phi_m'' dx \tag{A.26}$$

$$< (\bar{D}\phi_j'')'', \phi_m > = (\bar{D}\phi_{ij}'')'\phi_{im}\Big|_0^{l_r} - \bar{D}\phi_{ij}''\phi_{im}'\Big|_0^{l_r} + \int_0^{l_r} \bar{D}\phi_j''\phi_m'' dx \tag{A.27}$$

Substituting Eqs. A.26 and A.27 into Eq. 3.95

$$\begin{aligned}
&\sum_{j=1}^{N_w}(\ddot{q}_j + \frac{c_a}{\mu}\dot{q}_j) < \mu\phi_j, \phi_m > + \sum_{j=1}^{N_w}\dot{q}_j(< c_s J\phi_j'', \phi_m'' > + \phi_{3m}(l_r)(c_s J\phi_{3j}'')'|_{x=l_r} - \phi_{3m}'(l_r)c_s J_r\phi_{3j}''(l_r) + \\
&+ \phi_{1m}'(0)c_s J_0\phi_{1j}''(0)) + \sum_{j=1}^{N_w} q_j(< \bar{D}\phi_j'', \phi_m'' > + \phi_{3m}(l_r)(\bar{D}\phi_{3j}'')'|_{x=l_r} - \phi_{3m}'(l_r)\bar{D}_r\phi_{3j}''(l_r) \\
&+ \phi_{1m}'(0)\bar{D}_0\phi_{1j}''(0)) - \theta\dot{\lambda}\Big[\phi_{2m}'(L_p) - \phi_{1m}'(l_1)\Big] = F_m(t)
\end{aligned} \tag{A.28}$$

that can be rearranged as

$$\begin{aligned}
&\sum_{j=1}^{N_w}(\ddot{q}_j + \frac{c_a}{\mu}\dot{q}_j) < \mu\phi_j, \phi_m > + \sum_{j=1}^{N_w}\dot{q}_j < c_s J\phi_j'', \phi_m'' > + \sum_{j=1}^{N_w} q_j < \bar{D}\phi_j'', \phi_m'' > + \\
&+ \sum_{j=1}^{N_w}\dot{q}_j\phi_{3m}(l_r)(c_s J\phi_{3j}'')'|_{x=l_r} + \sum_{j=1}^{N_w} q_j\phi_{3m}(l_r)(\bar{D}\phi_{3j}'')'|_{x=l_r} - \sum_{j=1}^{N_w}\dot{q}_j\phi_{3m}'(l_r)c_s J_r\phi_{3j}''(l_r) + \\
&- \sum_{j=1}^{N_w} q_j\phi_{3m}'(l_r)\bar{D}_r\phi_{3j}''(l_r) + \sum_{j=1}^{N_w}\dot{q}_j\phi_{1m}'(0)c_s J_0\phi_{1j}''(0) + \sum_{j=1}^{N_w} q_j\phi_{1m}'(0)\bar{D}_0\phi_{1j}''(0) + \\
&- \theta\dot{\lambda}\Big[\phi_{2m}'(L_p) - \phi_{1m}'(l_1)\Big] = F_m(t)
\end{aligned} \tag{A.29}$$

Substituting Eq. 3.69 into the expression of the boundary condition at $x = l_r$ yields:

$$J_r\sum_{j=1}^{N_w}\dot{q}_j c_s\,\phi_{3j}'''|_{x=l_r} + \bar{D}_r\sum_{j=1}^{N_w} q_j\,\phi_{3j}'''|_{x=l_r} = m_{tip}\sum_{j=1}^{N_w}\ddot{q}_j\left[\phi_{3j} + \frac{l_{tip}}{2}\phi_{3j}'\right]_{x=l_r} \tag{A.30}$$

$$J_r\sum_{j=1}^{N_w}\dot{q}_j c_s\phi_{3j}''|_{x=l_r} + \bar{D}_r\sum_{j=1}^{N_w} q_j\,\phi_{3j}''|_{x=l_r} = -\frac{m_{tip}l_{tip}}{2}\sum_{j=1}^{N_w}\ddot{q}_j\left[\phi_{3j} + \frac{l_{tip}}{2}\phi_{3j}'\right]_{x=l_r} - J_{tip}\sum_{j=1}^{N_w}\ddot{q}_j\phi_{3j}'|_{x=l_r}. \tag{A.31}$$

Similarly, substituting Eq. 3.69 into the expression of the boundary condition at $x = 0$ (*i.e.*, $[\bar{D}w''(0) + c_s J\dot{w}''(0)]|_{x=0} = k_{rot}w'(0)|_{x=0}$) yields:

$$J_0\sum_{j=1}^{N_w}\dot{q}_j c_s\phi_{1j}''|_{x=0} + \bar{D}_0\sum_{j=1}^{N_w} q_j\phi_{1j}''|_{x=0} = k_{rot}\sum_{j=1}^{N_w} q_j\phi_{1j}'|_{x=0} \tag{A.32}$$

Taking into account relations A.30, A.31, and 3.105, one can write Eq. A.29 as:

$$\begin{aligned}
&\sum_{j=1}^{N_w}\Big[M_{jm} + m_{tip}\,\phi_{3j}(l_r)\phi_{3m}(l_r) + \frac{m_{tip}l_{tip}}{2}\,\left[\phi_{3j}'(l_r)\phi_{3m}(l_r) + \phi_{3j}(l_r)\phi_{3m}'(l_r)\right] + \frac{m_{tip}l_{tip}^2}{4}\phi_{3j}'(l_r)\phi_{3m}'(l_r) + \\
&+ J_{tip}\,\phi_{3j}'(l_r)\phi_{3m}'(l_r)\Big]\,\ddot{q}_j + \sum_{j=1}^{N_w}\left(\frac{c_a}{\mu}M_{jm} + \frac{c_s J}{\bar{D}}K_{jm}\right)\dot{q}_j + \sum_{j=1}^{N_w}\Big(K_{jm} + k_{rot}\,\phi_{1j}'(0)\phi_{1m}'(0)\Big)q_j + \\
&- \theta\,(\phi_{2m}'(l_2) - \phi_{1m}'(l_1))\dot{\lambda} = F_m(t),
\end{aligned} \tag{A.33}$$

with $M_{jm} =< \mu\phi_j, \phi_m >$ and $K_{jm} =< \bar{D}\phi_j'', \phi_m'' >$. The chosen normalization condition, *i.e.*, modes must be orthogonal with respect to the PEH mass distribution, is expressed as:

$$\begin{aligned}
&M_{jm} + m_{tip}\,\phi_{3j}(l_r)\phi_{3m}(l_r) + \frac{m_{tip}l_{tip}}{2}\,\left[\phi_{3j}'(l_r)\phi_{3m}(l_r) + \phi_{3j}(l_r)\phi_{3m}'(l_r)\right] + \\
&\left(J_{tip} + m_{tip}\frac{l_{tip}^2}{4}\right)\,\phi_{3j}'(l_r)\phi_{3m}'(l_r) = \delta_{jm},
\end{aligned} \tag{A.34}$$

where δ_{jm} is a Kronecker delta, the overall mass matrix is diagonal with unit elements and consequently we have also an overall diagonal stiffness matrix $K_{jm} + k_{rot}\phi'_{j1}(0)\phi'_{m1}(0) = \delta_{jm}\omega_m^2$. Thus the previous equation becomes:

$$\ddot{q}_m + 2\zeta_m\omega_m\dot{q}_m + \omega_m^2 q_m - \theta[\phi'_{2m}(L_p) - \phi'_{1m}(l_1)]\dot{\lambda} = F_m(t) \tag{A.35}$$

$$C_p\ddot{\lambda} + \theta\sum_{j=1}^{N_w}\chi_j\dot{q}_j = -I_c \tag{A.36}$$

The modal forcing term $F_m(t)$ is defined as the component of the excitation over the m-th mode, *i.e.*,

$$F_m(t) = -\int_0^{l_r}\left\{[\mu(x) + m_{tip}\delta(x - l_r)]\ddot{w}_b + c_a\dot{w}_b + m_{tip}\frac{l_{tip}}{2}\delta'(x - l_r)\ddot{w}_b\right\}\phi_m(x)\,dx \tag{A.37}$$

which, using the property of Dirac-δ distributions and the dependence of w_b on time alone, becomes:

$$F_m(t) = -\ddot{w}_b\left[\int_0^{l_r}\mu\phi_m(x)\,dx + m_{tip}\phi_{3m}(l_r) + m_{tip}\frac{l_{tip}}{2}\phi'_{3m}(l_r)\right] - c_a\dot{w}_b\int_0^{l_r}\phi_m(x)\,dx \tag{A.38}$$

and introducing $\beta_m = \int_0^{l_r}\mu\phi_m\,dx$ and $\gamma_m = \int_0^{l_r}\phi_m\,dx$, Eq. **??** can be written as:

$$F_m(t) = -\ddot{w}_b\left[\beta_m + m_{tip}\phi_{3m}(l_r) + m_{tip}\frac{l_{tip}}{2}\phi'_{3m}(l_r)\right] - c_a\gamma_m\dot{w}_b \tag{A.39}$$

Bibliography

[1] Abdelmoula, Hichem; Sharpes, Nathan; Abdelkefi, Abdessattar; Lee, Hyeon, and Priya, Shashank. "Low-frequency Zigzag energy harvesters operating in torsion-dominant mode". In: *Applied Energy* 204 (2017), pp. 413–419.

[2] Abdelmoula, Hichem; Sharpes, Nathan; Lee, Hyeon; Abdelkefi, Abdessattar, and Priya, Shashank. "Design and experimental verification of torsion-bending low-frequency piezoelectric energy harvesters". In: *International Design Engineering Technical Conferences and Computers and Information in Engineering Conference*. Vol. 50206. American Society of Mechanical Engineers. 2016, V008T10A060.

[3] Acciari, Gianluca et al. "Piezoelectric rainfall energy harvester performance by an advanced Arduino-based measuring system". In: *IEEE Transactions on Industry Applications* 54.1 (2018), pp. 458–468.

[4] Ajitsaria, Jyoti; Choe, Song-Yul; Shen, D, and Kim, DJ. "Modeling and analysis of a bimorph piezoelectric cantilever beam for voltage generation". In: *Smart Materials and Structures* 16.2 (2007), p. 447.

[5] Akdogan, Koray; Allahverdi, Mehdi, and Safari, Ahmad. "Piezoelectric composites for sensor and actuator applications". In: *IEEE transactions on ultrasonics, ferroelectrics, and frequency control* 52.5 (2005), pp. 746–775.

[6] Anton, Steven R. and Sodano, Henry A. "A review of power harvesting using piezoelectric materials (2003–2006)". In: *Smart materials and Structures* 16.3 (2007), R1.

[7] Apo, Daniel Jolomi. "Low frequency microscale energy harvesting". PhD thesis. Virginia Tech, 2014.

[8] Aranda, Jesus Javier Lechuga; Oelmann, Bengt, and Bader, Sebastian. "Fluid coupling interfaces for hydraulic pressure energy harvesters". In: *2017 IEEE International Conference on Advanced Intelligent Mechatronics (AIM)*. IEEE. 2017, pp. 1556–1562.

[9] Arroyo, Emmanuelle; Jia, Yu; Du, Sijun; Chen, Shao-Tuan, and Seshia, Ashwin A. "Experimental and theoretical study of a piezoelectric vibration energy harvester under high temperature". In: *Journal of Microelectromechanical Systems* 26.6 (2017), pp. 1216–1225.

[10] Arroyo, Emmanuelle; Jia, Yu; Du, Sijun; Chen, Shao-Tuan, and Seshia, Ashwin A. "High temperature performance of a piezoelectric micro cantilever for vibration energy harvesting". In: *Journal of Physics: Conference Series*. Vol. 773. 1. IOP Publishing. 2016, p. 012001.

[11] Arshak, Khalil; Moore, Padraic; Lyons, Gerard M.; Harris, John, and Clifford, Seamus. "A review of gas sensors employed in electronic nose applications". In: *Sensor review* (2004).

[12] Audet, Charles and Dennis Jr, John E. "Analysis of generalized pattern searches". In: *SIAM Journal on optimization* 13.3 (2002), pp. 889–903.

[13] Ayala-Garcia, I. Nuria; Zhu, Dibin; Tudor, Michael J., and Beeby, Stephen P. "A tunable kinetic energy harvester with dynamic over range protection". In: *Smart materials and structures* 19.11 (2010), p. 115005.

[14] Badel, Adrien et al. "Piezoelectric vibration control by synchronized switching on adaptive voltage sources: Towards wideband semi-active damping". In: *The Journal of the Acoustical Society of America* 119.5 (2006), pp. 2815–2825.

[15] Balato, Marco; Costanzo, Luigi; Schiavo, Alessandro Lo, and Vitelli, Massimo. "Optimization of both perturb & observe and open circuit voltage MPPT techniques for resonant piezoelectric vibration harvesters feeding bridge rectifiers". In: *Sensors and Actuators A: Physical* 278 (2018), pp. 85–97.

[16] Berdy, David F.; Jung, Byunghoo; Rhoads, Jeff F., and Peroulis, Dimitrios. "Wide-bandwidth, meandering vibration energy harvester with distributed circuit board inertial mass". In: *Sensors and Actuators A: Physical* 188 (2012), pp. 148–157.

[17] Betts, David N.; Bowen Christopher R. and, H. Alicia; Gathercole, Nicholas; Clarke, Christopher T., and Inman, Daniel J. "Nonlinear dynamics of a bistable piezoelectric-composite energy harvester for broadband application". In: *The European Physical Journal Special Topics* 222.7 (2013), pp. 1553–1562.

[18] Boisseau, Sebastien; Despesse, Ghislain; Ricart, Thibaud; Defay, E, and Sylvestre, Alain. "Cantilever-based electret energy harvesters". In: *Smart Materials and Structures* 20.10 (2011), p. 105013.

[19] Boisseau, Sebastien; Despesse, Ghislain, and Seddik, B. Ahmed. "Electrostatic conversion for vibration energy harvesting". In: *Small-Scale Energy Harvesting* (2012), pp. 1–39.

[20] Cady, Walter Guyton. "Piezoelectricity". In: McGraw-Hill, 1946, pp. 1–20.

[21] Cao, Junyi; Syta, Arkadiusz, et al. "Regular and chaotic vibration in a piezoelectric energy harvester with fractional damping". In: *The European Physical Journal Plus* 130.6 (2015), p. 103.

[22] Cao, Junyi; Wang, Wei; Zhou, Shengxi; Inman, Daniel J, and Lin, Jing. "Nonlinear time-varying potential bistable energy harvesting from human motion". In: *Applied Physics Letters* 107.14 (2015), p. 143904.

[23] Cao, Junyi; Zhou, Shengxi; Inman, Daniel J, and Chen, Yangquan. "Chaos in the fractionally damped broadband piezoelectric energy generator". In: *Nonlinear Dynamics* 80.4 (2015), pp. 1705–1719.

[24] Cao, Junyi; Zhou, Shengxi; Inman, Daniel J., and Lin, Jing. "Nonlinear dynamic characteristics of variable inclination magnetically coupled piezoelectric energy harvesters". In: *Journal of Vibration and Acoustics* 137.2 (2015).

[25] Cao, Junyi; Zhou, Shengxi; Wang, Wei, and Lin, Jing. "Influence of potential well depth on nonlinear tristable energy harvesting". In: *Applied Physics Letters* 106.17 (2015), p. 173903.

[26] Challa, Vinod R.; Prasad, Marehalli G.; Shi, Yong, and Fisher, Frank T. "A vibration energy harvesting device with bidirectional resonance frequency tunability". In: *Smart Materials and Structures* 17.1 (2008), p. 015035.

[27] Chen, Shih-Nung; Wang, Gou-Jen, and Chien, Ming-Chun. "Analytical modeling of piezoelectric vibration-induced micro power generator". In: *Mechatronics* 16.7 (2006), pp. 379–387.

[28] Company, East Japan Railway. “Demonstration Experiment of the "Power-Generating Floor" at Tokyo Station”. In: (2008).

[29] Conn, A; Gould, Nick, and Toint, Ph. “A globally convergent Lagrangian barrier algorithm for optimization with general inequality constraints and simple bounds”. In: *Mathematics of Computation* 66.217 (1997), pp. 261–288.

[30] Cook, William R.; Jaffe, Hans, and Jaffe, Bernard. *Piezoelectric ceramics*. Academic Press London and New York, 1971.

[31] Cottone, Francesco; Vocca, Helios, and Gammaitoni, Luca. “Nonlinear energy harvesting”. In: *Physical Review Letters* 102.8 (2009), p. 080601.

[32] Damjanovic, Dragan. “Ferroelectric, dielectric and piezoelectric properties of ferroelectric thin films and ceramics”. In: *Reports on Progress in Physics* 61.9 (1998), p. 1267.

[33] Daqaq, Mohammed F.; Masana, Ravindra; Erturk, Alper, and Dane Quinn, D. “On the role of nonlinearities in vibratory energy harvesting: a critical review and discussion”. In: *Applied Mechanics Reviews* 66.4 (2014).

[34] Daqaq, Mohammed F.; Stabler, Christopher; Qaroush, Yousef, and Seuaciuc-Osório, Thiago. “Investigation of power harvesting via parametric excitations”. In: *Journal of Intelligent Material Systems and Structures* 20.5 (2009), pp. 545–557.

[35] De Paula, Aline S.; Inman, Daniel J., and Savi, Marcelo A. “Energy harvesting in a nonlinear piezomagnetoelastic beam subjected to random excitation”. In: *Mechanical Systems and Signal Processing* 54 (2015), pp. 405–416.

[36] Dessi, Daniele and Camerlengo, Gabriele. “Damage identification techniques via modal curvature analysis: overview and comparison”. In: *Mechanical Systems and Signal Processing* 52 (2015), pp. 181–205.

[37] Deterre, M. et al. “Micromachined piezoelectric spirals and ultra-compliant packaging for blood pressure energy harvesters powering medical implants”. In: *2013 IEEE 26th International Conference on Micro Electro Mechanical Systems (MEMS)*. IEEE. 2013, pp. 249–252.

[38] Doremus, L. William. “Charge Release of Several Ceramic Ferroelectrics under Various Temperature and Stress Conditions”. In: *Proceedings of the IRE* 47.5 (1959), pp. 921–924.

[39] Du, Sijun; Amaratunga, Gehan A. J., and Seshia, Ashwin A. “A cold-startup SSHI rectifier for piezoelectric energy harvesters with increased open-circuit voltage”. In: *IEEE Transactions on Power Electronics* 34.1 (2018), pp. 263–274.

[40] Du, Sijun; Jia, Yu; Chen, Shao-Tuan, et al. “A new electrode design method in piezoelectric vibration energy harvesters to maximize output power”. In: *Sensors and Actuators A: Physical* 263 (2017), pp. 693–701.

[41] Du, Sijun; Jia, Yu, and Seshia, Ashwin A. “Piezoelectric vibration energy harvesting: A connection configuration scheme to increase operational range and output power”. In: *Journal of Intelligent Material Systems and Structures* 28.14 (2017), pp. 1905–1915.

[42] Emam, Samir A.; Hobeck, Jared, and Inman, Daniel J. "Experimental study of nonlinear vibration energy harvesting of a bistable composite laminate". In: *Smart Materials, Adaptive Structures and Intelligent Systems*. Vol. 58257. American Society of Mechanical Engineers. 2017, V001T07A001.

[43] Emam, Samir A. and Inman, Daniel J. "A review on bistable composite laminates for morphing and energy harvesting". In: *Applied Mechanics Reviews* 67.6 (2015).

[44] Erturk, Alper. "Assumed-modes modeling of piezoelectric energy harvesters: Euler–Bernoulli, Rayleigh, and Timoshenko models with axial deformations". In: *Computers & Structures* 106 (2012), pp. 214–227.

[45] Erturk, Alper; Hoffmann, J., and Inman, Daniel J. "A piezomagnetoelastic structure for broadband vibration energy harvesting". In: *Applied Physics Letters* 94.25 (2009), p. 254102.

[46] Erturk, Alper and Inman, Daniel J. "A distributed parameter electromechanical model for cantilevered piezoelectric energy harvesters". In: *Journal of vibration and acoustics* 130.4 (2008).

[47] Erturk, Alper and Inman, Daniel J. "Broadband piezoelectric power generation on high-energy orbits of the bistable Duffing oscillator with electromechanical coupling". In: *Journal of Sound and Vibration* 330.10 (2011), pp. 2339–2353.

[48] Erturk, Alper and Inman, Daniel J. "Issues in mathematical modeling of piezoelectric energy harvesters". In: *Smart Materials and Structures* 17.6 (2008), p. 065016.

[49] Erturk, Alper and Inman, Daniel J. *Piezoelectric energy harvesting*. John Wiley & Sons, 2011.

[50] Erturk, Alper and Inman, Daniel J. "Piezoelectric energy harvesting". In: John Wiley & Sons, 2011. Chap. 4.

[51] Essink, Brittany C.; Owen, Robert B., and Inman, Daniel J. "Optimization of a zigzag shaped energy harvester for wireless sensing applications". In: *Special Topics in Structural Dynamics, Volume 6*. Springer, 2017, pp. 85–89.

[52] Fabbri, Gualtiero. "Studio di un attuatore piezoelettrico ceramico per motore diesel e sperimentazione preliminare". MA thesis. Master degree thesis in Electronic Engineering, Bologna University, 1998.

[53] Fan, Kangqi; Chang, Jianwei; Pedrycz, Witold; Liu, Zhaohui, and Zhu, Yingmin. "A nonlinear piezoelectric energy harvester for various mechanical motions". In: *Applied Physics Letters* 106.22 (2015), p. 223902.

[54] Fan, Kangqi; Tan, Qinxue, et al. "A monostable piezoelectric energy harvester for broadband low-level excitations". In: *Applied Physics Letters* 112.12 (2018), p. 123901.

[55] Ferrari, Carolina. "I materiali piezoelettrici". MA thesis. Milan Politech.

[56] Ferrari, M; Bau, M; Guizzetti, M, and Ferrari, V. "A single-magnet nonlinear piezoelectric converter for enhanced energy harvesting from random vibrations". In: *Sensors and Actuators A: Physical* 172.1 (2011), pp. 287–292.

[57] Ferrari, Marco et al. "Improved energy harvesting from wideband vibrations by nonlinear piezoelectric converters". In: *Sensors and Actuators A: Physical* 162.2 (2010), pp. 425–431.

[58] Fu, Hailing and Yeatman, Eric M. "Effective piezoelectric energy harvesting using beam plucking and a synchronized switch harvesting circuit". In: *Smart Materials and Structures* 27.8 (2018), p. 084003.

[59] Gaglione, Andrea et al. "Energy neutral operation of vibration energy-harvesting sensor networks for bridge applications". In: (2018).

[60] Galchev, Tzeno; Aktakka, Ethem Erkan, and Najafi, Khalil. "A piezoelectric parametric frequency increased generator for harvesting low-frequency vibrations". In: *Journal of Microelectromechanical Systems* 21.6 (2012), pp. 1311–1320.

[61] Galchev, Tzeno; McCullagh, Jeffrey; Peterson, Rebecca L., and Najafi, Khalil. "Harvesting traffic-induced bridge vibrations". In: *2011 16th International Solid-State Sensors, Actuators and Microsystems Conference*. IEEE. 2011, pp. 1661–1664.

[62] Gardini, Davide; Deluca, Marco; Nagliati, Marco, and Galassi, Carmen. "Flow properties of PLZTN aqueous suspensions for tape casting". In: *Ceramics International* 36.5 (2010), pp. 1687–1696.

[63] Goldfarb, Michael and Jones, Lowell D. "On the efficiency of electric power generation with piezoelectric ceramic". In: (1999).

[64] Gupta, K.C. *Classical Mechanics of Particles and Rigid Bodies*. Wiley, 1988. ISBN: 9788122400045. URL: `https://books.google.it/books?id=bK7vAAAAMAAJ`.

[65] Haertling, Gene H. "Ferroelectric ceramics: history and technology". In: *Journal of the American Ceramic Society* 82.4 (1999), pp. 797–818.

[66] Haftaka, Raphael T. and Gurdal, Zafer. "Elements of Structural Optimization". In: Kluwer academic publishers, 1992. Chap. 1.

[67] Hajati, Arman and Kim, Sang-Gook. "Ultra-wide bandwidth piezoelectric energy harvesting". In: *Applied Physics Letters* 99.8 (2011), p. 083105.

[68] Halim, Miah A. and Park, Jae Y. "A non-resonant, frequency up-converted electromagnetic energy harvester from human-body-induced vibration for hand-held smart system applications". In: *Journal of Applied Physics* 115.9 (2014), p. 094901.

[69] Han, Dongjae and Yun, Kwang-Seok. "Piezoelectric energy harvester using mechanical frequency up conversion for operation at low-level accelerations and low-frequency vibration". In: *Microsystem Technologies* 21.8 (2014), pp. 1669–1676.

[70] Heywang, Walter; Lubitz, Karl, and Wersing, Wolfram. *Piezoelectricity: evolution and future of a technology*. Vol. 114. Springer Science & Business Media, 2008.

[71] Hu, Yuantai; Xue, Huan, and Hu, Hongping. "A piezoelectric power harvester with adjustable frequency through axial preloads". In: *Smart materials and structures* 16.5 (2007), p. 1961.

[72] Hua-Bin, Fang et al. "A MEMS-based piezoelectric power generator for low frequency vibration energy harvesting". In: *Chinese Physics Letters* 23.3 (2006), p. 732.

[73] Iannacci, Jacopo; Serra, Enrico, et al. "Multi-modal vibration based MEMS energy harvesters for ultra-low power wireless functional nodes". In: *Microsystem technologies* 20.4-5 (2014), pp. 627–640.

[74] Iannacci, Jacopo; Sordo, Guido; Serra, Enrico, and Schmid, U. "The MEMS four-leaf clover wideband vibration energy harvesting device: design concept and experimental verification". In: *Microsystem Technologies* 22.7 (2016), pp. 1865–1881.

[75] Illumra, self-powered wireless controls. *Self-powered switch technology*. URL: `https://illumra.com/self-powered-switch-technology/`.

[76] Ilyas, Mohammad Adnan and Swingler, Jonathan. "Piezoelectric energy harvesting from raindrop impacts". In: *Energy* 90 (2015), pp. 796–806.

[77] Inman, Daniel J. "Engineering vibration". In: 3rd ed. Pearson Education, 2008. Chap. 1, pp. 52–53.

[78] Jackson, Nathan; Olszewski, Oskar Z.; O'Murchu, Cian, and Mathewson, Alan. "Shock-induced aluminum nitride based MEMS energy harvester to power a leadless pacemaker". In: *Sensors and Actuators A: Physical* 264 (2017), pp. 212–218.

[79] Jackson, Nathan; Stam, Frank; Olszewski, Oskar Z.; Houlihan, Ruth, and Mathewson, Alan. "Broadening the bandwidth of piezoelectric energy harvesters using liquid filled mass". In: *Procedia engineering* 120 (2015), pp. 328–332.

[80] Jeon, Y. B.; Sood, R.; Jeong, J.-H., and Kim, S.-G. "MEMS power generator with transverse mode thin film PZT". In: *Sensors and Actuators A: Physical* 122.1 (2005), pp. 16–22.

[81] Ji, Hongli; Qiu, Jinhao; Cheng, Li, and Nie, Hong. "Semi-active vibration control based on unsymmetrical synchronized switch damping: Analysis and experimental validation of control performance". In: *Journal of Sound and Vibration* 370 (2016), pp. 1–22.

[82] Jia, Yu. "Review of nonlinear vibration energy harvesting: Duffing, bistability, parametric, stochastic and others". In: *Journal of Intelligent Material Systems and Structures* 31.7 (2020), pp. 921–944.

[83] Jia, Yu; Arroyo, Emmanuelle; Du, Sijun, and Seshia, Ashwin A. "Interdigitated cantilever array topology for low frequency MEMS vibration energy harvesting". In: *Journal of Physics: Conference Series*. Vol. 1052. 1. 2018.

[84] Jia, Yu; Du, Sijun; Arroyo, Emmanuelle, and Seshia, Ashwin A. "A micromachined device describing over a hundred orders of parametric resonance". In: *Applied Physics Letters* 112.17 (2018), p. 171901.

[85] Jia, Yu; Du, Sijun; Arroyo, Emmanuelle, and Seshia, Ashwin A. "Autoparametric resonance in a piezoelectric MEMS vibration energy harvester". In: *2018 IEEE Micro Electro Mechanical Systems (MEMS)*. IEEE. 2018, pp. 226–229.

[86] Jia, Yu and Seshia, Ashwin A. "Five topologies of cantilever-based MEMS piezoelectric vibration energy harvesters: a numerical and experimental comparison". In: *Microsystem Technologies* 22.12 (2016), pp. 2841–2852.

[87] Jia, Yu and Seshia, Ashwin A. "Power optimization by mass tuning for MEMS piezoelectric cantilever vibration energy harvesting". In: *Journal of Microelectromechanical Systems* 25.1 (2015), pp. 108–117.

[88] Jia, Yu; Yan, Jize; Du, Sijun, et al. "Real world assessment of an auto-parametric electromagnetic vibration energy harvester". In: *Journal of Intelligent Material Systems and Structures* 29.7 (2018), pp. 1481–1499.

[89] Jia, Yu; Yan, Jize; Soga, Kenichi, and Seshia, Ashwin A. "Parametric resonance for vibration energy harvesting with design techniques to passively reduce the initiation threshold amplitude". In: *Smart Materials and Structures* 23.6 (2014), p. 065011.

[90] Jung, Hyung-Jo; Kim, In-Ho, and Jang, Seon-Jun. "An energy harvesting system using the wind-induced vibration of a stay cable for powering a wireless sensor node". In: *Smart Materials and Structures* 20.7 (2011), p. 075001.

[91] Jung, Seok-Min and Yun, Kwang-Seok. "Energy-harvesting device with mechanical frequency-up conversion mechanism for increased power efficiency and wideband operation". In: *Applied Physics Letters* 96.11 (2010), p. 111906.

[92] Karami, M Amin; Farmer, Justin R, and Inman, Daniel J. "Parametrically excited nonlinear piezoelectric compact wind turbine". In: *Renewable energy* 50 (2013), pp. 977–987.

[93] Khan, Farid Ullah. "Review of non-resonant vibration based energy harvesters for wireless sensor nodes". In: *Journal of Renewable and Sustainable Energy* 8.4 (2016), p. 044702.

[94] Kim, Miso; Hoegen, Mathias; Dugundji, John, and Wardle, Brian L. "Modeling and experimental verification of proof mass effects on vibration energy harvester performance". In: *Smart Materials and Structures* 19.4 (2010), p. 045023.

[95] Kuang, Yang and Zhu, Meiling. "Characterisation of a knee-joint energy harvester powering a wireless communication sensing node". In: *Smart Materials and Structures* 25.5 (2016), p. 055013.

[96] Kuang, Yang and Zhu, Meiling. "Design study of a mechanically plucked piezoelectric energy harvester using validated finite element modelling". In: *Sensors and Actuators A: Physical* 263 (2017), pp. 510–520.

[97] Lallart, Mickaël and Guyomar, Daniel. "An optimized self-powered switching circuit for non-linear energy harvesting with low voltage output". In: *Smart Materials and Structures* 17.3 (2008), p. 035030.

[98] Laura, P.A.A.; Maurizi, M.J., and Pombo, J.L. "A note on the dynamic analysis of an elastically restrained-free beam with a mass at the free end". In: *Journal of Sound and Vibration* 41.4 (1975), pp. 397–405.

[99] Lecce, Leonardo. "Materiali piezoelettrici e loro applicazioni". In: Workshop at Sannio University. May 2002.

[100] Lee, Andrew J. and Inman, Daniel J. "A multifunctional bistable laminate: snap-through morphing enabled by broadband energy harvesting". In: *Journal of Intelligent Material Systems and Structures* 29.11 (2018), pp. 2528–2543.

[101] Lee, Hyeon; Sharpes, Nathan; Abdelmoula, Hichem; Abdelkefi, Abdessattar, and Priya, Shashank. "Higher power generation from torsion-dominant mode in a zigzag shaped two-dimensional energy harvester". In: *Applied Energy* 216 (2018), pp. 494–503.

[102] Leland, Eli S. and Wright, Paul K. "Resonance tuning of piezoelectric vibration energy scavenging generators using compressive axial preload". In: *Smart Materials and Structures* 15.5 (2006), p. 1413.

[103] Lewis, Robert Michael; Torczon, Virginia Joanne, and Kolda, Tamara Gibson. *A generating set direct search augmented Lagrangian algorithm for optimization with a combination of general and linear constraints.* Tech. rep. Sandia National Laboratories, 2006.

[104] Li, Shuguang and Lipson, Hod. "Vertical-stalk flapping-leaf generator for wind energy harvesting". In: *Smart materials, adaptive structures and intelligent systems*. Vol. 48975. 2009, pp. 611–619.

[105] Liang, Junrui and Liao, Wei-Hsin. "Improved design and analysis of self-powered synchronized switch interface circuit for piezoelectric energy harvesting systems". In: *IEEE Transactions on Industrial Electronics* 59.4 (2011), pp. 1950–1960.

[106] Lin, JH; Wu, XM; Ren, TL, and Liu, LT. "Modeling and simulation of piezoelectric MEMS energy harvesting device". In: *Integrated Ferroelectrics* 95.1 (2007), pp. 128–141.

[107] Liu, Huicong; Zhong, Junwen; Lee, Chengkuo; Lee, Seung-Wuk, and Lin, Liwei. "A comprehensive review on piezoelectric energy harvesting technology: Materials, mechanisms, and applications". In: *Applied Physics Reviews* 5.4 (2018), p. 041306.

[108] Lu, Feng; Lee, Heow Pueh, and Lim, Suang P. "Modeling and analysis of micro piezoelectric power generators for micro-electromechanical-systems applications". In: *Smart materials and structures* 13.1 (2003), p. 57.

[109] Magrab, Edward B. *Vibrations of elastic systems: With applications to MEMS and NEMS*. Vol. 184. Springer Science & Business Media, 2012.

[110] Manzoor, Ali; Rafique, Sajid; Usman Iftikhar, Muhammad; Mahmood Ul Hassan, Khalid, and Nasir, Ali. "Study of Piezoelectric Vibration Energy Harvester with non-linear conditioning circuit using an integrated model". In: *International Journal of Electronics* 104.8 (2017), pp. 1317–1331.

[111] Marzencki, Marcin; Defosseux, Maxime, and Basrour, Skandar. "MEMS vibration energy harvesting devices with passive resonance frequency adaptation capability". In: *Journal of Microelectromechanical Systems* 18.6 (2009), pp. 1444–1453.

[112] Masana, R and Daqaq, Mohammed Farid. "Energy harvesting in the super-harmonic frequency region of a twin-well oscillator". In: *Journal of Applied Physics* 111.4 (2012), p. 044501.

[113] Masana, Ravindra and Daqaq, Mohammed F. "Relative performance of a vibratory energy harvester in mono-and bi-stable potentials". In: *Journal of Sound and Vibration* 330.24 (2011), pp. 6036–6052.

[114] Masana, Ravindra and Daqaq, Mohammed F. "Response of duffing-type harvesters to band-limited noise". In: *Journal of Sound and Vibration* 332.25 (2013), pp. 6755–6767.

[115] Mateu, Loreto and Moll, Francesc. "Review of energy harvesting techniques and applications for microelectronics". In: *VLSI Circuits and Systems II*. Vol. 5837. International Society for Optics and Photonics. 2005, pp. 359–373.

[116] Maurya, Deepam et al. "Energy harvesting and strain sensing in smart tire for next generation autonomous vehicles". In: *Applied Energy* 232 (2018), pp. 312–322.

[117] Meirovitch, Leonard. "Fundamentals of vibrations". In: McGraw Hill, 2001. Chap. 8.

[118] Memaya, Mounil; Moorthy, C Balakrishna; Tahiliani, Sahitya, and Sreeni, Siddarth. "Machine learning based maximum power point tracking in solar energy conversion systems". In: *International Journal of Smart Grid and Clean Energy* (2019).

[119] Mohan, Ned. "Power electronics: a first course". In: Wiley, 2011.

[120] Mohan, Ned. "Power electronics: a first course". In: Wiley, 2011.

[121] Moheimani, Reza. "A survey of recent innovations in vibration damping and control using shunted piezoelectric transducers". In: *IEEE transactions on control systems technology* 11.4 (2003), pp. 482–494.

[122] Monroe, JG et al. "Energy harvesting via thermo-piezoelectric transduction within a heated capillary". In: *Applied Physics Letters* 111.4 (2017), p. 043902.

[123] Morita, Koji and Tago, Makoto. "Operational characteristics of the Gaia snow-melting system in Ninohe, Iwate, Japan". In: *GHC Bulletin* 21.4 (2000), pp. 5–11.

[124] Moure, A et al. "Feasible integration in asphalt of piezoelectric cymbals for vibration energy harvesting". In: *Energy Conversion and Management* 112 (2016), pp. 246–253.

[125] Nabavi, Seyedfakhreddin and Zhang, Lihong. "Portable wind energy harvesters for low-power applications: A survey". In: *Sensors* 16.7 (2016), p. 1101.

[126] Nguyen, D. S.; Halvorsen, E.; Jensen, G. U., and Vogl, A. "Fabrication and characterization of a wideband MEMS energy harvester utilizing nonlinear springs". In: *Journal of Micromechanics and Microengineering* 20.12 (2010), p. 125009.

[127] AL-Oqla, Faris M.; Omar, Amjad A., and Fares, Osama. "Evaluating sustainable energy harvesting systems for human implantable sensors". In: *International Journal of Electronics* 105.3 (2018), pp. 504–517.

[128] Ottman, Geffrey K.; Hofmann, Heath F.; Bhatt, Archin C., and Lesieutre, George A. "Adaptive piezoelectric energy harvesting circuit for wireless remote power supply". In: *IEEE Transactions on power electronics* 17.5 (2002), pp. 669–676.

[129] Ottman, Geffrey K.; Hofmann, Heath F., and Lesieutre, George A. "Optimized piezoelectric energy harvesting circuit using step-down converter in discontinuous conduction mode". In: *IEEE Transactions on power electronics* 18.2 (2003), pp. 696–703.

[130] Pan, Pan; Wu, Shaopeng; Xiao, Yue, and Liu, Gang. "A review on hydronic asphalt pavement for energy harvesting and snow melting". In: *Renewable and Sustainable Energy Reviews* 48 (2015), pp. 624–634.

[131] Passacantilli, Fabio; Galassi, Carmen; Leonardi, Giorgia, and Dessi, Daniele. "Performance testing of piezoelectric energy harvesting for extracting energy from vibration". In: Workshop of Young Ceramists. Nov. 2018.

[132] Perez, Matthias; Boisseau, Sebastien; Gasnier, Pierre; Willemin, Jean, and Reboud, Jean-Luc. "An electret-based aeroelastic flutter energy harvester". In: *Smart materials and structures* 24.3 (2015), p. 035004.

[133] Pillatsch, Pit; Yeatman, Eric M, and Holmes, Andrew S. "A piezoelectric frequency up-converting energy harvester with rotating proof mass for human body applications". In: *Sensors and Actuators A: Physical* 206 (2014), pp. 178–185.

[134] Pillatsch, Pit; Yeatman, Eric M; Holmes, Andrew S, and Wright, Paul K. "Wireless power transfer system for a human motion energy harvester". In: *Sensors and Actuators A: Physical* 244 (2016), pp. 77–85.

[135] Power, Undergroung. *Lybra us a smart "Speed Absorber"*. URL: http://www.upgen.it/en/underground-power-lybra-speed-absorber/.

[136] Pozzi, Michele; Aung, Min SH; Zhu, Meiling; Jones, Richard K, and Goulermas, John Y. "The pizzicato knee-joint energy harvester: characterization with biomechanical data and the effect of backpack load". In: *Smart Materials and Structures* 21.7 (2012), p. 075023.

[137] Pozzi, Michele and Zhu, Meiling. "Plucked piezoelectric bimorphs for knee-joint energy harvesting: modelling and experimental validation". In: *Smart Materials and Structures* 20.5 (2011), p. 055007.

[138] Priya, Shashank. "Advances in energy harvesting using low profile piezoelectric transducers". In: *Journal of electroceramics* 19.1 (2007), pp. 167–184.

[139] Priya, Shashank. "Modeling of electric energy harvesting using piezoelectric windmill". In: *Applied Physics Letters* 87.18 (2005), p. 184101.

[140] Priya, Shashank; Chen, Chih-Ta; Fye, Darren, and Zahnd, Jeff. "Piezoelectric windmill: A novel solution to remote sensing". In: *Japanese journal of applied physics* 44.1L (2004), p. L104.

[141] Priya, Shashank; Song, Hyun-Cheol, et al. "A review on piezoelectric energy harvesting: materials, methods, and circuits". In: *Energy Harvesting and Systems* 4.1 (2019), pp. 3–39.

[142] Ramezanpour, Reza; Nahvi, Hassan, and Ziaei-Rad, Saeed. "Electromechanical behavior of a pendulum-based piezoelectric frequency up-converting energy harvester". In: *Journal of Sound and Vibration* 370 (2016), pp. 280–305.

[143] Rezaeisaray, Mehdi; El Gowini, Mohamed; Sameoto, Dan; Raboud, Don, and Moussa, Walied. "Low frequency piezoelectric energy harvesting at multi vibration mode shapes". In: *Sensors and Actuators A: Physical* 228 (2015), pp. 104–111.

[144] Rödig, Thomas; Schönecker, Andreas, and Gerlach, Gerald. "A survey on piezoelectric ceramics for generator applications". In: *Journal of the American Ceramic Society* 93.4 (2010), pp. 901–912.

[145] Romani, Aldo; Filippi, Matteo, and Tartagni, Marco. "Micropower design of a fully autonomous energy harvesting circuit for arrays of piezoelectric transducers". In: *IEEE Transactions on Power Electronics* 29.2 (2013), pp. 729–739.

[146] Roosegaarde, Studio. *Sustainable dance floor*. URL: https://www.studioroosegaarde.net/project/sustainable-dance-floor.

[147] Roundy, Shad and Zhang, Yang. "Toward self-tuning adaptive vibration-based microgenerators". In: *Smart structures, devices, and systems II*. Vol. 5649. International Society for Optics and Photonics. 2005, pp. 373–384.

[148] Sachan, Vibhav Kumar; Imam, Syed Akhtar, and Beg, Mirza Tariq. "Energy-efficient communication methods in wireless sensor networks: A critical review". In: *International Journal of Computer Applications* 39.17 (2012), pp. 35–48.

[149] Santos, Auteliano Antunes Dos; Hobeck, Jared D, and Inman, Daniel J. "Orthogonal spiral structures for energy harvesting applications: Theoretical and experimental analysis". In: *Journal of Intelligent Material Systems and Structures* 29.9 (2018), pp. 1900–1912.

[150] Sebald, Gael; Kuwano, Hiroki; Guyomar, Daniel, and Ducharne, Benjamin. "Experimental Duffing oscillator for broadband piezoelectric energy harvesting". In: *Smart materials and structures* 20.10 (2011), p. 102001.

[151] Sebald, Gael; Kuwano, Hiroki; Guyomar, Daniel, and Ducharne, Benjamin. "Simulation of a Duffing oscillator for broadband piezoelectric energy harvesting". In: *Smart Materials and Structures* 20.7 (2011), p. 075022.

[152] Sharma, Sukesha et al. "Piezoelectric energy harvesting and management in WSN using MPPT algorithm". In: *2016 International Conference on Wireless Communications, Signal Processing and Networking (WiSPNET)*. IEEE. 2016, pp. 2228–2232.

[153] Sharpes, Nathan; Abdelkefi, Abdessattar; Abdelmoula, Hichem, et al. "Mode shape combination in a two-dimensional vibration energy harvester through mass loading structural modification". In: *Applied Physics Letters* 109.3 (2016), p. 033901.

[154] Sharpes, Nathan; Abdelkefi, Abdessattar, and Priya, Shashank. "Two-dimensional concentrated-stress low-frequency piezoelectric vibration energy harvesters". In: *Applied Physics Letters* 107.9 (2015), p. 093901.

[155] Sharpes, Nathan; Vučković, Dušan, and Priya, Shashank. "Floor tile energy harvester for self-powered wireless occupancy sensing". In: (2016).

[156] Shenck, Nathan S. and Paradiso, Joseph A. "Energy scavenging with shoe-mounted piezoelectrics". In: *IEEE micro* 21.3 (2001), pp. 30–42.

[157] Shung, K. Kirk; Cannata, J.M., and Zhou, Qifa. "Piezoelectric materials for high frequency medical imaging applications: A review". In: *Journal of Electroceramics* 19.1 (2007), pp. 141–147.

[158] Sojan, Shancymol and Kulkarni, Ramesh K. "A Comprehensive Review of energy harvesting techniques and its potential applications". In: *International Journal of Computer Applications* 139.3 (2016), pp. 14–19.

[159] Song, Hyun-Cheol; Kumar, Prashant; Maurya, Deepam, et al. "Ultra-low resonant piezoelectric MEMS energy harvester with high power density". In: *Journal of Microelectromechanical Systems* 26.6 (2017), pp. 1226–1234.

[160] Song, Hyun-Cheol; Kumar, Prashant; Sriramdas, Rammohan, et al. "Broadband dual phase energy harvester: Vibration and magnetic field". In: *Applied Energy* 225 (2018), pp. 1132–1142.

[161] Stanton, Samuel C; Erturk, Alper; Mann, Brian P, and Inman, Daniel J. "Nonlinear piezoelectricity in electroelastic energy harvesters: modeling and experimental identification". In: *Journal of Applied Physics* 108.7 (2010), p. 074903.

[162] Stanton, Samuel C; McGehee, Clark C, and Mann, Brian P. "Reversible hysteresis for broadband magnetopiezoelastic energy harvesting". In: *Applied Physics Letters* 95.17 (2009), p. 174103.

[163] Tang, Liping and Wang, Jianguo. "Size effect of tip mass on performance of cantilevered piezoelectric energy harvester with a dynamic magnifier". In: *Acta Mechanica* 228.11 (2017), pp. 3997–4015.

[164] Tashiro, Ryoichi; Kabei, Nobuyuki; Katayama, Kunimasa; Tsuboi, E, and Tsuchiya, Kiichi. "Development of an electrostatic generator for a cardiac pacemaker that harnesses the ventricular wall motion". In: *Journal of Artificial Organs* 5.4 (2002), pp. 0239–0245.

[165] Tavakkoli, S Mehdi; Weaver, Paul M; Bowen, Christopher R; Inman, Daniel J, and Alicia, H. "AN ANALYTICAL STUDY ON PIEZOELECTRIC-BISTABLE LAMINATES WITH ARBITRARY SHAPES FOR ENERGY HARVESTING". In: (2015).

[166] Tianchen, Yuan; Jian, Yang; Ruigang, Song, and Xiaowei, Liu. "Vibration energy harvesting system for railroad safety based on running vehicles". In: *Smart materials and structures* 23.12 (2014), p. 125046.

[167] Todaro, Maria Teresa et al. "Biocompatible, flexible, and compliant energy harvesters based on piezoelectric thin films". In: *IEEE Transactions on Nanotechnology* 17.2 (2018), pp. 220–230.

[168] Toma, Daniel Mihail; Carbonell Ventura, Montserrat; Pujol Bresco, David; Manuel Lázaro, Antonio, and Miquel Masalles, Jaume. "An impacting energy harvester through piezoelectric device for oscillating water flow". In: *MARTECH 2013: 5th International Workshop on Marine Technology: 19th-20th of November, Vilanova i la Geltrú*. 2013, pp. 39–42.

[169] Tressler, James F.; Alkoy, Sedat, and Newnham, Robert E. "Piezoelectric sensors and sensor materials". In: *Journal of electroceramics* 2.4 (1998), pp. 257–272.

[170] Tung, Yen-Jung; Hu, Aiguo P., and Nair, Nirmal-Kumar. "Evaluation of micro controller based maximum power point tracking methods using dSPACE platform". In: *Australian university power engineering conference*. 2006.

[171] Turner, Kimberly L. et al. "Five parametric resonances in a microelectromechanical system". In: *Nature* 396.6707 (1998), pp. 149–152.

[172] Varghese, Ronnie Paul. "MEMS technologies for energy harvesting and sensing". PhD thesis. Virginia Tech, 2013.

[173] Viñolo, C; Toma, Daniel; Mànuel, A, and Rio, J del. "An ocean kinetic energy converter for low-power applications using piezoelectric disk elements". In: *The European Physical Journal Special Topics* 222.7 (2013), pp. 1685–1698.

[174] Viñolo, Carlos; Toma, Daniel; Mànuel, Antoni, and Rio, Joaquin del. "Sea motion electrical energy generator for low-power applications". In: *2013 MTS/IEEE OCEANS-Bergen*. IEEE. 2013, pp. 1–7.

[175] Vullers, Ruud J. M.; Elfrink, R.; Matova, S., and Wang, Yaming. "Large power amplification of MEMS harvester by a secondary spring and mass assembly". In: *Proc. PowerMEMS* (2012), pp. 211–4.

[176] Wang, Wei; Cao, Junyi; Bowen, Chris R; Inman, Daniel J, and Lin, Jing. "Performance enhancement of nonlinear asymmetric bistable energy harvesting from harmonic, random and human motion excitations". In: *Applied Physics Letters* 112.21 (2018), p. 213903.

[177] Wang, Wei; Cao, Junyi; Bowen, Chris R; Zhou, Shengxi, and Lin, Jing. "Optimum resistance analysis and experimental verification of nonlinear piezoelectric energy harvesting from human motions". In: *Energy* 118 (2017), pp. 221–230.

[178] Weimer, Michael A.; Paing, Thurein S., and Zane, Regan A. "Remote area wind energy harvesting for low-power autonomous sensors". In: *2006 37th IEEE Power Electronics Specialists Conference*. IEEE. 2006, pp. 1–5.

[179] Winter, Martin; Barnett, Brian, and Xu, Kang. "Before Li ion batteries". In: *Chemical reviews* 118.23 (2018), pp. 11433–11456.

[180] Xu, Chundong et al. "Bi-stable energy harvesting based on a simply supported piezoelectric buckled beam". In: *Journal of Applied Physics* 114.11 (2013), p. 114507.

[181] Yu, Qiangmo et al. "3D, wideband vibro-impacting-based piezoelectric energy harvester". In: *AIP Advances* 5.4 (2015), p. 047144.

[182] Zhang, Hongjiang; Jiang, Senlin, and He, Xuefeng. "Impact-based piezoelectric energy harvester for multidimensional, low-level, broadband, and low-frequency vibrations". In: *Applied Physics Letters* 110.22 (2017), p. 223902.

[183] Zhang, Jinhui et al. "A novel ropes-driven wideband piezoelectric vibration energy harvester". In: *Applied Sciences* 6.12 (2016), p. 402.

[184] Zhao, Sihong and Erturk, Alper. "On the stochastic excitation of monostable and bistable electroelastic power generators: relative advantages and tradeoffs in a physical system". In: *Applied Physics Letters* 102.10 (2013), p. 103902.

[185] Zhou, Maoying et al. "Modeling and preliminary analysis of piezoelectric energy harvester based on cylindrical tube conveying fluctuating fluid". In: *Meccanica* 53.9 (2018), pp. 2379–2392.

[186] Zhou, Shengxi; Cao, Junyi; Erturk, Alper, and Lin, Jing. "Enhanced broadband piezoelectric energy harvesting using rotatable magnets". In: *Applied physics letters* 102.17 (2013), p. 173901.

[187] Zhou, Shengxi; Cao, Junyi; Inman, Daniel J; Lin, Jing, et al. "Broadband tristable energy harvester: modeling and experiment verification". In: *Applied Energy* 133 (2014), pp. 33–39.

[188] Zhou, Shengxi; Cao, Junyi; Inman, Daniel J; Liu, Shengsheng, et al. "Impact-induced high-energy orbits of nonlinear energy harvesters". In: *Applied Physics Letters* 106.9 (2015), p. 093901.

[189] Zhou, Shengxi; Chen, Weijia; Malakooti, Mohammad H.; Cao, Junyi, and Inman, Daniel J. "Design and modeling of a flexible longitudinal zigzag structure for enhanced vibration energy harvesting". In: *Journal of Intelligent Material Systems and Structures* 28.3 (2017), pp. 367–380.

[190] Zhou, Shengxi; Hobeck, Jared D.; Cao, Junyi, and Inman, Daniel J. "Analytical and experimental investigation of flexible longitudinal zigzag structures for enhanced multi-directional energy harvesting". In: *Smart Materials and Structures* 26.3 (2017), p. 035008.

[191] Zhou, Zhiyong; Qin, Weiyang, and Zhu, Pei. "A broadband quad-stable energy harvester and its advantages over bi-stable harvester: simulation and experiment verification". In: *Mechanical Systems and Signal Processing* 84 (2017), pp. 158–168.

[192] Zhou, Zhiyong; Qin, Weiyang, and Zhu, Pei. "Harvesting performance of quad-stable piezoelectric energy harvester: modeling and experiment". In: *Mechanical Systems and Signal Processing* 110 (2018), pp. 260–272.

[193] Zhu, Dibin; Tudor, Michael J., and Beeby, Stephen P. "Strategies for increasing the operating frequency range of vibration energy harvesters: a review". In: *Measurement Science and Technology* 21.2 (2010), p. 022001.

[194] Zhu, Yang and Zu, Jean W. "Enhanced buckled-beam piezoelectric energy harvesting using mid-point magnetic force". In: *Applied Physics Letters* 103.4 (2013), p. 041905.